A Photoluminescence Study of Cadmium and Aluminium-Related Defects in Silicon

A Thesis for the degree of
DOCTOR OF PHILOSOPHY

Presented to
DUBLIN CITY UNIVERSITY

By
ENDA McGLYNN B.Sc.

Research Supervisor
PROF. MARTIN O. HENRY
School of Physical Sciences
Dublin City University

January 1996

Declaration

I hereby certify that this material, which I now submit for assessment on the programme of study leading to the award of Doctor of Philosophy is entirely my own work and has not been taken from the work of others save and to the extent that such work has been cited and acknowledged within the text of my work.

Signed: Enda McGlynn I.D. No.: 91700507

Enda McGlynn

Date: 17/1/1996

Table of Contents

Title Page i

Declaration ii

Table of Contents iii

Acknowledgements vi

Abstract vii

Chapter 1: Introduction

1.1: Basic Properties of Silicon 1

1.2: Impurities and Defects in Silicon 3

1.3: Common Impurities in Silicon 4

1.4: Oxygen-Related Defects 6

1.5: Cadmium in Silicon 8

1.6: Aluminium-Related Centre in Silicon 11

1.7: Concluding Remarks 12

Chapter 2: Basic Theory of Band Structure, Point Defects and Recombination Processes

2.1: Introduction 17

2.2: Electronic States 17

2.2.1: Impurity States 21

2.3: Vibrational States 22

2.3.1: Perfect Crystal 22

2.3.2: Crystal with Defects 23

2.4: Exciton States 24

2.4.1: Excitons bound to Donors and Acceptors 27

2.4.2: Excitons bound to Neutral Defects 28

2.5: Radiative Recombination 30

2.6: Interaction of Electron State with Vibrating Lattice 35

2.7: Temperature Dependence of Luminescence 40

2.8: Uniaxial Stress 45

2.8.1: Introduction 45
2.8.2: Rhombic I Centres 46
2.8.3: Interacting States 54
2.9: Zeeman Spectroscopy 58
2.10: Isotope Substitution 61
2.11: Conclusions 66

Chapter 3: Experimental Apparatus and Techniques
3.1: Introduction 73
3.2: Cryogenic Apparatus 74
3.3: Magnetic Field Facilities 76
3.4: Uniaxial Stress Facilities 81
3.5: FT Spectrometer System 83
3.6: Techniques 90
3.7: Conclusions 92

Chapter 4: 983meV Defect in Cadmium-Doped Silicon
4.1: Introduction 94
4.2: Sample Preparation and Defect Production 94
4.3: Spectral Features 96
4.4: Temperature Dependence of Cd_A Luminescence Band 99
4.5: Uniaxial Stress and Zeeman Spectroscopy of Cd_A Line 101
4.6: Chemical Identity of the Cd_A Defect Complex 111
4.7: Vibrational Sideband Structure 120
4.8: Conclusions 125

Chapter 5: 935meV Cadmium-Related Defect
5.1: Introduction 131
5.2: Sample Preparation and Defect Production 131
5.3: Spectral Features 132

5.4: Temperature Dependence of Cd_B Line 133
5.5: Uniaxial Stress and Zeeman Measurements on the Cd_B Line 134
5.6: Chemical Identity of the Cd_B Defect 141
5.7: Local Mode Behaviour of Cd_B Defect 143
5.8: Conclusions 144

Chapter 6: 1026meV Cadmium-Related Defect
6.1: Introduction 146
6.2: Sample Preparation and Defect Production 146
6.3: Spectral Features 148
6.4: Temperature Dependence of 1026meV System 149
6.5: Uniaxial Stress and Zeeman Spectroscopy of the 1026meV System 152
6.6: Chemical Identity of the 1026meV System 161
6.7: Vibrational Sideband Structure 168
6.8: Conclusions 171

Chapter 7: 922meV Aluminium-Related Defect
7.1: Introduction 175
7.2: Sample Preparation and Defect Production 175
7.3: Spectral Features 176
7.4: Temperature Dependence of 922meV System 177
7.5: Uniaxial Stress and Zeeman Spectroscopy of the 922meV Line 179
7.6: Conclusions 188

Chapter 8: Conclusions and Suggestions for Further Research
8.1: Conclusions 192
8.2: Suggestions for Further Work 195

Appendix 1 A1

Acknowledgements

I would like to thank my supervisor Prof. Martin O. Henry for giving me the opportunity to pursue very interesting research in his group and for the valuable help and guidance which he has given me throughout the course of my studies at D.C.U. In addition I would like to thank Dr. Siobhan Daly for giving so much of her time and knowledge in all aspects of the laboratory and analytical work during my Ph.D. I would like also to thank Dr. Kevin McGuigan for many enlightening discussions on and around the subject of PL and uniaxial stress and Dr. Celeste Do Carmo for devoting so much of her time to the subject matter of this thesis during her short visit to D.C.U in 1995.

I am extremely grateful to all my collegues at D.C.U. for their contribution of positive good humour, and would like to mention just a few who have made a lasting impact; Jim, Ciaran, Brian, Owen, Bill, Shane, Kate, Dirk, Pat, Ken, Ruth, Brigid, Will, Andy, Charles, Kevin, Aisling and Fidelma. The technical staff of the Physics Dept. deserve a special mention, especially Des Lavelle, without whose skill and apparently boundless patience this work could not have been completed, and also Al Devine for his much needed and appreciated help with the image scanner. Thanks also to my friends outside D.C.U.

Most of all though I would like to thank my father and mother for all their love, help and support throughout the years, and it is to them that I dedicate this thesis.

Abstract

Photoluminescence measurements of cadmium-implanted and aluminium-doped oxygen-rich silicon are presented in this thesis. Temperature dependence, uniaxial stress and Zeeman measurements were carried out on all the defects reported.

In the case of cadmium-implanted silicon, three new cadmium related defects are reported with zero phonon lines at ~ 1026meV, 983 meV and 935 meV. Temperature dependence studies indicate that the thermal binding energies of all the defects are in the range 13-17meV and no excited thermalising states are seen for the 983meV and 935meV lines. The 1026meV line shows clear evidence of an excited state at higher energy (~1.1meV). Uniaxial stress measurements reveal rhombic I (C_{2v}) symmetry for the 1026 meV and 983 meV lines. The 935 meV line is tentatively ascribed to monoclinic I symmetry. None of the cadmium-related lines show either a shift or splitting in magnetic fields up to 5 Tesla. Cadmium isotope substitution studies reveal the involvement of a single cadmium atom in each defect. Circumstantial evidence indicates the involvement of oxygen in the defects, as none of the defects are observed in oxygen lean silicon. The relationship between these cadmium-related defects and previously reported zinc-related defects is discussed.

In the case of aluminium-doped silicon, a previously reported defect with a zero phonon line at 922meV was investigated further. Measurements as a function of temperature reveal that the thermal binding energy is ~15meV and no evidence of thermalising states is seen. Uniaxial stress measurements reveal a low symmetry configuration for the 922meV line (monoclinic I, C_{1h}). This line neither shifts nor splits under magnetic fields of up to 5 Tesla. Similiarities in the behaviour under uniaxial stress of this defect and a previously reported aluminium-related defect are presented.

Chapter 1: Introduction

1.1: Basic Properties of Silicon

Silicon is the second most abundant element on earth, and makes up over twenty percent of the earth's crust. It is never found naturally in its elemental form, but mostly as silica (SiO_2) and silicates. The earliest use of elemental silicon was as an alloying element in the steel industry. The use of silicon in the electronics industry began in the early twentieth century with the fabrication of silicon-metal point contacts. The second world war produced great advances in the refinement and use of silicon. The first silicon monolithic integrated circuit was produced in 1959. Silicon is now by far the most important material in the semiconductor industry and the techniques used in its growth and refinement have reached a high level of sophistication. As an example of the worldwide production levels of silicon, in 1980 over 2500 tonnes of high-purity silicon were produced for the electronics industry. A comprehensive general review of the properties of silicon and the behaviour of impurities in silicon is given by Landolt (1984) and references to original work can be found there.

The most widely used growth method is the Czochralski, or vertical pull method. Czochralski originally developed this method to measure the crystallisation speed of metals. This technique involves preparing a melt of the semiconductor in a silica crucible. A small, oriented single crystal of the semiconductor, the seed, is then slowly pulled from the melt, and the crystal forms around this seed. When crucible contamination is a problem, the crystal can be purified using the float-zone technique. This involves heating a small section of the crystal until it is molten, and passing this molten section down the length of the crystal. Because of the difference in equilibrium impurity concentration levels in the solid and molten sections, impurities move into the molten section, and are finally frozen in the end of the crystal. One of the means of classifying silicon is on the basis of the growth technique used, either Czochralski (CZ) or float-zone (FZ).

The majority of silicon used nowadays for the electronics industry is CZ

grown. Because the crystals are pulled from silica crucibles they contain a large amount of dissolved O (Landolt 1984). The effects of the dissolved O on the silicon will be discussed later.

The quality of the crystal for use in device applications is crucial, and device failure is intimately linked to crystal quality. In order to ensure reliable, high yields for complex device structures such as those required for VLSI (very large scale integration), accurate knowledge of crystal quality and defect properties is required. The nature of these defects will be discussed later in this chapter.

Silicon crystallises in a diamond-like structure, with the translational symmetry of the face-centred cubic lattice, and a non-symmorphic space group O^7_h (octahedral point group, Koster 1957). The structure can be envisaged as two interpenetrating face-centred cubic Bravais lattices (figure 1.1.1). Each atom is tetrahedrally bonded to four others. The interatomic spacing at room temperature is 0.543nm.

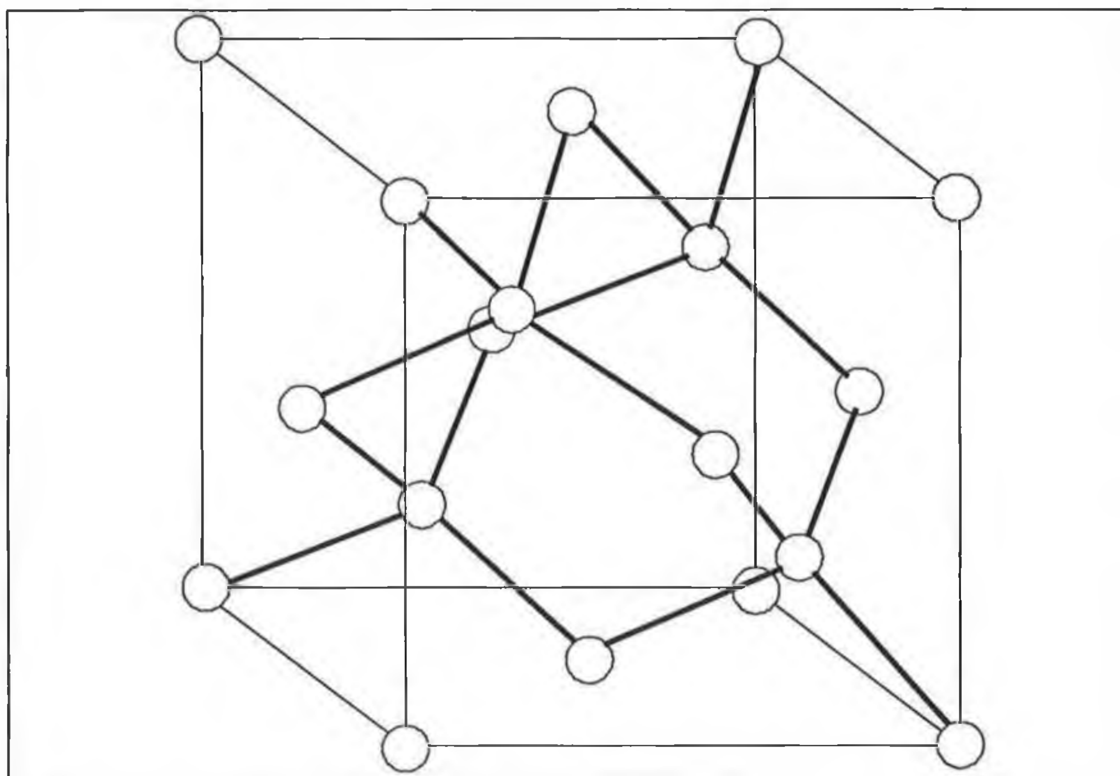

Figure 1.1.1: Diamond Crystal Structure, with Tetrahedral Bonding Shown

1.2: Impurities and Defects in Silicon

Crystal defects can be defined as any structure which disturbs the translational symmetry of the crystal. Defects can either be extended (such as edge dislocations or screw dislocations) involving many atoms and sometimes of macroscopic dimensions, or point defects involving a small number of atoms over a microscopic length scale (such as foreign impurity atoms, or native defects such as vacancies or self interstitials). The defects considered in this thesis are point defects. The study of point defects in semiconductors has been the focus of a great deal of attention throughout the past four decades, and many different point defects have been identified and studied in silicon and other semiconductors. A general review of this area is given by Bridges *et al.* (1990), while Davies (1989) gives a review of the properties of photoluminescence (PL) centres in silicon.

Because the crystal structure of silicon is relatively "open" with a packing fraction of ~0.34 (compared to a value of 0.74 for a close packed arrangement), impurity atoms are readily incorporated into the lattice structure, either as substitutional or interstitial atoms. The ability of defects to move through the lattice, an extremely important factor in the formation of complexes of defect atoms, is determined by many factors such as the defect size, bonding to other atoms in the lattice, position (substitutional or interstitial) and temperature. In general the diffusion coefficient of a defect can be given by the formula in equation 1.2.1;

$$D = D_0 \exp\left(-\frac{Q}{kT}\right) \qquad (1.2.1)$$

where Q is considered to be the activation energy for the defect to overcome the potential barrier between two adjacent sites, and D_0 is a constant (over temperature ranges of ~100°C) which can be thought of as the attempt frequency. The diffusion coefficient can vary over many orders of magnitude (Landolt 1984). Atoms which diffuse interstitially typically have diffusion coefficients of the order of 10^{-4} to 10^{-9} cm^2/s, while atoms which diffuse substitutionally can have diffusion coefficients as low as $10^{-16} cm^2/s$. The activation energies also vary a great deal, from typically ~0.3-

2eV for interstitial diffusion (although the silicon self-interstitial is mobile at very low temperatures, Watkins 1975) to ~2.5-4eV for substitutional diffusion (Landolt 1984).

Defects in silicon can have both beneficial and detrimental effects upon device operation. Intentional introduction of defects such as boron or phosphorous allows one to tailor the conductivity range and type of the silicon. This technology is the basis for all modern semiconductor devices. On the other hand, small quantities of unwanted defects such as chromium or iron can introduce deep recombination centres which destroy the operation of devices such as solar cells.

1.3: Common Impurities in CZ Silicon

Approximately 80% of the silicon grown by industry is CZ silicon. The two most common impurities in CZ silicon are O and C. Both of these impurities can complex with other impurities introduced into the material. The effects of these impurities on the silicon will be discussed in turn. A great deal of research has been done on the behaviour of these impurities in silicon and a detailed discussion is given in Davies (1989).

Oxygen: O, the most common contaminant in CZ silicon, is introduced into the molten silicon from the silica crucible during the crystal growth process. The solubility of O in silicon is given by (Mikkelsen 1986);

$$[O] = C \exp(-\frac{E}{kT}) \qquad (1.3.1)$$

with C=9 x 10^{22}cm^{-3} and E=1.52 ± 0.3eV. At the melt temperature of 1420°C this yields a value for [O] of ~2 x 10^{18}cm^{-3}. This concentration is mostly frozen in during the cooling process, leaving the silicon crystal supersaturated with O. The O atoms normally occupy interstitial sites in the crystal and are electrically neutral, preferentially bonding to 2 nearest neighbour silicon atoms (Kaiser *et al.* 1956, Hrostowski *et al.* 1957). The interstitial O atom readily diffuses at temperatures

greater than ~450°C (Corbett *et al.* 1964), with a thermal activation energy of 2.53eV and D_0=0.1 cm^2/s (Landolt 1984, Mikkelsen 1986). The O diffuses by jumping from one interstitial location to the next, and this allows it to complex with other defects in the silicon as will be seen later. The interstitial location of the O atom leads to an increase in volume of the crystal (Takano *et al.* 1973). The O interstitial (O_i) impurity gives rise to an infra-red (IR) absorption line at 1106 cm^{-1} which can be used to monitor the O content of the material (Kaiser *et al.* 1956, Krishnan *et al.* 1990). The presence of O in the silicon crystal can have both beneficial and harmful effects on the material. Among the detrimental effects of O in silicon is the formation of donor complexes during low temperature annealing (~450°C for tens of hours) due to O aggregation. The most commonly studied of these complexes are the thermal donor (TD) complexes which will be described later in this chapter. O precipitates can also cause dislocations which can adversely affect device performance by causing unwanted leakage currents, short circuits etc. (Landolt 1984). As the O atoms precipitate a large volume expansion (~250%) occurs locally due to the formation of silicon dioxide. This volume expansion causes a strain in the crystal which can be relieved by the emission of silicon self-interstitials. This relieves the strain, but causes the crystal to become supersaturated with point defects. These self-interstitials can aggregate into stacking faults which can have a detrimental effect upon device structures. Self-interstitials can also affect the diffusion of dopants, causing unwanted doping profiles.

There are also a number of beneficial aspects of the presence of O in silicon. The first of these is the intrinsic gettering effect cause by the precipitation of O impurity atoms. These precipitates act as gettering centres for fast-diffusing impurities such as Cu, Ni etc. which can adversely affect device performance. The second advantage of the presence of O in silicon is the wafer-hardening effect (Landolt 1984), which is particularly important during high-temperature processes.

Carbon: C is the second most common impurity in CZ silicon, generally occurring in concentrations 10-200 times less than those of O (Landolt 1984). C normally occupies a substitutional site in the silicon lattice (which is electrically neutral) and forms C-Si bonds. The vibrational modes of the C atom gives rise to an IR absorption band at 607cm^{-1}, and this band can be used to determine the substitutional C concentration in

the material (Krishnan *et al.* 1990 and references therein). The presence of substitutional C reduces the lattice parameter, in a manner consistent with linear interpolation between the extremes of pure diamond and pure silicon (Davies 1989). The diffusion of substitutional C is governed by the parameters D_0=1.9, Q= 3.15±0.2 eV in equation 1.2.1 (Newman *et al.* 1961, Landolt 1984). If the silicon lattice is subject to radiation damage which creates vacancies and interstitials, the substitutional C (C_s) can change places with an interstitial to become an interstitial C (C_i), which is highly mobile at temperatures greater than 300K. The activation energy of a C_i atom in equation 1.2.1 is in the range 0.72-0.88eV (Davies 1989 and references therein). C_i atoms produce IR absorption at 922cm^{-1} and 932cm^{-1}, which can be used to calibrate the interstitial C concentration (Chappell *et al.* 1987).

Carbon-Oxygen Complexes: In addition to the isolated O and C defects described above, O and C can complex to form defects also. A number of IR absorption bands have been attributed to C and O complexes (Krishnan *et al.* 1990 and references therein). A number of C-O complexes are produced by annealing radiation-damaged silicon. Examples of complexes of this nature are the "C centre" observed in PL which is a C_i-O_i complex and the "G centre" which is a C_i-C_s complex (Trombetta *et al.* 1987, Davies 1989 and references therein).

1.4: Oxygen-Related Defects

O is considered to be one of the most important elements in defect formation in CZ silicon. As has been mentioned previously, O atoms become mobile at T > 450°C and are available to complex with other defects in the crystal.

Among the most intensively studied O-related defects are the TD's. The TD's are a series of shallow double donors created by annealing O-rich, C-lean silicon at temperatures between 400°C and 500°C. These complexes were first reported in the mid 1950's (Fuller *et al.* 1954, Kaiser *et al.* 1958). It is generally believed that the TD's are O-related complexes, but despite intensive research over the past four decades their precise origin still remains unknown. A variety of theories have been put

forward to explain the observed TD properties and a review of the subject is given by Newman (1991). Other O-related defects such as the now-donors are formed at higher temperature anneals (600-700°C) in O-rich material (Kanamori *et al.* 1979).

O also complexes with the group III impurities Al (Drakeford *et al.* 1988, La Ferla *et al.* 1993) and boron (Van Kooten *et al.* 1987). The involvement of the group III acceptors in the formation of TD's has also been investigated, but no substantial evidence of acceptor involvement has been found (Van Kooten *et al.* 1987, Heijmink Liesert *et al.* 1993). No evidence of complex defect formation involving group VI elements has been reported (Irion *et al.* 1988).

Oxygen complexing with Group II Impurities: O reacts readily with group II compounds to form oxides such as ZnO and BeO, the bonding mechanism being largely ionic with the group II elements losing 2 outer electrons to fill the O valence shell. The incorporation of group II-O complexes in semiconductors has been verified for both Zn-O and Cd-O complexes in GaP (Henry *et al.* 1968). More recently, group II-O complexes have been associated with luminescence bands in CZ silicon. A number of PL bands have been associated with Zn-O complexes in CZ silicon (Henry *et al.* 1994), and a PL spectrum associated with Be-O complexes has also been reported (Daly 1994). A luminescence band in Hg-doped CZ silicon has been reported also, but it is attributed to a complex between a Hg atom and possibly C or Cu (Henry *et al.* 1994). Recent electrical and optical studies of Mg and Ca-related levels in silicon have been performed (Hassler *et al.* 1993) but preliminary investigations of Mg, Ca and Sr-implanted CZ silicon have yielded no new luminescence features (Daly 1995).

The role of O is extremely important in device manufacture, and the ability to control the behaviour of O in silicon requires knowledge of the interaction of O with other elements in the crystal. Knowledge of this nature will allow optimum control of the behaviour of the O content of a crystal. The study of Cd in CZ silicon was prompted mainly by the previous research carried out on Zn and Be complexes described above. The results for Be and Zn prompted an investigation of the properties of other group II impurities in silicon to establish whether the whole series of group II elements showed similar behaviour. The study of Cd was also prompted by research

on radioactive In isotopes (which decay to Cd) in silicon which is a continuing topic of research (Daly *et al.* 1994, Freehill 1995). The main aim of the research was to examine the behaviour of Cd in CZ silicon, and to compare and contrast this with the previously reported Be and Zn-related luminescence. The properties of Cd in silicon will now be described.

1.5: Cadmium in Silicon

In contrast to the other group II impurities Zn and Be, Cd impurities in silicon have received relatively little attention. Zn (and Zn-related) centres in silicon have been studied by electrical techniques (Fuller *et al.* 1957, Carlson 1957), IR spectroscopy (Merk *et al.* 1989), PL (Henry *et al.* 1994) and phonon spectroscopy (Staiger *et al.* 1994). Similarly Be (and Be-related) impurities have been studied by IR spectroscopy (Crouch *et al.* 1972) and PL (Gerasimenko *et al.* 1985, Campion *et al.* 1993 and Daly 1994).

Cd (and Cd-related) impurities in silicon have been studied using electrical techniques (Kapitonova *et al.* 1970, Gulamova *et al.* 1971, Dyunaidov *et al.* 1981, Arifov *et al.* 1984), capacitance techniques (Fahrner *et al.* 1972, Lebedev *et al.* 1978, Lang *et al.* 1991) and PAC techniques (Unterricker *et al.* 1983, Pasquevich *et al.* 1987, Achtziger *et al.* 1989, Wolf *et al.* 1989, Gebhard *et al.* 1991, Achtziger *et al.* 1993). To the best of our knowledge no other group has studied the behaviour of Cd in silicon using optical techniques, or, in particular, PL spectroscopy.

A brief review of previous studies on Cd-related defects in silicon will now be given. Cd has the electronic configuration {Kr}$4d^{10}5s^2$, and hence has two valence electrons. The group II elements in germanium are incorporated substitutionally and behave as double acceptors (Fisher *et al.* 1960), but in silicon this is not always the case. Mg for example is incorporated interstitially and behaves as a donor (Crouch *et al.* 1972), while Zn is incorporated substitutionally and behaves as a double acceptor. Early experiments on the electrical characteristics of Cd-diffused silicon established that Cd behaves in a similar manner to Zn, and is a double acceptor (Kapitonova *et al.* 1970, Gulamova *et al.* 1971). Measurements of the energy of Cd-related levels

have revealed 4 states in the bandgap, although the precise identification of these levels has varied from author to author. Table 1.5.1 (taken from Lang *et al.* 1991) shows the energy levels reported by various authors and the assignments given to various levels. The levels Cd(A1) and Cd(B1) appear to behave as single acceptors and are assigned to Cd complexes with other defects. Cd complexes with H and donors have also been reported (Achtziger *et al.* 1989, Gebhard *et al.* 1991).

Perturbed angular correlation (PAC) measurements on the microscopic environment of the Cd atom (decay product of radioactive In) have revealed that the Cd atom occupies a site of tetrahedral symmetry (Pasquevich *et al.* 1987). Electron-positron channelling experiments (Hofsass *et al.* 1987) have revealed that Cd implanted into silicon initially occupies interstitial locations but transfers to substitutional locations when annealed at ~250°C. In addition to this, theoretical investigations (Passeggi *et al.* 1991) have found that only a Cd substitutional position in the lattice can account for the presence of deep levels in the bandgap. Another indication that the Cd atom occupies a substitutional lattice site is that Cd has a relatively low diffusion coefficient and a relatively large activation energy (D_0=4.5cm^2/s, Q=3.9eV, Arifov *et al.* 1984).

From the results summarised above it appears that the Cd atom is incorporated substitutionally into the lattice and behaves as a double acceptor, in a similar manner to Zn. Evidence is seen of complexing with other defects, although none of the reports mention O as a constituent in these complexes.

In the study which forms the basis of this thesis Cd-implanted CZ silicon annealed in the temperature range 500°C-700°C was found to produce three previously unreported luminescence bands (figure 1.5.1) with zero phonon lines (ZPL) at ~935meV, 983meV and 1026meV. Because these bands are seen exclusively in CZ silicon, they are assigned to Cd-O complexes. All ZPL and local mode features show clear Cd isotope shifts, and dual isotope experiments have established that each defect contains one Cd atom. Very good fits to a rhombic I centre are found for uniaxial stress data on the 983meV and 1026meV systems. Full stress data have not been obtained for the 935meV system. Striking similarities are found between the 983meV system and a previously reported Zn-related system (Henry *et al.* 1994), in terms of the defect response to uniaxial stress and magnetic fields, local mode phonon structure

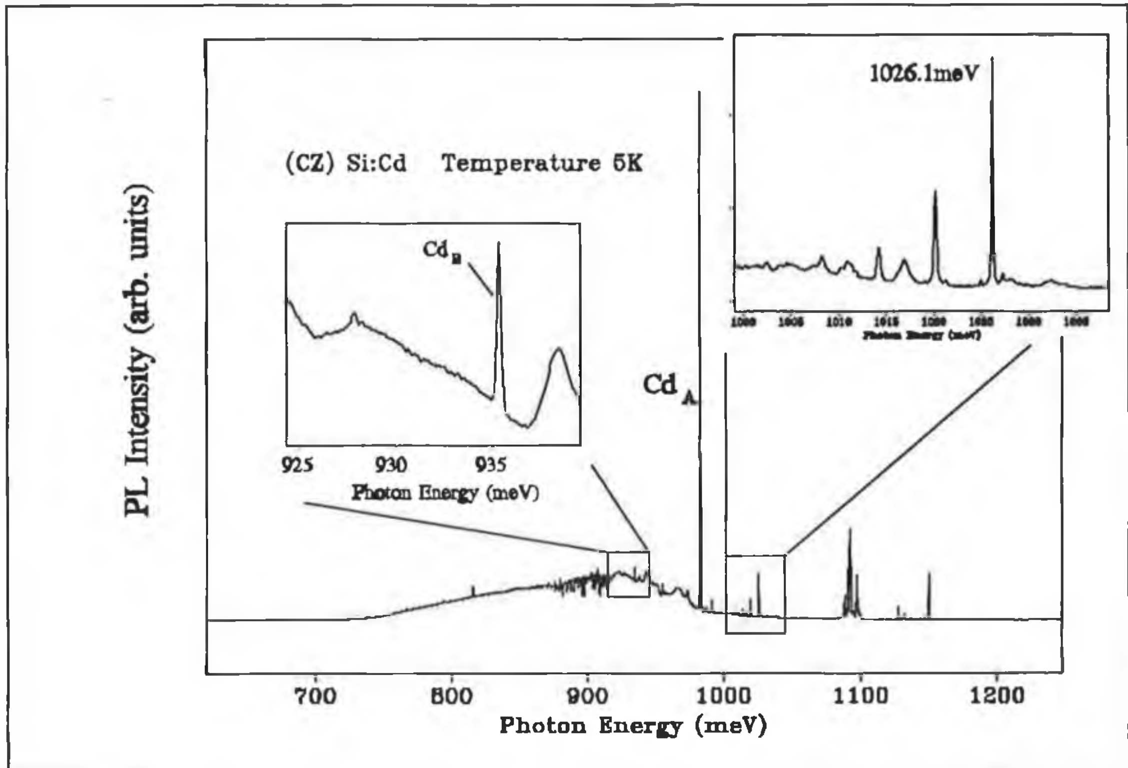

Figure 1.5.1: Cadmium-Related Luminescence Bands in CZ Silicon

and thermal binding energy indicating that the 983meV system is a Cd-related analog of the Zn-related defect. The 1026meV system has a pronounced local mode phonon sideband and a thermalising excited state ~1meV higher in energy. Very interesting behaviour is found in the behaviour of the luminescence as a function of temperature. A detailed analysis of the multi-phonon sideband is made in chapter 5, and excellent agreement between theory and experiment is found. Zeeman experiments for all three defects indicate a pseudodonor-type excited state structure.

The study of these luminescence bands forms the basis for the majority of the research in this thesis.

Table 1.5.1

Defect Level	Lang *et al.* 1991 E (meV)	Fahrner *et al.* 1972 E (meV)	Dyunaidov *et al.* 1981 E (meV)	Gulamova *et al.* 1971 E (meV)	Lebedev *et al.* 1978 E (meV)
$Cd^{0/-}$	E_v+485±27	-	E_c-540	E_v-550	-
$Cd^{-/2-}$	E_c-450±20	-	E_c-330	E_c-450	-
Cd-related levels (not identified)	Cd(B1) E_v+200±10 Cd(A1) E_v+205±10	E_v+300 E_c-200	E_c-450	-	E_c-320 E_c-420 E_c-560

1.6: Aluminium-Related Centre in Silicon

The study of Al-doped CZ silicon formed a small part of the research presented in this thesis. Once again the main thrust of the research was aimed at an understanding of the interaction of impurity elements in silicon. In a paper dealing with the formation of TD's in Al-doped material Drakeford *et al.* (1988) reported the presence of a PL system with ZPL at ~922meV. This PL system appears after anneals at 550°C for ~20 hours (or at 450°C for ~400 hours) in Al-doped C-rich CZ silicon. This line was assigned to an Al-C complex formed by mobile Al and C released from substitutional sites by self-interstitials. These self-interstitials are themselves thought to be released by the formation of O_2 dimers (Newman 1985). No evidence of a ^{13}C isotope shift was detected nor was the defect produced by Al diffusion into silicon. To account for this the authors proposed that the conditions necessary for defect formation were not present close to the surface. No subsequent details on the temperature dependence or uniaxial stress behaviour of the defect were reported.

Because of the lack of temperature dependence, uniaxial stress and Zeeman data, it was decided to investigate the behaviour of the defect under these perturbations. No attempt was made to investigate the detailed chemical nature of the defect or of its formation kinetics in different types of materials (C-rich, C-lean, FZ etc.). We have found striking similarities in the behaviour under uniaxial stress of the 922meV defect and another defect reported in Al-doped silicon (Irion *et al.* 1988) with a ZPL at ~886meV. Parallels between this result for C-rich Si:Al and similar results for C-rich Si:Be and Si:Li will be discussed later.

1.7: Concluding Remarks

In this chapter, the basic properties of silicon were considered and the effect of impurities on the silicon itself and on fabricated devices outlined. The behaviour of the native impurities (C and O) was considered, with particular attention paid to the behaviour of O and its interaction with foreign impurities. Three previously unreported PL systems in Cd-implanted CZ silicon were introduced and tentatively assigned to Cd-O complexes. As was described in section 1.5, these Cd-related defects exhibited very interesting properties and similarities with previously reported Zn-related systems are very striking. These luminescence systems form the basis for the majority of the work in this thesis. In addition a previously reported Al-related complex was introduced. This complex was also studied as part of the research.

Chapter 2 contains an introduction to the theory of the electronic and vibrational states of defects in silicon. Chapter 3 contains details on the experimental apparatus used to perform the research. Chapters 4, 5, 6 and 7 contain results on the defects mentioned in the previous paragraph. Chapter 8 contains conclusions drawn from the research and suggestions for further work needed.

Chronologically the study of the 922meV Al-related line began the research documented in this thesis. Subsequently the topicality of the question of O complexing with group II impurities resulted in the main focus of the research transferring to the Cd-related defects.

References

N. Achtziger, S. Deubler, D. Forkel, H. Wolf and W. Witthuhn (1989). Appl. Phys. Lett. **55**, 766.

N. Achtziger and W. Witthuhn (1993). Phys. Rev. B **47**, 6990.

A. A. Arifov and D. Rakhimbaev (1984). Sov. Phys. J. **27** no. 11, 967.

J. D. Campion, K. G. McGuigan, M. O. Henry and M. H. Nazare (1993). Mater. Sci. Forum **117-118**, 177.

R. O. Carlson (1957). Phys. Rev. **108**, 1390.

S. P. Chappel and R. C. Newman (1987). Semicond. Sci. and Technol. **2**, 691.

J. W. Corbett, R. S. McDonald and G. D. Watkins (1964). J. Phys. Chem. Solids **25**, 873.

R. K. Crouch, J. B. Robertson and T. E. Gilmer (1972). Phys. Rev. B **5**, 3111.

S. E. Daly (1994). Ph.D. Thesis, Dublin City University.

S. E. Daly (1995). Private Communication.

G. Davies (1989). "The Optical Properties of Luminescence Centres in Silicon", Physics Reports **176**, 3&4, 83.

A. C. T. Drakeford and E. C. Lightowlers (1988). Defects in Electronic Materials Symp., Boston MA. USA. Mater. Res. Soc., 209.

S. S. Dyunaidov, N. A. Urmanov, M. V. Gafurova (1981). Phys. Stat Solidi A **66,** K79.

W. Fahrner and A. Gotzberger (1972). Appl. Phys. Lett. **21,** 329.

P. Fisher and H. Y. Fan (1960). Phys. Rev. Lett. **5,** 195.

K. Freehill (1995). Private Communication.

C. S. Fuller, J. A. Ditzenberger, N. B. Hannay and E. Buehler (1954). Phys. Rev. **96,** 833.

C. S. Fuller and F. J. Morin (1957). Phys. Rev. **105,** 379.

M. Gebhard, B. Vogt and W. Witthuhn (1991). Phys. Rev. Lett. **67** no. 7, 847.

N. N. Gerasimenko, B. A. Zaltsev, L. N. Safronov and L. S. Smirnov (1985). Sov. Phys. Semicond. **19**, 762.

M. A. Gulamova, I. Z. Karimova and P. I. Knigin (1971). Sov. Phys. Semicond. **5,** 687.

C. Hassler and G. Pensl (1993). 17th Int. Conf. on Defects in Semiconductors ICDS-17, Gmunden (Austria).

B. J. Heijmink Liesert, T. Gregorkiewicz and C. A. J. Ammerlaan (1993). Phys. Rev. B **47,** 7005.

C. H. Henry, P. J. Dean and J. D. Cuthbert (1968). Phys. Rev. **166,** 754.

M. O. Henry, J. D. Campion, K. G. McGuigan, E. C. Lightowlers, M. C. doCarmo and M. H. Nazare (1994). Semicond. Sci. and Technol. **9,** 1375.

H. Hofsass, G. Lindner, S. Winter and E. Recknagel (1987). Nuclear Phys. Applicat. on Mater. Sci., Proc. NATO Advanced Sci. Inst., Portugal, Publ. Kluwer Acad.

H. J. Hrostowski and R. H. Kaiser (1957). Phys. Rev **107**, 966.

E. Irion, N. Burger, K. Thonke and R. Sauer (1988). Phys. Rev. B **38**, 13079.

W. Kaiser, P. H. Keck and C. F. Lange (1956). Phys. Rev. **101**, 1264.

W. Kaiser, H. L. Frisch and H. Reiss (1958). Phys. Rev. **112**, 1546.

A. Kanamori and M. Kanamori (1979). J. Appl. Phys. **50**, 8095.

L. M. Kapitanova, A. A. Lebedev and N. A. Sultanov (1970). Sov. Phys. Semicond **4**, 954.

G. F. Koster (1957). Solid State Physics **5**, 173.

K. Krishnan, P. J. Stout and M. Watanabe (1990). "Characterisation of Semiconductor Silicon Using Fourier Transform Infrared Spectroscopy", chap. 6 in "Practical Fourier Transform Infrared Spectroscopy", Academic Press.

A. La Ferla, L. Torrisi, G. Galvagno, E. Rimini, G. Ciavola, A. Carnera and A. Gasparotto (1993). Appl. Phys. Lett. **62**, 393.

Landolt-Bornstein (1984). "Numerical Data and Functional Relationships in Science and Technology; Group III: Crystals and Solid State Physics" vol. 17: Technology of Si, Ge and SiC, editors O. Madelung, M. Schultz and H. Weiss, Springer-Verlag

M. Lang, G. Pensl, M. Gebhard, N. Achtziger and M. Uhrmacher (1991). Appl. Phys. A **53**, 95.

A. A. Lebedev, A. T. Mamadalimov, M. A. Tairov (1978). Izv. Akad. Nauk. Uzbek SSR, Ser. fiz.-mat. Nauk No. **2**, 38.

E. Merk, J. Heyman and E. E. Haller (1989). Solid State Commun. **72**, 851.

J. C. Mikkelsen (1986). Mater. Res. Soc. Symp. Proc. **59**, 19.

R. C. Newman and J. Wakefield (1961). J. Phys. Chem. Solids **19**, 230.

R. C. Newman (1985). J. Phys. C: Solid State Physics **18**, L967.

R. C. Newman (1991). Vacuum **42** nos. 5-6, 379.

A. F. Pasquevich and R. Vianden (1987). Phys. Rev. B **35**, 1560.

M. C. G. Passeggi, S. J. Sferco and M. A. Caravaca (1991). 5th Brazilian School Semiconductor Phys, Sao Paulo, Brazil World Scientific.

J. Staiger, P. Gross, K. Lassman, H. Bracht and N. A. Stolwijk (1994). Mater. Sci. Forum. **143-147**, 675.

Y. Takano and M. Malei (1973). In "Semiconductor Silicon", editors H. R. Huff and R. B. Burgess, Electrochemical Society, Princeton, 469.

J. M. Trombetta and G. D. Watkins (1987). Appl. Phys. Lett. **51**, 1103.

S. Unterricker and F. Schneider (1983). Phys. Stat Solidi A **75**, 155.

J. J. van Kooten, T. Gregorkiewicz, A. J. Blaakmeer and C. A. J. Ammerlaan (1987). J. Phys. C: Solid State Physics **20**, 2183.

G. D. Watkins (1975). Phys. Rev. B **12**, 5824.

Chapter 2: Basic Theory of Band Structure, Point Defects and Recombination Processes

2.1: Introduction

When the translational symmetry of a perfect crystal is broken by the introduction of an impurity, new energy states appear in the crystal. These states can appear either in the valence or conduction bands (and are called resonances) or in the previously forbidden energy gap. The electronic structure of these levels is sensitive to the defect properties in the crystal, such as chemical identity, valence state, site symmetry, vibrational coupling etc. In this chapter the basic theory concerning defect energy levels is discussed. Particular attention is paid to the interaction of these crystal defects with light; these interactions determine the nature and extent of the optical transitions between levels. In addition, the behaviour of the spectrum of the material as a function of temperature, uniaxial stress, isotope substitution etc. is discussed with a view to extracting the maximum information on the defect from the spectra. It is these "perturbation" techniques which provide the majority of information concerning the defect, such as site symmetry, binding energy and chemical identity.

2.2: Electronic States

For the case of perfect periodic lattice structure the Schrodinger equation can be written as;

$$-\frac{h^2}{8\pi^2 m}\nabla^2\psi(r) + V(r)\psi(r) = E\psi(r) \qquad (2.2.1)$$

The potential V(r) is a periodic function with the period of the lattice and thus the eigenfunctions of this equation can be written in the Bloch form;

$$\psi(r) = u_k(r)\, e^{ik.r} \qquad (2.2.2)$$

where $u_k(r)$ is a function with the periodicity of the lattice. The parameter $\boldsymbol{k}$ is related to the lattice translation operator and is known as the crystal momentum (Kittel 1986). If the case of a simple one dimensional lattice is considered, the $\boldsymbol{k}$ values can range from $-\pi/a$ to π/a, where a is the primitive lattice translation. This range is known as the first Brillouin zone. All other $\boldsymbol{k}$ values outside this range can be shown to give identical eigenvalues (under a lattice translation) as a $\boldsymbol{k}$ value within the first Brillouin zone and are therefore equivalent. Applying the Born-Von Karman boundary conditions to the problem, it emerges that the $\boldsymbol{k}$ values form a quasi-continuous range from $-\pi/a$ to π/a. The parameter $\boldsymbol{k}$ is also known as the wavevector, in analogy with the free electron wavevector ($k_{free} = 2\pi/\lambda_{DeBroglie}$). Good general introductions to energy band structure are given by Kittel (1986) and Ashcroft and Mermin (1976).

By inserting the Bloch equation (2.2.2) into equation (2.2.1), the energy eigenvalues (for fixed $\boldsymbol{k}$) are characterised by the band index n. Allowing the $\boldsymbol{k}$ value to vary continuously generates the so-called energy bands of the lattice, shown schematically for a hypothetical example in figure 2.2.1., where the energy in each band varies smoothly with $\boldsymbol{k}$.

If the argument is extended to three dimensional lattices, such as the silicon lattice, the full energy bands cannot be drawn in three dimensions. It generally suffices to plot the energy as a function of $\boldsymbol{k}$ along specific high-symmetry directions in the crystal (Tinkham 1964). An example of such a plot is shown for the silicon lattice in figure 2.2.2. The labels $\Gamma^{25'}$ etc. are group theoretical notations describing the symmetry and irreducible representation of the Bloch functions at that point in $\boldsymbol{k}$-space (Bouckaert *et al.* 1936). It can be seen that a "forbidden" energy gap exists between the $\Gamma^{25'}$ band and the Γ^{15} band. This means that there are no solutions to the Schrodinger equation for this range of energies.

The occupation of the bands and the size of the energy gap between the bands determine whether the material is a conductor, insulator or semiconductor. In pure silicon at low temperatures, the band up to the point $\Gamma^{25'}$ (valence band) is filled with electrons, while the next highest band (Γ^{15}, conduction band) is completely empty.

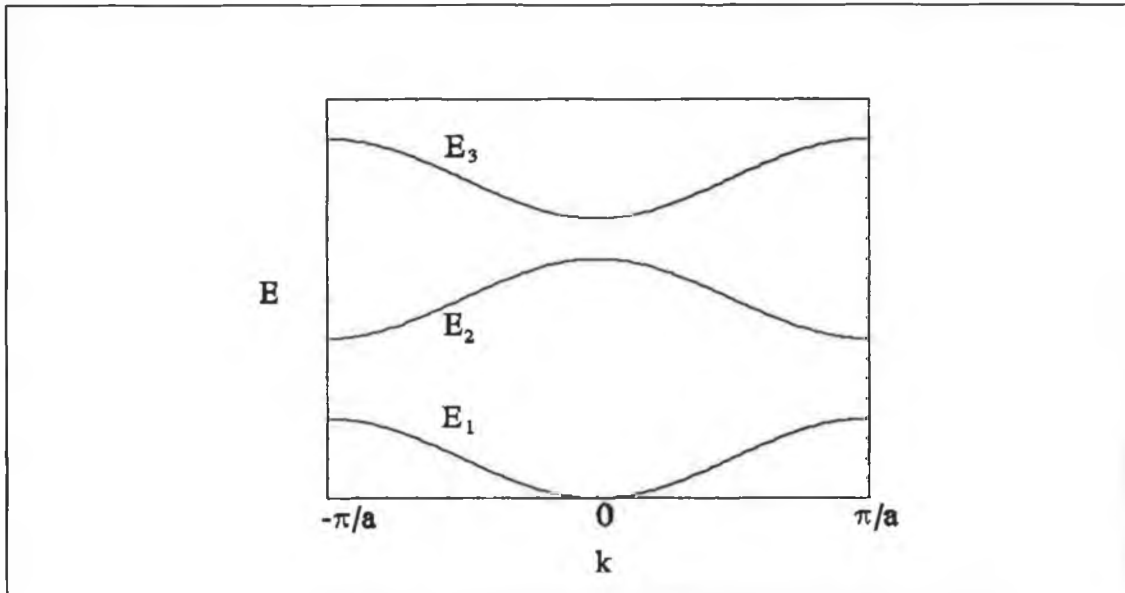

Figure 2.2.1: Energy bands plotted for simple one-dimensional lattice

This fact, combined with the relatively small band gap of silicon (~ 1.17eV at low temperatures) causes silicon to behave as a semiconductor. It will be noticed from figure 2.2.2 that the minimum energy of the conduction band occurs at the point X^1 whereas the maximum energy of the valence band occurs at $\Gamma^{25'}$. Because these extrema are not at the same point in k-space, the band gap of silicon is termed indirect. The band gap type has a significant effect on the optical properties of the material in question. Table 2.2.1 lists some common semiconductors with their band gap energies and type (direct or indirect).

When an electron is excited from the top of the valence band into the conduction band (by optical or electrical energy sources for example), an empty state is left behind in the valence band. The excited electron can contribute to the conductivity of the material and behaves as a negative particle of effective mass;

$$m_e^* = \frac{1}{\frac{4\pi}{h}\frac{d^2E_c(k)}{dk^2}} \qquad (2.2.3)$$

The empty state can also contribute to the conductivity of the material, and is

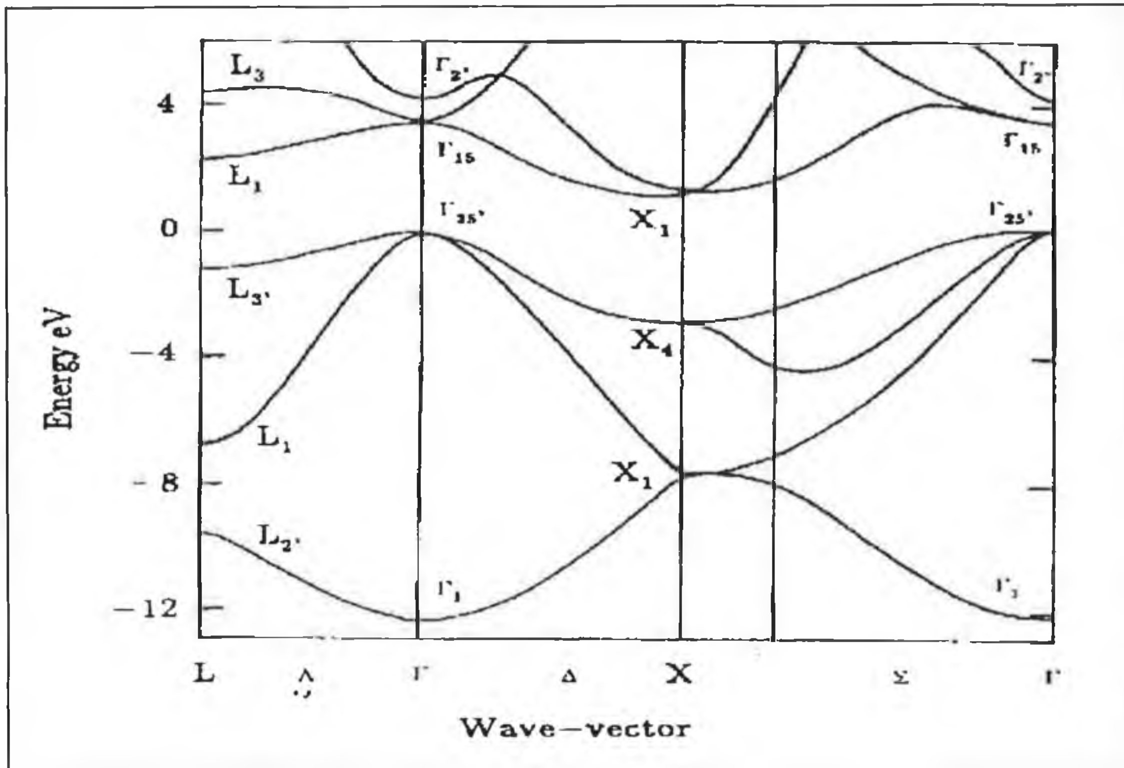

Figure 2.2.2: Energy band structure of silicon plotted along major symmetry directions (Chelikowsky *et al.* 1974)

Table 2.2.1:

Material	Bandgap(eV) at 300K	Gap Type
Diamond (C)	5.48	indirect
Silicon	1.17	indirect
Germanium	0.74	indirect
GaN	3.47	direct
InP	1.42	direct

termed a hole. This empty state behaves as a positive particle with positive effective mass;

$$m_h^* = \frac{1}{\frac{4\pi}{h}\frac{d^2E_v(k)}{dk^2}} \qquad (2.2.4)$$

In the case of silicon (and other III-V and diamond-like semiconductors) there exist two hole bands degenerate in energy at k=0 and these have different masses. They are referred to as the light hole and heavy hole band. A single electron band with six equivalent minima along <100>-type directions (X axis in figure 2.2.2) forms the conduction band edge in silicon.

2.2.1: Impurity States

As was mentioned in section 2.1, when an impurity is introduced into the crystal, the translational symmetry of the crystal is disturbed, and new energy states appear, either resonant with the bands or in the energy gap. The impurity states in the energy gap are of most interest in semiconductor science, because they can be used to tailor the conductivity level and carrier type.

Defects which create energy levels close to the conduction or valence band edge usually can be described by effective mass theory (EMT). This model treats the impurity potential as a small perturbation to the crystal, and constructs the impurity eigenfunctions from a summation of band eigenfunctions close to the band extremum. The final result is an eigenfunction which takes the form of a Bloch band edge function multiplied by a hydrogenic envelope function (with corrections for the effective mass and dielectric constant). This use of a hydrogenic solution allows one to neglect the complicated details of the crystal potential. The crystal potential only enters the solution in the form of the effective mass parameter, hence the origin of the EMT title (Kohn 1957). This approach would seem to indicate that elements of the same column in the periodic table would give identical energy states in the band gap (for example an electron bound to either P or As would see a potential of $4\pi e/r^2$ in both cases). The ground state of the defect however is subject to a large defect specific chemical shift (valley-orbit interaction, Kohn 1957). The EMT works well for

the excited states of shallow donors and acceptors in silicon (Kohn 1957), and allows one to classify the energy states according to the standard hydrogenic notation s, p, d etc..

Defects which create energy levels far from the band edges cannot be described using EMT. The energy eigenfunctions have contributions from Bloch functions with wavevectors from all points in the Brillouin zone. In this case many of the assumptions made in the formulation of EMT are invalid. These defects require specialised theoretical treatment (Pantelides 1978).

2.3: Vibrational States

2.3.1: Perfect Crystal

Thermal energy in crystals takes the form of mechanical vibrations of the crystal structure. These vibrations occur at a range of frequencies, and are referred to as the normal modes of the crystal. A perfect crystal containing N atoms will have 3N normal modes of vibration (corresponding to 3 degrees of freedom for each atom). All the information on these normal modes can be contained in the first Brillouin zone, because all other wavevector values correspond to identical atomic motions. Figure 2.3.1 shows a graph of frequency versus wavevector for the silicon lattice, showing the acoustic and optical modes (Zdetsis 1979).

When a quantum mechanical analysis is applied to the normal modes, each mode is characterised by its $\boldsymbol{k}$ value, frequency and occupation number. The occupation number is related to the classical amplitude of vibration. Each normal mode can have an occupation number $n_k \geq 0$. A normal mode with $n_k = p$ is said to have p phonons involved in the vibration. The energy of a mode containing p phonons is given by equation 2.3.1;

$$E_p = (p + \frac{1}{2})\hbar\omega \qquad (2.3.1)$$

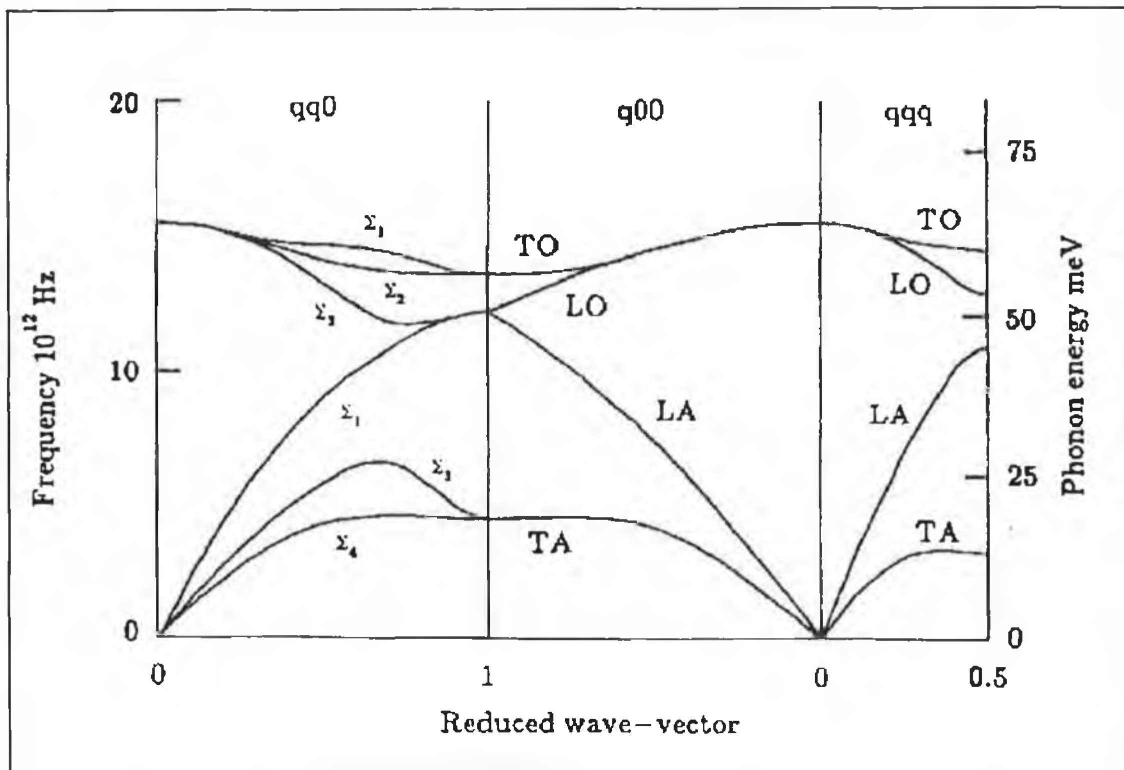

Figure 2.3.1: Phonon dispersion curves for silicon plotted along major symmetry directions (Zdetsis 1979)

where ω is the angular frequency of the normal mode.

Phonons can be considered to behave as particles of energy $\hbar\omega$ and wavevector k when interacting with electrons or photons.

2.3.2: Crystal With Defects

When the translational symmetry of the crystal is broken by the introduction of a defect, the crystal normal modes are disturbed and new modes of vibration will be introduced analogous to the situation for electronic states. These vibrational modes will involve vibrations of the defect and its immediate surroundings, i.e. the vibrations will be localised about the defect. This type of mode is known as a local mode. When the frequency of the mode lies in the frequency range of the lattice vibrations it is known as a resonance.

Local modes will have defect specific frequencies, but as a general rule light atoms will have high frequencies as would be expected. Atoms such as C in silicon have local mode energies greater than the largest lattice vibrational energy (~ 64meV). Heavier atoms such as Cd have smaller local mode frequencies (local mode of 983meV Cd_A line is ~ 9meV, see chapter 4) which are resonant with the lattice modes. Resonant modes tend to have a broader width because of their interaction with the degenerate lattice modes. Because the local mode vibration is concentrated around the impurity atom, it is sensitive to changes in the impurity state, such as electronic transitions and changes in isotopic mass. Examples of the effect of isotopic substitution on local modes is shown for Cd-related defects in chapters 4, 5 and 6 and is discussed in detail in section 2.10. A general introduction to local mode vibrations in solids is given by Watts (1977) and Stoneham (1985).

Electronic transitions can couple to both local and lattice modes to produce a phonon sideband. Information on the strength of electron-lattice coupling can be obtained from a study of this sideband (section 2.6).

2.4: Exciton States

When an electron-hole pair has been excited, it would be natural to assume that both particles would be free to move independently in the conduction and valence bands, respectively. This picture neglects the Coulomb attraction between the particles, which causes the electron and hole to become bound together. This state is known as an exciton, and tends to be short-lived because the electron and hole can recombine. The original concept of the exciton was reported by Frenkel (1931, 1936) and Wannier (1937).

Because the electron-hole pair is free to move as an entity throughout the crystal, the exciton is referred to as a free exciton (FE). When the electron-hole pair recombine and emit optical radiation, the emission lineshape is characteristically broad (~ kT) and asymmetric, with a high energy tail and sharp low energy cut-off. The high energy tail is due to the recombination of free excitons with varying degrees of kinetic energy (which can be determined approximately by Maxwell-Boltzmann statistics).

The electron-hole pair can be tightly bound together and in close proximity to each other (on the same atomic site), in which case the excitation is known as a Frenkel exciton (Frenkel 1931, 1936). A Frenkel exciton can be visualised as an excitation of a single atom, and this excitation can be transferred from atom to atom throughout the crystal. Frenkel excitons are generally associated with ionic solids such as KCl. The opposite extreme of a loosely bound electron-hole pair, with the electron and hole widely separated in space is known as a Wannier exciton (Wannier 1937, Mott 1938). Wannier excitons are generally associated with covalent solids such as Ge, Si and other common semiconductors.

In the Wannier picture the electron and hole orbit each other and a hydrogenic-type model is used to calculate the energy level structure of the exciton. The equation for the energy levels of the exciton is given by the well-known Bohr formula with appropriate dielectric constant and reduced mass (Bransden 1992);

$$E_{exc} = \frac{-m_r q^4}{2h^2 \varepsilon n^2} \quad (2.4.1)$$

where n is the term number (n is an integer ≥ 1), m_r is the reduced mass, ε is the dielectric constant, q the electronic charge and h is Planck's constant. The reduced mass m_r is given by;

$$\frac{1}{m_r} = \frac{1}{m_e} + \frac{1}{m_h} \quad (2.4.2)$$

with m_e and m_h given by equations 2.2.3 and 2.2.4. Figure 2.4.1 shows schematically the hydrogenic levels in relation to the conduction and valence bands. The ionisation limit corresponds to the conduction band edge.

The exciton binding energy is usually ~0.01eV and for this reason exciton phenomena are only observed in high-purity crystals at low temperatures.

If an electron-hole pair becomes localised at a defect site in a crystal, the exciton is then termed a bound exciton (BE). The existence of bound excitons was predicted in the late 1950's when the similarity between hydrogenic systems and donor(acceptor) bound excitons was noticed (Lampert 1958). Bound excitons were

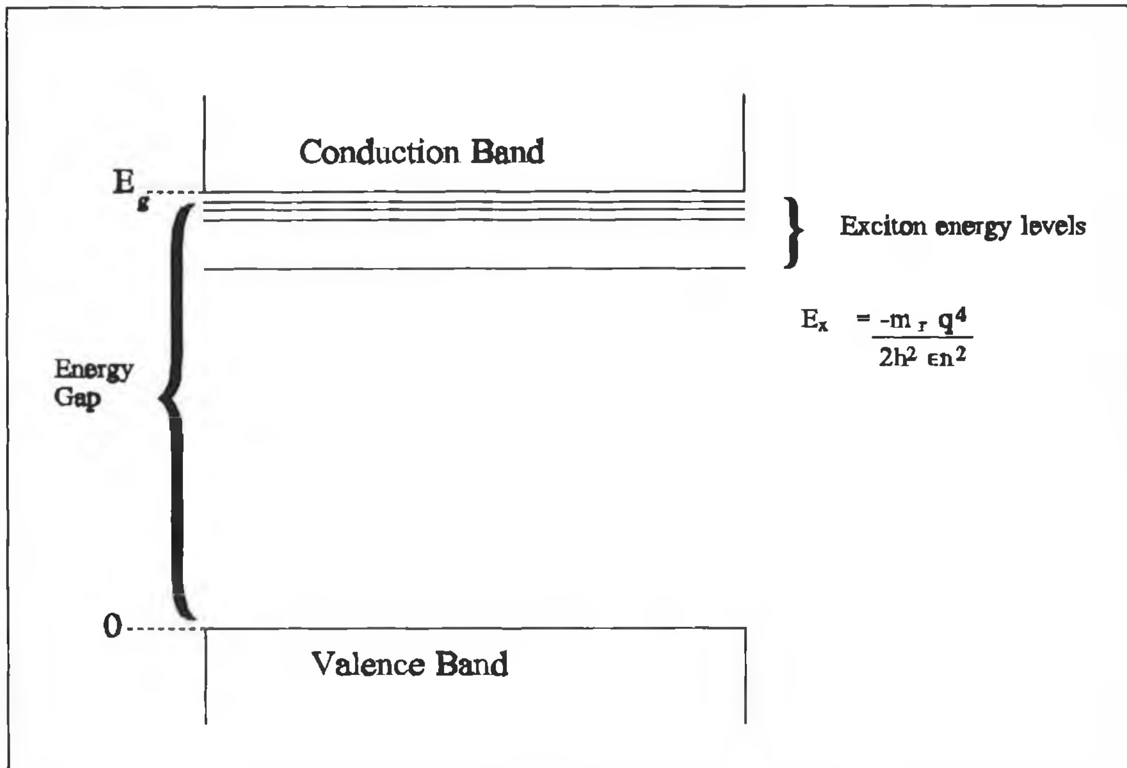

Figure 2.4.1: Hydrogenic series of excitonic levels in the band gap

first observed by Haynes (1960) through the discovery of sharp lines in the PL spectra of silicon containing small dopant concentrations. The exciton can be localised by a variety of mechanisms, including strain fields, electronegativity variations around the defect and coulombic attractions. The excitonic energy states are determined by factors such as which particle is weakly bound and which is strongly bound, and also by the number of particles in the excitonic complex. Therefore, donor BE's, acceptor BE's and neutral(isoelectronic) BE's all show different energy level structure (sections 2.4.1 and 2.4.2). There are a number of excellent review papers on the structure of BE's including Dean *et al.* (1979) and Monemar *et al.* (1987). A review of the use of PL in the characterisation of BE states of impurities in silicon is given by Davies (1989).

The lineshape of recombination of a bound exciton is narrow and symmetrical, indicating that the transition is not broadened by the kinetic energy present for a free particle in a crystal. A comparison of free exciton (upper curve) and bound exciton (lower curve) lineshapes is shown in figure 2.4.2. The lines labelled B_1, B_2 and B_3

correspond to luminescence (in the transverse optic (TO) phonon replica region) from multi-bound exciton complexes with 1, 2 or 3 bound excitons respectively. The FE TO phonon replica can also be seen in the lower curve.

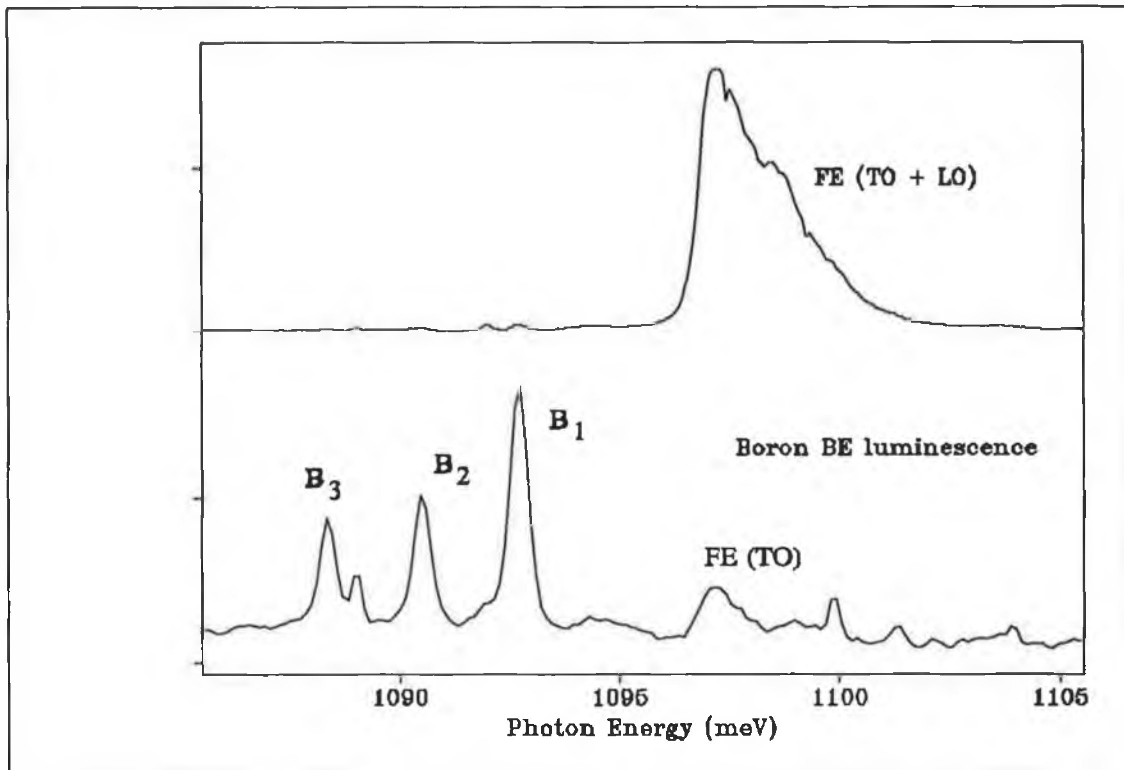

Figure 2.4.2: Comparison of free exciton (FE) and bound exciton (BE) luminescence line shapes

Bound excitons often give rise to shallow or weakly bound states in the band gap, such as the boron BE which has a no-phonon (NP) transition at ~ 1150meV (Kosai *et al.* 1974). In other cases (such as the Cd_A line presented in chapter 4) one of the particles is tightly bound to the defect, while the second particle is more loosely bound via Coulomb attraction.

2.4.1: Excitons Bound to Donors and Acceptors

A neutral, substitutional donor can bind an electron initially (due to its electron-attractive core). The bound electron will subsequently bind a hole via

Coulomb attraction of the negatively charged donor ion. The defect complex then consists of three particles, two electrons and a single hole. The electrons will have j_e=1/2 (Γ_6), while the hole will have j_h=3/2 (Γ_8). The electrons are paired with opposite spin into a J=0 state. Both the electron-electron and electron-hole interactions are very weak (Monemar *et al.* 1987). From the point of view of the shell model (Kirzenow 1977), the two electrons are in the Γ_1 valley-orbit state, with opposite spins, while the hole is in the Γ_8 state.

A neutral, substitutional acceptor will usually bind two holes via its hole-attractive core potential, with the electron subsequently bound via Coulomb attraction. The two Γ_8 holes (j_h=3/2) couple to form Pauli-allowed states with J=0 and J=2. The Γ_6 electron then couples to these states to form BE states of total angular momentum j=1/2, 3/2 and 5/2 (Monemar *et al.* 1987). Figure 2.4.3 and 2.4.4 show examples of luminescence from donor and acceptor BE luminescence respectively.

The shell model developed by Kirczenow (1977) assigns the particles in the BE states to the donor and acceptor levels, with interparticle interactions neglected. Further refinements of this model to include interaction effects (Karasyuk *et al.* 1992, Karasyuk *et al.* 1993) have been prompted by high-resolution PL measurements of donor and acceptor BE's (Thewalt *et al.* 1990).

2.4.2: Excitons Bound to Neutral Defects

Electrically neutral defects in the lattice are referred to as isoelectronic defects. Isoelectronic defects were first reported for the case of ZnTe:O by Dietz (1962). These impurities can be substitutional in nature (N in GaP, Merz *et al.* 1969), or complex (Cd-O in GaP, Henry 1968). The defect core presents a short-range potential (due to electronegativity differences or strain fields) which can strongly bind the primary particle. This bound particle cannot be described by EMT (Davies 1984). The secondary particle is loosely bound in the Coulomb field of the primary particle and can be described by EMT. The defects are classified on the basis of the identity of the primary particle. Electron-attractive core defects are known as pseudo-acceptors, and hole-attractive core defects are known as pseudo-donors (Hopfield 1966). This model

was confirmed by Cohen et al. (1977) for N_p-N_p pairs in GaP.

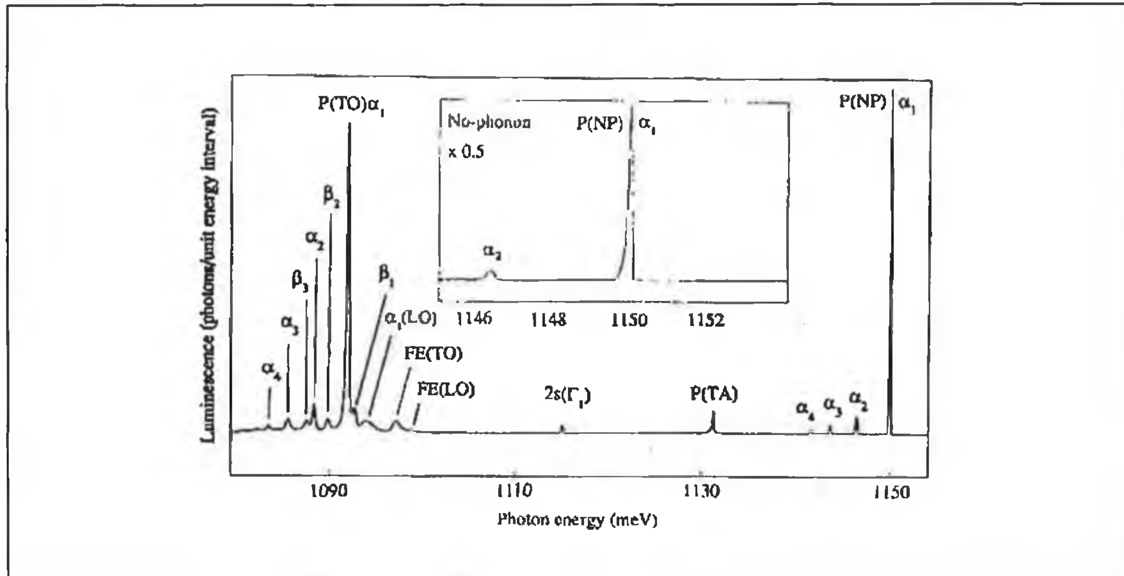

Figure 2.4.3: Low temperature PL spectrum of silicon showing phosphorous BE luminescence (Lightowlers 1990)

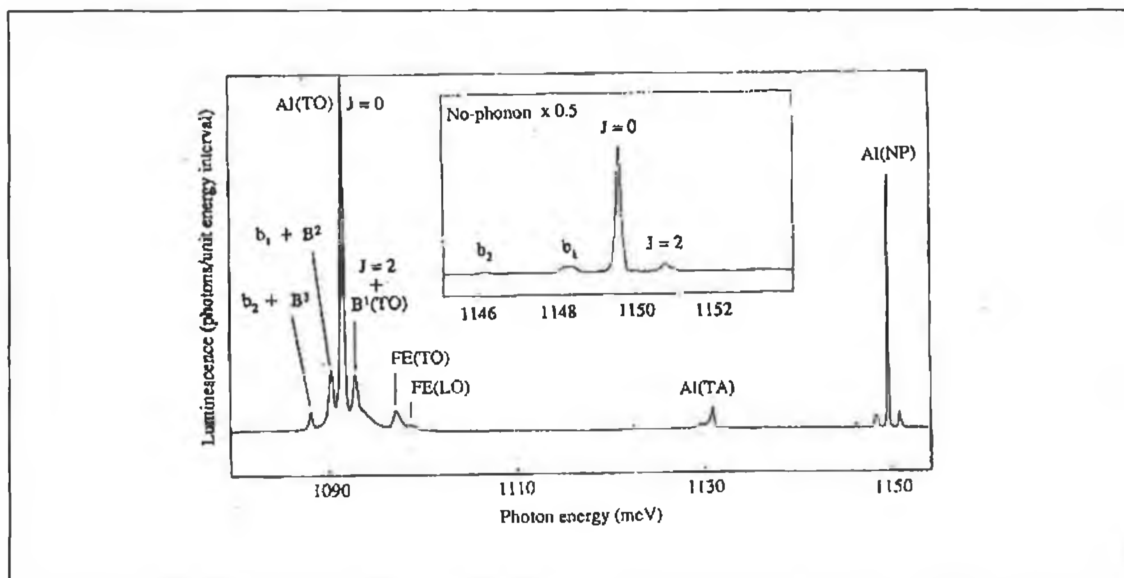

Figure 2.4.4: Low temperature PL spectrum of silicon showing aluminium BE luminescence (Lightowlers 1990)

A schematic diagram of a pseudo-acceptor is shown in figure 2.4.5 (a). The primary particle (electron) is bound by a very localised potential, while the secondary

particle (hole) is loosely bound in the Coulomb potential of the primary particle (suitably screened for core potential). The electron state (j_e=1/2) couples to the hole state (j_h=3/2), to form states with J=1 and 2. The J=1 state is split from the J=2 state by the electron-hole electrostatic interaction (e-h exchange). These states can be further split by a low symmetry crystal field (Monemar *et al.* 1987). PL has been reported from pseudo-acceptor centres in silicon such as the Be pair (Thewalt 1982) and the ABC centre (Weber 1980).

A schematic diagram of a pseudo-donor is shown in figure 2.4.5 (b). The primary particle (hole) is tightly bound at the hole attractive core, while the electron is loosely bound in the Coulomb field of the hole. The electron state will once again be j_e=1/2, orbitally non-degenerate. The degenerate hole state will be strongly affected by the localised defect potential, and if the defect symmetry is low enough (e.g. rhombic I, C_{2v}) so that only one-dimensional irreducible representations of the point group exist, then the hole angular momentum will be quenched (Monemar *et al.* 1987). This result is approximate because the inclusion of spin-orbit coupling can reintroduce angular momentum character into low symmetry states (Monemar *et al.* 1987). In the case of quenched angular momentum the hole is in a state j_h=1/2. Therefore the electron and hole couple to give singlet and triplet exciton states with J=0 and 1. Because these are purely spin-like states they are often written S=0 and 1. The electron-hole interaction splits these states as shown in figure 2.4.4 (b). The well-known C-line (Thonke 1985) and P-line (Wagner 1985) defects in silicon show pseudo-donor character.

2.5: Radiative Recombination

The process of optical absorption and emission in a perfect crystal is governed by integrals such as the example in equation 2.5.1;

$$\int_{-\infty}^{\infty} g(r)\, e^{i(k_i + k_p - k_f)\cdot r}\, dr \qquad (2.5.1)$$

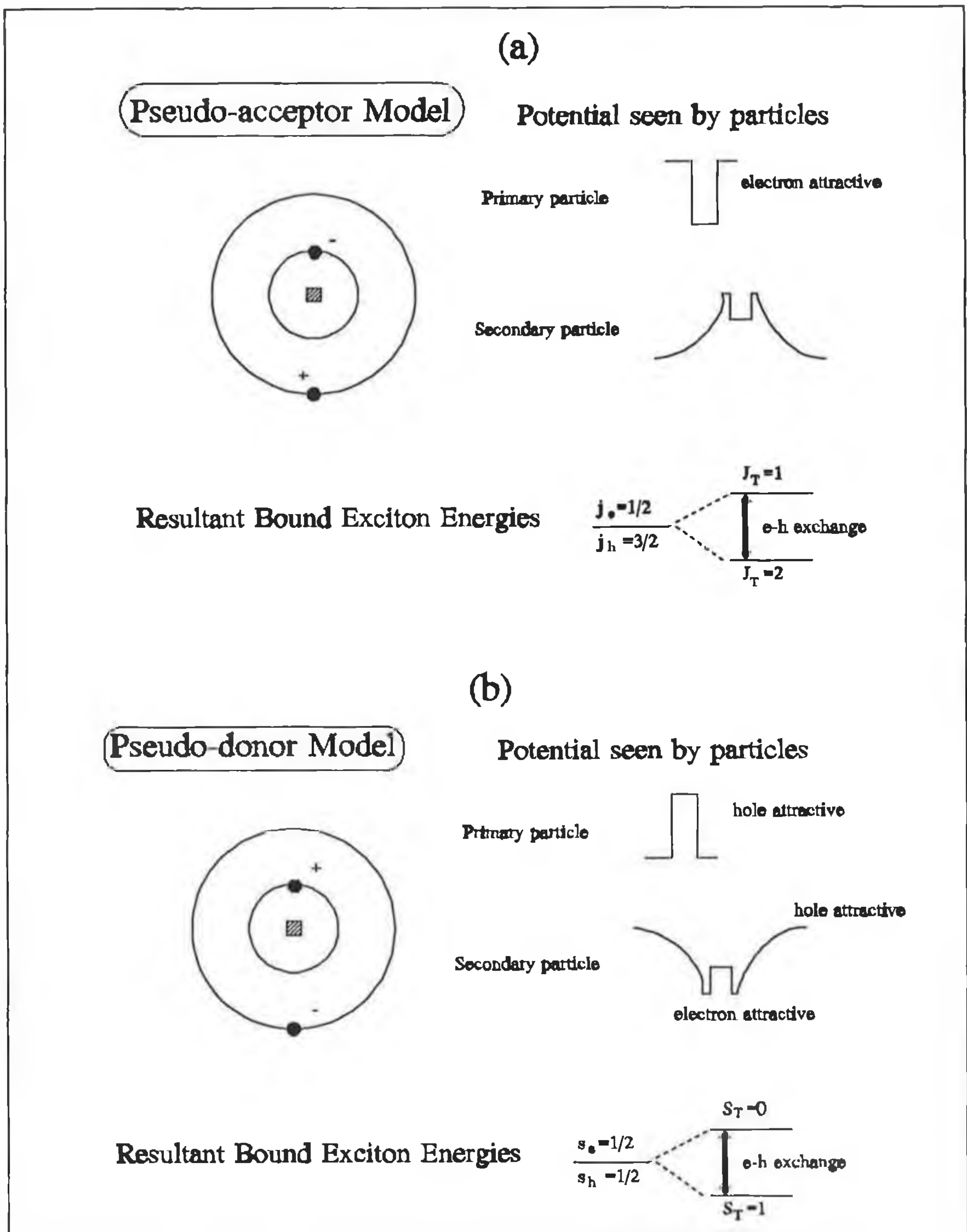

Figure 2.4.5: Formation of (a) pseudo-acceptor
(b) pseudo-donor

(Monemar 1987)

where g(r) has the lattice periodicity, k_i is the k vector of the initial state, k_p is the

photon wavevector and k_f is the wavevector of the final state. When the integral is carried out over the entire lattice, the condition that the result is non-zero is that;

$$k_i + k_p = k_f \qquad (2.5.2)$$

Because the photon wavelength is so large (~ 1μm) compared to interatomic distances (2.35e10^{-10}m, from Landolt 1984), the value of k_p is negligibly small compared to k_i and k_f. The approximation is then made that for optical transitions $k_i = k_f$. Because of this rule, only transitions that involve states with the same initial and final k vectors are allowed.

Transitions of energy close to the band gap energy in indirect bandgap materials (such as silicon) require the presence of a second particle in order to supply the "missing" crystal momentum. Phonons can fulfil this role. Figure 2.5.1 shows an example of a transition in both an indirect band gap material and a direct band gap material.

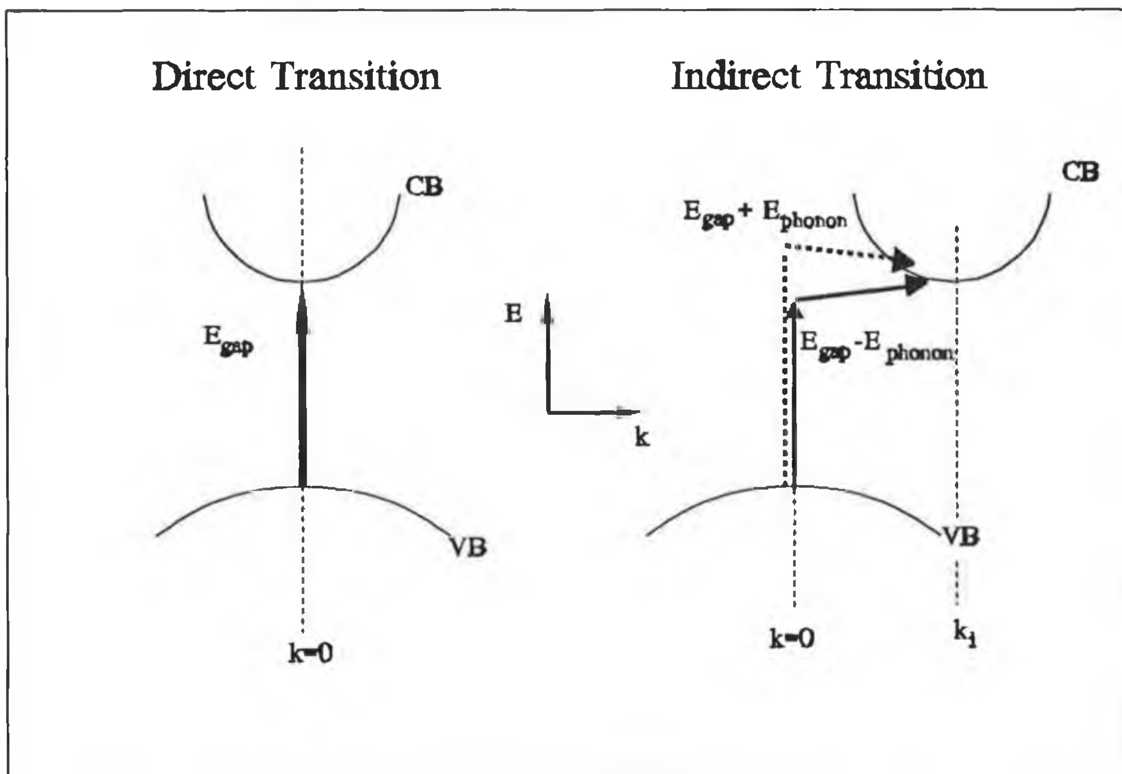

Figure 2.5.1: Band edge transitions in direct and indirect gap materials

The transition in the direct band gap material requires only a photon, but the transition in the indirect gap material requires either the absorption or emission of a phonon of wavevector $\boldsymbol{k}_i$, where $\boldsymbol{k}_i$ is the separation in $\boldsymbol{k}$-space of the conduction and valence band minima. In order to conserve energy, the relationship between photon energy and the band gap is given by;

$$E_{photon} = E_{gap} \pm E_{phonon} \qquad (2.5.3)$$

where the + sign implies phonon emission and the - phonon absorption.

Recombination of free excitons (or very loosely bound excitons, with considerable free particle character) in an indirect gap material therefore requires the absorption or emission of a phonon (at low temperatures emission is the more probable route). Referring back to figure 2.3.1, the $\boldsymbol{k}$ value at ~0.86 of the distance to the zone boundary along the Γ-X axis is equal to the separation of the conduction and valence bands in silicon. There are three allowed phonon assisted transitions corresponding to TO, LO and TA phonons (LA assisted transitions are forbidden). These are known as phonon replicas and are discussed by Dean *et al.* (1967). More tightly bound excitons tend to have a spatially localised wavefunction (therefore more widely dispersed in $\boldsymbol{k}$-space), and thus transitions are allowed without a wavevector conserving phonon.

Luminescence is the term given to the radiation emitted by a system (e.g. solid, liquid or gas) following a transition from an excited state to a lower energy state. In a semiconductor this transition generally involves the recombination of electrons and holes, but can also arise from internal transitions at a defect complex. An energy source is required to excite the electrons and holes initially, and this source of energy can be electrical (cathodoluminescence), chemical (chemiluminescence), mechanical (triboluminescence) or optical (PL). The study of the wavelength content of the PL emitted from a sample can provide information on the sample purity, defect content and identity etc. (Lightowlers 1990).

In addition to optical energy emitted during exciton recombination, the exciton energy can also be transferred to a third particle (electron or hole), without the emission of light. This is known as the Auger effect (Pankove 1975). The Auger effect

is a non-radiative process and tends to reduce the radiative efficiency of the defect. Because a third particle is required, this effect cannot occur in isoelectronic defects, and for this reason isoelectronic defects tend to be more radiatively efficient than donor(acceptor) BE luminescence.

Unlike absorption, PL is usually not a quantitative technique. As was mentioned in the previous paragraph, both non-radiative and radiative processes compete in exciton recombination. In addition to this, the PL intensity is not simply dependant on the oscillator strength and concentration of a defect in the lattice, but also on its relative ability to trap and bind excitons, temperature and excitation density. There are competitive processes between any one defect and the other impurities in the lattice. Because the background impurity profile can vary widely from sample to sample, the PL intensity of a fixed concentration of defects can vary from sample to sample. Figure 2.5.2 shows a diagram detailing the various competitive processes in exciton recombination (Lightowlers 1990).

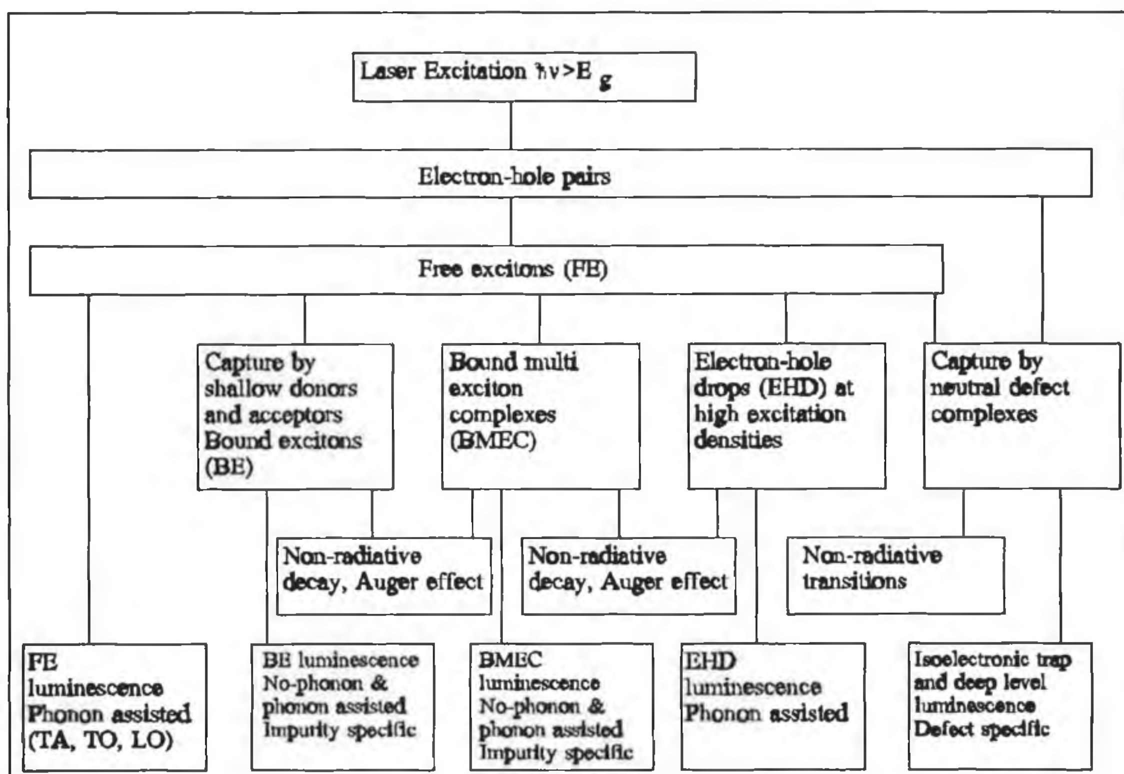

Figure 2.5.2: Luminescence decay processes stimulated by above band gap radiation (Lightowlers 1990)

The principal advantage of PL lies in its ability to detect very low defect concentrations (< 10^{12} cm^{-3}, Lightowlers 1990). The PL spectrum is also defect specific in terms of spectral position, behaviour under stress, magnetic fields etc.

2.6: Interaction of Electron States with Vibrating Lattice

The electronic and vibrational states of a crystal cannot be considered in isolation. Transitions between electronic states can affect the vibrational state of the crystal. This fact has already been noted in section 2.5, where the requirement for momentum-conserving phonons for electrons undergoing band edge transitions in indirect gap materials was noted. Defects with tightly bound particles can couple to phonons from all points in the Brillouin zone. When an electron undergoes an electronic transition, the change in the wavefunction and bonding may cause the lattice around the defect to relax to a new equilibrium position. This relaxation process can excite both lattice and localised defect vibrational modes and is known as electron-phonon coupling.The resultant spectrum consists of both a ZPL, which has a narrow lineshape (and can thus be used to monitor small shifts and splittings in uniaxial stress experiments etc.) and a broad sideband spectrum. The sideband structure will be temperature dependant, and its energy will depend on whether the defect is examined in absorption or emission.

In order to explain how this coupling comes about, a number of preliminary assumptions concerning vibronic states must be made. The first of these assumptions is the first-order adiabatic (or Born-Oppenheimer) approximation. This assumes that the nuclear mass is sufficiently large in comparison to the electronic mass, so that the total wavefunction can be written as a simple product of the electronic wavefunction in a fixed nuclear field and the nuclear wavefunction in the effective potential caused by the electrons (Born *et al.* 1927);

$$\phi(r_{elec}, Q) = \psi(r_{elec})\chi(Q) \qquad (2.6.1)$$

where Q represents the nuclear coordinates and r_{elec} the electron coordinates.

This decoupling allows one to draw the various electronic levels and nuclear levels as shown schematically in figure 2.6.1.

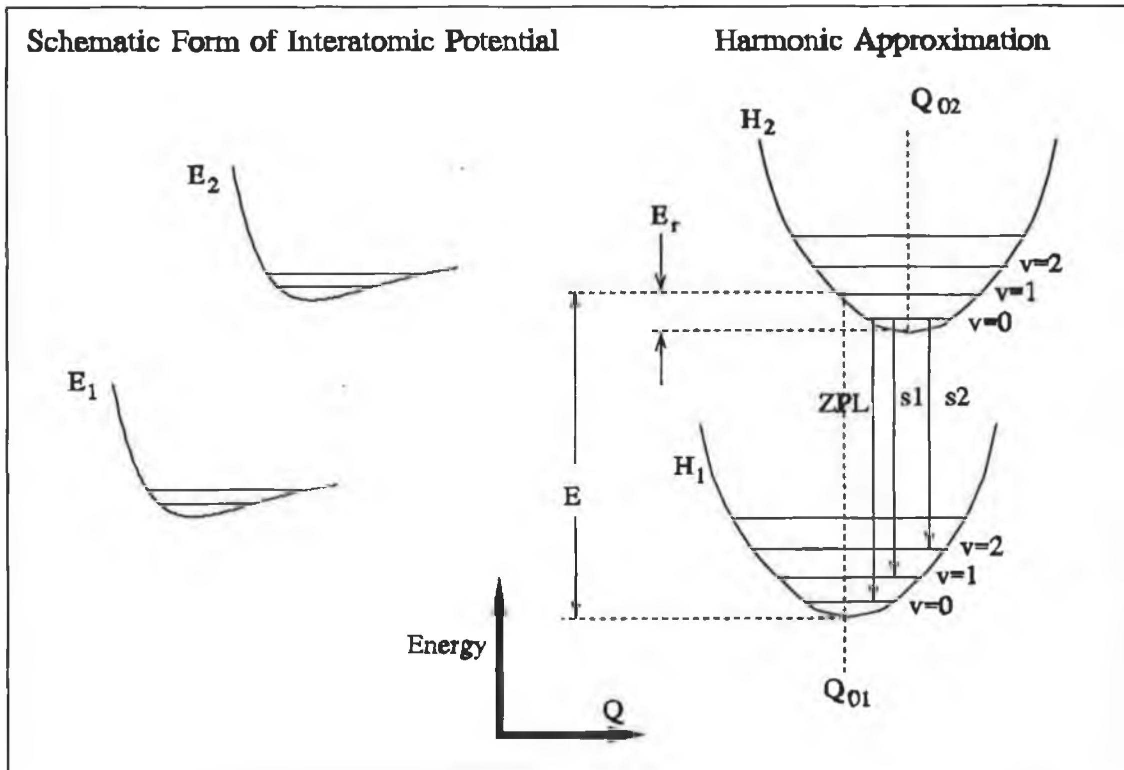

Figure 2.6.1: Example of configurational coordinate diagram

Diagrams of the type 2.6.1 are known as configurational coordinate (C.C.) diagrams. They represent the simplest case of electronic coupling to a single vibrational mode (generally the totally symmetric breathing mode). The coordinate Q represents the distance of the defect atom(s) to its nearest lattice neighbours. The curves represent the variation of the total defect energy as a function of Q for different electronic levels E_i. The vibrational modes are shown as levels v_i.

The second approximation to be made is the harmonic approximation, where the complicated potential curves E_i are replaced by the much simpler parabolic curves H_i. With this approximation the energy of each level can be written as $\frac{1}{2}M\omega^2_i(Q-Q_{0i})^2$, where Q_{0i} is the equilibrium Q value for the level E_i. Each level E_i may have different equilibrium positions Q_{0i}, but the ω_i values are all considered identical for simplicity. When the ω_i values are not identical, a quadratic term is introduced into the potential. This quadratic electron-phonon coupling is dealt with by Davies (1989). The harmonic

approximation is valid for small values of $Q-Q_{0i}$. The harmonic approximation implies that the functions $\chi(Q)$ in equation 2.6.1 are solutions of the quantum simple harmonic oscillator problem which can be found in standard quantum mechanics textbooks.

The third approximation made is the Franck-Condon approximation, which states that the timescale of electronic transitions is so short compared to that of nuclear vibrations that the nuclei can be considered stationary during the course of an electronic transition. Therefore electronic transitions are represented by vertical lines on the C.C. diagrams. Because the electric dipole operator connects only the electronic parts of the wavefunctions and is therefore constant for transitions between the same electronic states, the transition probability is determined by the overlap integral between states of the form $\chi(Q-Q_{01})$ and $\chi(Q-Q_{02})$. These overlap integrals are well known (Keil 1965).

These three approximations allow calculations of the relative probabilities of phonon emission and absorption during and optical transition between two electronic levels. The treatment presented here closely follows that of Watts (1977) and Henderson and Imbusch (1989) and further details and references can be found there.

The C.C. diagram can be used to describe the vibronic coupling mechanisms during electronic transitions. The energy of the ground state 1 is defined so that;

$$H_1 = \frac{1}{2}m\omega^2(Q-Q_{01})^2 \qquad (2.6.2)$$

and the excited state 2 is given by;

$$H_2 = \frac{1}{2}m\omega^2(Q-Q_{02})^2 + E - E_r \qquad (2.6.3)$$

where E and E_r are defined on figure 2.6.1. By writing equation 2.6.3 in terms of the linear electron-phonon coupling term a;

$$a = -m\omega^2(Q_{02}-Q_{01}) \qquad (2.6.5)$$

where a is defined by;

$$H_2 = \frac{1}{2}m\omega^2(Q-Q_{01})^2 + a(Q-Q_{01}) + E \qquad (2.6.4)$$

The relaxation energy E_r and the change in equilibrium position are given by;

$$E_r = \frac{a^2}{2m\omega^2} \; : \; |Q_{01} - Q_{02}| = \frac{a}{m\omega^2} \qquad (2.6.6)$$

Since most of the measurements presented in this thesis are performed at low temperatures, it can be assumed that all the transitions take place between the v_2=0 level and the different v_1 states. At higher temperatures so-called anti-Stokes sidebands appear, with energies greater than the zero-phonon line. The ZPL transition is from the v_2=0 level to the v_1=0 level. The first phonon sideband (labelled s1) is from the v_2=0 level to the v_1=1 level, and so on for s2 etc.. The phonon sideband lines occur at lower energy because some of the excited state energy has been given up in creating a vibrational mode. The relative intensities of these transitions is determined by the overlap integrals of the harmonic oscillator functions as mentioned above. These overlap integrals depend critically on the difference Q_{01}-Q_{02}. The values of these integrals are given by (Keil 1965);

$$F_m = \langle\chi_2(m)|\chi_1(0)\rangle^2 = \frac{\exp(-s)\,s^m}{m!} \qquad (2.6.7)$$

where F_m is proportional to the transition probability for the mth phonon sideband, and S is the Huang-Rhys factor,

$$S = \frac{E_r}{\hbar\omega} = \frac{a^2}{2m\hbar\omega^3} \qquad (2.6.8)$$

The Huang-Rhys factor represents the difference in electron-lattice coupling between the upper and lower levels. As the value of S increases, more energy is "transferred" from the ZPL to the sideband, as shown in figure 2.6.2.

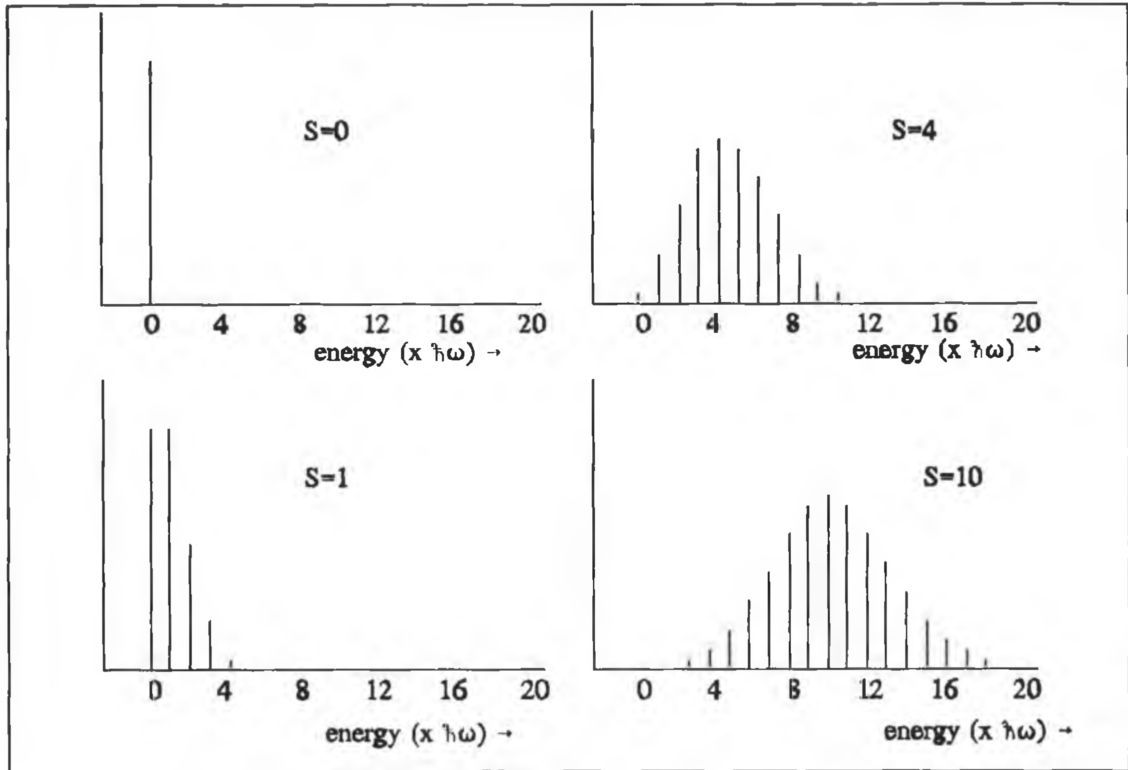

Figure 2.6.2: Sideband intensities for various S values (Henderson *et al.* 1989)

The overall sideband shape is found by summing over all the terms in equation 2.6.2. The Huang-Rhys factor is found in practice by measuring the fraction of the total (ZPL + sideband) intensity in the ZPL;

$$S = \ln(I_{total}) - \ln(I_{ZPL}) \qquad (2.6.9)$$

The above analysis applies to a defect coupled to a single vibrational mode. In general defects will be coupled to many vibrational modes. In this case equations 2.6.2 and 2.6.3 generalise to;

$$H_1 = \frac{1}{2}\sum_i m_i \omega^2{}_i (Q - Q_{01})^2 \qquad (2.6.10)$$

$$H_2 = \frac{1}{2}\sum_i m_i\omega^2{}_i(Q_{02}-Q_{01})^2 - \sum_i S_i\hbar\omega_i + E \qquad (2.6.11)$$

where S_i is the Huang-Rhys factor for the ith vibrational mode. In the linear coupling approximation the vibrational modes do not mix and therefore the phonon sideband is constructed by summing the contributions from all the different modes i.

A electronic transition can excite more than one phonon of a specific mode and can also excite phonons of different modes simultaneously. The phonon sideband shapes can be quite complicated, but can be reconstructed if an accurate 1st phonon sideband is known. A review of vibronic coupling to a number of modes is given by Davies (1981).

2.7: Temperature Dependence of Luminescence

The luminescence intensity of defect centres is in general affected by temperature changes. The behaviour of the luminescence intensity as a function of temperature can provide information on both the exciton binding energy and the excited state structure of the defect. The description given here closely follows that given by Davies (1989) and further details and references may be found there.

At very low temperatures (close to 0K), optically excited excitons are trapped at the lowest energy excited states of the defect centres in the crystal. The luminescence will consist entirely of luminescence from these lowest excited states to the ground state. As the temperature is increased, higher energy excited states of defects are populated, leading to the appearance of new lines in the spectrum. This process is known as thermalisation, and the excited state populations follow a Boltzmann-type distribution as the temperature is increased. In addition to thermalising processes, excitons may be released from shallow trap centres and captured at deeper trap centres. This leads to changes in the luminescence intensity of the lines in the spectrum. Because the profile of shallow trap centres will be sample dependant (different samples having different doping concentrations, species etc.) some of these

thermally induced processes will vary from sample to sample.

The first situation to consider is the simple scenario of a defect with two ZPL's, with thermalisation processes occurring between the two levels. No other processes are involved. A schematic energy level diagram is shown in figure 2.7.1.

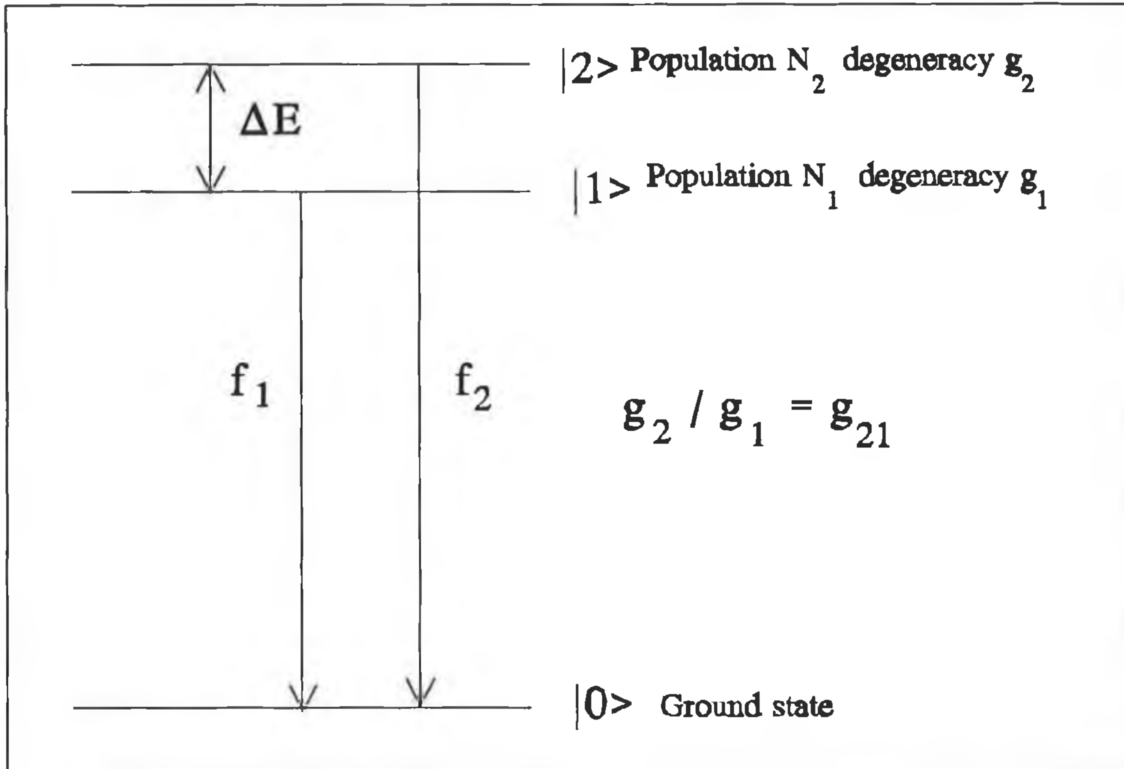

Figure 2.7.1: Schematic diagram of thermalisation processes between levels

N_i = Population of the ith level

f_i = transition probability of the ith level

g_{21} = ratio of degeneracies of level 2 to level 1

ΔE = separation of levels 1 and 2

Assuming that $N_1(T)+N_2(T)=N_1(0)$, then the total intensity as a function of temperature can be written as;

$$I_{TOT}(T) = F_1(T) = \frac{I(0)\,(1+\frac{f_2}{f_1}g_{21}e^{\frac{-\Delta E}{kT}})}{1+g_{21}e^{\frac{-\Delta E}{kT}}} \qquad (2.7.1)$$

and the ratio of the intensities $I_1(T)$ to $I_2(T)$ is given by;

$$\frac{I_2(T)}{I_1(T)} = \left(\frac{f_2 g_{21}}{f_1}\right) e^{\frac{-\Delta E}{kT}} \tag{2.7.2}$$

By plotting $\ln(I_2/I_1)$ vs. $1/T$ the slope of the graph is equal to $-\Delta E/k$ and the intercept is equal to $\ln(f_2 g_{21}/f_1)$. Using this procedure allows one to check whether two levels are thermalising. If the graph of $\ln(I_2/I_1)$ vs. $1/T$ is linear this is a good indication that the levels are thermalising. The value of ΔE can be compared with the spectroscopic splitting and if they are not equal this indicates that transitions to a split ground state are occurring.

The preceding analysis is valid only if the role of phonon sidebands is neglected. If the Huang-Rhys factor of the two ZPL's is not equal , then the equation relating the line intensities is;

$$\frac{I_2(T)}{I_1(T)} = \frac{g_{21} f_2}{f_1} e^{\frac{-\Delta E}{kT}} e^{-(S_2-S_1)(2n+1)} \tag{2.7.3}$$

where S_2 and S_1 are the Huang-Rhys factors for the two ZPL's, and n is given by;

$$n = \left(e^{\frac{\hbar\omega}{kT}}-1\right)^{-1} \tag{2.7.4}$$

where ω is the phonon frequency.

In reality there is likely to be more than one defect type present in the material. At low temperatures it is likely that shallower defect levels will compete for excitons with the defect under study. As the temperature is raised the excitons on the shallower traps will become unbound before they can recombine and are available for capture at the defect of interest. This will cause the luminescence intensity to increase initially as the temperature rises. Because this increase in intensity depends on the number and energy position of the shallow trap levels it is sample dependant.

As the temperature rises further the excitons bound to the defect of interest will also begin to dissociate before they recombine, and this will lead to a decrease in the

luminescence intensity. This decrease in luminescence will depend on the binding energy of the exciton relative to the free particle states.

Consider the schematic energy level diagram shown in figure 2.7.2.

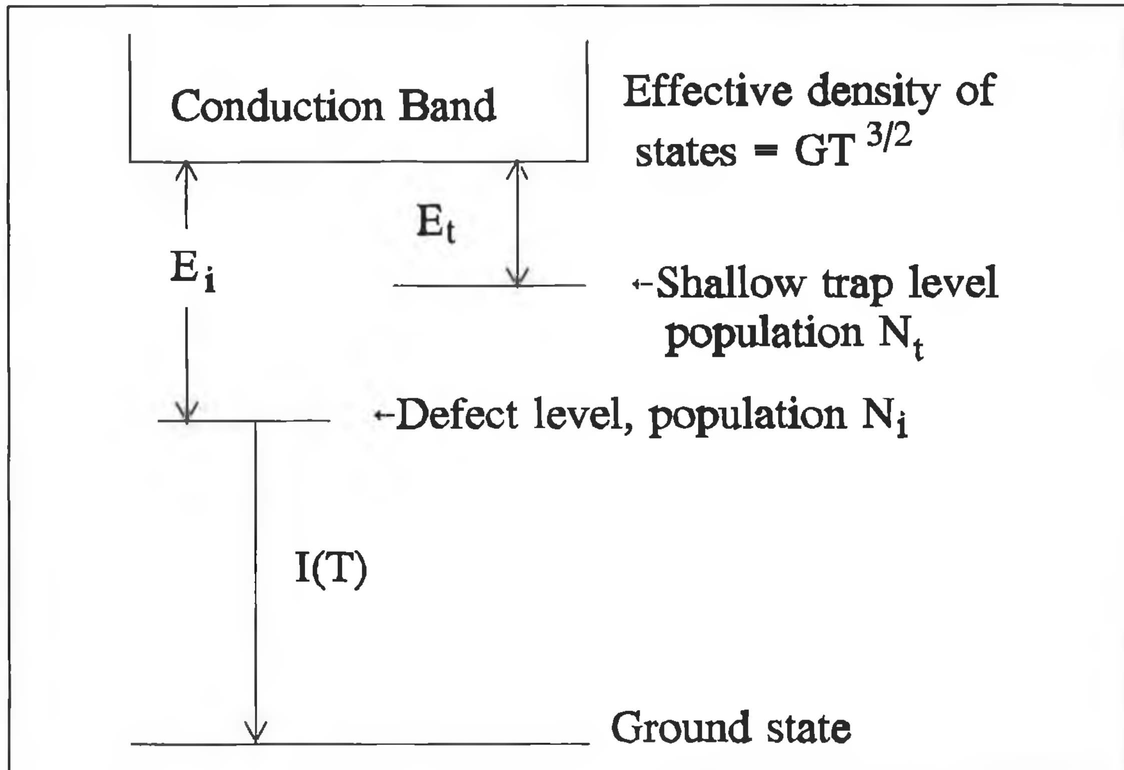

Figure 2.7.2: Schematic diagram showing the effect of shallow traps on luminescence intensity

In this diagram the shallower trap levels are represented by a single trap level (for simplicity) at energy E_T below the conduction band. The defect level is represented by a single level at energy E_i below the conduction band. The value E_i represents the effective ionisation energy of the exciton, and is given by the binding energy of the more loosely bound component. As the temperature increases the fraction of shallow traps competing for excitons decreases, as excitons are ionised off the traps almost immediately. The fraction f competing is equal to the fraction left in the trap level, which Davies (1989) writes as;

$$f = \frac{1}{1+G_1 T^{\frac{3}{2}} e^{-\frac{\Delta E_T}{kT}}} \qquad (2.7.5)$$

where the term $G_1T^{3/2}$ describes the temperature dependant ratio of the band state concentration to the trap state concentration (analogous to the g_{21} in equation 2.7.1). The intensity of the luminescence as a function of temperature is then written as;

$$I(T) = F_{trap}(T) = \frac{I(0)}{1 + r.f} \qquad (2.7.6)$$

where r is the probability of exciton capture at trap centres relative to capture at the defect centre. As r increases the trap centres become more dominant.

The other process occurring is the loss of excitons from the defect centre (before they can radiate) to the band. The equation describing this loss is given by Davies (1989);

$$I(T) = F_{decay}(T) = \frac{I(0)}{1 + G_2 T^{\frac{3}{2}} e^{\frac{-\Delta E_i}{kT}}} \qquad (2.7.7)$$

The overall luminescence intensity as a function of temperature is given by combining the three factors in equations 2.7.1, 2.7.6 and 2.7.7. This gives the total intensity as a function of temperature;

$$I_{tot}(T) = I_0 . F_1(T) . F_{trap}(T) . F_{decay}(T) \qquad (2.7.8)$$

The equations above can be used to fit experimental intensity versus temperature data using eight adjustable parameters; g_{21}, G_1, G_2, f_1/f_2, r, ΔE, E_t and E_i. The role of non-radiative processes has not been considered in this simple analysis because it has been assumed that the temperature dependence of these processes is negligible.

2.8: Uniaxial Stress

2.8.1: Introduction

Uniaxial stress spectroscopy (piezo-spectroscopy) is a technique employed to identify the symmetry of a defect centre. The technique involves compressing (or extending) oriented samples (using the type of apparatus described in chapter 3) and monitoring the behaviour of the spectral lines or bands (usually the ZPL). In general the ZPL splits into a specific number of components for stress along each crystal axis <100>, <111> and <110>. The splitting rates of the lines along specific directions is related by a set of equations. These equations are tabulated for different symmetry centres (Kaplyanskii 1964, Mohammed *et al.* 1982). By monitoring the number of components, their relative intensities and polarisations, an accurate indication of the defect symmetry can be found.

The splitting of the ZPL's is due to removal of the degeneracy of the defect states. The origin of this degeneracy may be twofold. The first source is orientational degeneracy, illustrated in figure 2.8.1 (a). Consider the defects lying along the x,y, and z (labelled 1, 2, 3) axes respectively of the cubic crystal. Because the $S_{4x,y,z}$ rotations of the cubic group connect all the defect orientations, all the defects have the same energy due to the equivalence of different sites in the cubic lattice. When a stress is applied along the z-axis of the crystal, the $S_{4x,y}$ operations are destroyed and therefore the defects 1 and 2 are perturbed to a different extent than the defect 3 and the ZPL splits into two components (figure 2.8.1 (b)).

The second source of degeneracy is the electronic (or quantum mechanical) degeneracy. This type of degeneracy is best illustrated using the example of the p orbitals of the hydrogen atom. At an unperturbed defect, the p_x, p_y and p_z orbitals will all have the same energy. When a stress is applied along the z-axis, the p_z orbital energy becomes different to the p_x and p_y orbital energies. Thus the electronic degeneracy is removed as illustrated in figure 2.8.2. The presence of electronic degeneracy is determined by the symmetry group of the defect (only groups D_{2d} or higher have irreducible representations of order > 1). In general both electronic and

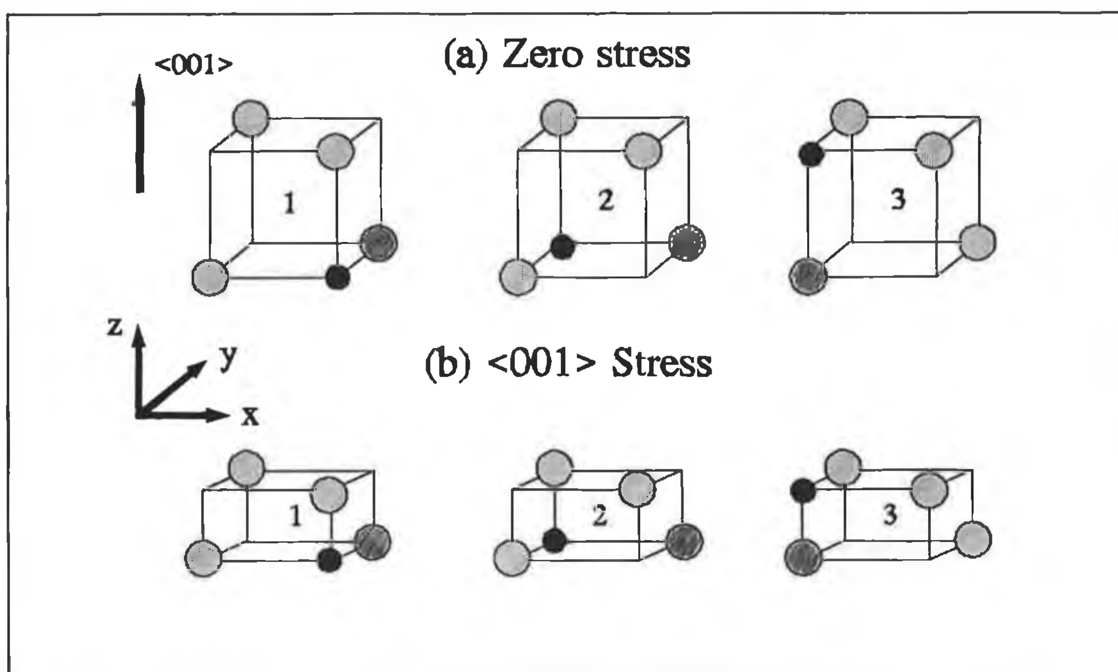

Figure 2.8.1: (a) Orientational degeneracy, no stress
(b) Orientational degeneracy, <001> stress

orientational degeneracy will be present, and the analysis must take account of both of these degeneracies (Hughes *et al.* 1967).

The defects studied in this thesis possess low symmetry crystal sites (rhombic I and monoclinic I). For this reason the defect states were not electronically degenerate, i.e. the character table for the point groups (e.g. C_{2v} for rhombic I and C_{1h} for monoclinic I) contains only one dimensional irreducible representations. In order to explain the theory used in the analysis of uniaxial stress data, the details of the procedure for rhombic I centres will be presented here. Details of the analysis for monoclinic I can be found in Kaplyanskii (1964).

2.8.2: Rhombic I Centres

Defect centres which have similar point groups and which behave in the same manner under the application of stress are classified under the same heading (cubic, tetragonal, trigonal, rhombic, monoclinic or triclinic). The details of these headings can be found in Kaplyanskii (1964). For example the groups D_{3d} and C_{3v} are both

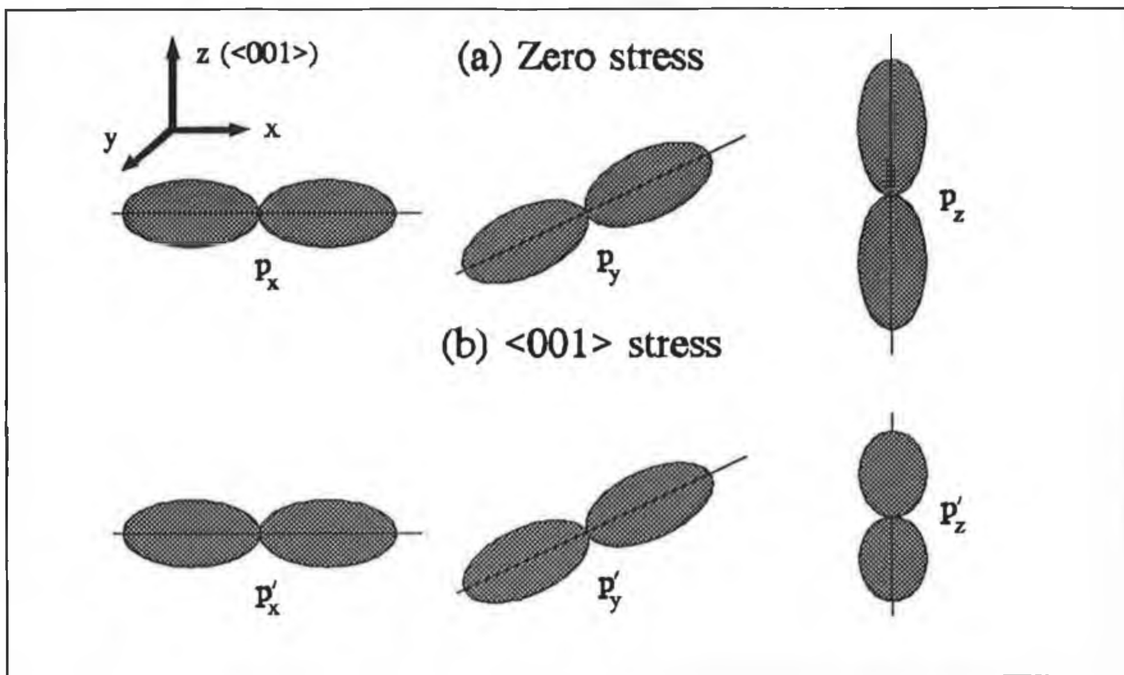

Figure 2.8.2: (a) Electronic degeneracy, zero stress
(b) Electronic degeneracy ,<001> stress

classed under the heading trigonal. The point group C_{2v} is classed as rhombic I. The C_{2v} character table is reproduced in table 2.8.1 (Tinkham 1964);

Table 2.8.1

C_{2v}	E	C_2	σ	σ'	Basis Functions
A_1	1	1	1	1	x^2, y^2, z^2
A_2	1	1	-1	-1	xy
B_1	1	-1	1	-1	xz
B_2	1	-1	-1	1	yz

In order to place a defect into the silicon lattice so that the defect plus lattice has C_{2v} symmetry, it is necessary to align the two-fold rotation axis (C_2) along <001> type

crystal axes, and to align the vertical reflection planes (σ) along <110> type axes.

Because all the irreducible representations are one dimensional, all the states of the defect are non-degenerate, as was mentioned previously. The Hamiltonian for the system including the effect of stress may be written;

$$H = H_0 + V_{stress} \tag{2.8.1}$$

The perturbation operator (assumed to depend linearly on the stress because we are working in the limit of low stresses) may be written in terms of the components of the stress tensor as;

$$V_{stress} = \sum_{ijk} a_k s_{ij} \tag{2.8.2}$$

where the a_k are the electronic stress operators. The factors s_{ij} represent a force applied to the ith face in the jth direction and are given by the formula;

$$s_{ij} = |P| \cos(i,P) \cos(j,P) \tag{2.8.3}$$

where P is the applied stress and cos(i,P) is the angle between the stress direction and the ith direction. For the case of a cubic crystal, six stress tensors are required to specify the stress (Kaplyanskii 1964). A set of coordinates is defined relative to the defect in question, with the defect Z-axis customarily defined as the rotation axis of highest order in the group. The stress potential may then be written as;

$$V_{stress} = a_1 s_{XX} + a_2 s_{YY} + a_3 s_{ZZ} + a_4 s_{XY} + a_5 s_{YZ} + a_6 s_{ZX} \tag{2.8.4}$$

the quantities s_{ij} transforming as the coordinate product ij (see character table). The situation displayed in figure 2.8.3 is considered where the PL transition is between two non-degenerate levels well separated from all the other levels of the system. The energy of the PL transition before stress is given by E_{e0}-E_{g0}. When stress is applied, the energy levels E_e and E_g change by (assuming first order perturbation corrections only);

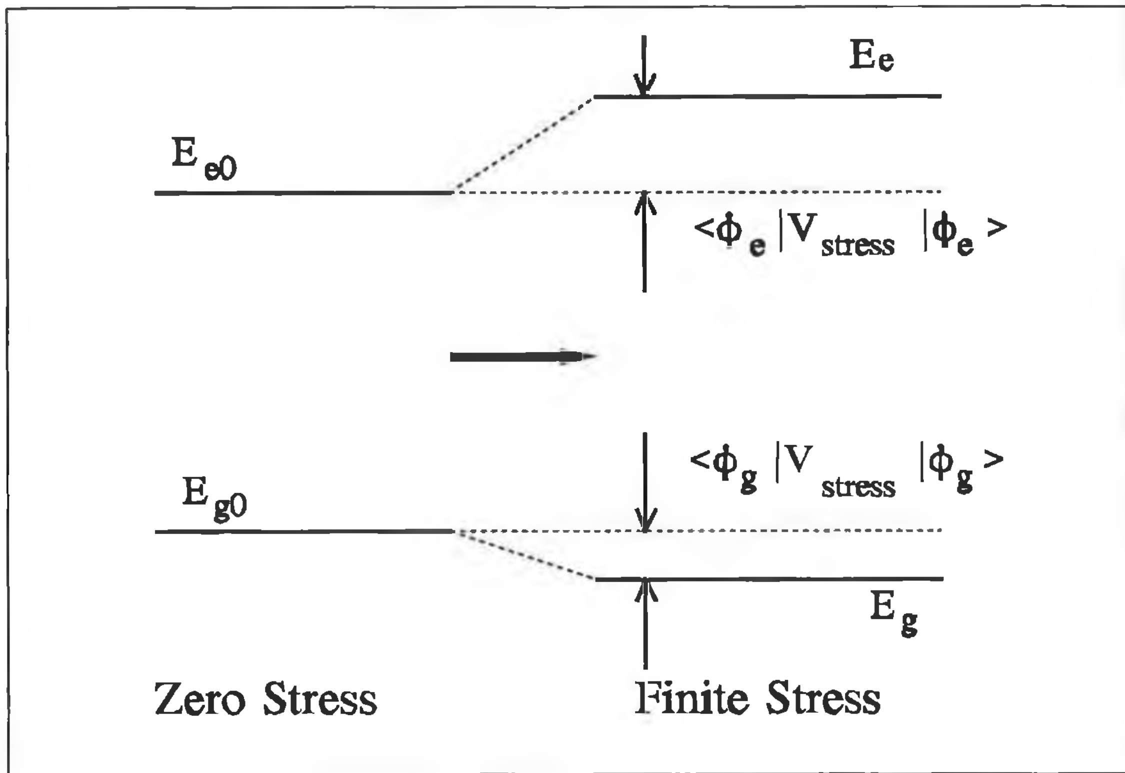

Figure 2.8.3: Perturbation of non-degenerate levels by stress potential

$$E_e \rightarrow E_{e0} + \langle \phi_e | V_{stress} | \phi_e \rangle \ : \ E_g \rightarrow E_{g0} + \langle \phi_g | V_{stress} | \phi_g \rangle \qquad (2.8.5)$$

where ϕ_e and ϕ_g are the unstressed excited and ground state wavefunctions respectively. By a fundamental group theoretical law (Tinkham 1964), the only elements of the potential V_{stress} which contribute to the expectation values in equation 2.8.5 are those elements transforming as the A_1 irreducible representation. Consulting the character table for C_{2v} it can be verified that the only elements of V_{stress} contributing to the expectation values are $a_1 s_{XX}$, $a_2 s_{YY}$ and $a_3 s_{ZZ}$. When these elements are entered into equations 2.8.4 and 2.8.5, the change in line energy $\delta = E_e - E_g$ as a function of stress is given by;

$$\delta = \overline{a_1} s_{XX} + \overline{a_2} s_{YY} + \overline{a_3} s_{ZZ} \qquad (2.8.6)$$

where;

$$\overline{a_i} = [\langle\phi_e|a_i|\phi_e\rangle - \langle\phi_g|a_i|\phi_g\rangle] \qquad (2.8.7)$$

Therefore it can be seen how the change in transition energy can be written in terms of the stress tensor.

Having examined the effect of the stress upon a particular defect in the crystal, it is now necessary to enumerate the different defect orientations in the crystal. The point group of silicon is octahedral of order 48, but each element is related to one other by the inversion operator and since uniaxial stress cannot distinguish between centres related by inversion (stress is an equal "push" from both sides), the order of the group is effectively the tetrahedral group of order 24. The number of inequivalent orientations of a defect in the crystal is given by Kaplyanskii (1964) as N=G/g, where G is the order of the point group of the host lattice and g is the order of the defect group. Now, for C_{2v} g=4 and for silicon G=24 and hence N=6. The six inequivalent orientations are listed in table 2.8.2 with their coordinates and schematic diagrams of the possible atomic arrangements leading to them are shown in figure 2.8.4.

Table 2.8.2

Defect	X	Y	Z
1	110	$\bar{1}10$	001
2	$\bar{1}10$	110	$00\bar{1}$
3	011	$0\bar{1}1$	100
4	$01\bar{1}$	$0\bar{1}\bar{1}$	$\bar{1}00$
5	101	$10\bar{1}$	010
6	$\bar{1}01$	$\bar{1}0\bar{1}$	$0\bar{1}0$

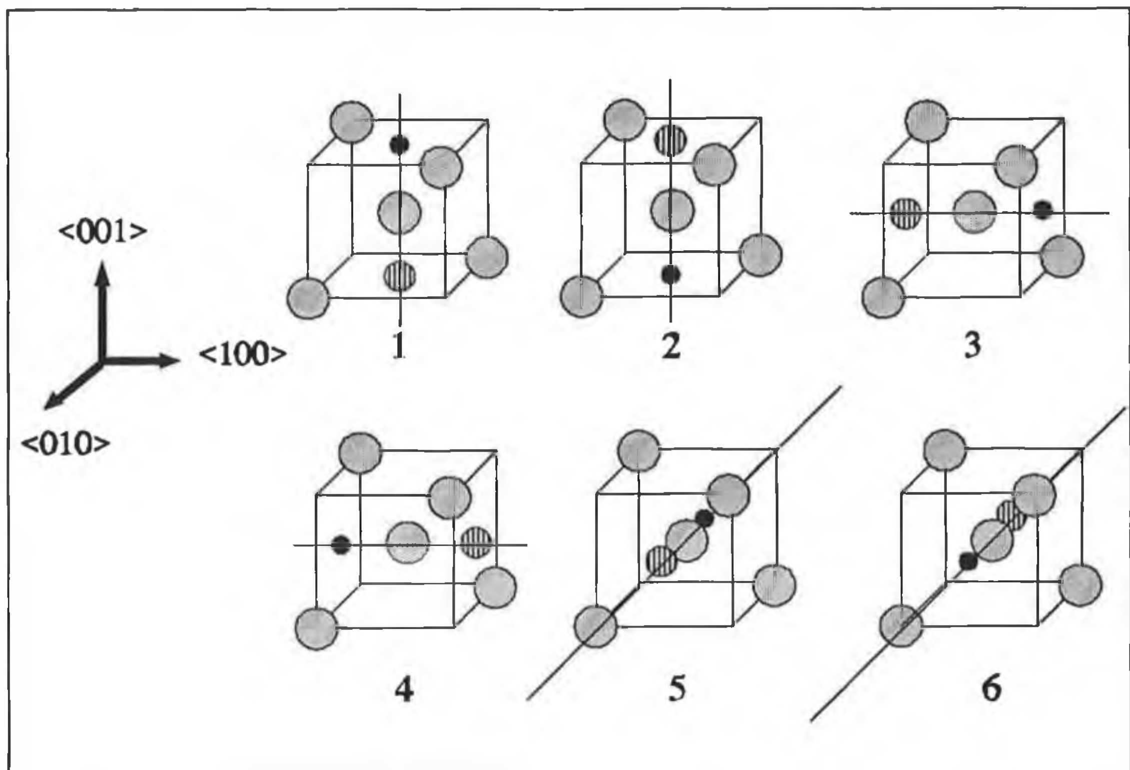

Figure 2.8.4: Schematic diagram of possible atomic arrangements corresponding to centres 1-6 in table 2.8.2

The removal of orientation degeneracy can now be understood on the basis of equation 2.8.6 and the contents of table 2.8.2. To calculate δ for each defect it is necessary to calculate the values of s_{XX}, s_{YY} and s_{ZZ} for each defect for a particular stress direction. The number of different δ's calculated gives the number of components and the shift rates of these components. Consider the case of stresses along the <001>, <111> and <110> directions. Calculated s_{XX}, s_{YY} and s_{ZZ} values for the defects 1-6 above are shown in table 2.8.3.

For <001> stress the original transition splits into two components with shift rates;

$$\delta 1 = \bar{a}_3$$

$$\delta 2 = 1/2(\bar{a}_1+\bar{a}_2)$$

For <111> stress the line splits into 2 components with shift rates;

$$\delta 3 = 1/3(2\bar{a}_1+\bar{a}_3)$$

$$\delta 4 = 1/3(2\bar{a}_2+\bar{a}_3)$$

For <110> stress the line splits into 3 components with shift rates;

$$\delta 5 = \bar{a}_1$$

$$\delta 6 = \bar{a}_2$$

$$\delta 7 = 1/4(\bar{a}_1+\bar{a}_2+2\bar{a}_3)$$

The above analysis has been carried out entirely in defect coordinates, where the stress direction is kept fixed and the effect on different defects is considered. An alternative (and entirely equivalent) viewpoint is the so-called crystal coordinate system, where the defect is kept constant, and the stress is applied along the different inequivalent axes. This approach for rhombic I defects is described in Davies (1994). The stress potential operator must be changed to crystal coordinates in this case, using the procedure described by Davies (1994). The results are equivalent in the sense that only three parameters are needed to describe the splittings. The only difference involves a change of notation effected by the transformation;

$$A_1=\bar{a}_3$$

$$A_2=1/2(\bar{a}_1+\bar{a}_2)$$

$$A_3=1/2(\bar{a}_1-\bar{a}_2)$$

When this transformation is applied to the line shift rates $\delta 1$-$\delta 7$, the results obtained by Kaplyanskii (1964) are duplicated precisely. In fitting experimental data, the equations for the shift rates for stress along <001>, <111> and <110> give seven simultaneous equations in the three unknowns A_1, A_2 and A_3. These equations can then be solved to give a best fit for the parameters A_1, A_2 and A_3.

Having calculated the number of stress-split components and the shift rates of these components for the three stress directions, it is now necessary to calculate the intensity ratios and polarisation content of these components. In practice, a knowledge of these quantities enables one to fit the data more easily, because the intensity ratios and polarisation data allow one to identify a particular stress-split component with a particular equation. The relative intensities and polarisations of the components can be calculated by assuming that the electric dipole of the transition lies along some particular direction, which is usually the defect Z-axis. The parallel polarised (π) intensity is then calculated by taking the square of the cosine of the angle between the stress direction and the electric dipole direction for each defect and summing over the number of equivalent defects. The perpendicular polarised (σ) intensity

Table 2.8.3: s_{ij} values for centres 1-6 under stress

Defect	s_{XX}	s_{YY}	s_{ZZ}
<001> stress			
1	0	0	1
2	0	0	1
3	1/2	1/2	0
4	1/2	1/2	0
5	1/2	1/2	0
6	1/2	1/2	0
<111> stress			
1	2/3	0	1/3
2	0	2/3	1/3
3	2/3	0	1/3
4	0	2/3	1/3
5	2/3	0	1/3
6	0	2/3	1/3
<110> stress			
1	1	0	0
2	0	1	0
3	1/4	1/4	1/2
4	1/4	1/4	1/2
5	1/4	1/4	1/2
6	1/4	1/4	1/2

is found by taking the square of the cosine of the angle between the electric dipole direction and a vector perpendicular to the stress. If the measured data do not agree with the calculated ratios this indicates that the electric dipole direction has been incorrectly chosen. With good quality polarisation data it is possible to deduce the electric dipole direction in the crystal. An example of such an analysis is performed by Jeyanathan (1994).

Taking the case of an A-B transition at a rhombic I site (Mohammed *et al.*

1982), the polarisation and intensity ratios are given in table 2.8.4 for stress directions <001> and <111>.

In the case of <110> stress, there will be two sets of inequivalent σ polarisation data corresponding to the two inequivalent perpendicular viewing axes <001> and $<1\bar{1}0>$. The polarisation ratios for <110> stress are shown in table 2.8.5.

Table 2.8.4

Stress-split Component	π : σ
<001> stress	
δ1	0 : 1
δ2	2 : 1
<111> stress	
δ3	4 : 1
δ4	0 : 3

Table 2.8.5

Stress-split Component	$\pi : \sigma_{<1\bar{1}0>} : \sigma_{<001>}$
<110> stress	
δ5	1 : 0 : 0
δ6	0 : 0 : 1
δ7	1 : 2 : 1

This information is often represented graphically as in figure 2.8.5.

2.8.3: Interacting States

One of the assumptions made in section 2.8.2 was that the excited state and ground state were well separated in energy from any other electronic states of the defect. This is often an unrealistic assumption, since many defect complexes give rise to a series of excited states which can interact strongly with each other upon the application of stress. When two or more levels interact with each other, the simple

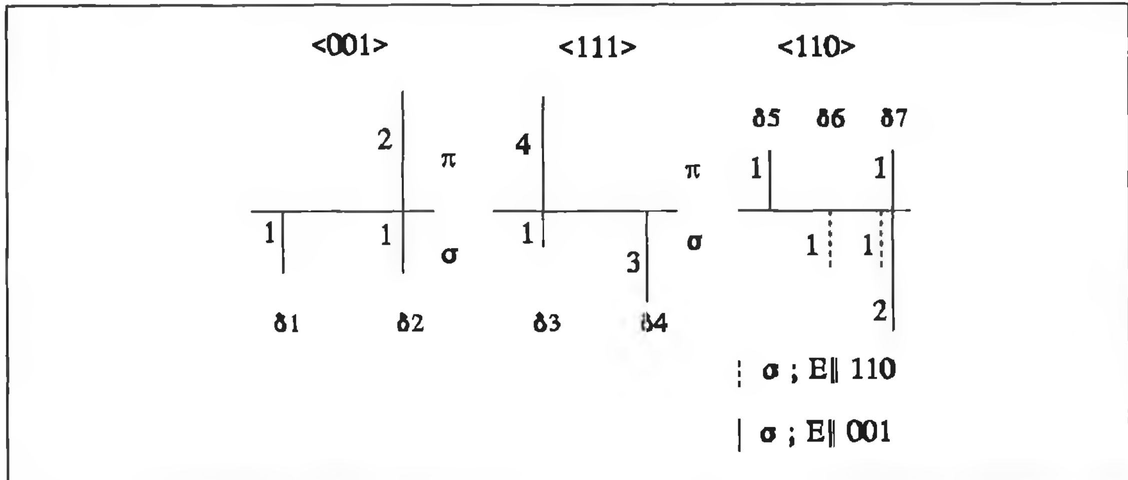

Figure 2.8.5: Splittings and polarisation intensities for rhombic I A-B transitions

theory presented in the previous section requires modification. The matrix elements of equation 2.8.5 are replaced by matrices (of dimension greater than one), with the elements depending on the applied stress. The behaviour of the energy levels of the system is found by diagonalising such matrices to obtain the eigenvalues.

In order to explain the details of the analysis, the example of a rhombic I defect with two closely-spaced excited states and an isolated ground state will be considered. This case is particularly relevant to this thesis work, as the 1026meV Cd-related line appears to behave in this manner under stress (chapter 5).

The first step in analysing the behaviour of the two interacting levels under stress is to write down the matrix for the two excited states, for which we use the labels ϕ_{e1} and ϕ_{e2}. The interaction matrix can be written in the form shown in equation 2.8.8;

$$\begin{bmatrix} \langle\phi_{e1}|V_{stress}|\phi_{e1}\rangle & \langle\phi_{e1}|V_{stress}|\phi_{e2}\rangle \\ \langle\phi_{e2}|V_{stress}|\phi_{e1}\rangle & \langle\phi_{e2}|V_{stress}|\phi_{e2}\rangle \end{bmatrix} \qquad (2.8.8)$$

If the levels interact, the off-diagonal elements of the type $\langle\phi_{e1}|V_{stress}|\phi_{e2}\rangle$ are non-zero. This interaction may lead to a non-linear shift rate as a function of stress of the type shown in figure 2.8.6.

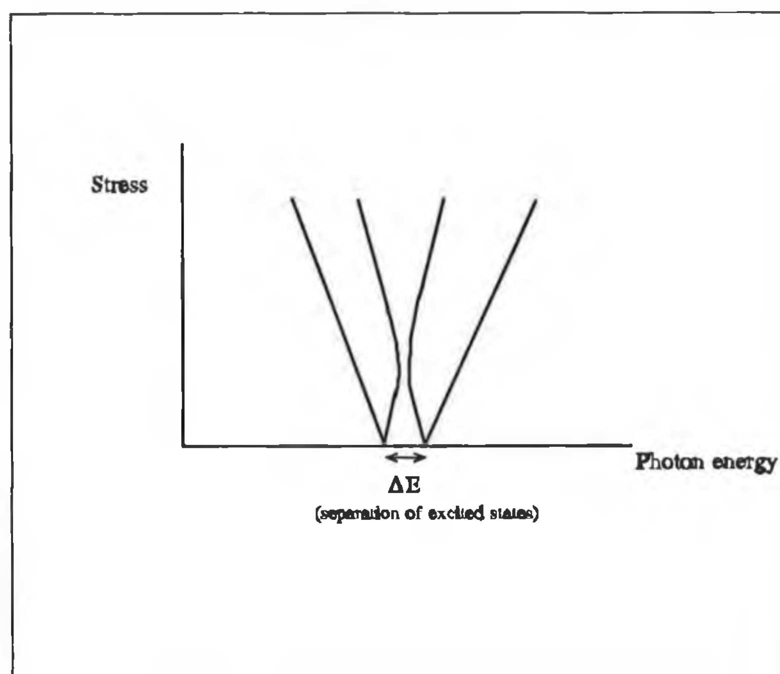

Figure 2.8.6: Schematic diagram of non-linear shift rates for interacting states

The matrix elements in equation 2.8.8 can be analysed using the same group theoretical arguments employed for the non-interacting case.

The same group theoretical rules apply to the diagonal matrix elements as apply to the matrix elements for the situation with no interactions, i.e. the stress potential only involves those elements of the stress tensor which transform as the A_1 representation of the group. Therefore the matrix element $<\phi_{e1}|V_{stress}|\phi_{e1}>$ can be replaced by the term $a_1s_{XX}+a_2s_{YY}+a_3s_{ZZ}$. The matrix element $<\phi_{e2}|V_{stress}|\phi_{e2}>$ can be replaced by $b_1s_{XX}+b_2s_{YY}+b_3s_{ZZ}+\Delta E$, where ΔE is the energy separation between the interacting levels.

The form of the off-diagonal matrix elements will depend on the transformation properties of the excited state functions ϕ_{e1} and ϕ_{e2} (A_1, A_2, B_1 or B_2, see table 2.8.1). The elements of the stress potential connecting the two states can be found using the Wigner-Eckhart theorem (Tinkham 1964). The different possibilities are outlined in table 2.8.6.

In order to fit the data to the theoretical model it is necessary to diagonalise the matrix in equation 2.8.8 as a function of stress, allowing the parameters a_i, b_i and c_i to vary, until the best fit parameters are found. In practice this is accomplished

using a computer to fit the theory to the data, allowing some of the matrix parameters to vary to find a good fit. A custom written P.C. based fitting package (McCarren 1994) was used to fit the data presented in this thesis.

Careful examination of the experimental data can narrow down the possibilities even further. Using the values of the intensity ratios in the low stress regime, the transition type (A-A, B-B or A-B) can be determined if good polarisation data are available. It is possible that no interactions between states might occur for certain stress directions (i.e. linear shift rates), and this implies that the off-diagonal elements connecting the two excited states are zero for that particular direction. Careful study of the behaviour of the stress elements s_{ij} for different directions can help identify the possible states involved. Details of an analysis of this nature can be found for a defect in diamond in Davies *et al.* (1976).

Table 2.8.6

Representation of States		Matrix Element (Defect Coordinates)
ϕe_1	ϕ_{e2}	$<\phi_{e1}\|V_{stress}\|\phi_{e2}>$
A_1	A_1	$c_1s_{XX}+c_2s_{YY}+c_3s_{ZZ}$
A_1	A_2	cs_{XY}
A_1	B_1	cs_{XZ}
A_1	B_2	cs_{YZ}
A_2	A_2	$c_1s_{XX}+c_2s_{YY}+c_3s_{ZZ}$
A_2	B_1	cs_{YZ}
A_2	B_2	cs_{XZ}
B_1	B_1	$c_1s_{XX}+c_2s_{YY}+c_3s_{ZZ}$
B_1	B_2	cs_{XY}
B_2	B_2	$c_1s_{XX}+c_2s_{YY}+c_3s_{ZZ}$

When two states interact under stress, the intensity ratios of the stress split components will tend to vary as a function of stress, due to thermalisation processes between the levels and also due to stress-induced mixing of levels which can alter the electric dipole transition probability for the transitions originating on the two levels.

Consequently great care is required in the analysis of the data.

2.9: Zeeman Spectroscopy

The technique of Zeeman spectroscopy involves monitoring the behaviour of spectral lines as a function of magnetic field intensity along a particular crystal direction. In many respects it is a complementary technique to uniaxial stress, providing information on the spin states of defects. Zeeman spectroscopy was first used in the analysis of the spectral lines of atomic species, but is now commonly used in the area of solid state spectroscopy (Dean *et al.* 1979) and can provide valuable information concerning both the energy level structure and binding mechanisms of the defect in question.

In order to present a brief description of the effect of a magnetic field on defect energy levels the energy level structure of an isoelectronic donor (pseudo-donor) will be considered. It is assumed that the defect has rhombic I symmetry. The electronic structure of pseudo-donors was discussed in section 2.4. The energy levels will be examined more fully here and their behaviour under a magnetic field analysed.

In the case of a pseudo-donor, the hole is the tightly bound particle, and hence is strongly perturbed by the low symmetry crystal field, which removes the j=3/2 degeneracy of the valence band states. This quenches the hole angular momentum, and the resultant hole state is purely spin-like with s=1/2. Orbital angular momentum quenching is seen in many isoelectronic defects such as the indium related system (Watkins *et al.* 1986), Zn_A system (Daly 1995), Be_A system (Daly 1994) and is also seen in the Cd_A and 1026meV defect systems reported in chapters 4 and 5. The loosely bound electron is weakly perturbed by the local field, and hence it retains the s=1/2 nature of the conduction band states. Hence the electron state is also purely spin-like. The final states of the system will depend on the degree of coupling between electron and hole (e-h coupling). Two cases will be considered corresponding to strong e-h coupling and weak e-h coupling.

Strong e-h coupling leads to a singlet S=0 state and a triplet S=1 state (with the S=1 state customarily lower in energy) split by the e-h exchange electrostatic

interaction (Condon 1957). When a magnetic field is applied to the system, the singlet state is unaffected by the field (S=0) and the triplet state splits into three components with the splitting patterns given by;

$$\Delta E = m_S \mu_B g_m B \qquad (2.9.1)$$

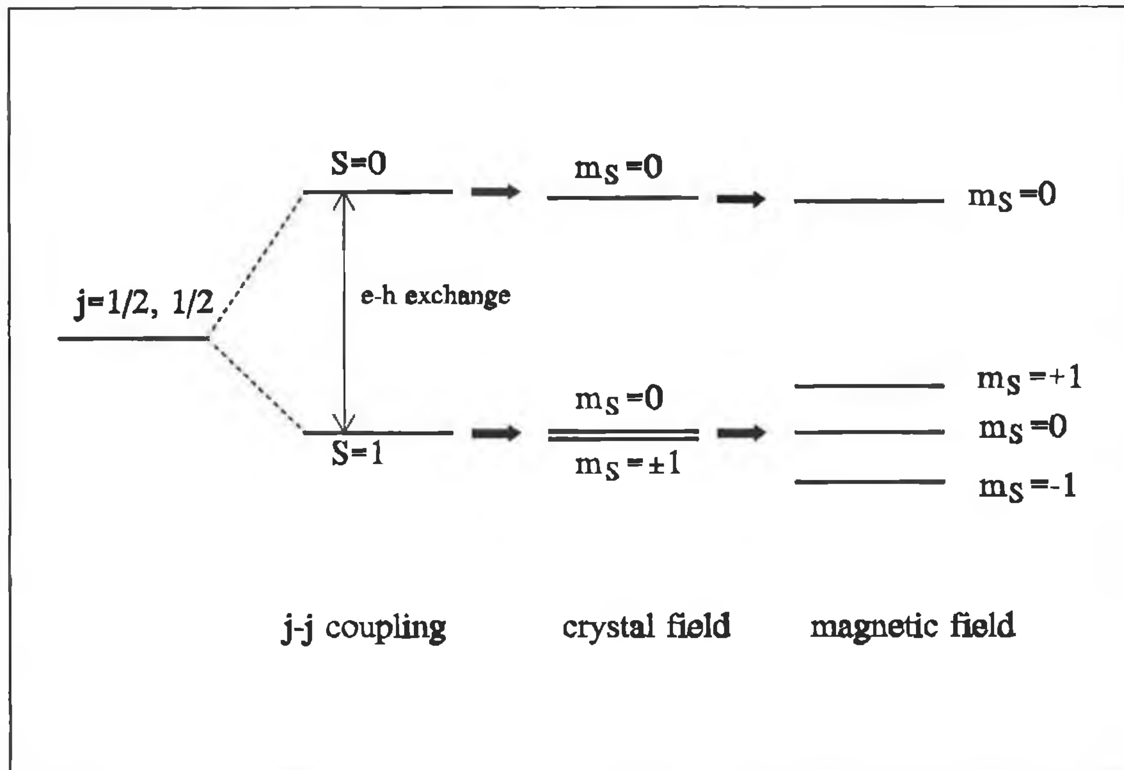

Figure 2.9.1: Schematic diagram of energy level structure of singlet-triplet system in magnetic field

where g_m is the Lande g-factor, μ_B is the Bohr magneton and B is the magnetic field. A schematic diagram of the energy level structure is shown in figure 2.9.1. This type of singlet-triplet splitting pattern is common for many hole-attractive defects in silicon, such as the 1044meV lithium related system (Davies 1989), 955meV and 772meV Se-Cu systems (Jeyanathan 1994). The transition from the excited triplet (S=1) state to ground singlet (S=0) state is ideally forbidden when the wavefunctions of the particles are purely spin-like, but in practice the states are not purely spin-like and therefore the $\Delta S=0$ selection rule is relaxed and the singlet-triplet transition becomes weakly

allowed. By measuring the intensity ratio of the two lines, the degree of internal strain in the defect can be measured (Davies 1984, 1989). The spectral separation between the two lines gives the value of the e-h exchange energy.

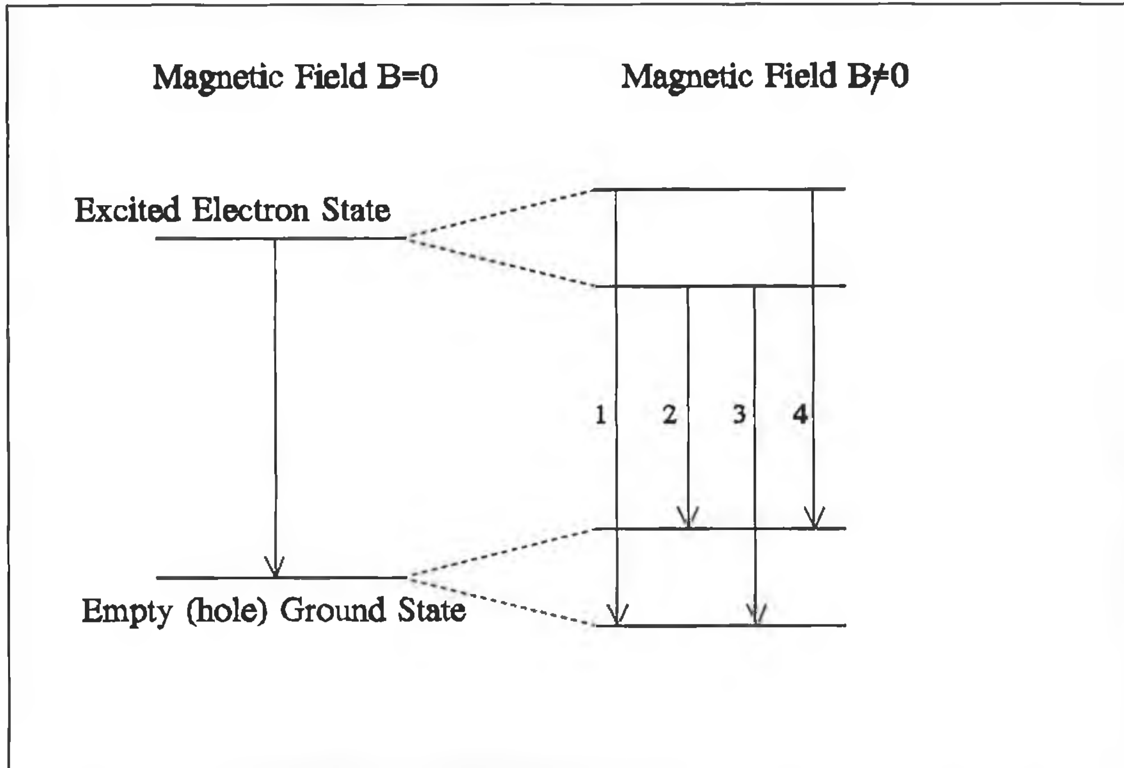

Figure 2.9.2: Energy Level Diagram of Electron and Hole States in the Limit of Weak j-j Coupling

If the e-h coupling is weak, the hole state and electron state can be considered to be entirely independent, and the observed optical transitions correspond to the electron in the excited s=1/2 state dropping back into the ground s=1/2 (hole) state (Dean *et al.* 1979). A schematic diagram of the energy level structure is shown in figure 2.9.2 (taken from Dean *et al.* 1979). At zero magnetic field only one line is seen (unlike the case where coupling of the electron and hole is strong). As the magnetic field is increased, the upper electron state splits into $m_s=\pm1/2$ components as does the ground state. The splitting patterns are given by equation 2.9.1 with $m_s=\pm1/2$. Transitions from the excited $m_s=+1/2$ state to ground $m_s=-1/2$ state (labelled 1 in figure 2.9.2), and from the excited $m_s=-1/2$ state to ground $m_s=+1/2$ state (labelled 2 in figure 2.9.2) are forbidden by the spin selection rule $\Delta s=0$. Spin-orbit admixing

of orbital angular momentum into the hole wavefunction may cause the transitions labelled 1 and 2 to become weakly allowed (Irion *et al.* 1988). The only allowed transitions are from the excited m_s=-1/2 state to the ground m_s=-1/2 state (labelled 3 in figure 2.9.2) and from the excited m_s=+1/2 state to the ground m_s=+1/2 state (labelled 4 in figure 2.9.2). These transitions are degenerate in energy and, assuming that the electron and hole g-factors are identical, the line does not shift or split in a magnetic field. An example of a pseudo-donor centre of this type is given by Irion *et al.* (1988), and corrections to the theory for anisotropic hole g-factor and spin-orbit admixing of orbital angular momentum into the hole wavefunction are discussed.

The defect complexes reported in this thesis show no response to a magnetic field. For the three defects discussed in chapters 4, 5 and 7, no evidence of a triplet state is seen and therefore for these defects we favour the weak-coupling model in interpreting the Zeeman results. The defect discussed in chapter 6 shows evidence of an excited state but the magnetic properties of this state have not been examined as yet. These facts, in conjunction with the low symmetry defect configurations deduced from uniaxial stress measurements, indicate that these defects have a pseudodonor-type excited state electronic structure.

2.10: Isotope Substitution

Because of the large number of possible contaminants in even high purity silicon, it is very difficult to accurately define the chemical constituents of a defect complex. Certain defects may "catalyse" the formation of a defect centre without being directly involved in the centre itself. For example, self interstitials created by radiation damage can react with C substitutional atoms to create highly mobile C interstitial atoms, which can complex with elements such as Al (Drakeford 1988), substitutional C (Davies 1989) and O (Davies 1989, Trombetta *et al.* 1987). A more general discussion is given in Davies *et al.* (1987). Isotope substitution measurements can provide not only positive proof of the involvement of a particular chemical species in a defect centre but may also be used to find the number of atoms of a particular

species in a defect.

Isotope substitution experiments can take two forms. The first form is the replacement of a defect atom of mass m by an atom of the same atomic number but with isotopic mass m+Δm. The second form is to replace the host lattice with atoms of mass m by a host lattice of atoms of mass m+Δm. Examples of experiments of the second form have been performed using isotopically enhanced germanium (Davies et al. 1992) and diamond (Mainwood et al. 1994). The first form only of the experiment will be considered here, as it is the only one relevant to the work presented in this thesis. For a description of both forms of the technique see Fitchen (1968).

Samples are made with carefully chosen isotopes of the atomic species being studied. The greater the difference in mass, the easier it is to resolve isotope effects. In the work presented here, samples were implanted either with ^{106}Cd or ^{116}Cd or both. The ZPL and phonon sideband of the different samples are carefully examined under high resolution for any change in line position. If a consistent change in line position is seen as the isotope mass is varied, this can be taken as a very sure indication of the involvement of that atomic species in the defect. In the case of the dual-implant sample, a splitting of the ZPL would be expected. The number of lines into which the ZPL splits can be used to determine the number of atoms involved in the defect. If a single atom of the species is involved in the defect, then the line will be expected to split into 2 components with intensity ratios equal to the ratios of the implanted isotopes. The situation for more than one atom of a particular species being involved in the defect is analysed by Canham (1983) for the case of a 4 lithium atom complex in silicon. If atoms occupy sites which are inequivalent, then the situation can become very complex; a striking example of this has been reported recently for a H-related defect in silicon (Safanov *et al.* 1994). Although a positive result is unambiguous proof of the involvement of a particular element in a defect, a negative result does not necessarily rule out the involvement of the element. Many factors can influence the results of isotope experiments. The isotope shifts could, for example, be too small to be resolved. Certain systems exhibit isotope shifts in the phonon sidebands which are not present in the ZPL (Kurner *et al.* 1989). In addition to this, the processes used to incorporate the isotopes must be examined. Initial isotope experiments on Cd-related defects reported in chapters 4 and 5 showed a consistent isotope shift, but a negative

result for the dual isotope sample. This will be investigated further in chapter 4.

In order to understand the origin of the isotope effect it is necessary to return to the C.C. diagram introduced in section 2.6. The ZPL of a transition is defined as the transition from the lowest vibrational level v=0 of the excited state E_2 to the v=0 state of the ground state E_1, as shown in figure 2.10.1 (a). These two potential energy curves are identical to the curves for the simple harmonic oscillator. If it is assumed that the vibrational mode of the defect is due entirely to the vibration of the atomic (mass m) species of interest (neglecting vibrations of other defect constituents) against a restoring force of effective "spring constant" k_i (i=1,2 for the excited and ground state respectively), then the normal vibration frequency for the mode is given by equation 2.10.1. If the isotopic mass is changed to m+Δm, the value of ω is changed, and the parabolic curves change as shown in figure 2.10.1 (b).

$$\omega^i_m = \sqrt{\frac{k_i}{m}} \; : \; i=e,g \qquad (2.10.1)$$

If it is assumed that the k value remains constant, the new value for the vibration frequency is given by equation 2.10.2;

$$\omega^i_{m+\Delta m} = \sqrt{\frac{k_i}{m+\Delta m}} \; : \; i=e,g \qquad (2.10.2)$$

The ZPL energy for mass m is then given by;

$$E_m = E+\frac{1}{2}\hbar\left(\sqrt{\frac{k_e}{m}}-\sqrt{\frac{k_g}{m}}\right) \qquad (2.10.3)$$

and for mass m+Δm;

$$E_{m+\Delta m} = E+\frac{1}{2}\hbar\left(\sqrt{\frac{k_e}{m+\Delta m}}-\sqrt{\frac{k_g}{m+\Delta m}}\right) \qquad (2.10.4)$$

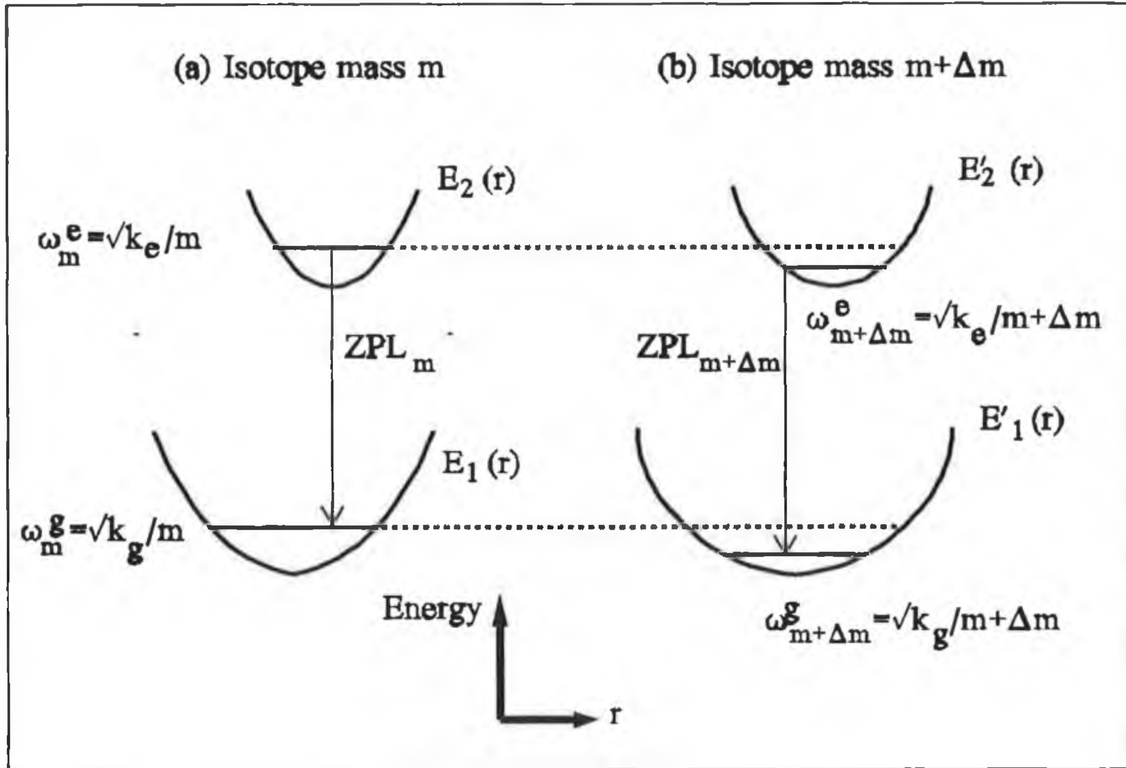

Figure 2.10.1: (a) C.C. diagram for isotope mass m
(b) C.C. diagram for isotope mass m+Δm

and the isotope shift in the ZPL can be written as;

$$E_m - E_{m+\Delta M} = \frac{1}{2}[\hbar\omega_g - \hbar\omega_e] \cdot [1 - \sqrt{\frac{m}{m+\Delta m}}] \qquad (2.10.5)$$

In reality a defect will couple to more than one mode. For the case of a defect coupling to a number of modes, equation 2.10.5 becomes (Davies 1989);

$$E_m - E_{m+\Delta M} = \frac{1}{2}\sum_i [\hbar\omega^i_g - \hbar\omega^i_e] \cdot [1 - \sqrt{\frac{m}{m+\Delta m}}] \qquad (2.10.6)$$

where the sum over i means a sum over all the defect vibrational modes (not just the ones which contribute to the phonon sideband. By calculating E_m-$E_{m+\Delta m}$, one can predict the isotope shift expected for a particular ZPL. This calculation shows the origin of the isotope effect. The magnitude of the isotope shift depends on both Δm

and k_e-k_g. As k_e-k_g tends to zero, the isotope shift tends to zero. Hence a negative isotope result can be observed in the ZPL, even though the atomic species is involved in the defect, as mentioned above. The sign of k_e-k_g determines the sign of the isotope shift. Most defects in silicon (Davies 1989, Canham 1983) show a positive isotope shift (the heavier isotope has a larger ZPL energy than the lighter) hence indicating that $k_e < k_g$. This means that the spring constant of the excited state is smaller, i.e. the excited state mode has been "softened".

Valuable information on the nature of the vibrational modes of defects may be gained from isotope substitution experiments. Using equations 2.10.1 and 2.10.2, the ratio of phonon frequencies for different isotopic masses (subject to the assumptions made for the case of ZPL isotope shifts) may be written as;

$$\frac{\omega^{m+\Delta m}}{\omega^{m}} = \sqrt{\frac{m}{m+\Delta m}} \qquad (2.10.7)$$

By measuring the frequencies of the sideband modes in samples prepared with different isotopes, it is possible to draw certain conclusions about the modes. If the ratio of the frequencies shows close agreement to the square root of the ratio of the masses (as predicted by equation 2.10.5) then it can be concluded that the mode of vibration predominantly involves the atom of interest vibrating with respect to an otherwise static lattice. If good agreement to the mass ratio is not found, then the mode of vibration involves one (or more) of the other defect constituents vibrating with the atom of interest. If the ratio of the phonon frequencies is unity (i.e. the frequency is unaffected by isotope mass), then the mode of vibration does not involve the atom of interest at all, e.g. lattice mode.

Because the ratio of phonon frequencies depends only on the mass ratio and not on quantities such as k_e-k_g, defects which show very small isotope shifts in the ZPL can show quite pronounced shifts in their phonon sidebands (Kurner *et al.* 1989). In general, isotope effects are more pronounced and easier to resolve in the phonon sideband regions, particularly when sharp local modes are present. A good example of this is the isotope behaviour of the 1026meV defect discussed in chapter 5.

2.11: Conclusions

In this chapter the theoretical concepts used in the analysis of the data presented in chapter 4,5 and 6 have been introduced. The main aim has been to explain the origin of the electronic and vibrational states of defect systems, and the behaviour of these states when subjected to perturbations. The main perturbative techniques of temperature dependence, uniaxial stress, Zeeman and isotope substitution were described, and the information they provide was discussed. Where possible, the discussion centred on aspects of the theories which will be of particular use in the analysis of results presented in this thesis.

References

N. W. Ashcroft and N. D. Merman (1976). "Solid State Physics", Saunders College.

A. Bar-Lev (1984). "Semiconductors and Electronic Devices", Prentice-Hall.

M. Born and J. R. Oppenheimer (1927). Ann. Phys. **84**, 457.

L. P. Bouckaert, R. Smoluchowski and E. P. Wigner (1936). Phys. Rev. **50**, 58.

B. H. Bransden and C. J. Joachain (1992). "Physics of Atoms and Molecules", Longman Scientific & Technical.

L. T. Canham (1983). Ph.D. Thesis, University of London.

J. R. Chelikowsky and M. L. Cohen (1974). Phys. Rev. B **10**, 5095.

E. Cohen and M. D. Sturge (1977). Phys. Rev. B **15**, 1039.

E. U. Condon and G. H. Shortley (1957). Chapter 13 in "The Theory of Atomic Spectra", Cambridge.

S. Daly (1994). Ph.D. Thesis, Dublin City University.

S. Daly, E. McGlynn, M. O. Henry, J. D. Campion, K. G. McGuigan, M. C. doCarmo and M. H. Nazare (1995). Accepted for publication in Mater. Sci. Forum.

G. Davies, M. H. Nazare and M. F. Hamer (1976). Proc. Roy. Soc. A **351**, 245.

G. Davies (1981). Rep. Prog. Phys. **44**, 787.

G. Davies (1984). J. Phys. C: Solid State Physics **17**, 6331.

G. Davies, E. C. Lightowlers, R. C. Newman and A. S. Oates (1987). Semicond. Sci. and Technol. **2**, 524.

G. Davies (1989). "The Optical Properties of Luminescence Centres in Silicon", Physics Reports **176**, 3&4, 83.

G. Davies, E. C. Lightowlers, V. Ozhogin, K. Itoh, W. L. Hansen and E. E. Haller (1992). Semicond. Sci. and Technol. **7**, 1271.

G. Davies (1994). Unpublished report titled "Stress in the Solid State Group", King's College London.

P. J. Dean, J. R. Haynes and W. F. Flood (1967). Phys. Rev. **161**, 3, 711.

P. J. Dean, R. A. Faulkner and J. L. Merz (1970). Solid State Commun. **8**, 2079.

P. J. Dean and D. C. Herbert (1979). Chapter 3 in "Excitons", editor K. Cho, Springer-Verlag.

R. E. Dietz, D. G. Thomas and J. J. Hopfield (1962). Phys. Rev. Lett. **8**, 319.

A. C. T. Drakeford and E. C. Lightowlers (1988). Defects in Electronic Materials Symp., Boston MA. USA. (Pittsburgh PA, USA. Mater. Res. Soc., 209).

D. B. Fitchen (1968). Chapter 5 in "Physics of Colour Centres", editor W. B. Fowler, Academic Press.

J. I. Frenkel (1931). Phys. Rev **37**, 1276.

J. I. Frenkel (1936). Phys. Z. Soviet Union **9**, 158.

J. R. Haynes (1960). Phys. Rev. Lett. **4**, 361.

B. Henderson and G. F. Imbusch (1989). "Optical Spectroscopy of Inorganic Solids", Clarendon Press, Oxford.

C. H. Henry, P. J. Dean and J. D. Cuthbert (1968). Phys. Rev. **166**, 3, 754.

M. O. Henry, E. C. Lightowlers, N. Killoran, D. J. Dunstan, B. C. Cavenett (1981). J. Phys. C: Solid State Physics **14**, 255.

M. O. Henry, J. D. Campion, K. G. McGuigan, E. C. Lightowlers, M. C. doCarmo and M. H. Nazare (1994). Semicond. Sci. and Technol. **9**, 1375.

J. J. Hopfield, D. G. Thomas and R. T. Lynch (1966). Phys. Rev. B **15**, 312.

A. E. Hughes and W. A. Runciman (1967). Proc. Phys. Soc. **90**, 827.

L. Jeyanathan (1994). Ph.D. Thesis, University of London.

A. Kaplyanskii (1964). Opt. Spectroscopy **16**, 329.

V. A. Karasyuk, A. G. Steele, A. Mainwood, E. C. Lightowlers, G. Davies, D. M. Brake and M. L. W. Thewalt (1992). Phys. Rev. B **45**, 20, 11736.

V. A. Karasyuk, D. M. Brake and M. L. W. Thewalt (1993). Phys. Rev. B **47**, 15, 9354.

T. H. Keil (1965). Phys. Rev. A **140**, 601.

G. Kirczenow (1977). Can. J. Phys. **55**, 1787.

C. Kittel (1986). "Introduction to Solid State Physics", 6th edition, John Wiley & Sons.

W. Kohn (1957). Solid State Phys. **5**, 257.

K. Kosai and M. Gershenzon (1974). Phys. Rev. B **9**, 723.

W. Kurner, R. Sauer, A. Dornen and K. Thonke (1989). Phys. Rev. B **39**, 18, 13327.

M. A. Lampert (1958). Phys. Rev. Lett. **1**, 12, 450.

Landolt-Bornstein (1984). "Numerical Data and Functional Relationships in Science and Technology; Group III: Crystals and Solid State Physics" vol. 17: Technology of Si, Ge and SiC, editors O. Madelung, M. Schultz and H. Weiss, Springer-Verlag.

R. L. Liboff (1980). "Introductory Quantum Mechanics", Holden-Day Inc.

E. C. Lightowlers (1990). Chapter 8 in "Growth and Characterisation of Semiconductors", editors R. A. Stradling and P. C. Klipstein, Adam-Hilger.

A. Mainwood, A. T. Collins and Peter Woad (1994). Mater. Sci. Forum **143-147**, 29.

A. L. McCarren, H. J. Ruskin, K. G. McGuigan and M. O. Henry (1994). IEE Proc. Sci. Meas. Technol. **141**, 185.

K. G. McGuigan (1989). Ph.D. Thesis, Dublin City University.

J. L. Merz, R. A. Faulkner and P. J. Dean (1969). Phys. Rev. **188**, 3, 1228.

K. Mohammed, G. Davies and A. T. Collins (1982). J. Phys. C: Solid State Physics **15**, 2779.

B. Monemar, U. Lindefelt and W. M. Chen (1987). Physica B **146**, 256.

N. F. Mott (1938). Proc. R. Soc. A **167**, 384.

J. I. Pankove (1975). "Optical Processes in Semiconductors", Dover Publications.

S. T. Pantelides (1978). Rev. Mod. Phys. **50**, 797.

A. M. Stoneham (1985). "Theory of Defects in Solids", Clarendon Press, Oxford.

M. L. W. Thewalt, S. P. Watkins, U. O. Ziemelis, E. C. Lightowlers and M. O. Henry (1982). Solid State Commun. **44**, 573.

M. L. W. Thewalt and D. M. Brake (1990). Mat. Sci. Forum **65-66**, 187.

K. Thonke, A. Hangleiter, J. Wagner and R. Sauer (1985). J. Phys. C: Solid State Physics **18**, 795.

M. Tinkham (1964). "Group Theory and Quantum Mechanics", McGraw-Hill.

J. M. Trombetta and G. D. Watkins (1987). Appl. Phys. Lett. **51**, 1103.

J. Wagner, A. Dornen and R. Sauer (1985). Phys. Rev. B **31**, 5561.

G. H. Wannier (1937). Phys. Rev. **52**, 191.

S. P. Watkins (1984). Phys. Rev. B **29**, 5727.

S. P. Watkins and M. L. W. Thewalt (1986). Phys. Rev. B **34**, 2598.

R. K. Watts (1977). "Point Defects in Crystals", John Wiley & Sons.

J. Weber, W. Schmid and R. Sauer (1980). Phys. Rev. B **21**, 2401.

A. D. Zdetsis (1979). Chem. Phys. **40**, 345.

Chapter 3: Experimental Apparatus and Techniques

3.1: Introduction

In this chapter the experimental apparatus and techniques used to investigate the electronic structure, symmetry and chemical identity of defects in silicon are described.

The band gap of silicon is ≈ 1.1eV and therefore spectral features from silicon excited with above band gap radiation are generally seen in the region 0.5-1.1eV. Excitons bound to defects in silicon often have binding energies of 10-50meV, and therefore dissociate thermally at temperatures ≤ 60K. In addition, the thermal broadening effects on spectral lines sets a limit to the possible resolution for temperatures ≥ 25K. Because many of the experimental techniques used in defect investigation require high resolution to separate closely-spaced lines (isotope studies, uniaxial stress and Zeeman studies for example), it is important that the samples can be studied at temperatures < 25K. In the work presented here, two different types of cryostat were used, one operating on a closed cycle system, and the other using liquid helium as the coolant. Details are given of the uniaxial stress and Zeeman spectroscopy facilities. PL spectroscopy of semiconductors such as silicon has advanced greatly in the last twenty years, due mainly to the introduction of sensitive cooled germanium detectors and also due to the use of Fourier transform (FT) spectrometers in the near infra-red (NIR) spectral region. These two factors have allowed high resolution studies of defects in silicon. The quality of the raw material has now become the limiting factor in determining the data quality, rather than instrumental limitations (Davies 1989). A high performance FT spectrometer coupled to a cooled germanium detector was used for the measurements reported here. The FT spectrometer system is described, and its advantages and disadvantages considered with respect to PL spectroscopy.

3.2: Cryogenic Apparatus

(i): Closed Cycle Cryostat

A Janis model CCS-500 closed cycle refrigeration cryostat was used for exploratory measurements and for experiments which did not require temperatures below ~ 15K. The cold head and compressor unit were manufactured by Leybold-Heraeus and operated using a two stage closed helium gas cycle.

The samples were mounted on a sample stick suspended inside an exchange gas tube. The exchange gas tube was in turn mounted on the second stage of the refrigerator, and the helium exchange gas provided the thermal link between sample and refrigerator. The sample tube was surrounded by an aluminium radiation shield, which is cooled by the refrigerator first stage mounting flange (~ 75K). A vacuum shroud thermally isolates the cold regions from the surroundings. The radiation shield and vacuum shroud have apertures which allow ~ F1 optical access on three sides of the cryostat. The inner and outer optical windows are made of fused quartz. A resistive heater and temperature sensor (Lakeshore Cryogenics silicon diode sensor) were available both on the refrigeration unit (heat exchanger) and on the sample stick itself. The sample holder was made of copper and the temperature sensor bonded to it using Oxford Instruments low temperature varnish, and the sample was held in place on the holder using PTFE tape. Up to six samples could be mounted on the holder at the same time. An Oxford Instruments automatic temperature controller (model ITC4) was used to monitor and control the temperature in the cryostat. A schematic diagram of the cryostat is shown in figure 3.2.1.

(ii): Helium Flow Cryostat

An Oxford Instruments continuous flow cryostat (model CF 1204) was used for experiments where accurate temperature control and variation were needed, and for experiments requiring temperatures down to 4.2K.

Continuous flow cryostats operate using a controlled and continuous flow of coolant (liquid helium in this case) from a storage vessel to the cryostat. The coolant flows through a heat exchanger, which has a temperature sensor and heater, and the temperature of the cool gas (liquid) in the sample space is varied by establishing an

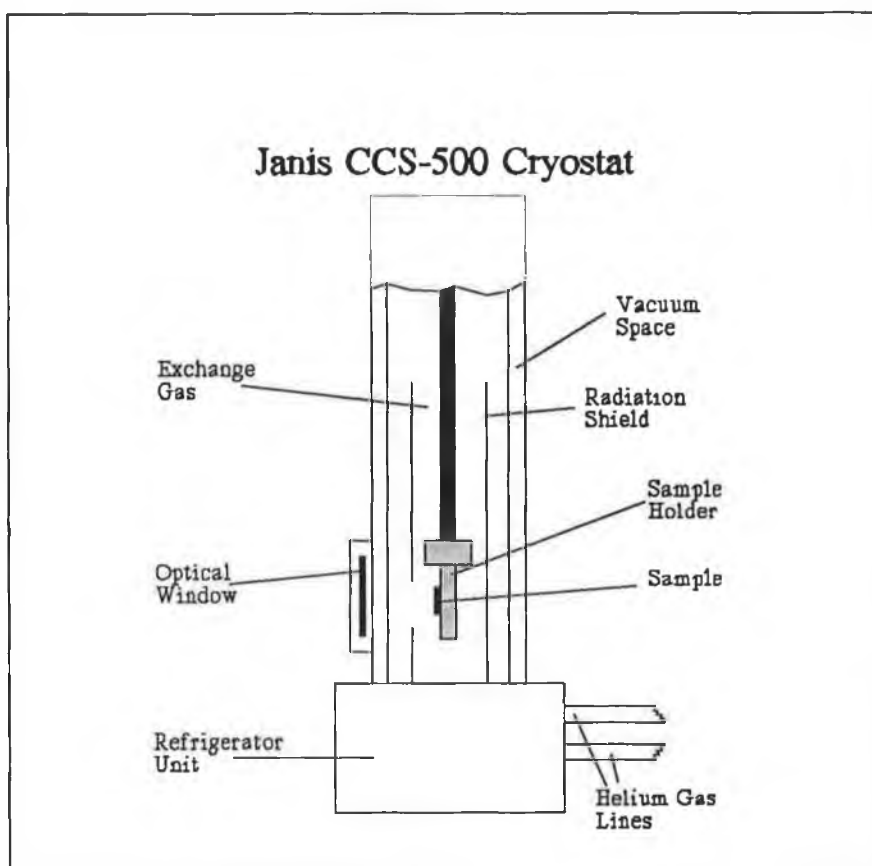

Figure 3.2.1: Janis Closed Cycle Cryostat

equilibrium between the heater power and the rate of coolant flow, allowing temperatures between 4.2K and room temperature to be established in the sample space. The coolant is drawn from the storage vessel into the cryostat, via a vacuum insulated transfer tube, using an oil-free vane pump. The samples were mounted on a sample stick suspended in the cool gas (liquid). The sample space was surrounded by a radiation shield (~ 75K), and a vacuum shroud isolates the cold regions from the surroundings. The vacuum shroud and radiation shield has apertures which allowed ~ F1.6 optical access on three sides of the cryostat. The outer windows were fused quartz, and the inner windows were made of sapphire. Resistive heaters and temperature sensors (Oxford Instruments rhodium iron resistance sensors) were available on both the heat exchanger and sample stick. The sample holder was made of copper and the sensor was secured to it using low temperature varnish, while the sample was held on the stick using PTFE tape. Up to three samples could be loaded on the stick at once. An Oxford Instruments ITC4 temperature controller was used to

monitor and control the temperature in the cryostat. A diagram of the cryostat and operating arrangement is shown in figures 3.2.2 (a) & (b).

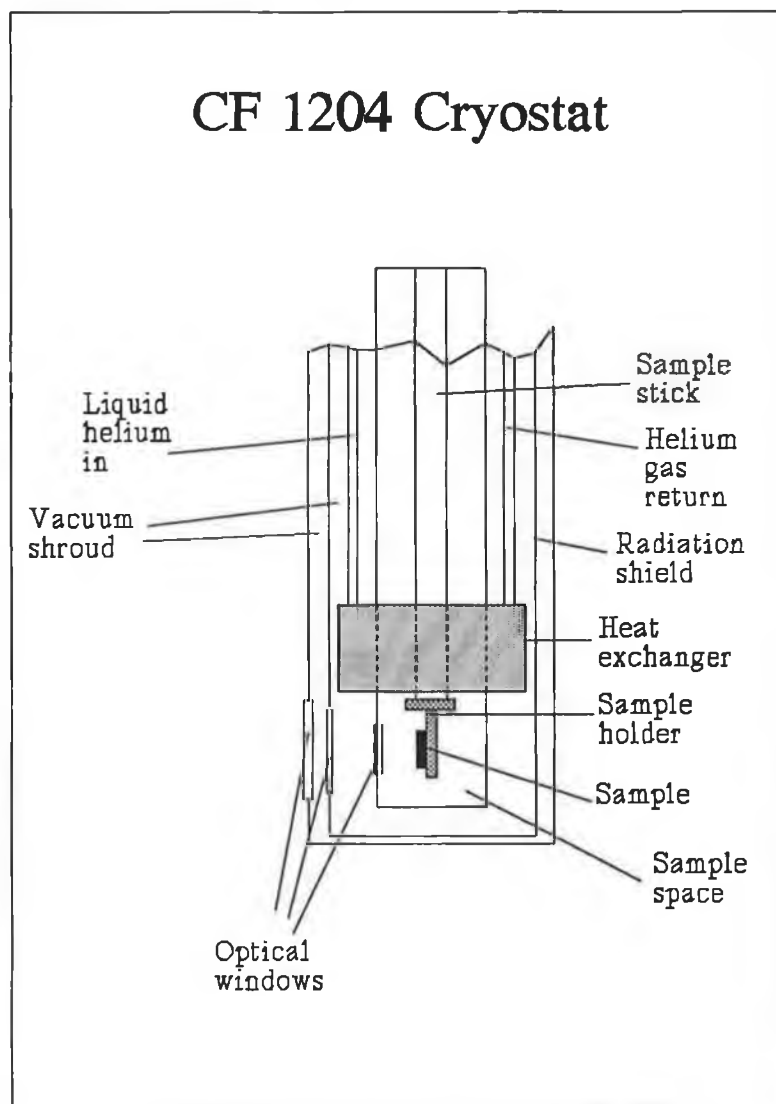

Figure 3.2.2 (a): Helium Flow Cryostat

3.3: Magnetic Field Facilities

In order to obtain information on the magnetic properties of defects, via Zeeman spectroscopy, magnetic fields up to five Tesla are commonly used. Two types of superconducting magnet were used during the course of this work, one with a split coil geometry, and the other used a single coil geometry. The advantage of using a

split coil geometry over single coil geometry is the ease of optical access, which is an important factor when working with weakly emitting samples. The disadvantages

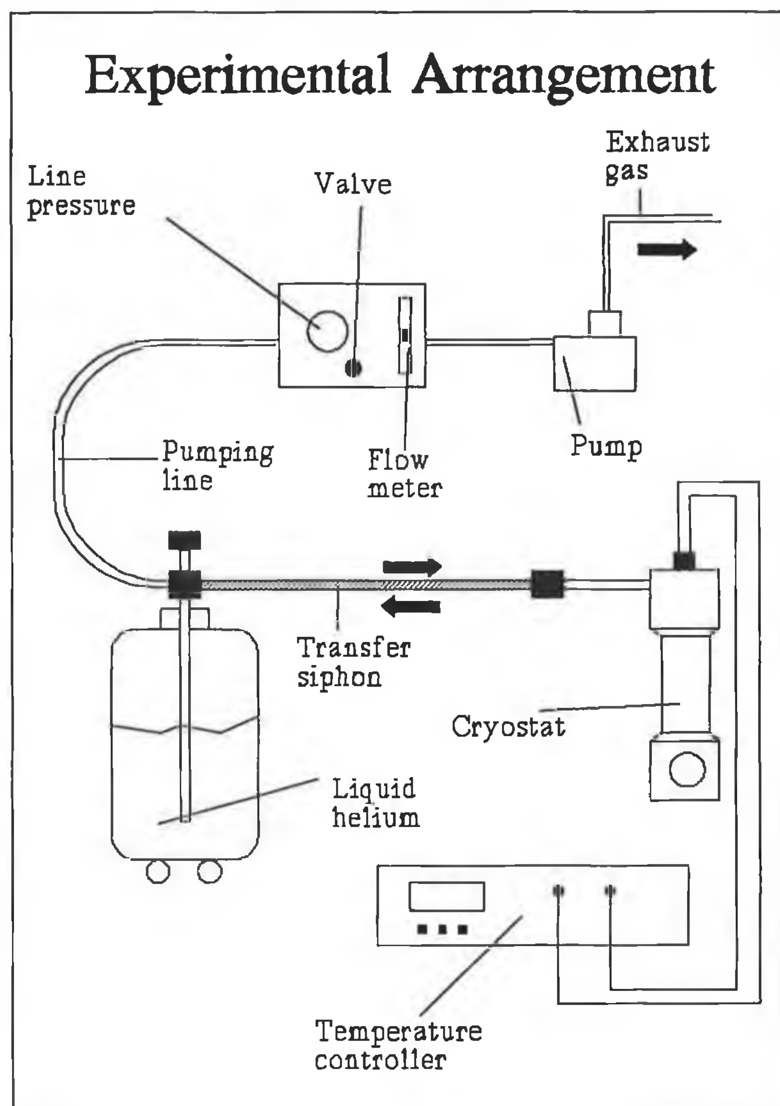

Figure 3.2.2 (b): Experimental Layout

however are that the ultimate field achievable is not as large as with a single coil geometry, nor is the field as homogenous as in the single core case.

A schematic diagram of both types of coil is shown in figure 3.3.1.

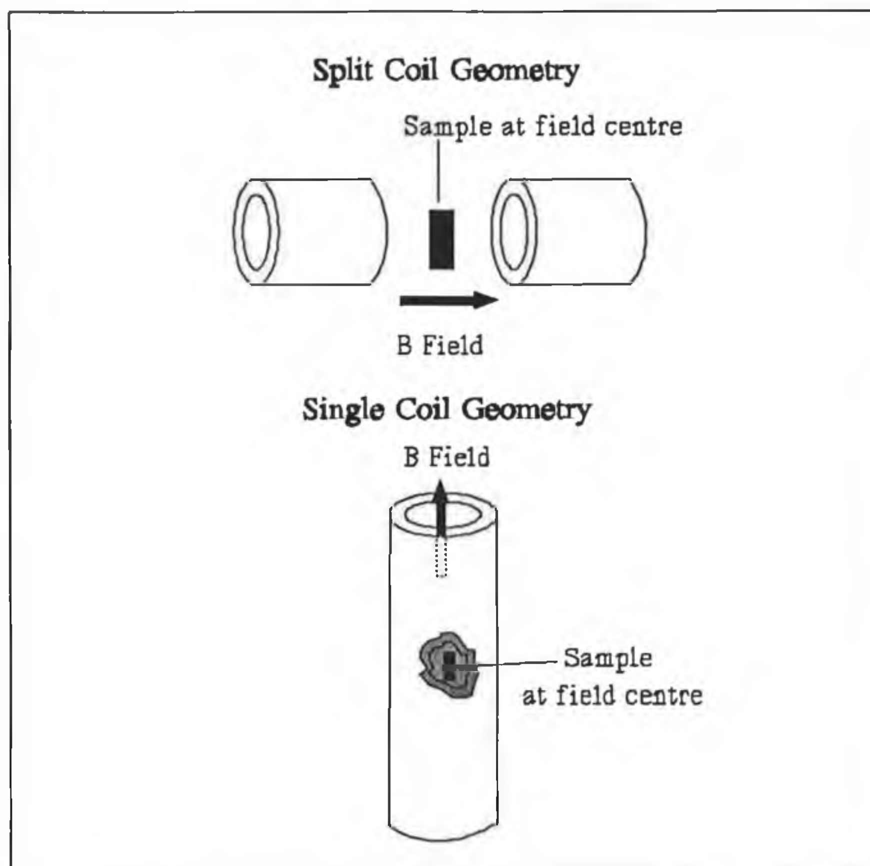

Figure 3.3.1: Magnetic Coil Geometries

Two configurations were available for mounting the samples in the magnetic field, the Faraday configuration and the Voight configuration, illustrated in figure. 3.3.2. For the measurements presented in this work the Faraday configuration was used, in which the magnetic field direction was parallel to the direction of the collected luminescence.

An Oxford Instruments SpectroMag 4 liquid helium bath cryostat was used at the University of Aveiro, which employed a superconducting split pair magnet mounted horizontally in the tail attachment. Fields up to 5T could be achieved with this magnet. Windows fitted to the tail assembly allow optical access to the sample in the magnetic field, and the experimental arrangement was similar to that for normal PL measurements, as described in section 3.6.

The magnet with the single coil geometry was an Oxford Instruments SMD6 cryostat and superconducting magnet, with vertical optical access (from the bottom).

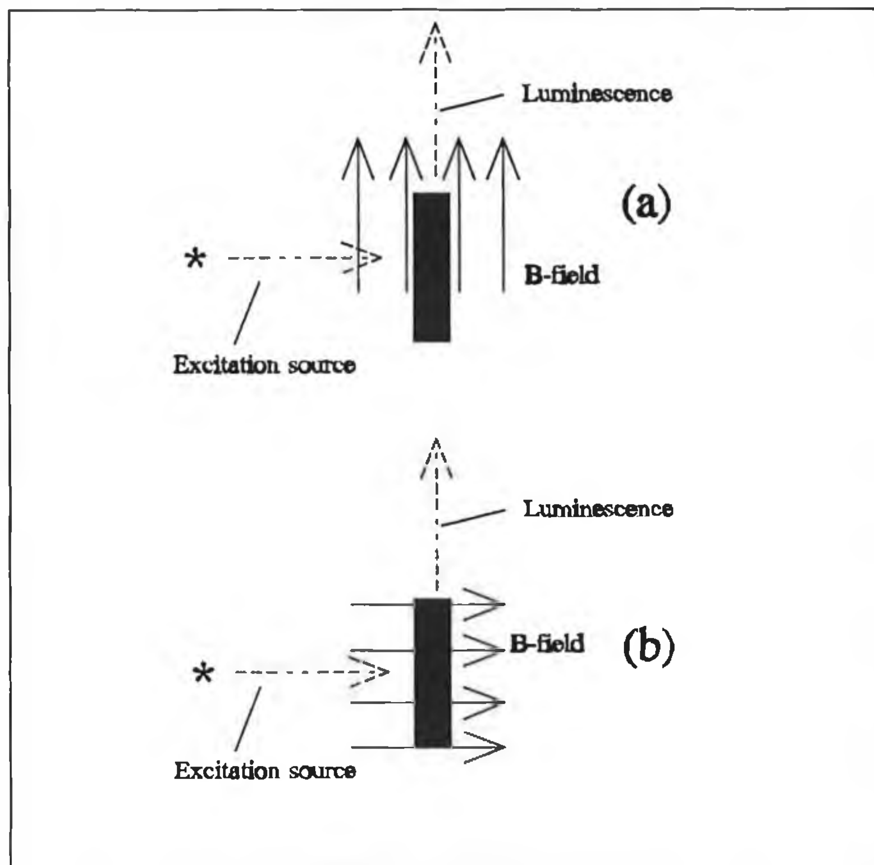

Figure 3.3.2: (a) Faraday configuration
(b) Voight configuration

The vertical optical access makes spectroscopic measurements far more difficult, compared to using the SpectroMag 4 system.

The maximum field attainable with this magnet was 9T at 4.2K (11T at 2.2K). The cryostat windows are sapphire. A magnet which can produce high fields must be kept at a distance of at least 1.5m from other lab equipment, especially computers, motors etc. and because of this particular care must be taken in the experimental design. Because of the restricted optical access which a magnet of this type has, it was necessary to design and build an optical system to maximise the signal levels collected from the magnet and coupled to the spectrometer.

A schematic diagram of the optical system used to excite and collect PL from the single coil magnet is shown below in figure 3.3.3. The laser source is directed onto mirror M1 by the small mirror SM1 and is reflected down onto mirror M2 and

onto the off-axis parabolic mirror OAP1 and focussed up onto the sample in the bore of the magnet. The luminescence emitted from that point is at the focus of OAP1 and is collected and collimated by OAP1 in the direction of M2. It is then reflected off M2 onto M1 and into the spectrometer (mostly bypassing the small, 4mm × 6mm, mirror SM1). The diameter of the other mirrors in the system is ~ 125mm, so a negligible percentage of the luminescence is lost by reflection off SM1. By adjusting both the x and y position of the OAP1 the sample remains in focus and OAP1 remains in the same position with respect to M2. Hence the luminescence is constantly on-axis with respect to the spectrometer and is independent of the position of OAP1 under the magnet. This means that the x and y position of OAP1 can be adjusted without fear of losing alignment with respect to the spectrometer. This optical arrangement allows one to optimise the system with relative ease, because only the x,y and z positions of the mirror OAP1 need adjustment. All the other mirrors automatically remain on-axis.

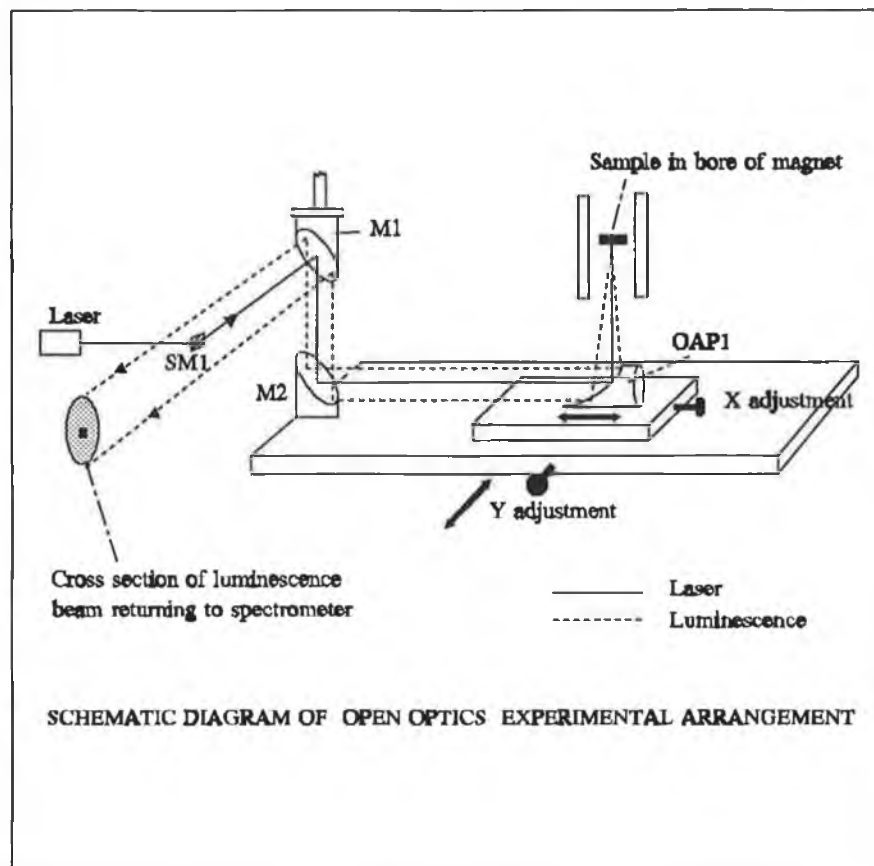

Figure 3.3.3: Optical Access to Vertical Bore Magnet

3.4: Uniaxial Stress Facilities

The technique of uniaxial stress spectroscopy has been introduced from a theoretical viewpoint in chapter 2, and the experimental details will be discussed in this section.

The samples used for these experiments were cut into rectangular parallelipipeds (dimensions ~ 10mm x 3mm x 1.5mm) with the long axis parallel to one of the crystal axes <100>, <111> or <110>. The long axis to width/thickness ratio is large in order to reduce inhomogeneities in the stress. In order to be able to resolve the closely spaced components, it was necessary to perform the experiments at low temperatures (4.2 - 10K) to minimise thermal broadening of the lines. The experiment was performed in the Oxford Instruments CF 1204 cryostat (section 3.2 (a) (i)).

The stress rig (O'Morain *et al.* 1992) was made of stainless steel and consisted of a hollow outer tube, with four apertures for optical access at the bottom of the tube positioned to coincide with the cryostat windows when the apparatus was assembled. The sample was mounted exactly perpendicularly (i.e. long axis parallel to the axis of the stress rig) between two small hardened steel push rods (with polished end-faces) at the bottom of this outer tube. Great care was taken to ensure that the samples were mounted parallel to the stress rig axis, otherwise the transmitted force would not be parallel to the crystal direction and spurious line splittings would result. Double-sided sellotape was used on the faces of the two small hardened steel push rods to make the process of mounting the samples easier and also to compensate for any residual roughness on the faces on the push rods. The stress was applied via a longer, hollow (to minimise heat conduction from the room) push rod which extended to the top of the outer tube. The entire assembly was inserted into the cryostat (see figure 3.2.6). O-ring seals prevented air from entering the cryostat at the joints between cryostat and stress rig, and between outer tube and long push rod. The stress was applied to the push rod by compressing a steel spring by turning a handle attached to a threaded bar arrangement. The force produced by this spring was measured using a Bofors KRA-1 piezoelectric load cell positioned between the spring and the push rod. The contact was made between push rod and load cell by a ball bearing (attached to the load cell) located into a slight depression in the push rod. This allowed accurate and

reproducible centring of the load cell on top of the push rod. The ball bearing could rotate freely, and this, along with the low area of contact, minimised the amount of friction between load cell and push rod, in principle stopping the push rod from rotating (and thus twisting and misaligning the sample) as the stress was increased. Even with this precaution, when removing the stress from the sample, a noticeable misalignment took place. The load cell gave an output voltage proportional to the applied load (0.3mV per 1kg load) over its working range (0 - 70mV) (Thewalt *et al.* 1990). The relationship between the applied stress and the load cell output voltage is given in equation 3.4.1;

$$Stress\ (MPa) = \frac{9.8(V-V_0)}{A(0.286)} \qquad (3.4.1)$$

where V_0 is the load cell zero stress reading in volts, V is the load cell reading in volts and A is the sample area in mm^2. This arrangement can produce stresses up to 150MPa, and with typical line shifts of the order of 0 - 5meV compared to line widths of < 0.2meV, the changes in line position can be accurately measured.

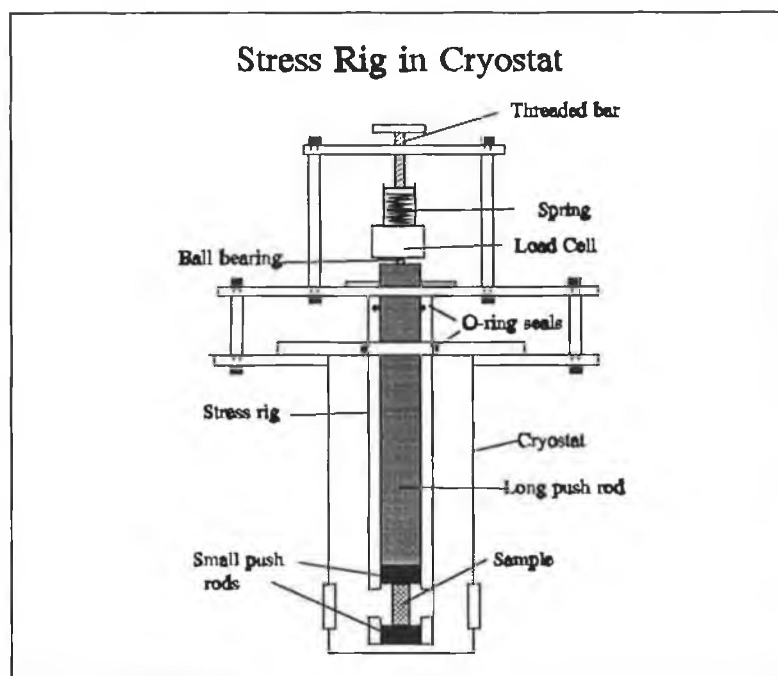

Figure 3.4.1: Schematic Diagram of Stress Rig

3.5: FT Spectrometer System

All the work presented in this thesis has been performed on a Bomem DA8 FT spectrometer. A large part of the initial period of the project was spent in setting up the instrument for PL, designing the optical layout of the system etc. FT spectroscopy has become one of the major tools in modern day spectroscopy, due to the vast increase in the availability and affordability of powerful computers which can perform the fast Fourier transform (FFT) algorithm for large arrays of numbers in very short times (~ 1s for 5000 point array). A brief description of the FT spectrometer and optics is given, along with an outline of its advantages and limitations. There are a number of problems associated specifically with the use of FT spectrometers for emission work in the NIR which will be discussed at the end of the section.

The main component in the Bomem DA8 FT spectrometer is a Michelson interferometer (figure 3.5.1).

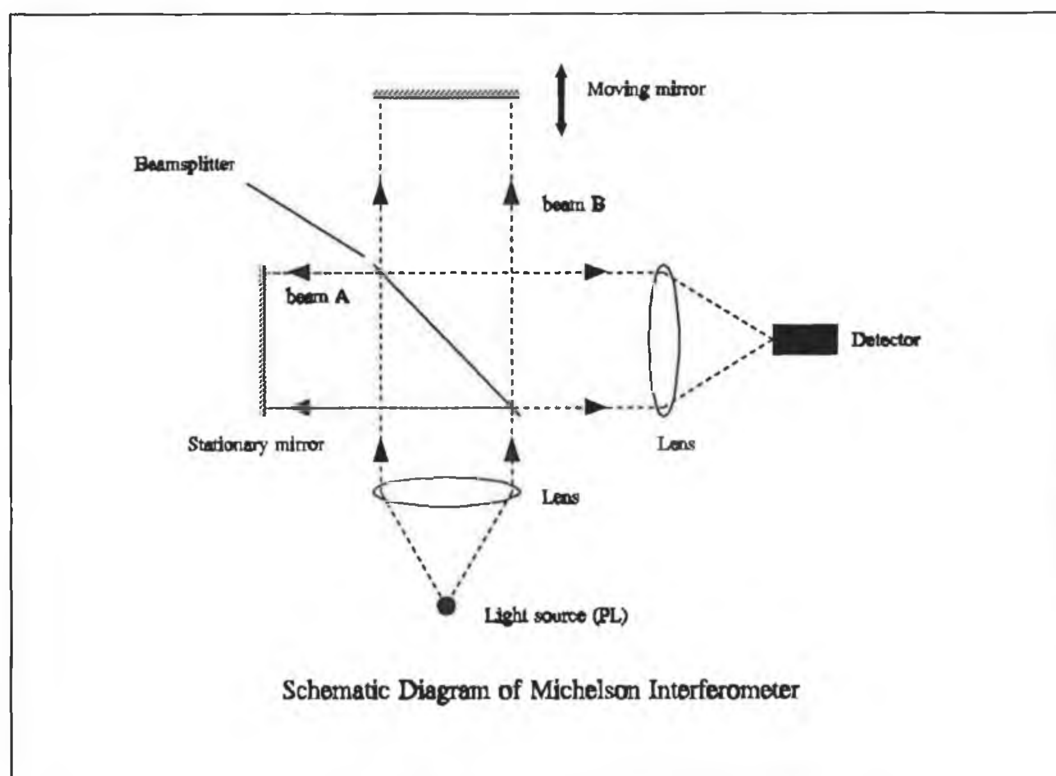

Figure 3.5.1: Schematic Diagram of Michelson Interferometer

The light source for our experiments was the source of PL, and this PL was directed onto the beamsplitter, which reflects half the light (beam A) and transmits the other half (beam B). Beam A is then passed through a constant path length while beam B passes through a path length which can be continuously varied by changing the position of the moving mirror. The two beams are recombined at the beamsplitter and the resultant intensity measured by the detector. Depending on the relative path lengths travelled by the two beams (and hence relative phase shifts) they will interfere either constructively or destructively, and thus the intensity at the detector will vary from high to low as the moving mirror scans. The detector signal is measured as a function of the moveable mirror position and this varying intensity signal I(x) is known as the interferogram. Each separate frequency component in the source will produce a cosinusoidal intensity variation in the detector signal. By integrating over all the frequencies in a polychromatic source one can find the expected interferogram; this is simply the mathematical operation of Fourier transformation, equation 3.5.1.

$$I(x) = \frac{1}{2}I_0 + \frac{1}{2}\int_0^{\infty}\cos(2\pi \nu x)S(\nu)d\nu \qquad \textbf{(3.5.1)}$$

I(x) is the detector intensity at mirror displacement x, I_0 is the total source intensity, $S(\nu)d\nu$ is the energy in the small spectral element $d\nu$ centred around ν. ν is called the wavenumber and is measured in units of cm^{-1}. It is related to wavelength by $\nu=1/\lambda$.

Conversely, the frequency distribution of the light source can be found by measuring the interferogram and taking the inverse Fourier transform. Details of this process can be found in Chamberlain (1979). Examples of different interferogram shapes for single frequency, dual frequency and polychromatic light sources are shown in figure 3.5.2.

The resolution of a FT spectrometer is inversely proportional to the maximum range of the moveable mirror (Chamberlain, 1979), $\Delta\nu_{max}=1/x_{max}$. The resolution of any particular spectrum is inversely proportional to the maximum mirror movement during that scan. Other factors such as apodisation and the entrance aperture size also affect the resolution and a detailed description of these factors can be found in Chamberlain

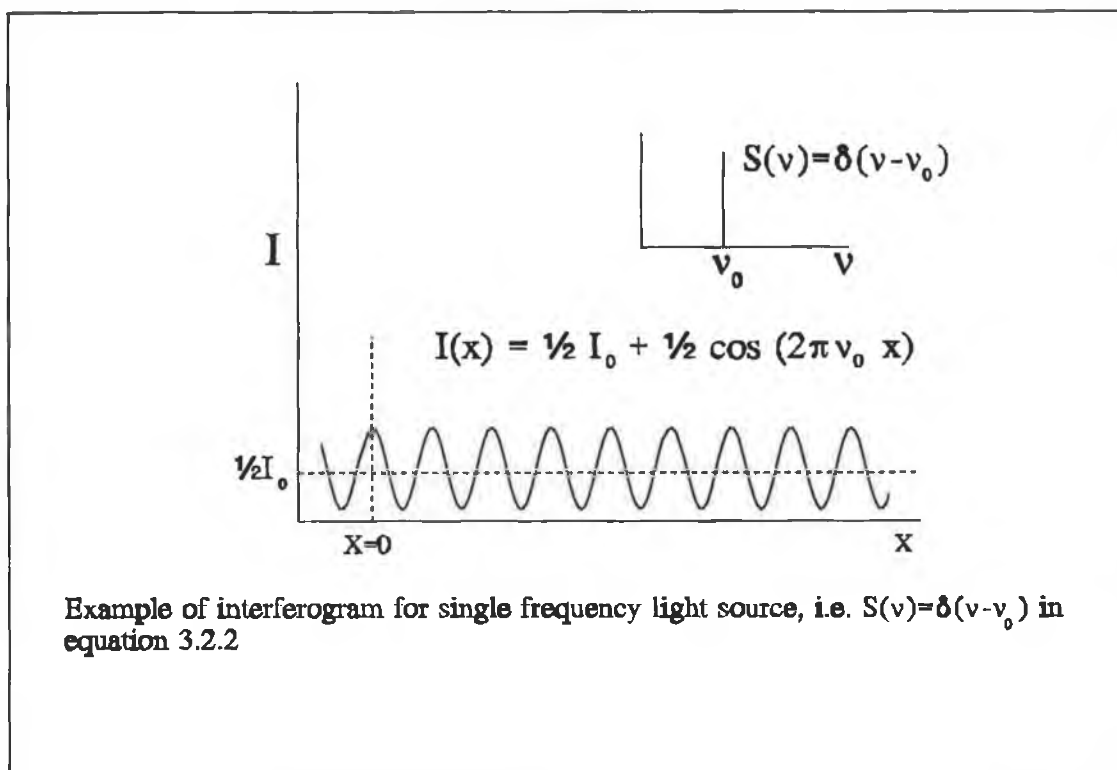

Example of interferogram for single frequency light source, i.e. $S(\nu)=\delta(\nu-\nu_0)$ **in equation** 3.2.2

Figure 3.5.2 (a): Single Frequency Interferogram

(1979). The moving mirror in the Bomem DA8 has a maximum range of 2.5 metres and this corresponds to a maximum unapodised resolution of 0.004 cm^{-1}.

The interferometer keeps track of the position and alignment of the moving mirror by using a reference interferogram generated by a single mode He-Ne laser. The zero path difference (ZPD) position of the instrument is measured using the interferogram generated by a broad band white light source (the interferogram of such broad band sources displays a large amplitude in the region of ZPD and small amplitude elsewhere (Chamberlain 1979)).

There are a number of advantages to be gained from the use of FT spectrometers instead of normal dispersive spectrometers.

a) Multiplex or Fellget advantage: In conventional dispersive instruments, the detector senses only one spectral element (small range of the spectrum, determined by the slit width) at a time. In FT spectroscopy however, the detector is sensing all the spectral

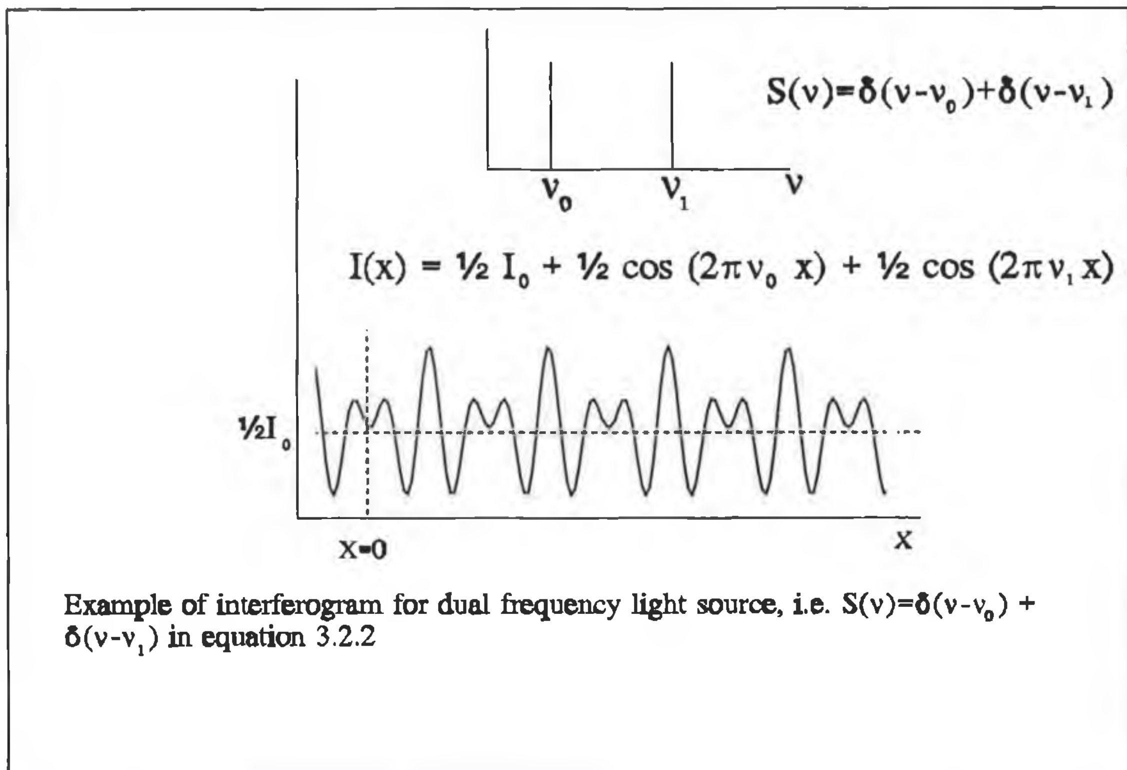

Example of interferogram for dual frequency light source, i.e. $S(\nu)=\delta(\nu-\nu_0) + \delta(\nu-\nu_1)$ in equation 3.2.2

Figure 3.5.2 (b): Dual Frequency Interferogram

elements simultaneously, and when the system is detector noise limited (the noise level from the detector is independent of the signal level impinging on it) this results in a gain in signal to noise ratio (SNR) of $N^{1/2}$, where N is the number of spectral elements, the number of points on the spectrum (Hirschfeld 1979). This multiplex advantage relies on the fact that the system is detector noise limited, and this is generally the case for IR work using photodiodes or photoconductors. For detectors which are not detector noise limited (e.g. photomultiplier tubes, which are shot noise limited i.e. the noise level is proportional to the square root of the signal), the multiplex advantage is cancelled out, and indeed becomes a disadvantage for systems which are dominated by flicker noise (Jeyanathan 1994). Because the detector is sensing all wavelengths at all times, this means that the entire spectrum is being recorded by the instrument, taking the same amount of time . This property is useful when broad, exploratory scans are being performed.

b) Jacquinot or throughput advantage: The second advantage which a FT spectrometer

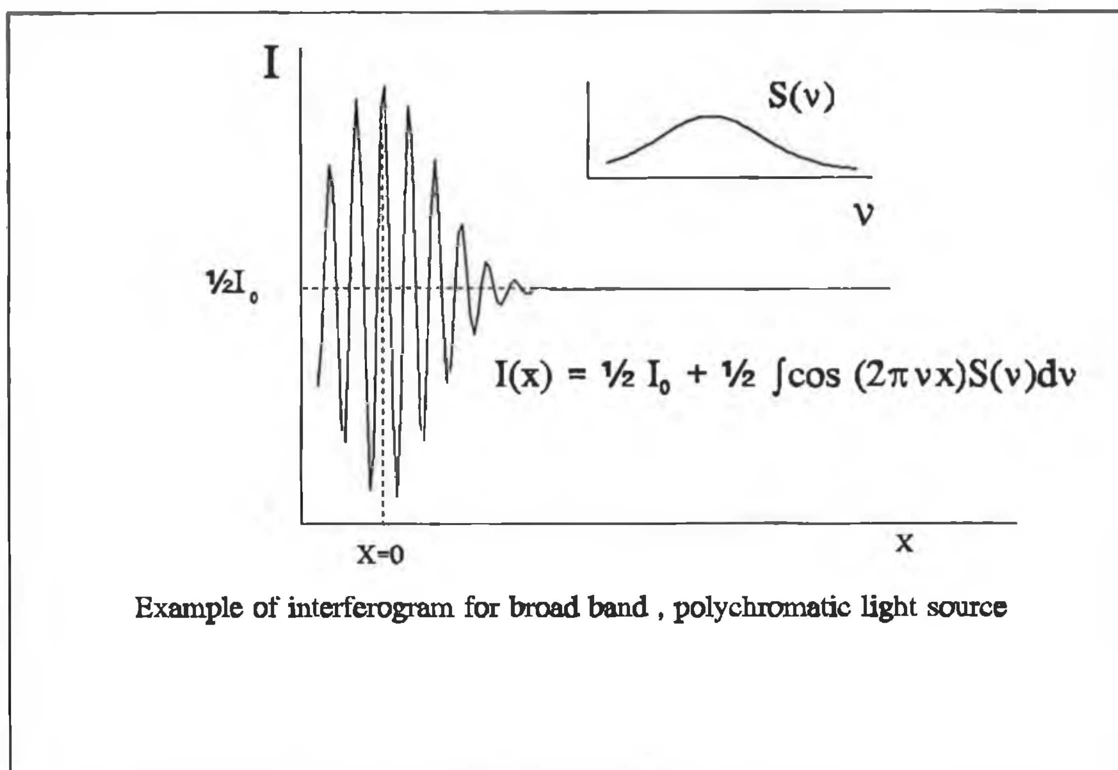

Figure 3.5.2 (c): Broadband Interferogram

offers is the increased throughput of radiation for a given resolution. This is because of the increased area offered by the circular entrance aperture of a FT spectrometer over the narrow slits of a grating spectrometer.

In addition to these two advantages, one can also use the FT spectrometer to average a large number of scans (SNR $\propto$ {number of scans}$^{1/2}$) and thus further increase the SNR. Although this can also be done with a dispersive instrument, the FT spectrometer generally can perform a single scan more quickly (especially a broad scan because of the previously mentioned multiplex advantage). Therefore more scans can be collected in the same amount of time it takes a dispersive instrument to perform one scan, hence improving the signal to noise ratio, while taking the same overall time for the experiment.

Other advantages of FT spectrometers include (Thewalt *et al.* 1990);

a) Wide spectral ranges available so that information can be collected from < 3000

cm^{-1} to 10,000 cm^{-1} in a single scan (without order-sorting problems, blazed grating efficiencies etc.). It is also possible to cover a wide spectral range (far infra-red (FIR) to ultra-violet (UV)) by using a small number of detector/beamsplitter combinations.

b) FT spectrometers have a high spectral accuracy (< 0.02 cm^{-1} at 10,000 cm^{-1}), because they use frequency-stabilised He-Ne lasers to measure the moving mirror position. This level of accuracy could only be achieved in a grating instrument by means of regular calibration with a known spectral source. In effect the FT spectrometer is continuously being calibrated.

There are a number of limitations also associated with FT spectrometers;

a) Cost; the cost of FT spectrometers can be prohibitive. In addition to the large amount of computing power needed for the mathematical transforms, FT spectrometers tend to be far more complicated pieces of machinery than ordinary grating instruments. A large amount of computer-interfaced optical and mechanical elements are required to drive the mirror motors, keep the mirrors aligned, sense the He-Ne reference interferogram etc. This is reflected not only in the initial cost, but also in the fact that "in-house" repairs to the system are very difficult, if not impossible for certain problems.

b) Dynamic Range (Jeyanathan 1994); because the FT spectrometer is sensing the entire spectral intensity, a weak line of interest in the otherwise strong spectrum will be only a small fraction of the total intensity, and if the intensity of the line is less than the smallest digitisation unit in the analog-digital convertor of the FT, it may be lost entirely. A grating spectrometer would be a more appropriate choice in this case. Alternatively, appropriate pre-filtering could be used to isolate the spectral region of interest.

c) Beamsplitter imperfections; an ideal beam splitter would transmit exactly 50% of the radiation and reflect 50% over the entire spectral range. In practice no beamsplitter will perform to this level of accuracy over a wide wavelength range (Griffiths *et al.*

1986).

Issues concerning the use of FT spectrometers for PL spectroscopy

a) Filtering; in addition to the PL signal incident on the detector there is also an appreciable amount of light from the white light source and He-Ne laser, scattered off the beamsplitter and mirror surfaces, incident on the detector. If the detector is very sensitive (cooled germanium detectors have a noise equivalent power (NEP) less than $10^{-14}WHz^{-1/2}$) then this scattered light can produce spurious effects in the observed spectrum, and can even cause the detector to saturate. In order to eliminate this effect it is necessary to ensure that the white light source is filtered so that it contains no wavelength components in the PL wavelength region (1μm → 2μm). For the results presented in this work, a long-pass filter (which transmits wavelengths > 1μm) was placed in front of the detector, and a band pass filter (0.5μmm < λ < 0.95μm) was placed in front of the white light source and He-Ne laser (laser plasma lines could be present in the wavelength region of interest). These filters ensured that the white light source was adequately spectrally separated from the PL wavelength region.

b) Phase Correction; the Bomem DA8 instrument collects data on one side of the ZPD position only, allowing for greater range of mirror movement (and hence higher resolution). Ideally the interferogram ought to be symmetrical about the ZPD position, allowing one to easily calculate the Fourier transform. However in practice due to the wavelength dependent properties of optical elements such as the mirror reflectivity, beamsplitter refractive index etc. the interferogram is not symmetrical about the ZPD. A correction factor must be obtained in order to symmetrise the interferogram. This is done by taking a very low resolution (~ 30 cm^{-1}, or a maximum mirror movement of 0.03cm) two-sided scan and calculating the correction factor from this. If the sample position is changed or a new sample is introduced into the beam, the source of luminescence moves, and therefore the radiation is entering the spectrometer at a slightly different angle, and hence is travelling through a slightly different path in an element like the beamsplitter. This means that the phase correction must change to compensate for this. In practice this means that very accurate phase correction factors

are required when detailed spectral information is being sought, in isotope substitution experiments for example.

The detector used for the work presented here was a North Coast cooled germanium diode detector (model ED2). The response time of this detector was optimised for use on a FT spectrometer (response time ~ 0.5ms). The detector consisted of a reverse-biased PIN diode with low noise pre-amplifier. The diode, feedback resistor and the FET of the pre-amplifier were cooled to 77K. This detector was highly sensitive (NEP < $10^{-14}WHz^{-1/2}$) in the 0.8μm → 1.8μm wavelength region.

The main problem noticed in using this detector in conjunction with an FT spectrometer is due to spikes caused by cosmic ray showers. The germanium detector is sensitive to these cosmic rays, which cause a large voltage spike on the output. When this spike is Fourier transformed, its effect is to cause a large ripple throughout the entire spectrum. By averaging a large number of scans, the relative magnitude of a spike on any one scan is greatly reduced.

3.6: Techniques

PL Spectroscopy

The technique of photoluminescence spectroscopy involves the study of luminescence from a sample which has been excited by a source of optical radiation (Davies 1989, Lightowlers 1990). The relevant theoretical background concerning the generation of this luminescence has been discussed in chapter two. While most of the individual components (such as the FT spectrometer, cryostats etc.) have been described in earlier sections, the purpose of this section is to describe the experimental arrangement used to collect and analyse this luminescence. A schematic diagram of the experimental arrangement is shown in figure 3.6.1.

The sample is placed in the cryostat, and the sample temperature can be varied between 4.2K and 300K by means of a temperature controller. The luminescence is excited using the 514nm line of an argon-ion laser. The laser output is suitably filtered

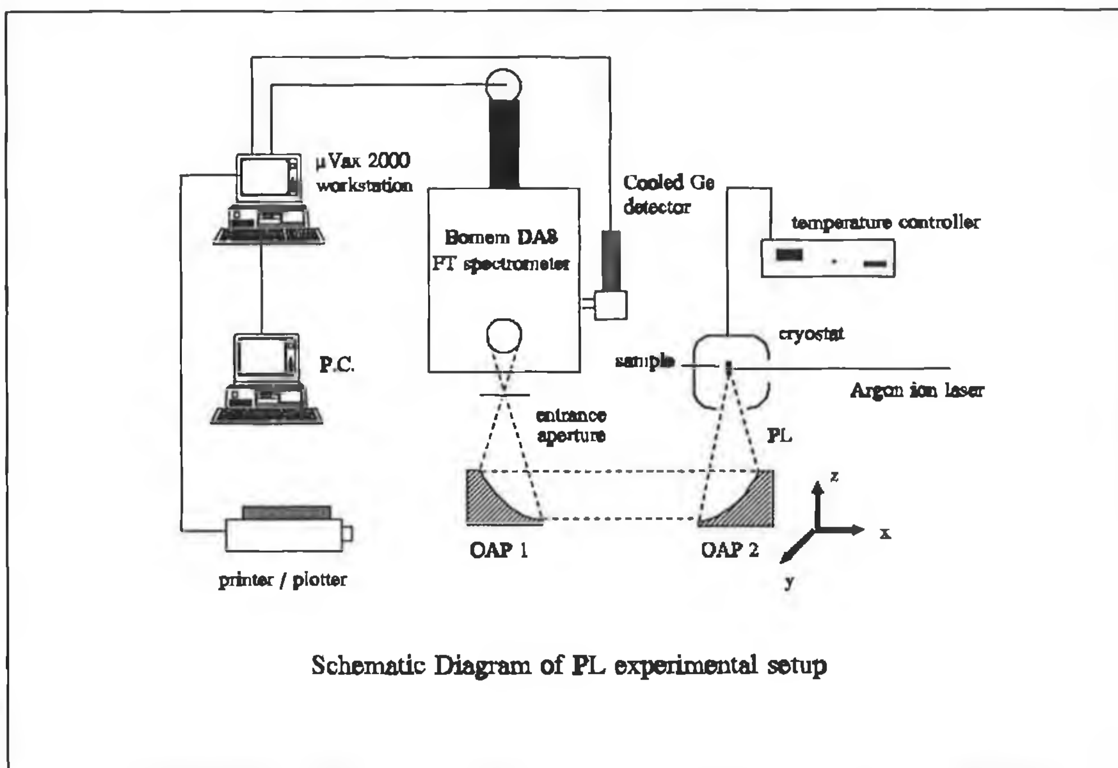

Figure 3.6.1: Schematic Diagram of Experimental Arrangement for PL Measurements

to remove unwanted plasma emissions. Typical excitation powers used were ≈ 250mW, unfocussed on the sample face. The luminescence is collected from the sample edge at 90° to the excitation direction in order to reduce the amount of laser light scattered into the spectrometer, as this scattered laser light can adversely affect the spectrometer alignment systems. Other luminescence collecting geometries such as the 135° geometry are discussed in Davies 1989 and Lightowlers 1990, which offer better collection efficiencies. The 90° geometry was found to be perfectly adequate for the studies presented here. The collected luminescence is collimated by an 90° off-axis parabolic mirror (labelled OAP 2 in figure 3.3.1). The collimated radiation is then incident on another 90° off-axis parabolic mirror (labelled OAP 1 in figure 3.3.1) and focussed into the FT spectrometer entry aperture. The two off-axis parabolic mirrors are chosen to match the f-number of the cryostat to that of the spectrometer, in order to maximise the throughput of the system. Both the off-axis parabolic mirrors have x, y and z adjustment capability.

The luminescence then travels through the interferometer and as the moving mirror travels in the scan tube the luminescence intensity incident on the detector is modulated to form an interferogram. A long wavelength pass filter is placed in front of the detector (as described in section 3.2 (d)). The spectrometer is controlled and the detector output sampled by a μVax 2000 workstation. This workstation is connected via a RS232 link to a P.C. and is also linked to a plotter.

3.7: Conclusions

The main purpose of this chapter has been to describe the experimental techniques and equipment used to obtain the results presented in the following chapters. As was mentioned previously, all the work in this thesis was performed on a Bomem DA8 FT spectrometer. The majority of experiments, especially those of an exploratory nature were performed on the closed cycle refrigeration cryostat in preference to the helium flow cryostat, for financial reasons. The helium flow cryostat was generally used when low temperatures were required for experiments such as uniaxial stress, isotope substitution studies and temperature dependence studies.

The uniaxial stress measurements using the stress rig described in section 3.4 were found to be extremely sensitive to the mounting of the samples, care taken in inserting the stress rig in the cryostat and so forth. Extreme care was required throughout both the preparation and execution of the experiment. For this reason all the uniaxial stress results were taken at least twice to ensure consistent results.

Having described the techniques and equipment used in the analysis of defects in semiconductors, the next chapter will present the results of experiments performed on the 983meV (Cd_A defect) in Cd-implanted silicon.

References

J. Chamberlain (1979). "The Principles of Interferometric Spectroscopy", Wiley Interscience.

G. Davies (1989). The Optical Properties of Luminescence Centres in Silicon, Physics Reports **176**, 3&4, 83.

P.R. Griffiths and J.A. de Haseth (1986). "Fourier Transform Spectroscopy", Wiley and Sons, New York.

T. Hirschfeld (1979). Quantitative FT-IR: A Detailed Look at the Problems Involved, "Fourier Transform Infrared Spectroscopy", Vol. 2, Academic Press.

A. E. Hughes and W. A. Runciman (1967). Proc. Phys. Soc., **90**, 827.

L. Jeyanathan (1994). PhD. Thesis, University of London.

E.C. Lightowlers (1990). "Photoluminescence Characterisation", edited by R. A Stradling and P. C. Klipstein, Adam Hilger.

C. O'Morain, K.G. McGuigan, M.O. Henry and J.D. Campion (1992). Meas. Sci. Technol. **3**, 337.

M.L.W. Thewalt, M.K Nissen, D.J.S. Beckett and K.R. Lundgren (1990). Impurities, Defects and Diffusion in Semiconductors: Bulk and Layered Structures, Mat. Res. Soc. Symp. Proc. **163**, 221.

Chapter 4: 983 meV Defect in Cadmium-Doped Silicon

4.1: Introduction

In this chapter, a description and analysis is presented of a previously unreported luminescence centre found exclusively in Cd-doped CZ silicon. The ZPL of the systems is at 983.21 (±0.05)meV. The defect is referred to in the text as Cd_A. A considerable amount of detail is found in the phonon sidebands of the main line. Measurements as a function of temperature reveal that the thermal binding energy is low and the defect is believed to be composed of one tightly bound and one loosely bound particle. Stress measurements reveal a low symmetry for the defect site (Cd_A - rhombic I), and Zeeman measurements indicate pseudo-donor nature for the excited state of the centre. Cd isotope substitution experiments confirm the involvement of one Cd atom in the defect complex. Isotope substitution experiments are reported for a range of common impurities in CZ silicon in an attempt to identify the defect constituents. Comparisons are drawn throughout the chapter with the previously reported Zn_A line (Henry *et al.* 1994) with which many similarities are observed.

4.2: Sample Preparation and Defect Production

The Cd_A system was produced by Cd ion implantation (beam energies of both 80keV and 200keV and ion doses of $10^{12} \rightarrow 10^{15}$ ions/cm^2 were used with no discernable differences in the production of the defect centre), followed by annealing at 550°C for 30 minutes in an atmosphere of flowing argon gas (appendix A). The sample was withdrawn from the furnace and allowed to cool slowly. Increasing the cooling rate by quenching in an isopropanol alcohol/water mixture was found to destroy the formation of the defect centre. The centre could be produced by 30 minute anneals in the temperature range 550°C→700°C, but 550°C was found to be the optimum temperature in order to obtain high signal levels. Figure 4.2.1 shows examples of spectra obtained from samples of Cd-implanted CZ silicon subject to

isochronal anneals (30 min) at different temperatures. At low temperature anneals (300-400°c), the features marked W, X, C and P are visible in the sample spectra. The W line at ~1018meV is produced by ion-implantation (or similar) damage. The X line (also known as I3) at ~1039meV is another product of ion-implantation damage and annealing. The C line at ~789meV is a radiation damage product involving C and O. The P line at ~767meV is also caused by radiation damage or annealing and is a C-related centre. All these centres are tabulated in the review by Davies (1989) and further details and references can be found there. At temperatures above 700°C, where the Cd_A centre is destroyed, a series of lines (marked with an L) with ZPL at ~996meV is seen. The phonon sideband shows a marked similarity to previously reported copper centres (McGuigan 1989). This centre has also been observed in quenched FZ material (Freehill 1995), but its origin has not been investigated in any further detail.

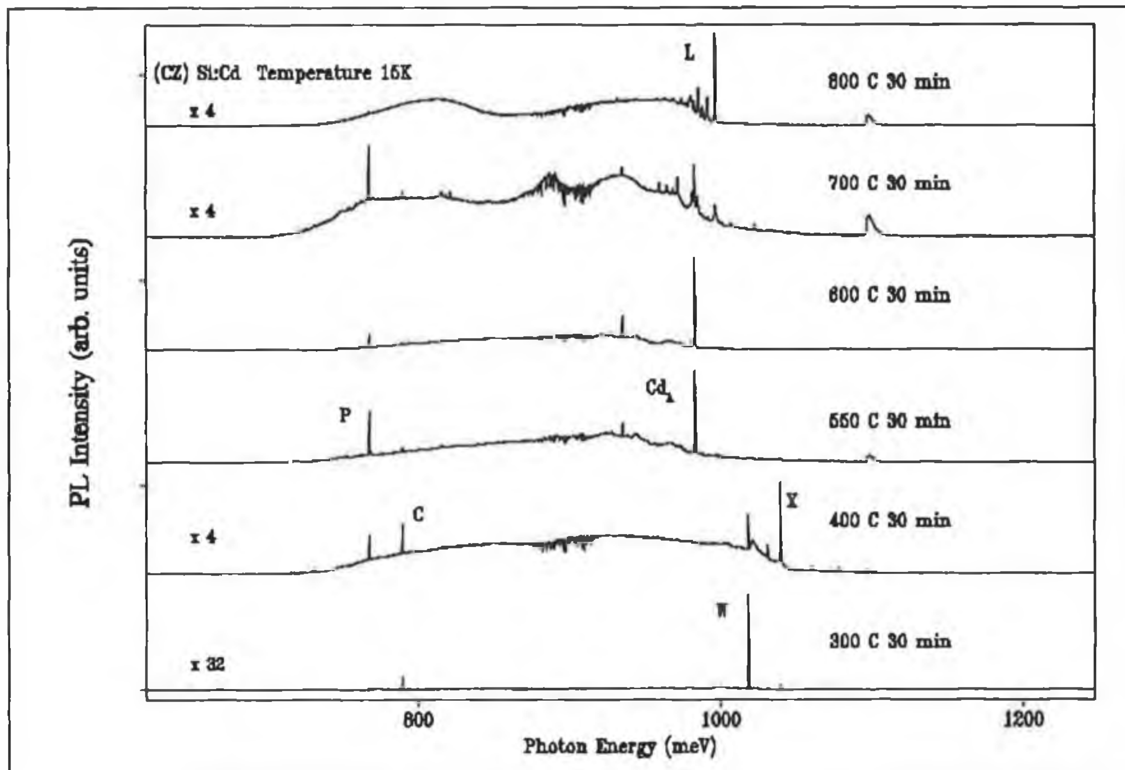

Figure 4.2.1: Effect of anneal temperature on Cd_A spectrum

4.3: Spectral Features

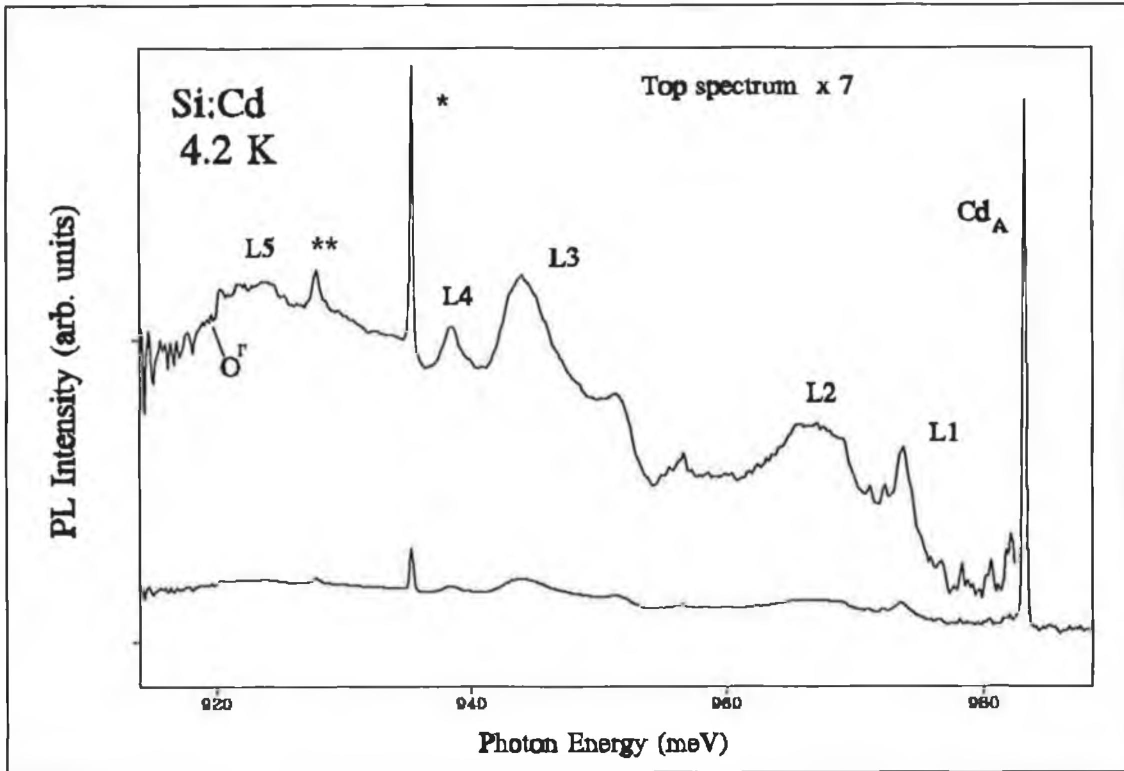

Figure 4.3.1: Low temperature Spectrum of Cd_A Luminescence

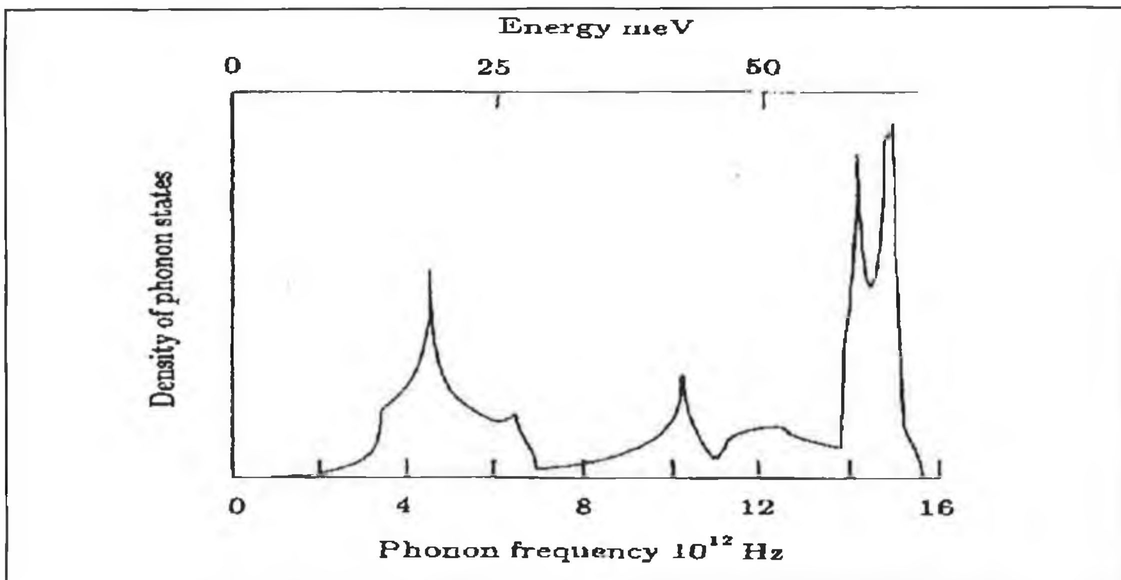

Figure 4.3.2: Calculated Phonon Density of States, taken from Davies (1989)

A low temperature PL spectrum of Cd-implanted silicon is shown in detail in figure 4.3.1. The ZPL occurs at 983.21 (±0.05)meV (for ^{116}Cd) and a detailed phonon sideband is observed on the lower energy side of this ZPL. The sideband contains peaks at different energies, some of which show local mode character and some of which show lattice mode character (see section 4.7). As can be seen in the spectrum, a water vapour absorption band at ~ 919meV (~ 64meV below the ZPL) hindered the observation of the two phonon sideband, and only features contained in the one phonon sideband were examined in this work.

Peaks in the phonon sideband are observed at ~965meV, 944meV, 938meV and 924meV. A weak O^{Γ} cut-off can be seen at ~920meV. These peaks correspond closely to the peaks in the phonon density of states (DOS) shown in figure 4.3.2. However the high intensity peaks in the phonon DOS at ~60meV (corresponding to the high frequency optical modes) are not reproduced with the same intensity in the phonon sideband of figure 4.3.1. This observation is consistent with the fact that the centre involves a heavy (116 a.m.u.) Cd atom, and hence favours the lower frequency acoustic mode vibrations.

In addition to these lattice modes, a band is observed at ~ 972meV (labelled L1 in figure 4.3.1), and this is assigned to a local mode vibration of the Cd atom in the defect. This is discussed in detail in section 4.7 below.

The feature labelled * is identified as a second Cd-related ZPL (Cd_B) and is discussed further in chapter 5. The feature labelled ** is a local mode of the Cd_B line (discussed in chapter 5).

In addition to the main features outlined above, a number of features of very small intensity are observed close to the ZPL on both the high energy and low energy side. The intensity of these features was extremely small (~ 1/250 of the main ZPL intensity) and their properties have not been explored further as yet.

Table 4.3.1 displays the energy of the various spectral features, their shift from the ZPL and their identification.

Table 4.3.1:

Spectral Feature	Position (mev)	Shift from ZPL (mev)	Identification values from Boer 1990 (meV)
Cd_A	983.21	0	ZPL
L1	973	9.8	Local mode
L2	965	18	DOS peak (18.6)
L3	943	40	DOS peak (41.3)
L4	938	45	DOS peak (~50)
L5	925	58	DOS (57.5)
O^{Γ}	919	64	O^{Γ} (63.2)

4.4: Temperature Dependence of Cd_A Luminescence Band

Figure 4.4.1 shows the Cd_A ZPL and sideband for a number of temperatures in the range 5K to 60K.

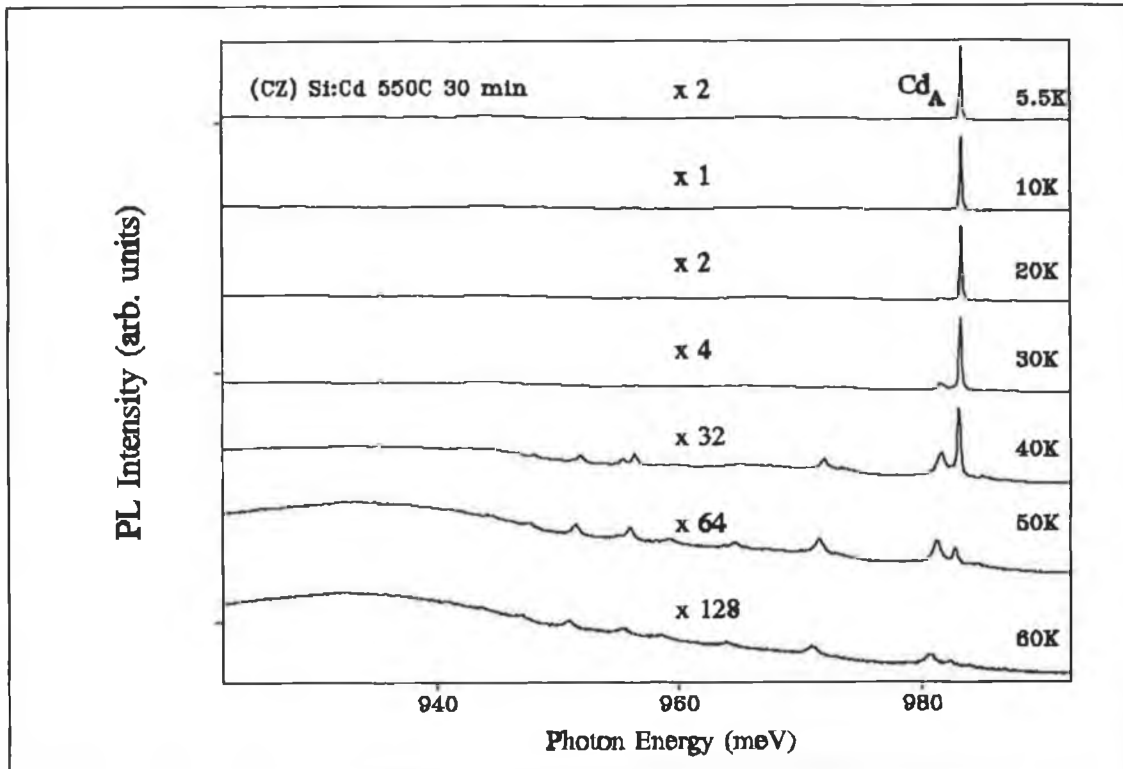

Figure 4.4.1: Temperature dependence of Cd_A Luminescence

The first point to note about the behaviour of the Cd_A line as a function of temperature is the absence of any thermalising excited states growing as the temperature is raised. This indicates that the defect has a single radiative excited state. Uniaxial stress measurements, discussed in detail in section 4.5, indicate that the defect excited state does not interact with any other states, and appears to be isolated.

The ZPL line intensity grows initially as the temperature is increased (consistent with the depopulation of shallower trap centres), reaching a maximum at 10K and then decreases as the temperature is raised further until the line disappears at temperatures greater than ~50K. This behaviour is characteristic of excitons with one of the particles loosely bound at the defect centre, and is discussed in detail in chapter 2. In order to estimate the dissociation energy of the loosely bound particle,

equation 2.7.10 was used to fit the intensity versus temperature data. The best fit parameter for the dissociation energy E_i was found to be 13(±2)meV. The data points and fit to equation 2.7.10 are shown in figure 4.4.2.

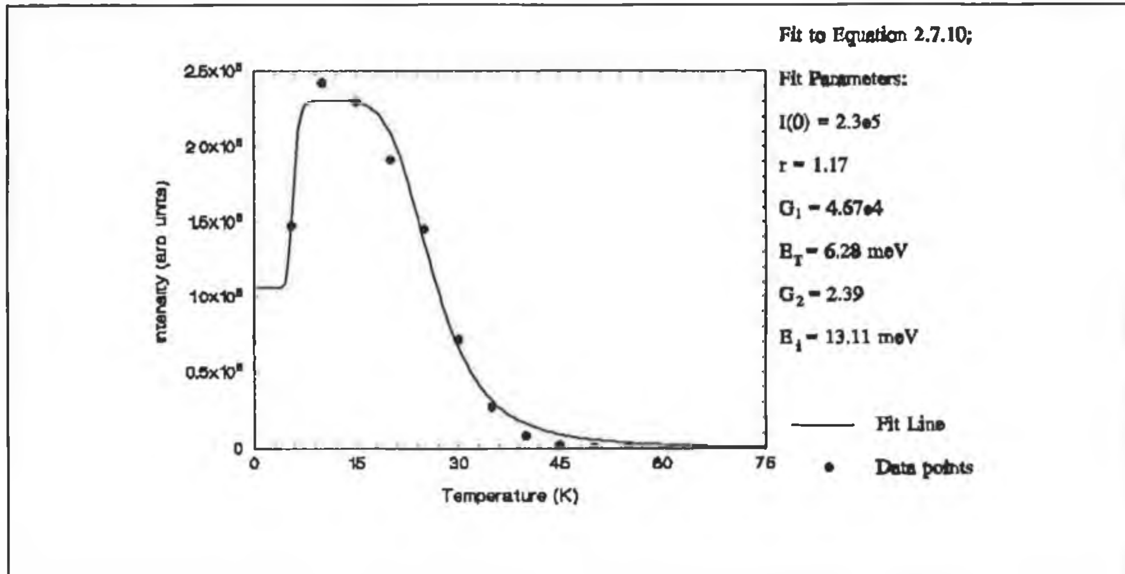

Figure 4.4.2: Intensity of Cd_A ZPL vs. Temperature

This value of the dissociation energy is low compared with the difference between the ZPL energy and the silicon band gap (~ 186meV) indicating that the dissociation energy of the complex is controlled by the dissociation energy of the secondary bound particle (~ 13meV), while the primary particle is tightly bound (~ 173meV). In light of the Zeeman measurements to be presented later, we identify the primary bound particle as a hole, and the secondary bound particle as an electron, i.e. the defect in the excited state is pseudo-donor in nature. Pseudo-donor type complexes have previously been observed for Group II impurity (Zn, Be) related defects in CZ silicon, and both these defect complexes have shown low dissociation energy values also (Daly *et al.* 1995, Henry *et al.* 1994). In all these cases the thermal binding energy of the secondary particle is lower than would typically be expected for a pseudo-donor. A similar anomaly is seen in the case of the 767meV "P" line, which has a thermal binding energy of ~15meV (Davies 1989) and a spectroscopic binding energy, measured using photoluminescence excitation (PLE), of ~35meV (Wagner *et al.* 1985) while in other defect systems such as the 790meV "C" line (Thonke *et al.* 1985) and

the 1122meV "ABC" centre (Weber *et al.* 1980, Wagner *et al.* 1982) good agreement is found between the thermal and spectroscopic binding energies. No solution to these questions has yet been found.

The feature at 981.5meV which becomes more prominent at higher temperatures shows no thermalisation behaviour with respect to the Cd_A line, and is not believed to be associated with the Cd_A system.

At temperatures higher than 50K when the Cd_A defect is completely gone a series of sharp lines appears in the spectral region 930meV to 1050meV. In addition the broad band observed on the low energy side of the Cd_A line survives to higher temperatures and becomes more prominent as the Cd_A line decreases in intensity above 30K. These lines have not been explored any further in this thesis.

4.5: Uniaxial stress and Zeeman Spectroscopy of Cd_A Line

(i) Uniaxial stress

Oriented CZ silicon samples were prepared by Cd implantation and annealing as described in section (a). There were three samples with axes oriented along <100>,<111> and <110> directions respectively. All the data shown were taken using a FT spectrometer. The stress rig used was described in chapter 3, along with the procedure for mounting the samples. Great care was needed in mounting the samples so that their axes were parallel to the stress direction. Even small deviations from correct alignment could produce very large discrepancies in the observed spectra, especially in the <111> direction. For this reason all the experiments were repeated at least once. Furthermore, small deviations from parallel alignment did not seem to degrade the linshape of the split components greatly, and therefore checks were made on the lineshape of other features in the spectrum. As was outlined in chapter 3, it is very difficult to obtain good quality polarisation data from samples using luminescence spectroscopy, due to depolarising multiple internal reflections, (McGuigan 1987, Singh 1992). For this reason no significant information was obtained from the attempts at measuring the polarisations of the different stress-split components.

Some of the initial attempts at performing the stress experiments led to line splittings which could not be reconciled with theoretical fits and the experiments were repeated. The data presented here are the most reliable data set and excellent fits are obtained to the data as we discuss below.

Stress ‖ <100>

Stress parallel to the <100> crystal direction caused the zero stress line to split into two components. The fan diagram along with representative spectra are shown in figure 4.5.1 (a) & (b). The shift rates for both the lines are linear, indicating the absence of any interaction with higher energy lines. The ratio of the line intensities will be discussed later.

Stress ‖ <111>

Stress applied parallel to the <111> crystal direction caused the line to split into two components. The fan diagram and representative spectra are shown in figure 4.5.2 (a) & (b). Again the shift rates are linear indicating the absence of any interaction between the stress-split components and any higher energy levels.

Stress ‖ <110>

Stress applied parallel to the <110> crystal direction caused the line to split into three components. The fan diagram and representative spectra are shown in figure 4.5.3 (a) & (b). The viewing direction for the data presented was along the <100> axis. Again the shift rates of all the lines are linear, indicating the absence of any interaction between the stress split components and higher lying energy levels.

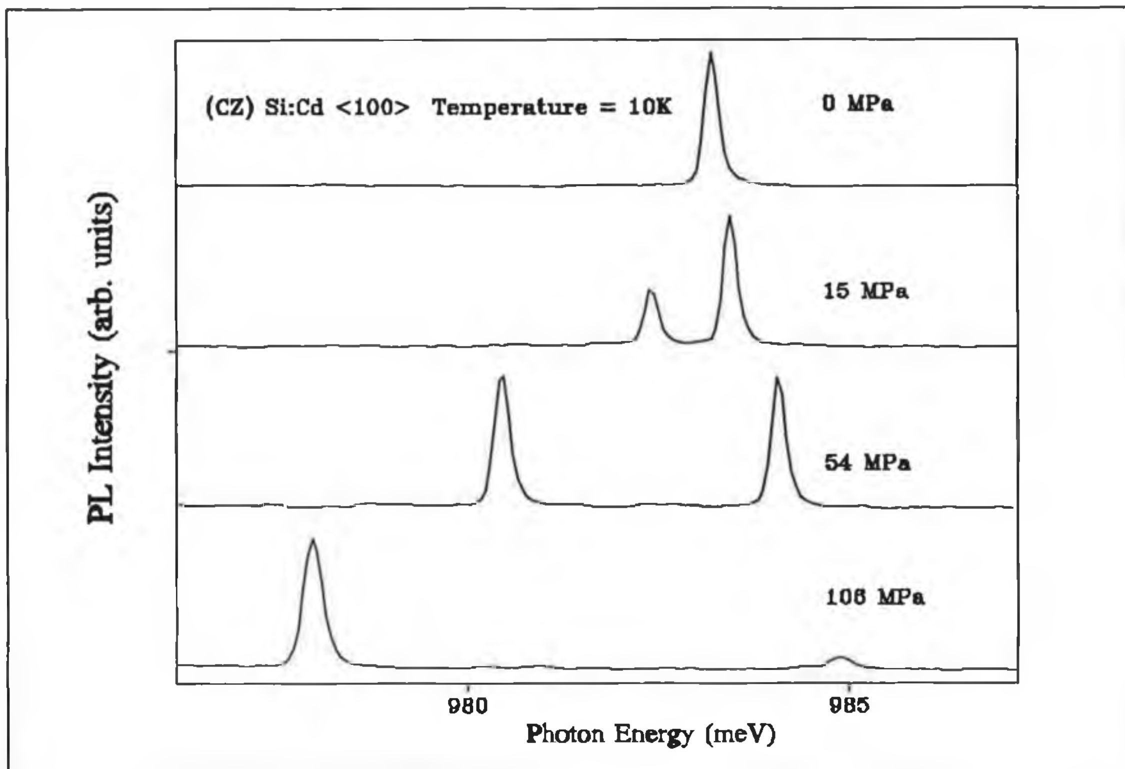

Figure 4.5.1 (a): Representative Spectra for <100> dir^n

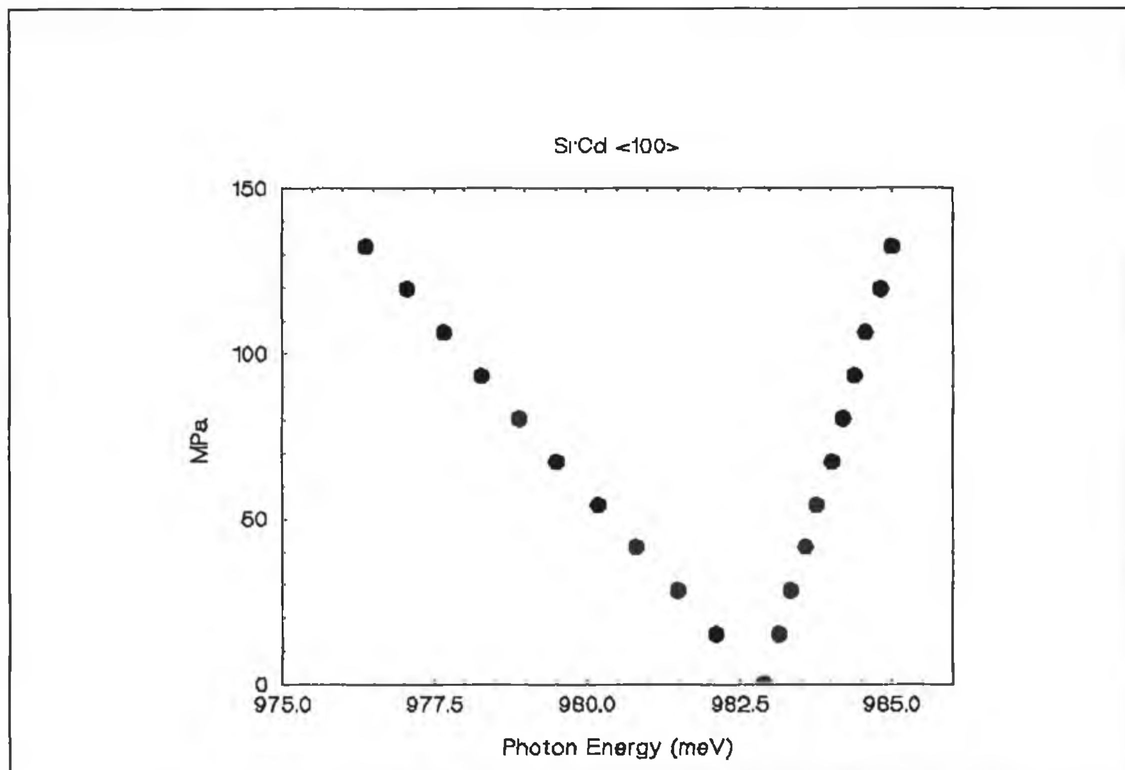

Figure 4.5.1 (b): Fan diagram for <100> stress

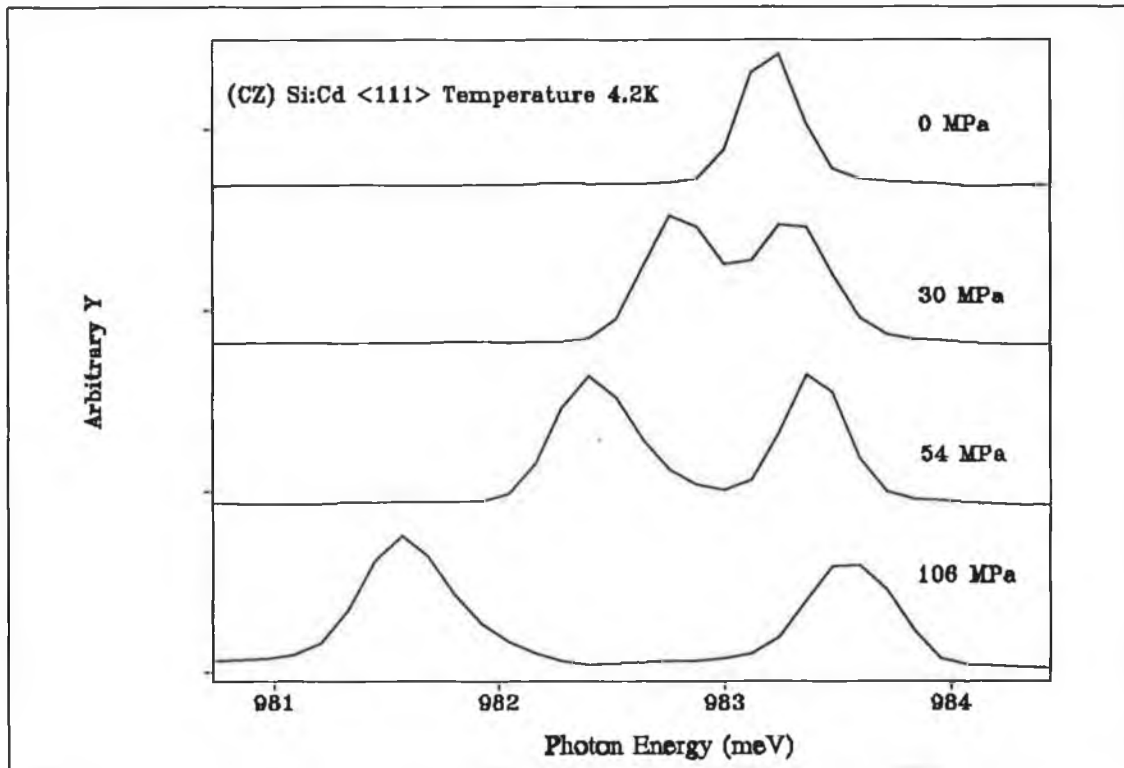

Figure 4.5.2 (a): Representative Spectra for <111> dir^n

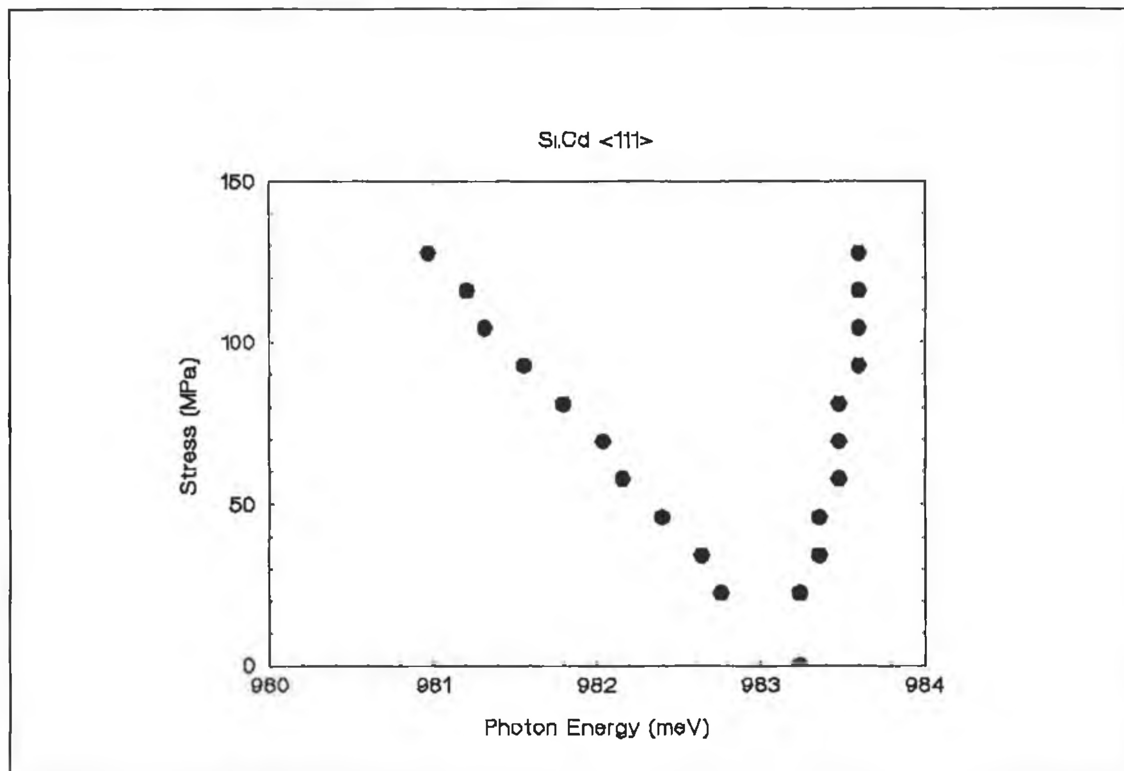

Figure 4.5.2 (b): Fan Diagram for <111> stress

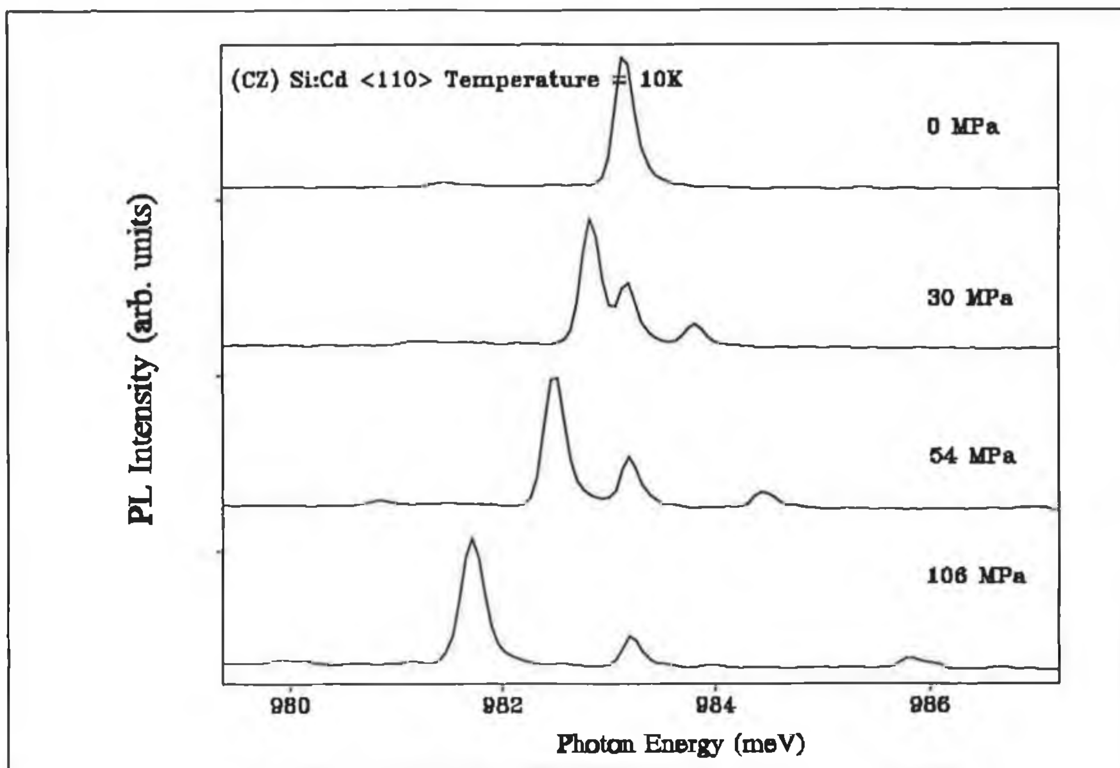

Figure 4.5.3 (a): Representative Spectra for <110> dir^n

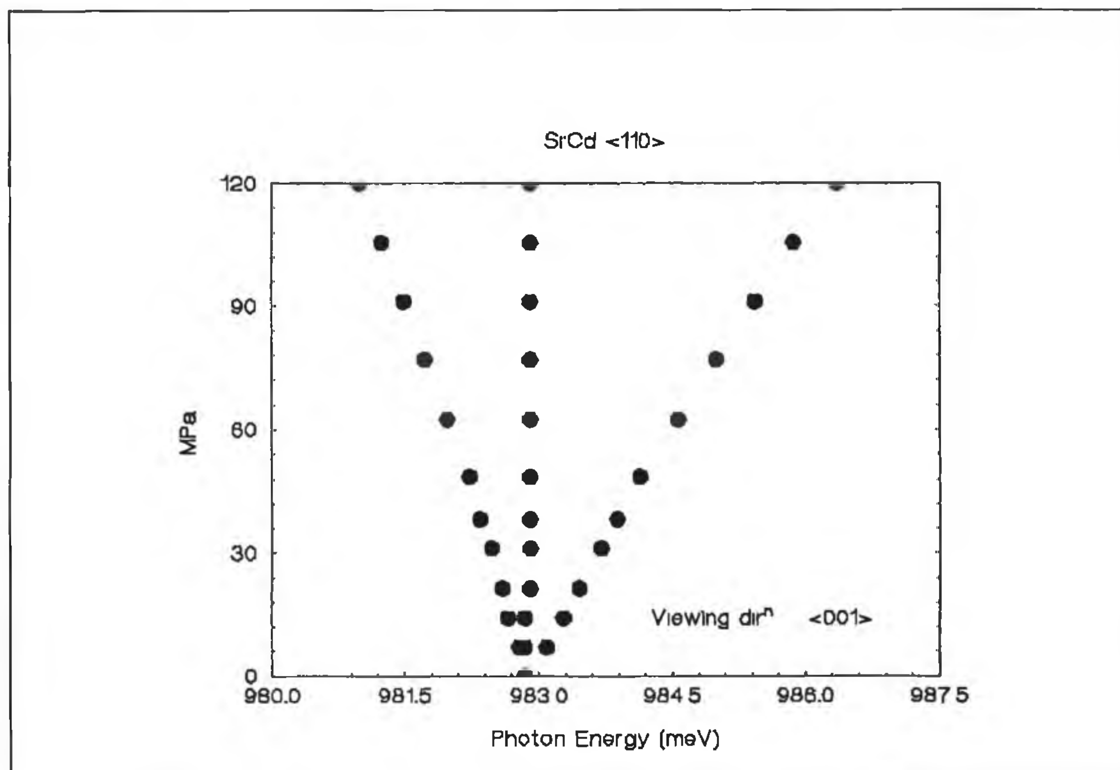

Figure 4.5.3 (b): Fan Diagram for <110> stress

As a final comment on the stress data shown, it is apparent that there is no evidence of any interactions between excited states of the defect and any of the stress split components, for any stress direction. This fact is supported by the temperature dependence data, which show no evidence of thermalising excited states of the Cd_A line.

A visual inspection of the number of components and comparison with the possibilities detailed by Kaplyanskii (1964) is the first step in narrowing down the possible symmetry type of the centre. The data in the review article by Mohammed *et al.* (1982) can be used to narrow down the possibilities. The types of centres which produce two lines in <100> & <111> and three in <110> are rhombic I and cubic A_1 to T_1. It was decided to try to fit the data to a rhombic I type centre for a number of reasons. Firstly, rhombic I type centres have previously been observed for group II impurities in CZ silicon, both Be and Zn (Daly *et al.* 1995), and secondly because the Zeeman data (to be discussed later) indicated a spin 1/2 to spin 1/2 transition (ie a nondegenerate state with quenched orbital angular momentum (Dean *et al.* 1979)). The quenching of orbital angular momentum would indicate a low symmetry crystal field, such as rhombic I (group C_{2v}), which has only one-dimensional irreducible representations (Tinkham 1964). The equations relating the shift rates for rhombic I symmetry were derived in chapter 2 and are:

Table 4.5.1

Stress Direction	Line Shift Rates
<001>	1: A_1 2: A_2
<111>	1: $1/3(A_1+2A_2+2A_3)$ 2: $1/3(A_1+2A_2-2A_3)$
<110>	1: A_2+A_3 2: $1/2(A_1+A_2)$ 3: A_2-A_3

These equations were applied to the shift rates of the data, using both the Eureka package for solving simultaneous equations, and also entered into a purpose written package for the identification of defect symmetry sites, **TRAN**sition **ID**entification or TRANID (McCarren 1994). The results of both these methods were nearly identical, and the best fit parameters A_1, A_2 and A_3 produced were;

A_1 = -49.2 meV/GPa

A_2 = 15 meV/Gpa

A_3 = -14.6 meV/Gpa

A plot of the expected lines is shown superimposed on the experimental data in figure 4.5.4. The solid lines represent the theoretical fit and the black circles represent the experimental data. As can be seen from the figure the fit is very good in all directions. The stress parameters are very close to those previously obtained for the Zn_A defect, reproduced in table 4.5.2 (Henry *et al.* 1994).

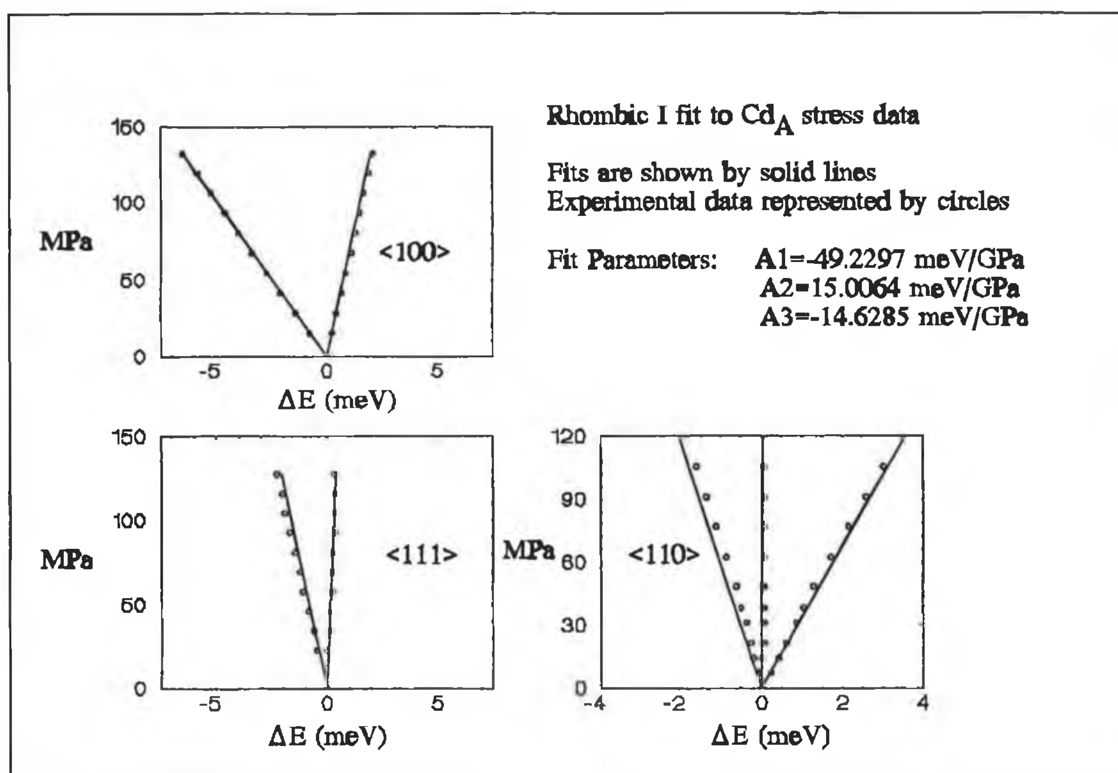

Figure 4.5.4: Rhombic I fit to Experimental Data Set

Table 4.5.2

Parameter	Cd_A (meV/GPa)	Zn_A (meV/GPa)
A_1	-49.2	-52
A_2	15	15
A_3	-14.6	-17.2

Table 4.5.2 shows a comparison of the experimental shift rates and the best fit theoretical shift rates.

Table 4.5.3

Stress Direction	Experimental (meV/GPa) (± 0.5)	Theoretical (meV/GPa)
<100>	15.8	15
	-49	-49.2
<111>	3.3	3.3
	-17.6	-16.1
<110>	28.7	29.6
	0	.3
	-15.7	-17.1

One notable feature of the spectra shown for different stresses is the fact that the intensity ratio of the stress split components changes as a function of stress. Ideally, for a rhombic I type defect with no electronic degeneracy and no interaction with higher lying states, the intensity ratio of the stress split components should be independent of stress. Effects similar to those reported here for Cd_A have also been observed in the uniaxial stress measurements performed on the Zn_A (Henry *et al.* 1994). These authors attributed this change in intensity ratio of the stress-split components to (stress-induced) differences in the thermal binding energies of the components. This effect is also observed in the Zn_B defect (Henry *et al.* 1994) and the Cd_B defect (chapter 5). Preliminary measurements as a function of temperature on the <001> components of the Cd_A centre show no evidence of differences in the thermal binding energies. Furthermore, no evidence is seen of a thermal distribution between the components at a number of stress values. The fact that similar behaviour is observed in a number of defects leads us to believe that this problem is worthy of a full study in its own right. We confine our analysis of the intensity ratios of the components to the low-stress regime, where stress-induced effects are minimal. For low stress values the line ratios are seen to be in reasonably good agreement with

those predicted by Kaplyanskii 1964 for the case of an A to B transition at a rhombic I centre. Figure 4.5.5 shows the predicted intensity ratios for a rhombic A-B transition (Mohammed *et al.* 1982).

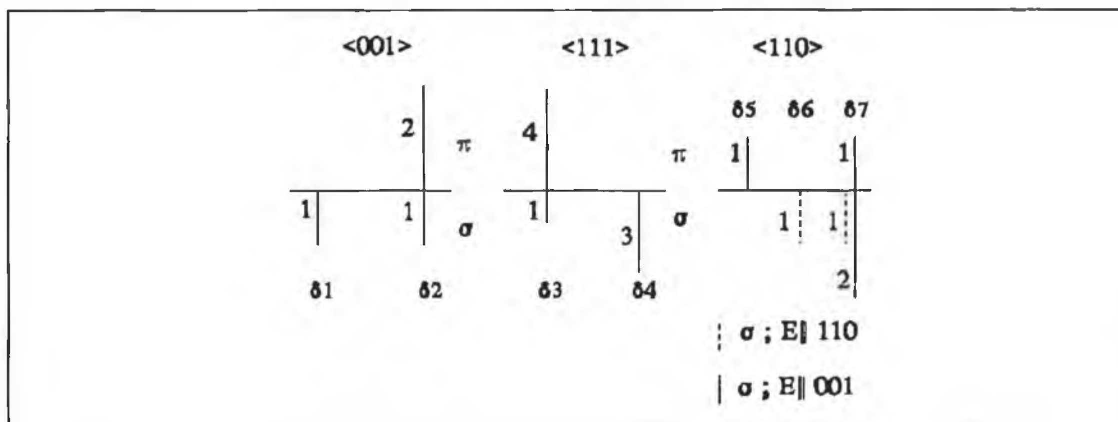

Figure 4.5.5: Intensity and polarisation ratios for rhombic I A-B transition

<100>

	ratio	predicted ratio
15 MPa	~1 : 2.3	1 : 3
54 MPa	~1 : 1	1 : 3
106 MPa	~1 : 0.1	1 : 3

<111>

	ratio	predicted ratio
28 MPa	~1 : 0.9	1 : 0.6
54 MPa	~1 : 1	1 : 0.6
106 MPa	~1 : 0.77	1 : 0.6

<110>

	ratio	predicted ratio
28 MPa	~4 : 2 : 0.68	4 : 1 : 1
54 MPa	~4 : 1.5 : 0.43	4 : 1 : 1
106 MPa	~4 : 0.87 : 0.18	4 : 1 : 1

In spite of the absence of polarisation data, it is possible to confidently assign this defect to a rhombic I symmetry type on the basis of the quality of the self-consistent fits to the data. Using the relative intensities (bearing in mind the comments of the previous paragraph) of the components as a guide one can assign the transition to be from an A state to a B state.

In order to fully understand the details of the symmetry of the defect and the variations in the intensities of the stress split components, it will be necessary to obtain good polarisation data and also to examine the variations of the stress split component intensities as a function of temperature. As yet no attempt has been made to examine this defect in absorption, but if this proves possible, it is to be expected that good polarisation data ought to be obtained (McGuigan 1987, Singh 1992).

(ii) Zeeman Spectroscopy

Under magnetic fields of up to 5T (<100> direction), the Cd_A line shows neither a line shift nor splitting. Representative spectra are shown in figure 4.5.6. While the experiment has not been performed for the other two directions due to persistent difficulties with the magnetic field apparatus, no shift or splittings would be expected for these directions either, as the defect appears to be a transition from a spin 1/2 excited state to a spin 1/2 ground state, as discussed in chapter 2. Zeeman splitting patterns of this nature for transitions between spin-like states are quite common (C centre, Thonke *et al.* 1985; Zn_A centre Henry 1995). In the above cases no shift or splitting is observed under magnetic fields up to 5T for any field direction, and we feel that the Cd_A centre will in all probability behave in the same way. Full Zeeman analysis of the defect at high resolution (including angular dependence measurements) are planned. High resolution Zeeman experiments on the 886meV Al-related line (discussed in more detail in chapter 7 and Irion *et al.* 1988) have yielded information on fine structure in the spectrum due to (nominally forbidden) transitions from m_s=-1/2 to m_s=+1/2 states (described in chapter 2). Similar experiments are planned for the Cd_A system.

The Zeeman data, when combined with the stress data and the thermalisation data point strongly towards the pseudo-donor model for the defect, with the hole

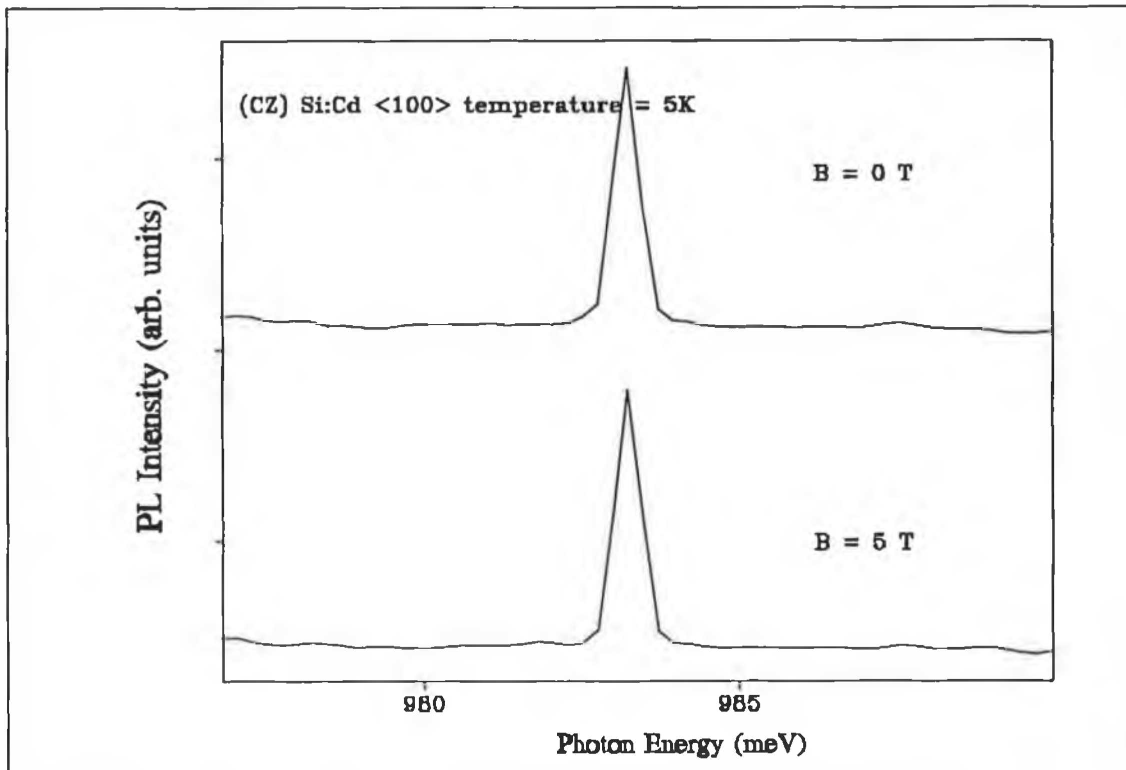

Figure 4.5.6: Spectra of Cd_A ZPL for B<100> = 0T & 5T

angular momentum fully quenched in the low symmetry defect potential (discussed in detail in chapter 2).

4.6: Chemical Identity of the Cd_A Defect Complex

Having examined the behaviour of the Cd_A line using temperature dependence, uniaxial stress and Zeeman techniques, in order to obtain information on the electronic structure and site symmetry of the defect, in this section we examine the chemical constituents of the defect.

While in general it can be said that ion implantation is a more reliable way of introducing foreign atoms into silicon with less danger of contamination from other species (as compared to diffusion (McGuigan 1987)), it is by no means certain that the implanted species is directly involved in luminescence observed from ion-implanted material. Because of the nature of ion implantation, a large amount of

damage is caused to the surface of the crystal, and these damage products could be the source of the luminescence (either directly or due to complexing with another species in the crystal). For example damage products like silicon self-interstitials and C interstitials are highly mobile at temperatures greater than 300K (Davies *et al.* 1987) and are available for complexing with other species. Similarly, the implanted species could take the part of a catalyst for the formation of a defect without being directly involved in the final product (Drakeford *et al.* 1988). Because of these factors it is very difficult to determine the chemical constituents of a defect solely from a knowledge of the implanted species, and it is for this reason that isotope substitution experiments were attempted for the constituent candidates discussed below wherever possible. As was discussed in chapter 2, isotope substitution experiments allow an unambiguous identification of the atoms involved in a defect complex, and dual isotope substitution experiments can, in favourable cases, indicate the number of atoms of the species involved in the defect.

In trying to determine the chemical identity of the defect, a number of possible constituents had to be considered. The different candidates are listed below;

Cadmium

Oxygen

Damage products (self interstitials etc.)

Hydrogen

Carbon

Donor / Acceptor

We now consider each of these candidates in turn.

Cadmium: As the implanted species, Cd was the considered the most likely candidate for involvement in the defect, and much of the initial evidence pointed to this fact. Firstly, the defect production was not affected by a changes in the implantation energy, from 200keV to 80keV. Secondly, the defect line was not produced by ion implantation with indium which has an almost identical mass ($mass_{In}$=115 amu, $mass_{Cd}$=116 amu). Thirdly, the defect luminescence originated from the surface implanted layer (to be discussed later in this section). This indicated that the defect

origin was not solely due to damage caused by the ion-implantation process.

Samples were prepared implanted with ^{106}Cd, ^{116}Cd and a dual implanted sample. The ZPL spectra of these samples are shown below in figure 4.6.1.

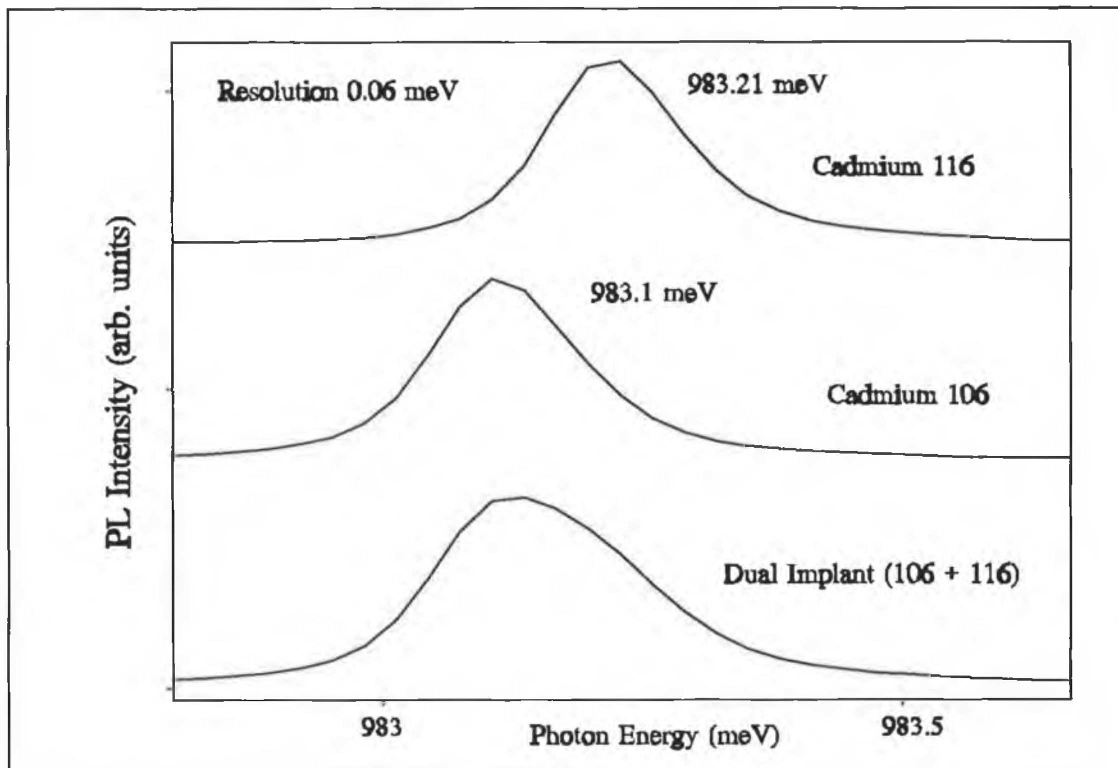

Figure 4.6.1: Effects of cadmium isotope substitution on Cd_A ZPL

It can be seen that the main Cd_A line undergoes an isotope shift of +0.11meV when the isotopic mass is varied from 106 amu to 116 amu. There is a notable similarity in magnitude and sign of isotope shifts for the Cd_A and Zn_A. The Zn_A defect shows a positive isotope shift of ~ +0.1meV with ^{64}Zn and ^{68}Zn isotopes. The local mode vibrations (which will be examined in detail in section 4.7) show even more striking similarities between the two defect complexes.

While it was not possible to resolve the two lines in the dual implant sample, a considerable line broadening was observed, and a good fit to the line shape could be obtained by adding the ^{106}Cd line to the ^{116}Cd line in the ratio 1:0.6. This indicates that a single Cd atom is involved in this defect. The reason that the two isotopes did not appear in equal proportions will be discussed later in this section. Based on the

results of these isotope experiments it is possible to positively identify a single Cd atom as a constituent of this defect.

When implanting the dual isotope sample, the nominal ratio of the ^{106}Cd to ^{116}Cd was 1:1. The spectra obtained from these samples indicate that the ratio of 106 to 116 was ~ 1 : 0.6. The same results are seen for the other two Cd defects reported in chapter 5. The initial attempts at dual implanted samples (total dose 1e14 cm^{-2}) gave negative results (i.e. no line splitting or broadening was observed), even though the samples implanted separately with ^{106}Cd and ^{116}Cd gave an unambiguous isotope shift. In preparing the samples for the next attempt at dual implantation it was decided to reduce the dose greatly (total dose 2e13 cm^{-2}) in an effort to reduce the amount of damage caused to the host crystal. This implantation gave a positive result, but the isotope ratio was not 1:1, as was nominally implanted. A tentative explanation of this result is that as the Cd is being implanted it is damaging the crystal in such a way as to constantly reduce or impede the successful implantation of further Cd. This would explain the initial negative dual isotope results, because after the first isotope dose had been implanted, none (or a negligibly small amount) of the second isotope was successfully introduced into the crystal. This corresponded well with the observed result that only the ^{106}Cd isotope (the first of the two to be implanted) was seen in the luminescence spectra of the defect. This explanation also accounts for the fact that the ratio of ^{106}Cd (first implanted) to ^{116}Cd was 1:0.6 in the second implantation attempt. Because the doses for this implantation were much smaller than for the first attempt, some of the ^{116}Cd isotope was successfully introduced into the crystal. This behaviour seems to apply also to the implantation of O into material previously implanted with Cd, and to implanting Cd into material previously implanted with O. Attempts at O isotope implantation, which will be discussed later in this section, have given negative results.

Oxygen: The circumstantial evidence that O is involved in this defect centre is quite strong. The defect is seen only in CZ material which has a high O concentration (~10^{18} atoms/cm^3). Figure 4.6.2 shows comparative spectra of Cd-implanted CZ and FZ silicon subjected to the same heat treatment. Although there is a considerable

amount of sharp line structure in the FZ material in the energy region close to the Cd_A ZPL, the nearest line observed in FZ material is > $10cm^{-1}$ from the Cd_A ZPL position (the resolution of the spectrometer was $4cm^{-1}$).

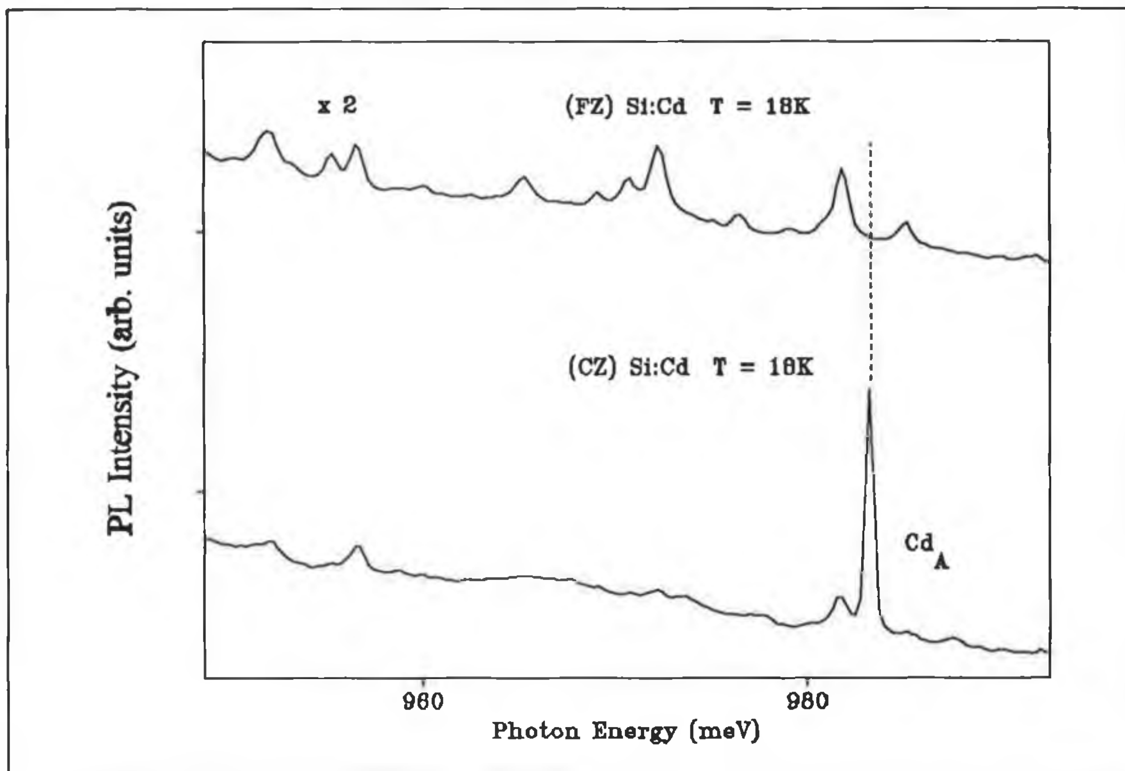

Figure 4.6.2: Comparison of Spectra for CZ & FZ Si:Cd

In addition there is no indication of the presence of any of the distinctive phonon sideband structure associated with the Cd_A system. Attempts at O isotope implantation to try and confirm the involvement of O in the defect have produced negative results, and this is believed to be a result of the effects described above regarding Cd implantation data. Currently, samples diffused with O isotopes are being prepared for Cd implantation, and this method of preparation ought to overcome the problems encountered with isotope implantation.

Damage Products: By the nature of the implantation process, energy will be transferred from the implanted species to the host crystal via collisions. These collisions will produce damage products such as self-interstitials, C interstitials

etc. which are highly mobile at temperatures > 300K (Davies *et al.* 1987, Davies 1989) and therefore available for complexing with other species in the crystal during the annealing process. Apart from the previously noted observation that the defect production does not appear to depend on the implantation energy, there is very little evidence either for or against the presence of damage products in this defect complex. A comparison of two spectra produced by Cd implantation at 80keV and 200keV is shown in figure 4.6.3.

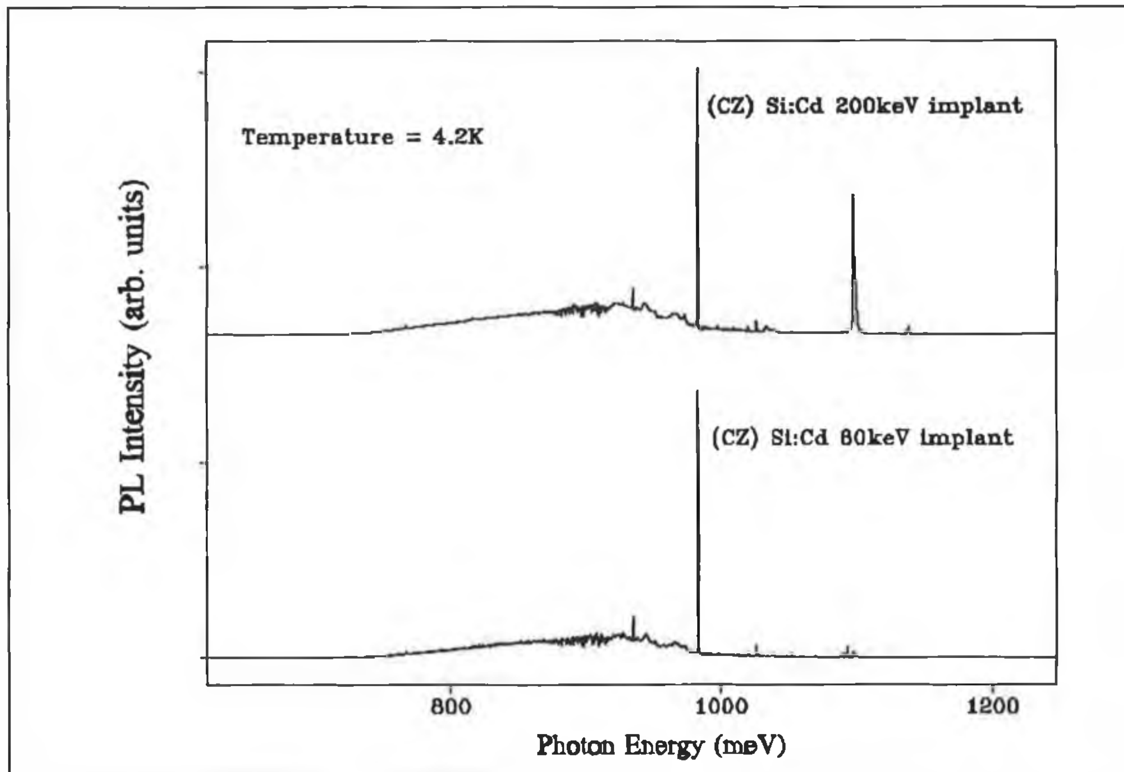

Figure 4.6.3: Comparison of Cd_A Spectra for 80kev & 200kev Implantations

Because of the low diffusion coefficient of Cd at the anneal temperatures ($D=10^{-13}cm^2/s$ at 1200°C, with no value available at 550°C but estimated to be $\sim 10^{-24}cm^2/s$ from $D_0=4.5cm^2/s$, Q=3.9eV, Arifov *et al.* 1984) the implanted Cd moves very little from its initial location after implantation. Computer simulations of the implantation process following the method of Ziegler *et al.* (1985) reveal that Cd implantation at 200keV into silicon produces an implanted layer approximately 0.09μm from the surface with an approximate width of 0.02μm. The depth distribution after annealing

is largely unchanged. Attempts to etch away the damaged layer therefore simultaneously etched away the Cd ions. A series of comparative spectra are shown in figure 4.6.4 which illustrate the effect of etching away varying depths of surface material. The Cd-related luminescence is seen to be almost completely gone at a depth of approximately 0.2μm.

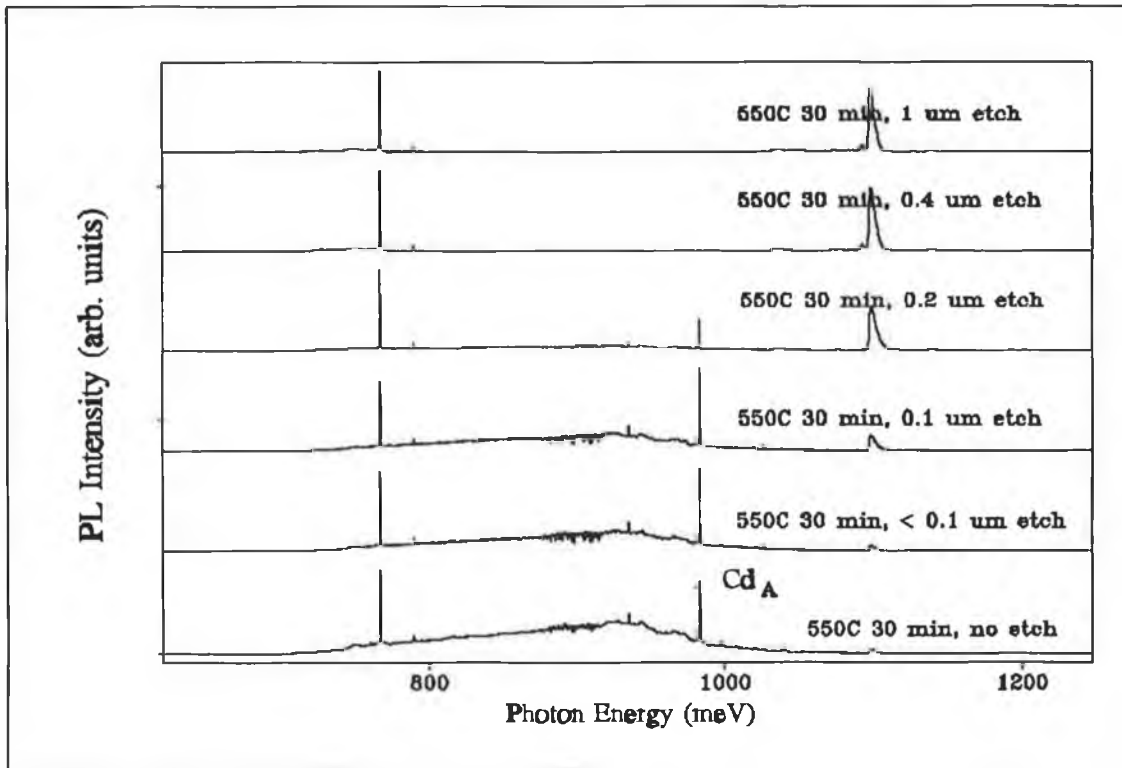

Figure 4.6.4: Effect of Etching on Cd_A Luminescence

This result is in good agreement with the predictions of the numerical simulation, considering the margin of error in accurately estimating the etch depth (~40% for small etch depths, see appendix A). This experiment therefore does not shed any light on the involvement of damage products in the production of the Cd_A luminescence.

A possible way to introduce Cd into silicon without causing structural damage is by diffusion. Cd has been successfully diffused into silicon (Gulamova *et al.* 1971), and this experiment would help in determining the role of damage products, if any, in the Cd_A centre. One of the main problems associated with the diffusion of Cd is the fact that it is a toxic element and great care must be taken during the diffusion experiments.

Hydrogen: H is quite easily introduced into silicon both intentionally and unintentionally, and has recently been shown to be involved in quite a number of common defects (Safonov *et al.* 1994, Lightowlers *et al.* 1994). Allied to this is the previous observation of Cd-H complexes in silicon using PAC (Wichert *et al.* 1987, Gebhard *et al.* 1991). In view of this evidence it was decided to attempt to introduce deuterium into a sample of Cd-implanted silicon, to try and observe an isotope splitting. Deuterium can be introduced into silicon simply by boiling the samples in heavy water in the dark (Wichert *et al.* 1987), by annealing the samples in a furnace in a deuterium atmosphere (Safonov *et al.* 1994) or by annealing the samples in a heavy water vapour atmosphere at 450°C for 16 hours (Lightowlers *et al.* 1994). This latter method was chosen. The treated samples did not show any increase in signal level nor did the Cd_A line or its sidebands show any isotope splitting (which is usually quite large for H_2-D_2 substitution (Safonov *et al.* 1994)). While a negative isotope substitution result does not necessarily exclude the participation of H in this defect, it is considered to be a less likely candidate than O.

Carbon: After O, C is the second most common contaminant in CZ silicon. C interstitials, which are damage products of ion-implantation, are known to be highly mobile at 550°C (see chapter 1 for details). For this reason it was decided to examine the formation of the Cd_A defect centre in both C-rich and C-lean material. In addition to this, samples of CZ silicon with C^{12}/C^{13} isotopes diffused into them were implanted with Cd. The defect formation appeared insensitive to the presence or absence of C in the sample. In addition to this, no line broadening or splitting was observed in the sample diffused with C^{12}/C^{13} isotopes in either the ZPL or the phonon sidebands. For these reasons, C is considered to be an unlikely constituent candidate in the Cd_A defect.

Donor/Acceptor: Even in high purity silicon there still remains a small concentration ($< 10^{13}$ atoms/cm^3) of residual impurities which determine the conductivity type (n-type or p-type) of the sample. The most common of these impurities are boron (p-type) and phosphorous (n-type). The role of these residual dopants in the formation of the Cd_A centre must also be considered. The most convenient way to examine the

effect of different dopants on the Cd_A centre is by implanting Cd into both n-type and p-type material, and comparative spectra are shown in figure 4.6.5. The spectra of the Cd_A luminescence regions are identical for both n and p-type conductivity material

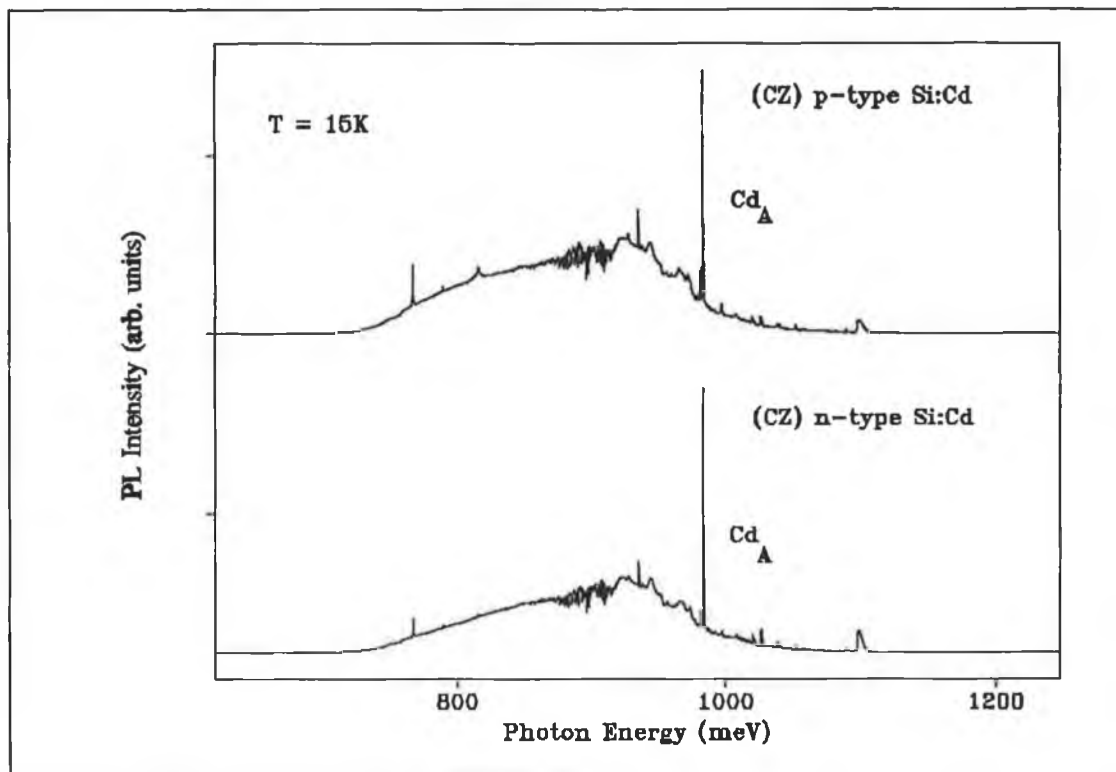

Figure 4.6.5: Comparison of Cd_A Spectra in n-type & p-type Si:Cd

and therefore it is concluded that the dopant in the starting material is an unlikely constituent in the formation of the defect centre. Minor differences in the spectrum are attributable to differences in the intensity of the previously mentioned damage features such as the P line (767meV) and X line (1039meV).

In light of the above evidence, the defect is tentatively assigned as a Cd-O complex. Interstitial Cd would be expected to act as a double donor, while substitutional Cd ought to act as a double acceptor. A Cd-O molecule would be isoelectronic in nature, and thus its radiative efficiency would be expected to be high. The high signal levels observed from the Cd_A line seem to indicate that it is indeed an isoelectronic complex, and thus a Cd-O complex would not be at odds with the

experimental data.

The Be_A and Zn_A lines (Daly *et al.* 1995) previously referred to are believed to be a group II-O complex, and because of the similarities observed in the uniaxial stress and Zeeman data especially with the Zn_A centre, the Cd_A line is tentatively assigned to a Cd-O complex.

4.7: Vibrational Sideband Structure

As was seen in section 4.3, the Cd_A line is accompanied by a phonon sideband, which displays both lattice and local mode characteristics. Because of the onset of the water vapour absorption band at ~919meV, the two phonon sideband could not be studied in any detail. The work presented in this chapter is based upon conclusions drawn mainly from the one-phonon sideband structure. Plans are being developed to overcome this problem, by housing the cryostat in a chamber purged with dry N_2.

Referring to figure 4.3.1, the line labelled L1 is associated with an in-band local mode of the ZPL. The local mode occurs quite close to the ZPL (9meV) as would be expected for a local mode of vibration of a heavy atom. This behaviour can be contrasted with the behaviour of the Be-related defect (Daly 1994). The mass of Be is much less than the mass of Cd (^9Be) and therefore one would expect its local modes to be well separated from the ZPL. This is indeed the case, with the local modes being separated from the ZPL by ~70meV. Isotope effects tend to be even more pronounced for local mode structure than for the ZPL. The ratio of local mode frequencies for two different isotope masses can be related to the isotope masses by the following equation (see chapter two);

$$\frac{\omega_1}{\omega_2} = \sqrt{\frac{m_2}{m_1}} \qquad (4.7.1)$$

This equation holds for the case of an atom vibrating with respect to an otherwise static lattice. The local mode of the Cd_A defect was investigated using ^{106}Cd and ^{116}Cd. The factor on the right side of equation 4.7.1 in this case is 0.956. Examples of the

local mode spectrum for both ^{106}Cd and ^{116}Cd are shown in figure 4.7.1.

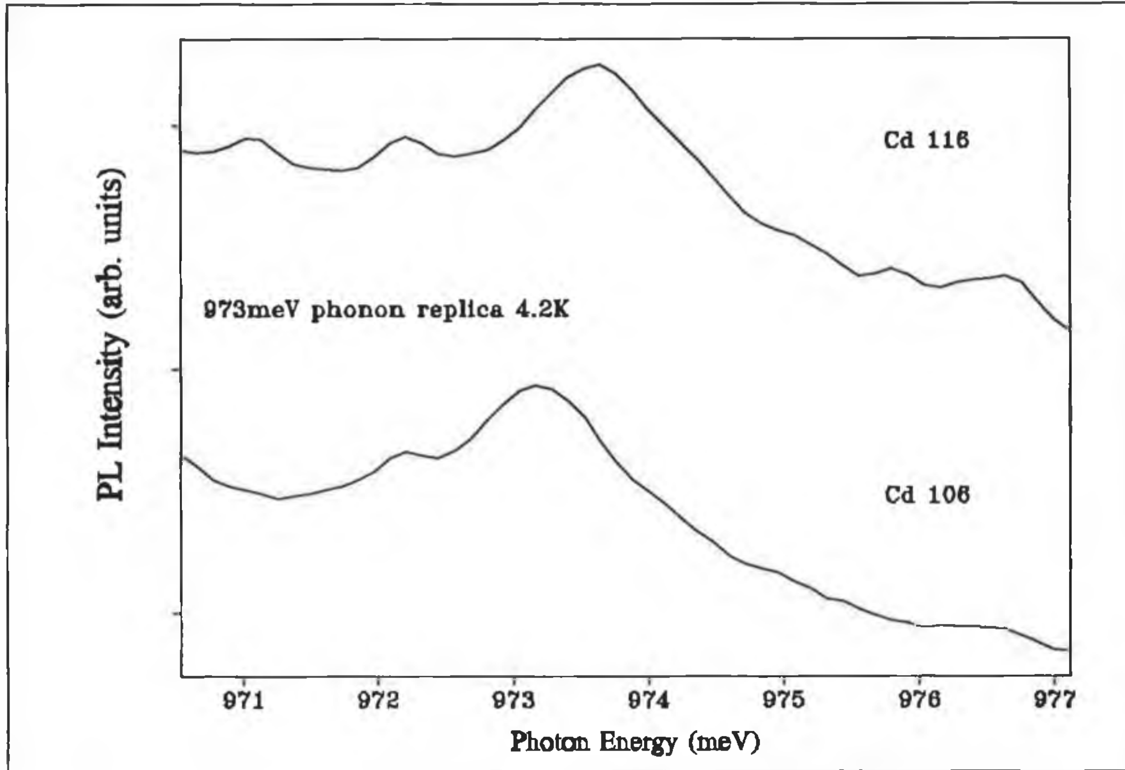

Figure 4.7.1: Effect of Cadmium Isotope Substitution on 972meV Phonon Replica

Table 4.7.1 shows the ZPL and local mode energies for ^{106}Cd and ^{116}Cd isotopes. The ratio of the phonon energies is ~0.96, in good agreement with the expected factor of 0.956.

Table 4.7.1

Isotope Mass (amu)	ZPL Position (meV)	Local Mode Position (meV)	Phonon Energy (meV)
106	983.09	973.2 (±0.1)	9.9 (±0.1)
116	983.21	973.7 (±0.1)	9.5 (±0.1)

If the Cd atom mass is replaced by the mass of the Zn atom (68 a.m.u.) an estimate can be found for the local mode energy of an equivalent Zn-related defect.

Putting the Zn mass in equation 4.7.1, the frequency expected for the Zn defect is calculated to be 12.4meV. This value is in very close agreement with the known value for the Zn_A local mode energy of 12meV (Henry 1994), indicating that the Cd atom in Cd_A experiences a very similar microscopic environment to the Zn atom in Zn_A, and provides more evidence of the link between the Zn_A and Cd_A centres.

By ratioing the integrated intensities of the local mode to that of the ZPL at low temperature, one can calculate a value for the Huang-Rhys factor S_1 (chapter two). The calculated value of S_1 for the 973meV local mode is;

$$S_1 = 0.095$$

Davies (1989) gives an equation relating the shift in equilibrium position Q_0 of the defect after recombination to the reduced mass μ, the mode frequency and S_1;

$$Q^2{}_0 = \frac{2\hbar\omega S_1}{\mu\omega^2} \qquad (4.7.2)$$

By using the mass of the Cd atom (116 amu) as the reduced mass, the value for Q_0 is calculated to be ~ 0.00269nm. This is a relatively small lattice relaxation, corresponding to ~1% of the bond length. Typical strains produced in uniaxial stress measurements are of the order of 0.2% (Irion *et al.* 1985).

In addition to the local mode structure observed beside the Cd_A ZPL, there is a large contribution to the phonon sideband from lattice modes. In the case of weakly bound excitons, the lattice phonon contributions occur mainly at the energies of the wavevector conserving phonons (Boer 1990). The phonon sideband of the Cd_A line is characterised by contributions from phonons throughout the Brillouin zone for all energies up to the O^{Γ} cutoff. In chapter two, it was shown that a defect undergoes relaxation via exciton decay. The magnitude of the relaxation energy is calculated by measuring the difference between the ZPL and the centroid E_c (or centre of gravity) of the luminescence band. When performing this calculation it is important to consider the system response. Because of the relatively flat response of the components in the FT spectrometer over the spectral range of interest, the overall system response for this particular case was relatively uniform and no corrections were made. Although measurements made at different resolutions will affect the measured value of E_c, we

found a maximum variation of only 5meV. When performing the integration, features not related to the luminescence band (ZPL of unrelated defects, background luminescence etc.) must be ignored. Figure 4.7.2 (a) shows a raw spectrum of the Cd_A line and sideband (at a resolution of 0.1meV), while 4.7.2 (b) shows the same spectrum with unrelated ZPL (e.g. at 935meV) removed and with a crude correction applied to the water vapour absorption features. In order to estimate the baseline correction shown in 4.7.2 (b), we must remember that the Cd_A ZPL and sideband sit on the high energy side of an unrelated broad luminescence band which survives to higher temperatures, as mentioned in section 4.4, and this band prevents the calculation of the exact baseline. We have estimated the approximate form of the baseline as shown and the corrected sideband is shown in 4.7.2 (c), along with the calculated value of E_c of ~930meV which gives a value of ~50meV for the relaxation energy. Because of the high degree of uncertainty in both the water vapour absorption and baseline corrections, the calculated values of both E_c and the relaxation energy can only be used as rough estimates, with an accuracy of ~±20meV.

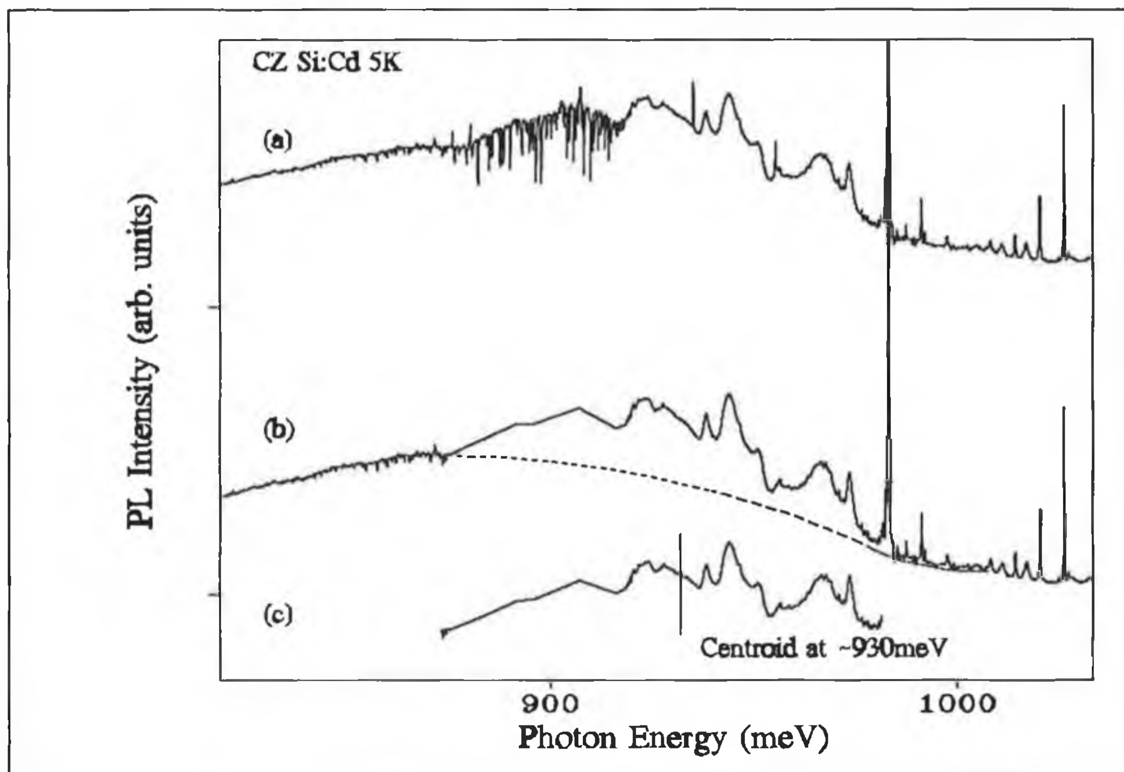

Figure 4.7.2: Effect of Background Correction on Spectrum; Position of Centroid Indicated

A comparison of the value of the relaxation energy (~50meV) with the spectroscopic binding energy (~186meV) shows that the relaxation energy is ~1/4 of the spectroscopic binding energy. The total Huang-Rhys factor S for the entire band is given by the ratio of the integrated intensity of the phonon sideband to the ZPL at low temperatures and is found to be ~3.

Having calculated the Huang-Rhys factor and relaxation energy for the Cd_A defect, we can now use the uniaxial stress parameters to check the overall consistency of our results. In order to do this we follow the procedure outlined in the review by Davies (1989). We will assume that the defect is primarily perturbed to first order by hydrostatic stresses, and this gives an energy change for a rhombic I defect of (A_1+2A_2)=-19meV/GPa. The electron-phonon coupling constant a is:

$$a = f(A_1+2A_2)\left(\frac{c_{11}+2c_{12}}{l}\right)$$

where the elastic constants for the crystal are c_{11}=168 GPa and c_{12}=65 GPa, l is assumed to be the bond length 0.234nm and f is a correction factor to take account of local deviations in the elastic constants due to the defect bonding. This gives a value for a/f= 38.71×10^{-10} J/m. The Huang-Rhys factor S is related to a by:

$$S = \frac{a^2}{2m\hbar\omega^3}$$

where m is assumed to be the Si atomic mass 28 amu (because the sideband is mainly due to lattice modes) and $\hbar\omega$ is assumed to be 35meV, the value of the relaxation energy, which is a reasonable average value for the phonon energy. Using the value of a/f calculated above gives S=10.26 f^2. The measured value of S is ~3 and therefore if agreement is to be obtained with experiment we require that f~0.54, indicating that the elastic constants in the region of the defect are smaller than those of the pure lattice. Because of the ω^3 term in the denominator of the previous equation, the calculated value of S is critically dependant on ω and since we are using an average value for the phonon energy, our results can only be treated as a rough estimate of the correct S value. The calculated value of f is not unreasonably small and thus our

uniaxial stress results appear consistent with the measurements on the vibronic sideband.

4.8: Conclusions

In this chapter comprehensive results on a Cd-related defect observed in CZ silicon have been described. The defect is produced by annealing Cd-implanted silicon at 550°C for 30 min, followed by a slow cool.

Temperature dependence studies have shown that the defect consists of one loosely bound particle (with a binding energy of ~13meV) and one tightly bound particle. Uniaxial stress measurements establish the symmetry of the defect as rhombic I. The transition type is found to be A-B. Zeeman measurements reveal no shift or splitting, indicating a spin 1/2 electron recombining with a spin 1/2 hole. These facts point to a pseudo-donor model for the defect, where the hole is the primary, tightly-bound particle and the electron is bound loosely by the Coulomb field of the trapped hole. Similarities with the previously reported Zn_A complex are demonstrated for the behaviour of the defect under uniaxial stress and magnetic fields.

Cd isotope studies have shown that the defect contains a single Cd atom. The sign and magnitude of the ZPL isotope shift are similar to the values found for the Zn_A defect (Henry *et al.* 1994). Because the defect is produced exclusively in CZ silicon the circumstantial evidence points to O as being involved in the defect also. Other group II-O complexes have been reported for Be and Zn (Daly *et al.* 1995). A Cd-O complex would form an isoelectronic defect in the lattice, and this would be consistent with the high signal levels observed from the Cd_A defect (Pankove 1975). Attempts at O isotope implantation have proved unsuccessful due to unforseen difficulties caused by Cd implantation. O-diffused samples are being prepared for this experiment. The role of damage products in the defect production have not been completely eliminated as yet. The defect showed no reaction to the introduction of H or C isotopes, and thus the role of these impurities in the defect is considered doubtful. A tentative model of the defect as a single Cd-O complex in a rhombic I configuration is proposed. An example of an atomic configuration consistent with this

model is shown in figure 4.8.1. This model envisages the Cd and O atoms either side of the substitutional site, aligned along a <001> axis, with both in a <110> plane. Based on the ionic bonding in the free Cd-O molecule we assign positive and negative charge densities as indicated in the figure. It is unlikely that confirmation of this model will be obtainable by optical spectroscopy, and other techniques will be needed to examine the detailed defect geometry.

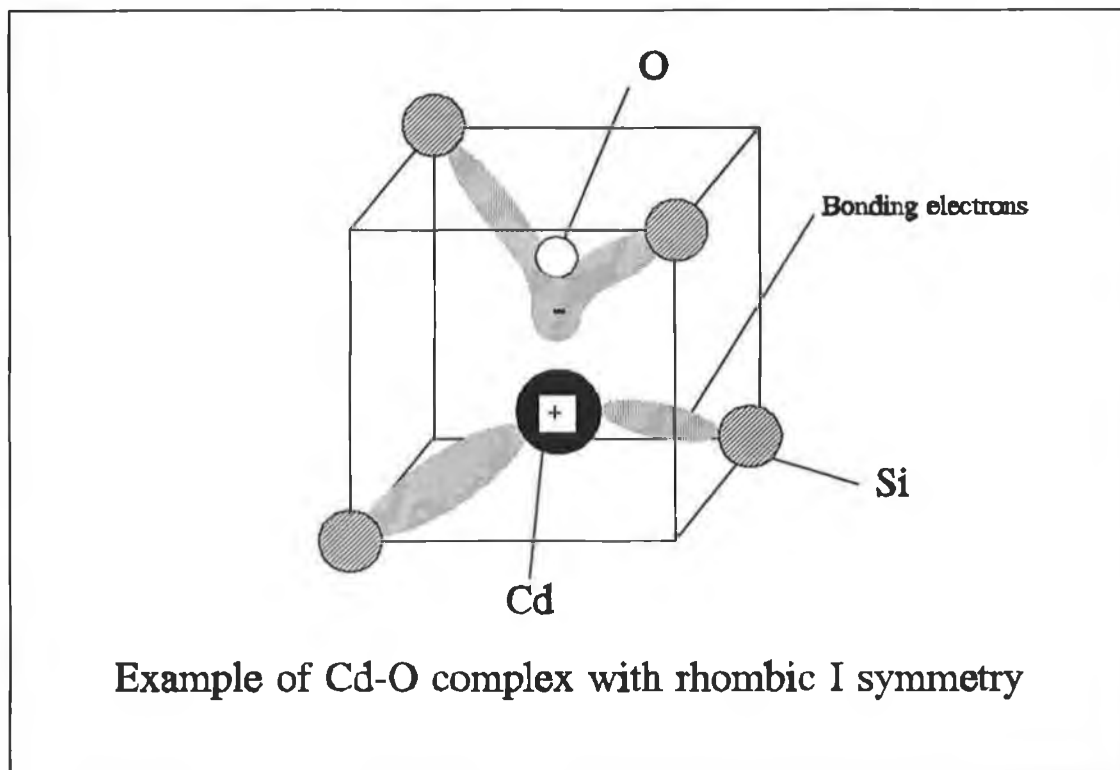

Figure 4.8.1: Model of Cd-O Complex with Rhombic I Symmetry

Examination of the phonon sideband of the defect showed the existence of a single local mode close to the main line ($\hbar\omega$ ~ 9meV). Similarities between the Zn_A and Cd_A local modes were discussed. The Huang-Rhys factor S_1 for this mode was found to be 0.095. This corresponded to a lattice relaxation of ~0.00269nm (~1% of the bond length), which would create a sufficiently large strain field to bind a particle. An examination of the one phonon sideband revealed the contributions from phonons from all points in the Brillouin zone, and the value for the relaxation energy due to exciton capture was found to be ~35meV, with a total Huang-Rhys factor S ~3.

The data presented above provide strong evidence that the Cd_A defect is a Cd-

related version of the Zn_A defect. The behaviour of the two defects as a function of stress and magnetic field are very similar as is the interaction of the defects with the lattice, and both defects appear to be group II - O complexes. This evidence opens up the possibility of a family of group II-O defects in silicon. As was mentioned in chapter 1, preliminary measurements on Ca and Mg-doped CZ silicon have yielded no new PL systems, but a full analysis of these samples has yet to be performed.

In chapter 5, a description and analysis will be given of a minor Cd-related defect studied during the course of the research. This defect exhibits links with both a previously reported Zn-related defect and with the Cd_A defect.

References

A. A. Arifov and D. Rakhimbaev (1984). Sov. Phys. J., **27** no. 11, 967.

K. W. Boer (1990). "Survey of Semiconductor Physics, Electrons and Other Particles in Bulk Semiconductors", Van Nostrand Reinhold.

S. E. Daly (1994). Ph.D. Thesis, Dublin City University.

S. E. Daly, E. McGlynn, M. O. Henry, J. D. Campion, K. G. McGuigan, M. C. do Carmo and M. H. Nazare (1995). Accepted for publication in Materials Science Forum.

G. Davies, E. C. Lightowlers, R. C. Newman and A. S. Oates (1987). Semicond. Sci and Technol. **2**, 524.

G. Davies (1989). Physics Reports, **176** nos. 3 & 4, 85.

P. J. Dean and D. C. Herbert (1979). In "Excitons", edited by K. Cho, Springer-Verlag.

A. C. T. Drakeford and E. C. Lightowlers (1988). Defects in Electronic Materials Symp., Boston MA. USA. Mater. Res. Soc., 209.

D. B. Fitchen (1968). In "Physics of Colour Centres", edited by W. B. Fowler, Academic Press.

M. Gebhard, B. Vogt and W. Witthuhn (1991). Phys. Rev. Lett., **67** no. 7, 847.

M. A. Gulamova, I. Z. Karimova and P. I. Knigin (1971). Sov. Phys. Semiconductors, **5**, 687.

M. O. Henry, J. D. Campion, K. G. McGuigan, E. C. Lightowlers, M. C. do Carmo and M. H. Nazare (1994). Semicond. Sci. Technol., **9**, 1375.

M. O. Henry (1995). Private Communication.

E. Irion, K. Thonke and R. Sauer (1985). J. Phys. C, **18**, 5069.

E. Irion, N. Burger, K. Thonke and R. Sauer (1988). Phys. Rev. B. **38**, 13079.

A. Kaplyanskii (1964). Opt. Spectroscopy, **16**, 329.

E. C. Lightowlers, R. C. Newman and J. H. Tucker (1994). Semicond. Sci. Technol., **9**, 1370.

K. G. McGuigan (1987). Ph.D. Thesis, Dublin City University.

J. I. Pankove (1975). "Optical Processes in Semiconductors", Dover, New York.

A. N. Safonov and E. C. Lightowlers (1994). Mat. Sci. Forum, **143-147**, 903.

M. Singh (1992). Ph.D. Thesis, University of London.

K. Thonke, A. Hangleiter, J. Wagner and R. Sauer (1985). J. Phys. C **18**, L795.

M. Tinkham (1964). "Group Theory and Quantum Mechanics", McGraw-Hill, New York.

J. Wagner and R. Sauer (1982). Phys. Rev. B **26**, 3502.

J. Wagner, A. Dornen and R. Sauer (1985). Phys. Rev. B **31**, 5561.

J. Weber, W. Schmid and R. Sauer (1980). Phys. Rev. B **21**, 2401.

Th. Wichert, H. Skudlik, M. Deicher, G. Grubel, R. Keller, E. Recknagel and L. Song (1987). Phys. Rev. Lett., **59** no.18, 2087.

J. F. Ziegler, J. P. Bersack and U. Littmark (1985). "The Stopping and Range of Ions in Matter", Pergamon Press, New York.

Chapter 5: 935meV Cadmium-Related Line

5.1: Introduction

In this chapter, a description and preliminary analysis is given of a minor Cd-related defect studied during the course of this research. Because of time constraints a full analysis of this defect was not possible.

The defect studied, labelled Cd_B, is a previously unreported luminescence line in Cd-doped CZ silicon with a ZPL at ~935meV. Detailed examination of the full Cd_B spectrum is hampered by low intensity, overlapping sideband features of the more intense Cd_A spectrum and water vapour absorption features beginning at ~919meV. Nevertheless, we have obtained some good data on the ZPL including isotope substitution effects in addition to uniaxial stress and Zeeman results. A weak local mode at ~928meV was observed. Measurements as a function of temperature reveal that the thermal binding energy is low (~15meV) and there is no evidence of thermalising excited states. Preliminary uniaxial stress measurements point towards a monoclinic I defect site and preliminary Zeeman measurements indicate a transition between pure spin 1/2 states. Once again the evidence points towards a pseudo-donor model for the defect. Cd isotope substitution confirm the involvement of a single Cd atom in the defect complex, and circumstantial evidence points towards the involvement of O in the defect also. Similarities between this defect and the previously reported Zn_B defect (Henry *et al.* 1994) and the Cd_A defect (chapter 4) are presented.

5.2: Sample Preparation and Defect Production

The Cd_B line is produced by annealing Cd-doped CZ silicon at 550°C for 30 minutes. The Cd_B defect always appears to be produced simultaneously with the Cd_A defect (see chapter 4). The relative intensities of the two defects can vary over a large range, but in general is ~20:1 (Cd_A:Cd_B). It is unfortunate that one of the samples in

which the Cd_B defect was weakest was the <110> oriented sample, and this limited the quality of the stress data which could be obtained for that direction. No systematic study has yet been made of the conditions needed to optimise Cd_B with respect to Cd_A, because to date the majority of interest has been in the more intense Cd_A system.

5.3: Spectral Features

A full range low temperature spectrum of Cd-implanted CZ silicon is given in figure 5.3.1 with details of the Cd_B system in the insert.

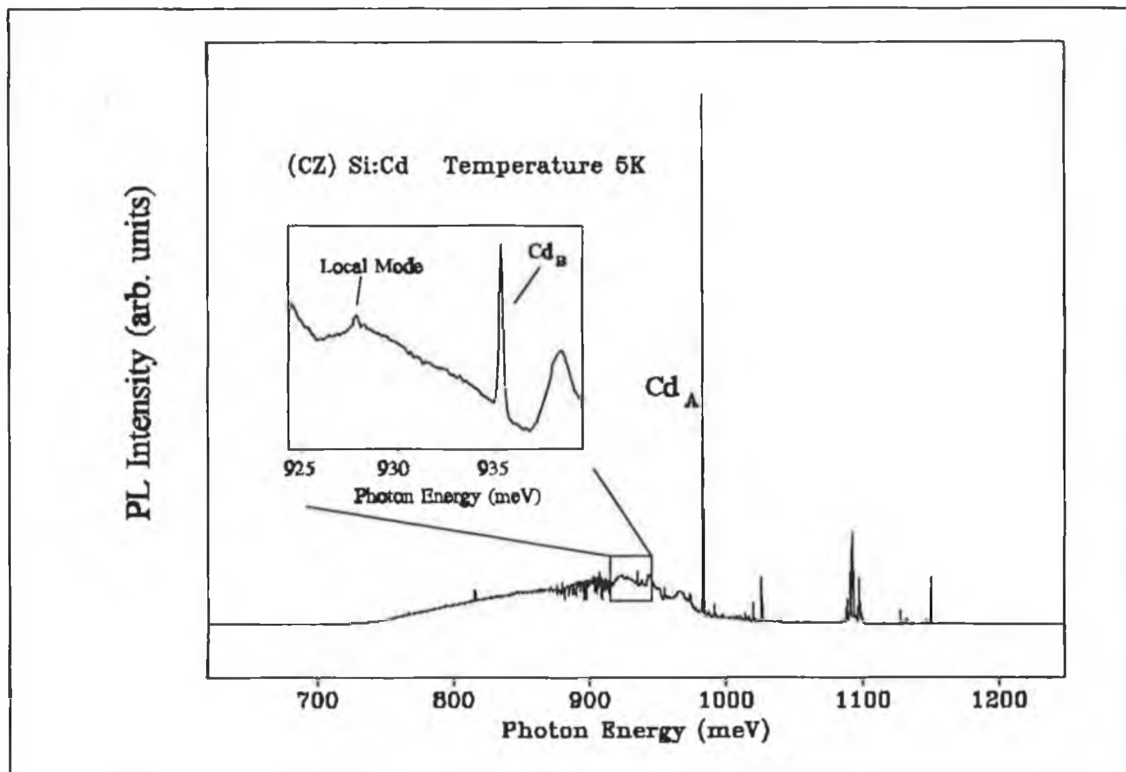

Figure 5.3.1: Low Temperature Spectrum of Cd_B Luminescence

The ZPL at 935.35 (±0.05)meV, is located in the phonon sideband of the stronger Cd_A line, and the broad feature at higher energy is part of the Cd_A sideband. A weak local mode phonon is seen at ~928meV. Because of the overlap of the Cd_A phonon sidebands with those of Cd_B, no study could be made of the latter. In addition, the Cd_B sideband was distorted by water vapour absorption features, with the result that our

study is confined to a preliminary investigation of the 928meV local mode.

5.4: Temperature Dependence of Cd_B Line

Representative spectra of the Cd_B ZPL and local mode as a function of temperature are shown in figure 5.4.1.

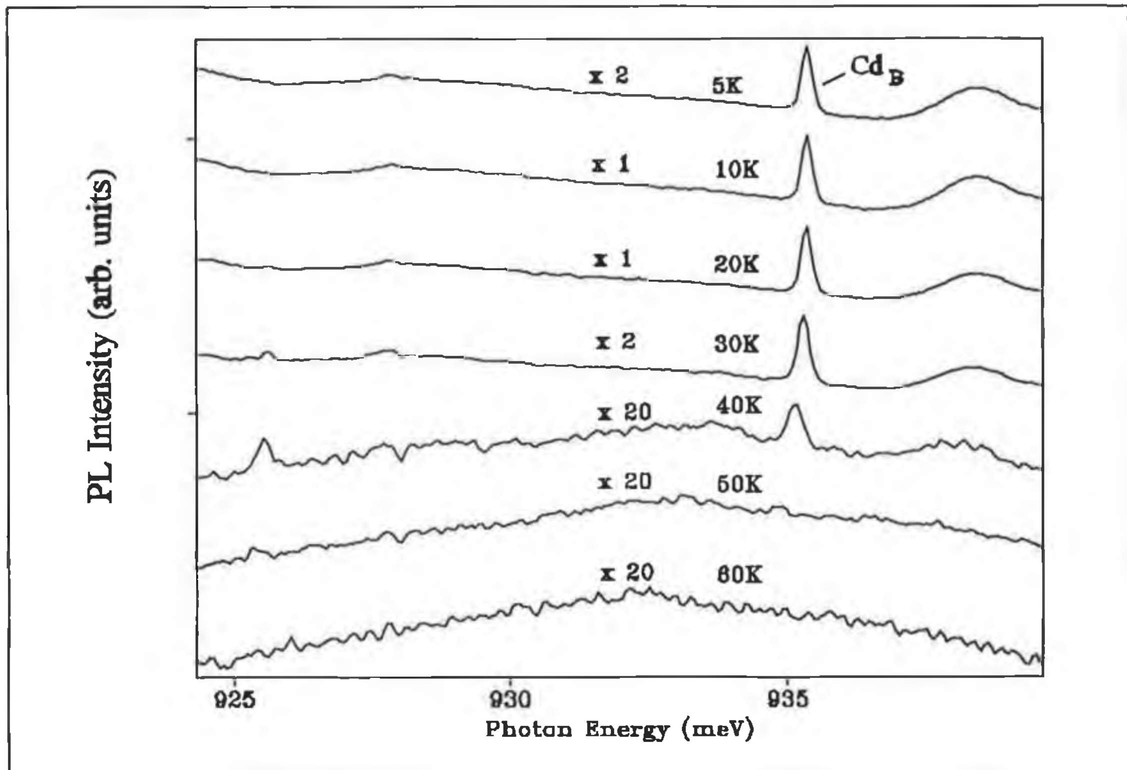

Figure 5.4.1: Temperature Dependence of Cd_B Luminescence

The intensity of the ZPL increases initially with increasing temperature, reaching a maximum at ~15K, and then decreases as the temperature rises above 15K, until the line is completely gone at temperatures greater than ~50K. No evidence of the growth of any thermalising excited states is seen in the spectrum. A plot of the ZPL intensity versus temperature is given in figure 5.4.2, with a best fit curve from equation 2.7.8 corresponding to a thermal binding energy of 17(±2)meV, small compared to the difference between the ZPL energy and the low temperature bandgap energy (~234meV), indicating that the defect is composed of one tightly bound particle, with

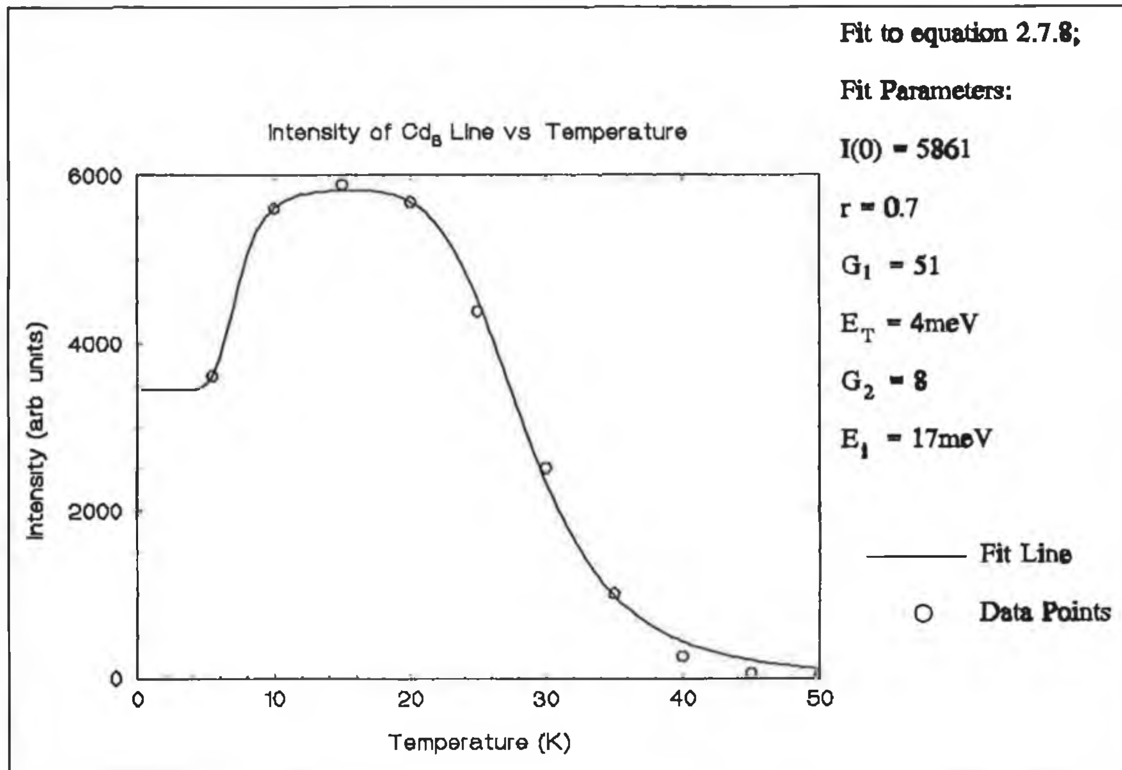

Figure 5.4.2: Plot of Cd_B Intensity vs. Temperature

a second particle bound in its Coulombic field.

5.5: Uniaxial Stress and Zeeman Measurements on the Cd_B Line

(i) Uniaxial Stress: Oriented Cd-implanted CZ silicon samples were annealed at 550°C for 30 minutes to produce the Cd_B luminescence. As was mentioned in section 5.2, the Cd_B defect luminescence was extremely weak in the <110> oriented sample. This limited the uniaxial stress data to effectively two directions. Although an estimate has been made of the <110> data, the signal quality for stress in this direction is very poor. As always, great care was taken in the sample mounting procedures. No significant information was obtained from polarisation experiments due to depolarising multiple internal reflections.

The ZPL splits into two and three components for uniaxial stress applied along the <001> and <111> crystal directions respectively. Fan diagrams and representative

spectra are shown in figures 5.5.1 and 5.5.2. For stress along the <110> direction the ZPL appears to split into four components. The fan diagram and representative spectra are shown in figure 5.5.3 (a) & (b). The components under <110> stress are very weak and are only visible in one case for very low stress (< 10MPa), while the others are only visible for stresses < 80MPa. Further experiments on a <110> sample with high Cd_B signal levels are needed to obtain good quality, reliable data. As far as we can tell there are no interaction effects occurring for any stress direction. This conclusion is supported by the temperature dependence data, which show no evidence of excited states.

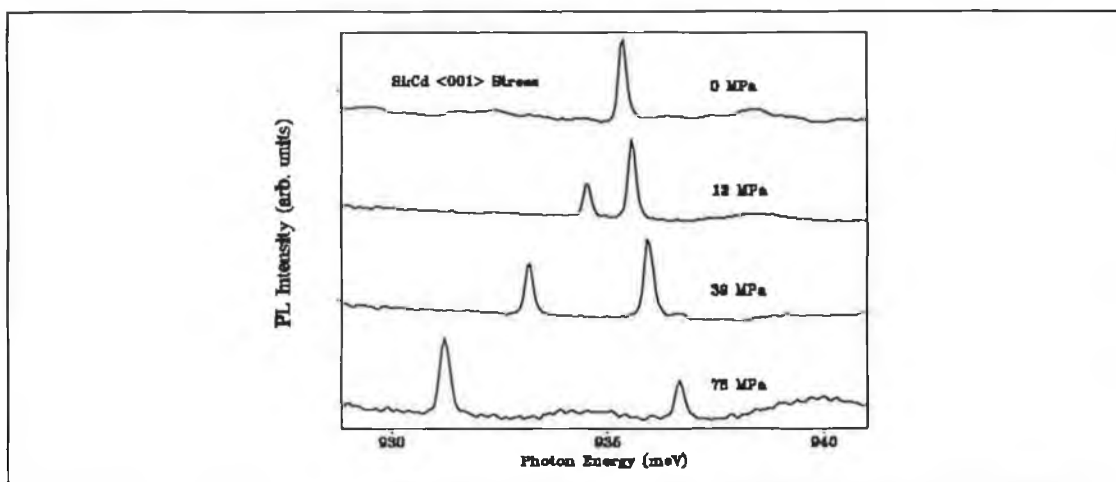

Figure 5.5.1 (a): Representative Spectra for <001> Stress

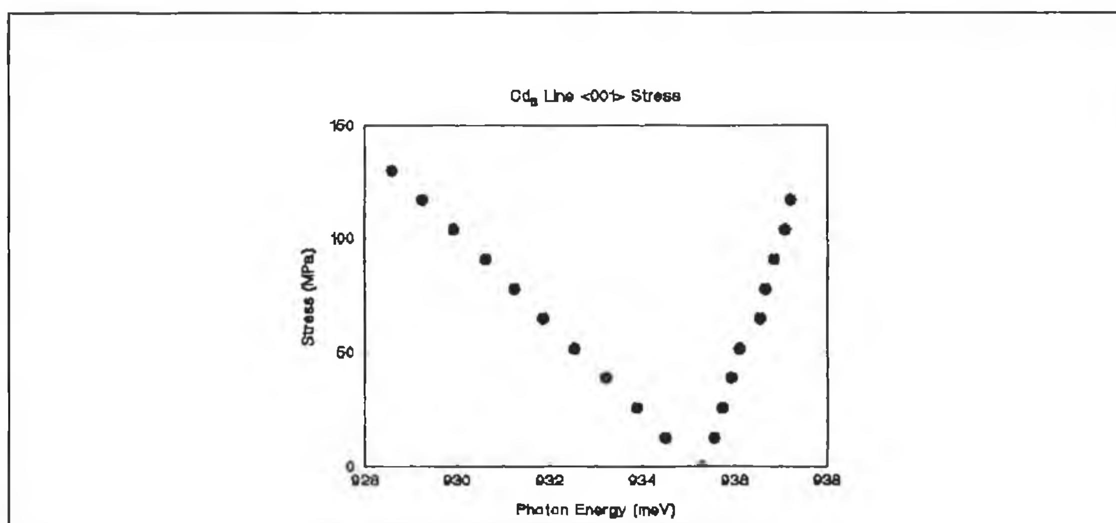

Figure 5.5.1 (b): Fan Diagram for <001> Stress

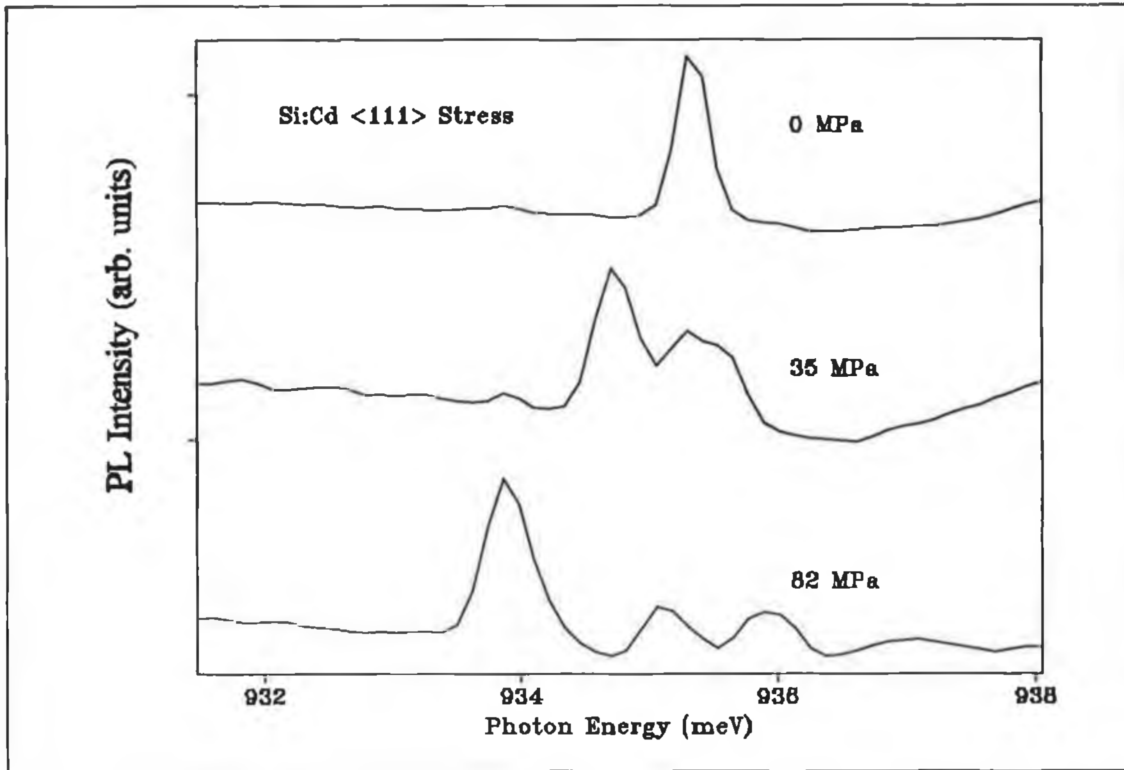

Figure 5.5.2 (a): Representative Spectra for <111> Stress

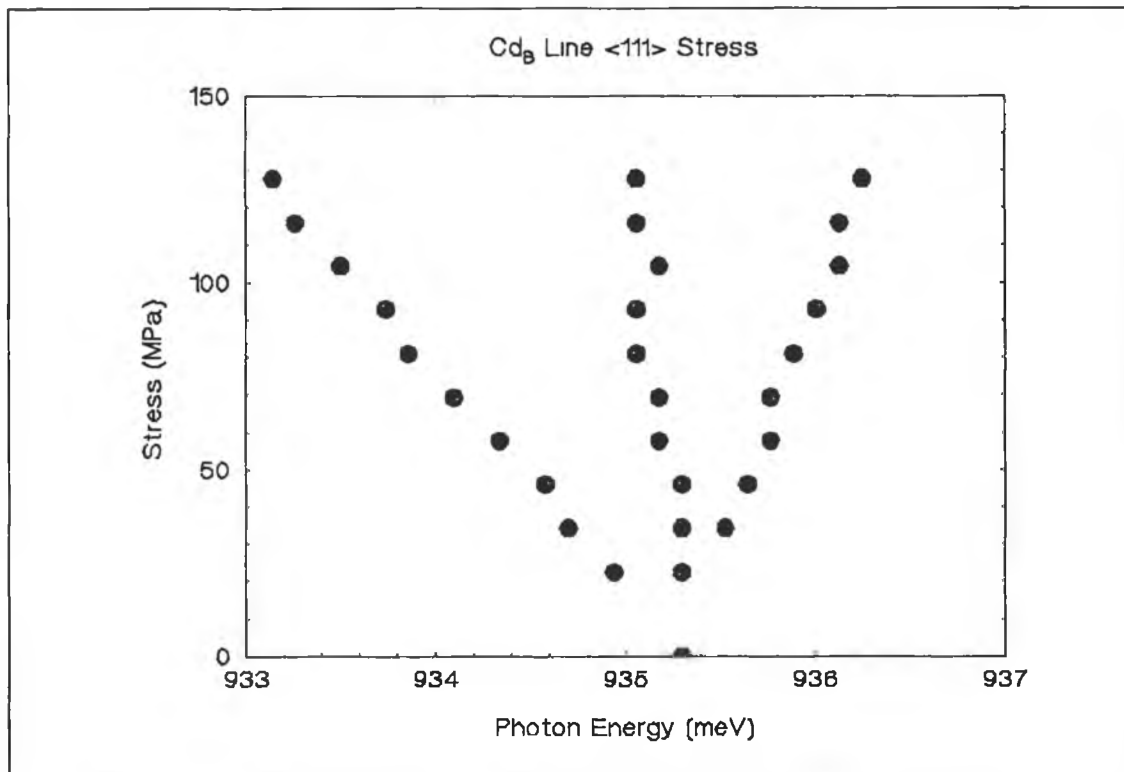

Figure 5.5.2 (b): Fan Diagram for <111> Stress

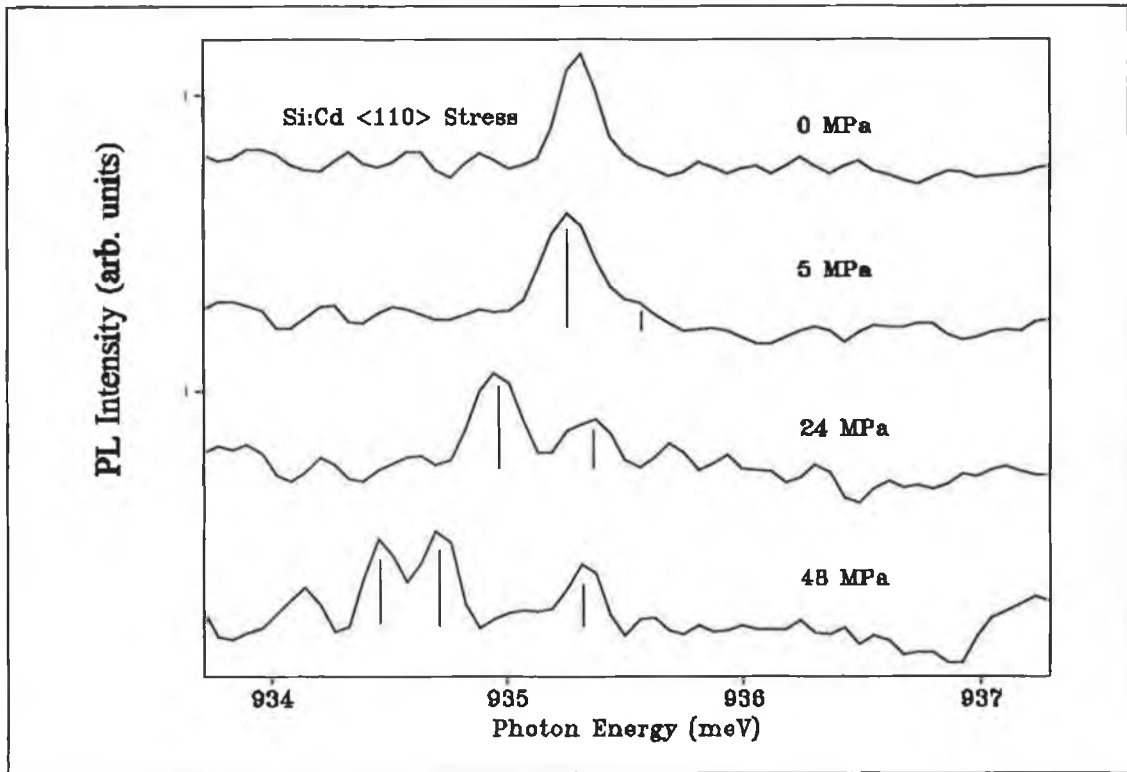

Figure 5.5.3 (a): Representative Spectra for <110> Stress

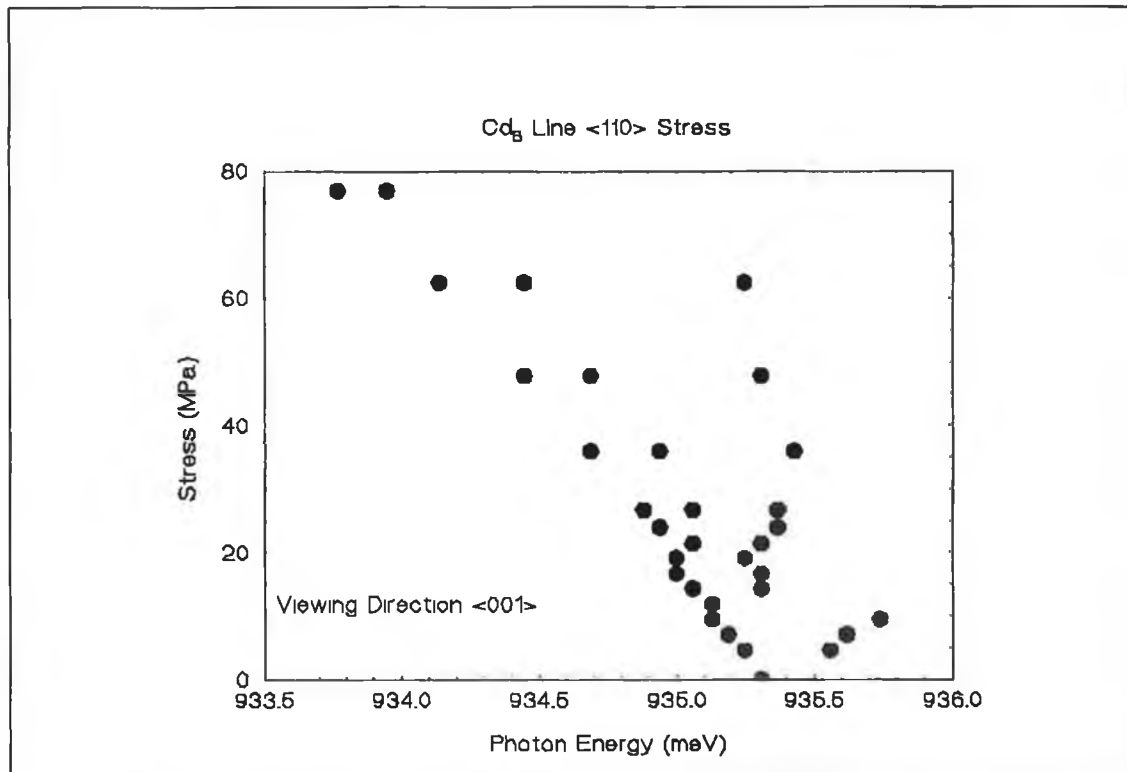

Figure 5.5.3 (b): Fan Diagram for <110> Stress

In order to narrow down the possible symmetry types for the defect, it is necessary to consider the possibilities outlined by Kaplyanskii (1964). Both trigonal A-E and monoclinic I defects have a splitting pattern with 2 lines in <100> stress, 3 in <111> and 4 in <110>. A good fit to the experimental data for the <001> and <111> directions was obtained only for a monoclinic I fitting. A plot of the expected lines for a monoclinic I fit are superimposed on the experimental data in figure 5.5.4.

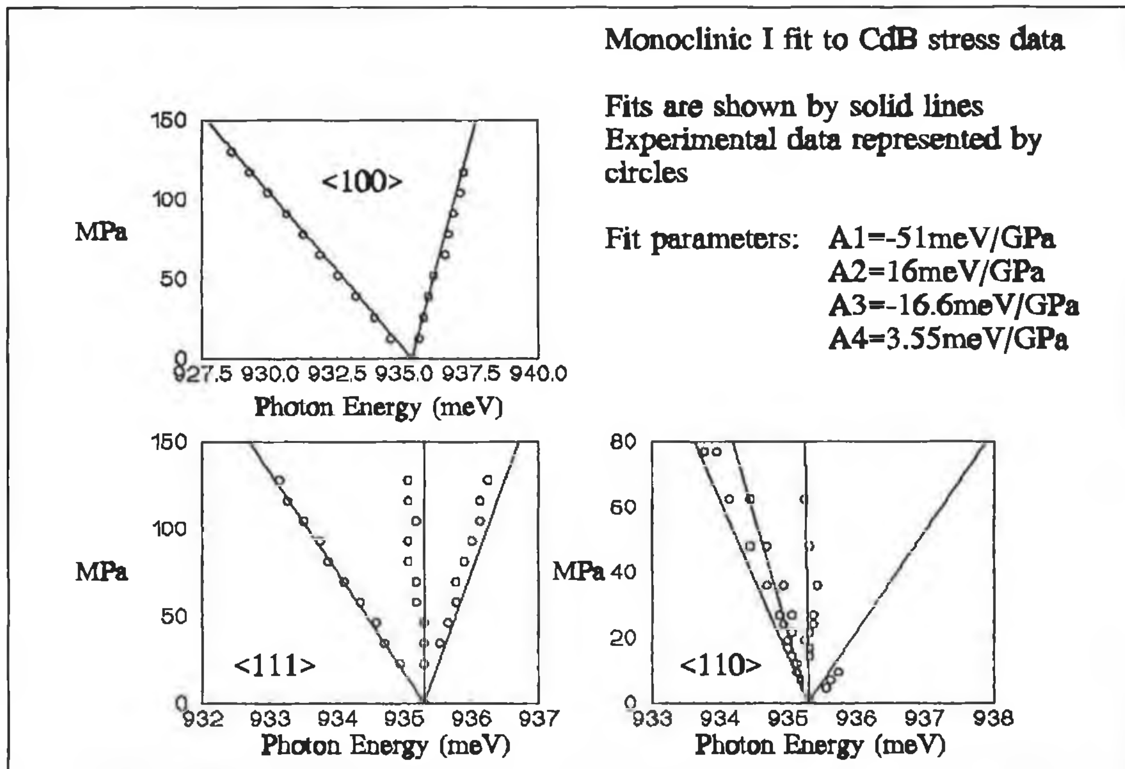

Figure 5.5.4: Monoclinic I Fit to Experimental Data Set

A good fit is seen for the <001> and <111> directions, and the fit appears reasonable for the <110> direction also. The parameters for the fit are;

A_1 = -51meV/GPa

A_2 = 16meV/GPa

A_3 = -16.6meV/GPa

A_4 = 3.55meV/GPa

A comparison of the theoretical and experimental shift rates for the Cd_B line with a monoclinic I fit are given in table 5.5.1.

Table 5.5.1

Monoclinic I fit to Cd_B centre	Experimental Shift Rate (meV/GPa)	Theoretical Shift Rate (meV/GPa)
<001>	-50.9	-51
	16.9	16
<111>	-17.4	-17.4
	-2.3	0
	7.5	9.4
<110>	-19.6	-21
	-17	-14
	-0.2	-0.6
	44.8	32.6

The defect symmetry appears to be monoclinic I. In order to establish the transition type it is necessary to examine the relative intensities of the stress-split components. The intensity ratios (at low stress) under <001> and <111> stress are listed in table 5.5.2 along with the expected values for A-A (dipole direction parallel to <$\bar{1}$10>, Mohammed *et al.* 1982, Jeyanathan 1994) and A-B transitions at monoclinic I sites.

Table 5.5.2

Stress Direction	Experimental Ratio	Theoretical Ratio Monoclinic I A-A	Theoretical Ratio Monoclinic I A-B
<001>	2.8 : 1	3 : 1	3 : 1
<111>	10 : 4.5 : 4.5	6 : 5 : 5	10 : 3 : 3

It can be seen from this table that the transition type is most probably A-B. The behaviour of the intensity ratio of the stress-split components under <001> stress is

remarkably similar to that of the Cd_A centre, with the higher energy component losing intensity very rapidly compared to the lower energy component, as discussed in chapter 4.

There are a number of interesting features of the uniaxial stress behaviour of the Cd_B centre. The first of these is the similarity between the Cd_B and Cd_A stress fitting parameters. The parameters are listed below in table 5.5.3.

Table 5.5.3

Stress Parameter	Cd_A (meV/GPa)	Cd_B (meV/GPa)
A_1	-49	-51
A_2	15	16
A_3	-14.6	-16.6
A_4 (not applicable for Cd_A)	0	3.55

The first three parameters are very similar, and the A_4 parameter is very small indicating that the centre is only weakly perturbed from a rhombic I centre. In addition the intensity ratios of the Cd_A and Cd_B components under <001> stress are very alike. These data are suggestive of a link between the two centres, perhaps with the Cd_B centre behaving like a slightly perturbed version of the Cd_A centre. The nature of this link has yet to be examined.

The Cd_B centre also behaves in a very similar manner under stress to the previously reported 1090 meV Zn_B centre (Henry *et al.* 1994), in terms of both fit parameters (similar to within ~10%, except for the A_4 parameter) and behaviour of the intensity ratios (particularly the behaviour of the intensities under <001> stress, see above). The Cd_A, Zn_B and Cd_B stress parameters are listed together in table 5.5.4 for purposes of comparison.

Strong evidence has been presented in chapter 4 for the similarity of the Zn_A and Cd_A defect, and the possibility of a Cd-related analog of the Zn_B centre is plausible. Further measurements on the Cd_B centre are required to examine this similarity, particularly reliable <110> stress data.

Table 5.5.4

Stress Parameter	Cd_A (meV/GPa)	Cd_B (meV/GPa)	Zn_B (meV/GPa)
A_1	-49	-51	-51.2
A_2	15	16	15.4
A_3	-14.6	-16.6	-16.8
A_4	Not applicable	3.55	2.5

(ii) Zeeman Spectroscopy of the Cd_B Line: Zeeman measurements on the Cd_B line in <001>-oriented magnetic fields up to 5T have shown that the ZPL neither shifts nor splits. On the basis of the model presented in chapter 2, the transition is thought to be between purely spin-like states. Because of the low symmetry of the defect potential the tightly bound hole must have quenched orbital angular momentum (neglecting spin-orbit coupling effects), and thus be purely spin-like, which is in agreement with the experimentally observed behaviour. This behaviour is very similar to that observed for the Cd_A defect and also for the Zn_B defect (Henry 1995). Because of the low intensity of the line and the relatively low resolution used, small effects due to deviations from the simple models in chapter 2 (such as transitions between $m_s=+1/2$ and $m_s=-1/2$ states, as described by Irion *et al.* 1988) cannot be resolved. Further high resolution experiments at high magnetic fields are required to examine any such fine structure.

5.6: Chemical Identity of the Cd_B Defect

A similar investigation was carried out for Cd_B to that carried out for Cd_A (see chapter 4 for experimental details) in terms of the impurities considered. The results obtained for the two defects are identical in all respects. To summarise, no evidence was found for the involvement of H, C or intrinsic dopants in Cd_B. The role of damage products could not be totally ruled out, and experiments to diffuse Cd into CZ

silicon are planned to answer this question.

Cd isotope substitution experiments have confirmed that Cd is a constituent of the defect. Our measurements show that only one Cd atom is involved in the defect. Figure 5.6.1 shows ZPL spectra of ^{106}Cd, ^{116}Cd and dual-implanted samples. A positive isotope shift of ~0.09meV is seen in the ZPL for the ^{106}Cd (ZPL at 935.25meV) and ^{116}Cd (ZPL at 935.34meV) samples. The ZPL in the dual implanted sample shows a considerable broadening, and the asymmetric lineshape is similar to that found for the Cd_A and 1026meV defects, the explanation for which is discussed in chapter 4.

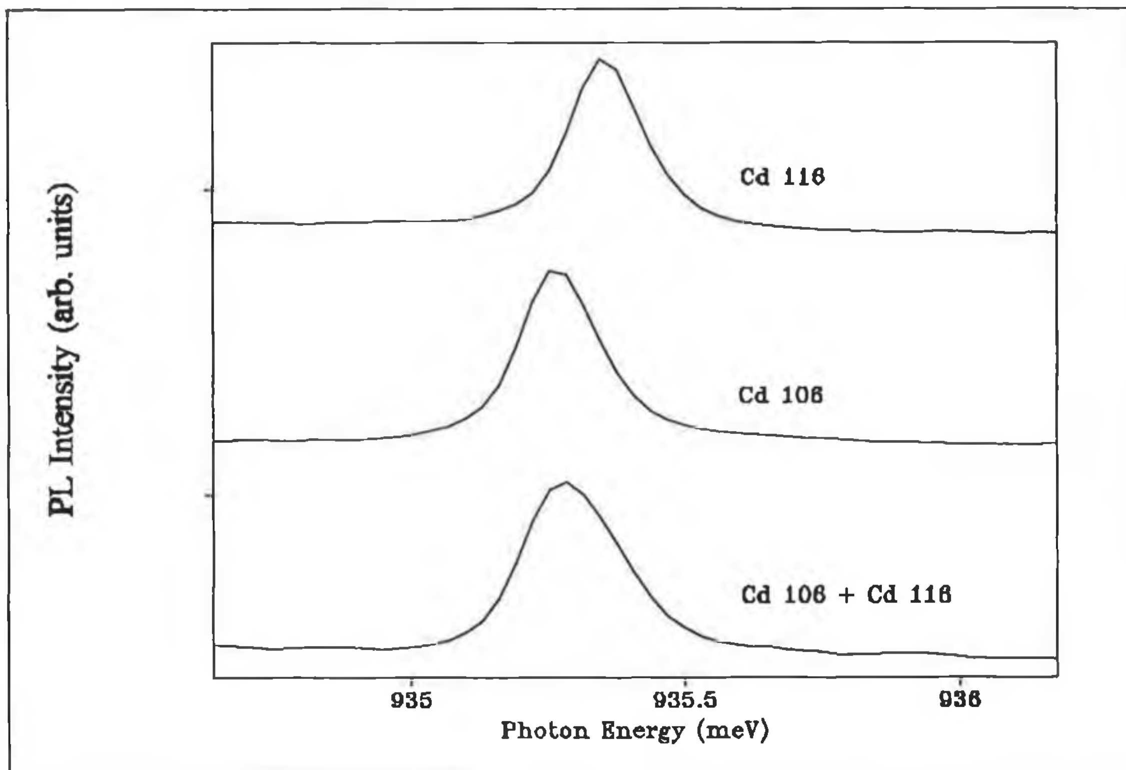

Figure 5.6.1: Effects of Cadmium Isotope Substitution on Cd_B ZPL

Because the defect is seen only in CZ silicon, there is considerable circumstantial evidence for the involvement of O. Attempts at O implantation have been unsuccessful, as was described in chapter 4, and samples are currently being prepared for O diffusion in an attempt to confirm the role of O in the defect.

5.7: Local Mode Behaviour of Cd_B Defect

As was stated in section 5.3, the phonon sideband structure of Cd_B was obscured both by water vapour absorption features and by the much stronger phonon sideband of the Cd_A line, precluding a detailed study of the phonon sideband. A weak local mode phonon with energy of ~7.5meV can be clearly seen however (figure 5.3.1) and the behaviour of this feature as a function of isotopic mass was examined. Figure 5.7.1 shows the Cd_B local mode for ^{106}Cd and ^{116}Cd implanted samples.

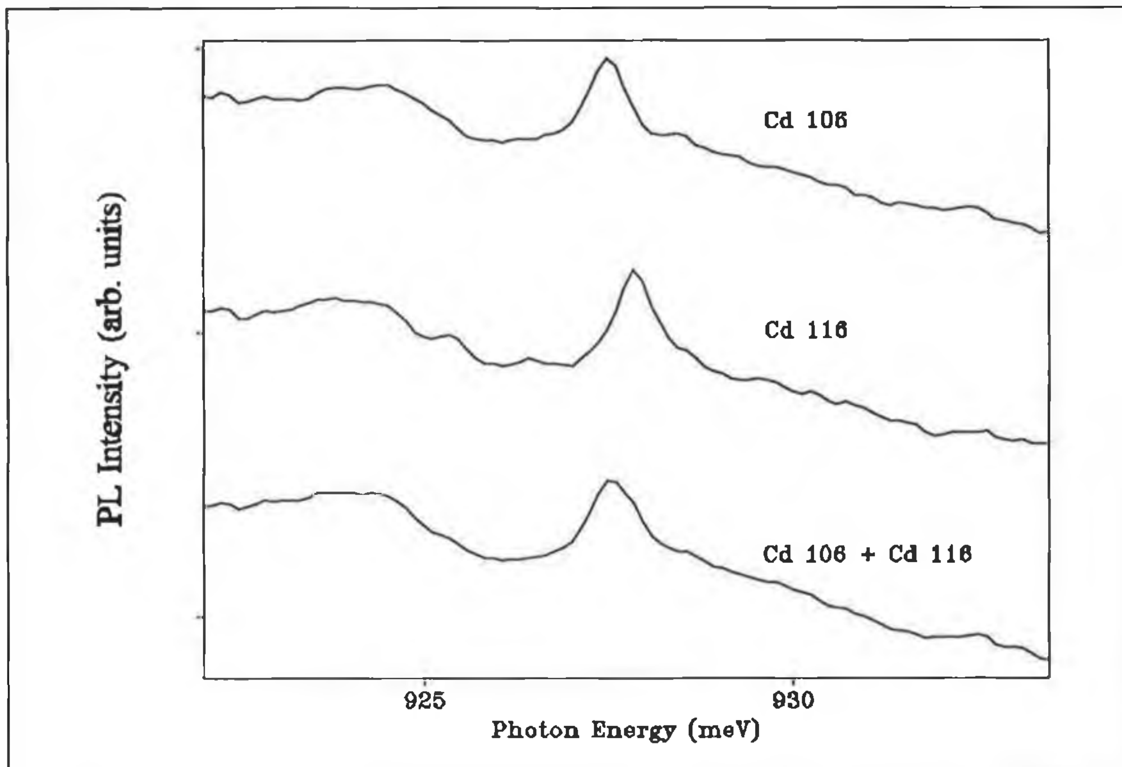

Figure 5.7.1: Effect of Cadmium Isotope Substitution on Cd_B Local Mode

The phonon energy changes from ~7.8meV for ^{106}Cd to ~7.5meV for ^{116}Cd. The ratio of these values, ~0.96, is in excellent agreement with the expected value of 0.956 if the vibration is due solely to the Cd atom.

5.8: Conclusion

A description and preliminary analysis of the Cd-related Cd_B defect has been presented in this section. Measurements as a function of temperature show that the defect has a low thermal binding energy of ~15meV, indicating that the defect excited state is composed of one tightly bound particle and a secondary particle bound in its Coulombic field. No evidence is seen of thermalising excited states in the temperature dependence data. Uniaxial stress measurements point towards monoclinic I symmetry for the defect (although the perturbation from rhombic is small), and the transition type is most probably A-B. Zeeman measurements indicate that the transition is from a spin 1/2 excited state to a spin 1/2 ground state. These data, combined with the stress data and the low thermal binding energy point towards a pseudodonor model for the defect excited state.

Isotope studies have shown that the defect consists of a single Cd atom. Strong circumstantial evidence exists that O is involved in the defect also, and hence the defect is assigned to a Cd-O complex at a site of monoclinic I symmetry.

There are notable similarities between Cd_B and Cd_A both in chemical composition and behaviour under uniaxial stress and magnetic fields which leads us to suspect that Cd_B is a perturbed version of Cd_A. In addition, there are similarities between Cd_B and the previously reported Zn_B defect, in terms of behaviour under stress, magnetic fields and chemical composition. It is suspected that the Cd_B defect may be a Cd-related analog of the Zn_B defect. Further study of the relationship between the two defects, including full stress data on all three directions are required.

References

M. O. Henry, J. D. Campion, K. G. McGuigan, E. C. Lightowlers, M. C. doCarmo and M. H. Nazare (1994). Semicond. Sci. and Technol. **9**, 1375.

M. O. Henry (1995). Private Communication.

E. Irion, N. Burger, K. Thonke and R. Sauer (1988). Phys. Rev. B **38**, 13079.

L. Jeyanathan (1994). Ph.D. Thesis, University of London.

A. Kaplyanskii (1964). Opt. Spectroscopy **16**, 329.

K. Mohammed, G. Davies and A. T. Collins (1982). J. Phys. C: Solid State Physics **15**, 2779.

Chapter 6: 1026meV Cadmium-Related Defect

6.1: Introduction

In this chapter, a description and analysis are presented of another previously unreported luminescence centre in Cd-doped CZ silicon. The ZPL of the system is at 1026.10 (± 0.05)meV. The defect is referred to in the text as the 1026meV system. The phonon sideband of the system reveals that the defect couples to two local mode vibrations. Measurements as a function of temperature show that the thermal binding energy is low and reveal the existence of a thermalising excited state at ~1.1meV above the first excited state. Uniaxial stress measurements reveal a low symmetry site for the defect (rhombic I), and Zeeman measurements on the lowest excited state indicate the pseudo-donor nature of this state. Cd isotope substitution experiments establish the involvement of one Cd atom in the defect complex. Isotope substitution experiments are reported for a number of common impurities in CZ silicon.

6.2: Sample Preparation and Defect Production

The 1026meV Cd-related system is produced by Cd ion implantation (beam energies of both 80keV and 200keV and ion doses of $10^{12} \rightarrow 10^{15}$ ions/cm^2 were used with no discernable differences in the production of the defect), followed by annealing at 550°C for 30 minutes in an atmosphere of flowing argon gas (appendix A). The sample was withdrawn from the furnace and allowed to cool slowly. Increasing the cooling rate by quenching in an isopropanol/water mixture was found to destroy the formation of the defect centre. The defect could be produced by annealing in the range 500°C→700°C, but 550°C was found to be the optimum temperature in order to obtain maximum signal, as was the case for the Cd_A and Cd_B defects described in chapters 4 and 5. The ratio of 1026meV intensity to Cd_A intensity was found to be typically ~ 1:15, though the precise value of this ratio depended both on the annealing temperature and the sample. The defect could also be produced by first annealing at

high temperatures (800°C→1100°C)for ~30s, with a subsequent anneal at 550°C for 30 min. This annealing procedure allowed one to produce the 1026meV system without simultaneously producing the Cd_A system. In general though, both the 1026meV and Cd_A centres were produced in the same samples. From an economic point of view this made sense because only one set of oriented sample was needed to study both defect complexes under uniaxial stress and Zeeman.

Figure 6.2.1 shows examples of spectra in the range 1010→1030meV obtained from samples of Cd implanted CZ silicon subject to isochronal anneals (30 minutes) at different temperatures.

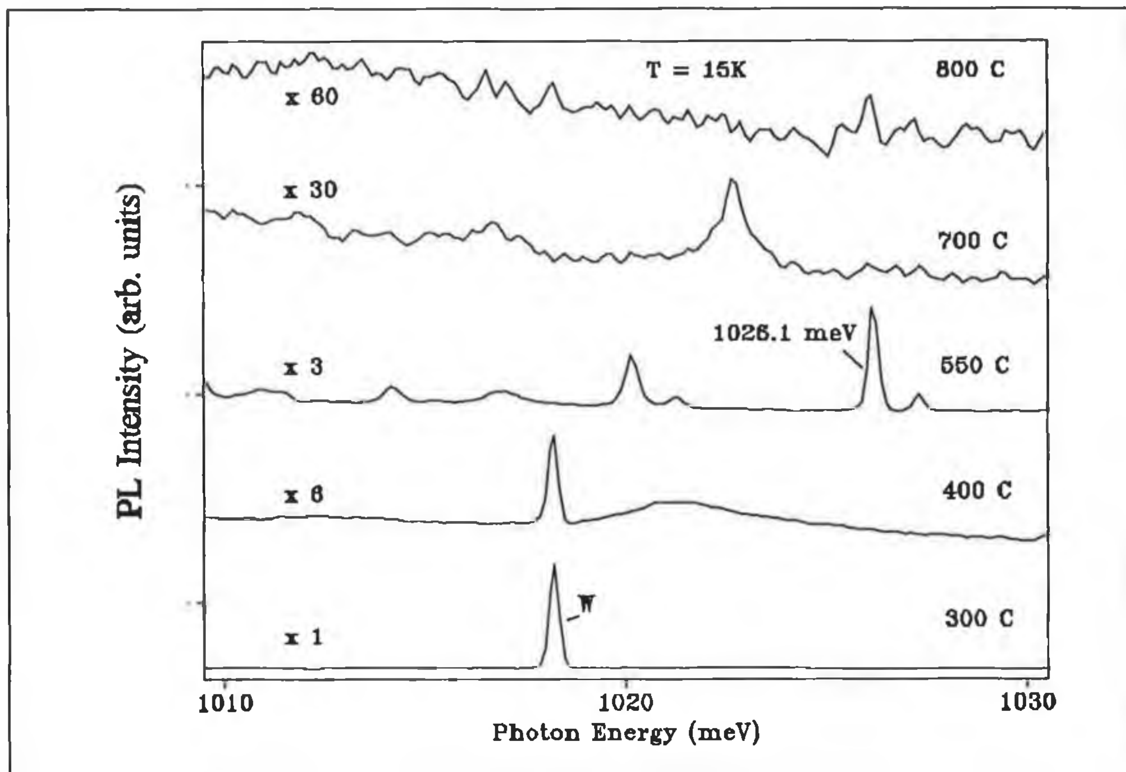

Figure 6.2.1: Effect of Annealing Temperature on 1026meV Spectrum (Isochronal Anneals 30 minutes)

Spectra of samples annealed at lower temperature (300-400°C) have the damage-related W line, while samples annealed at higher temperatures (700°C) have a weak feature of unknown origin at ~1022meV. Full range spectra from 700meV→1200meV showing the position and intensity of the 1026meV system in relation to other lines can be found in figures 1.5.1 and 4.2.1.

6.3: Spectral Features

A low temperature PL spectrum of the 1026meV system is shown in detail in figure 6.3.1.

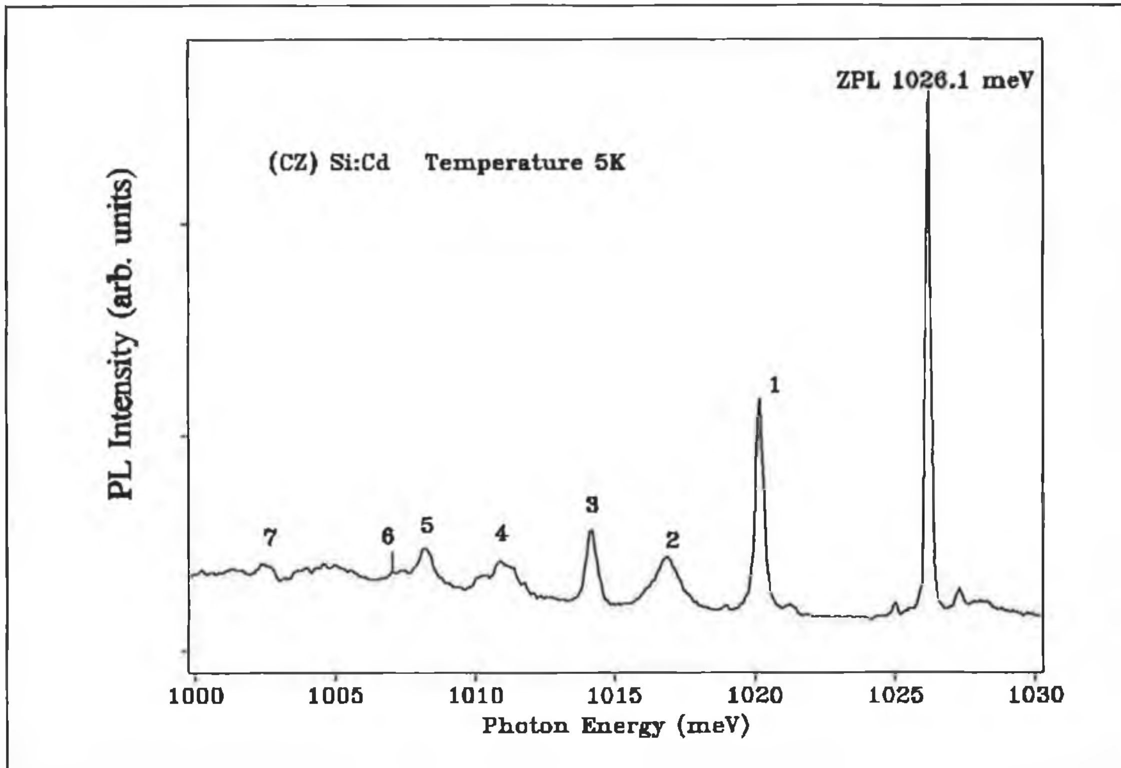

Figure 6.3.1: Low temperature spectrum of 1026meV system

The ZPL occurs at 1026.10 (± 0.05)meV (for ^{116}Cd) and a detailed phonon sideband is observed at lower energies. The peaks in the phonon sideband are associated with local modes of vibration of the defect (described in section 6.7). Two local modes can be recognised from the spectrum, one with energy 6.0 (±0.1)meV and the other with energy 9.2 (±0.1)meV. The phonon sideband can then be explained in terms of these local modes and multi-phonon combinations of these local modes. The defect couples strongly to these modes and lattice modes appear to have a negligible contribution to the phonon sideband. Table 6.3.1 displays the energy of the various spectral features, their shift from the ZPL and their assignments.

Table 6.3.1

Spectral Feature	Position (meV)	Shift from ZPL (meV)	Assignment
1	1020.12	5.98	Local mode L1
2	1016.85	9.25	Local mode L2
3	1014.13	11.97	L1+L1
4	1010.8	15.3	L1+L2
5	1008.15	17.95	L1+L1+L1
6	1007.34	18.76	L2+L2
7	1002.4	23.7	L1+L1+L1+L1

The local mode vibrational energies (~6, 9meV) are relatively small, which is characteristic of the vibrations of a heavy atom (Cd) in the lattice. The energy of the local modes is quite similar to the energy of the Cd_A local mode (~9.5meV), discussed in chapter 4.

6.4: Temperature Dependence of 1026meV System

Figure 6.4.1 shows the 1026meV and sideband for a range for temperatures in the region 5K to 60K. The most striking aspect of this data is the growth of a line at ~ 1027.2meV as a function of temperature. This feature, repeated in the phonon sidebands of the ZPL, is identified as being due to a transition from a thermalising excited state of the defect. An Arhennius diagram of the ratio of the 1027.2meV line intensity versus the 1026meV line intensity is shown in figure 6.4.2. A good linear fit to the data is found, and the best fit slope represents a value of ΔE=1.19(±0.2) meV in equation 2.7.2, with a y-axis intercept of -0.408, corresponding to a value of 0.665 for $f_2 g_{21}/f_1$ in equation 2.7.2. This value of ΔE is in excellent agreement with the observed spectroscopic splitting of the two lines (~1.1meV).

The total intensity (1026meV line + 1027.2meV line) as a function of temperature is plotted in figure 6.4.3. The intensity of the defect luminescence

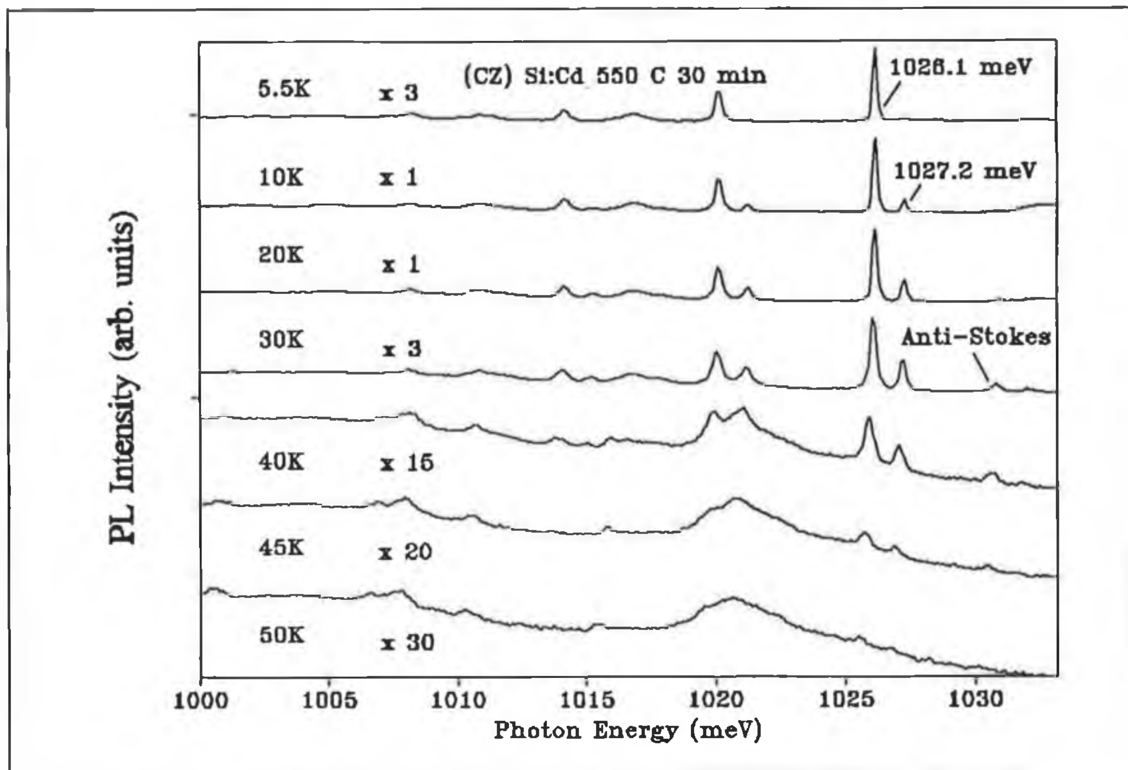

Figure 6.4.1: 1026meV system luminescence as a function of temperature

increases initially as a function of temperature, reaching a maximum at ~15K, and then decreases rapidly and is completely gone at temperatures > 50K. This behaviour is consistent with the model of carrier dissociation as a function of temperature discussed in detail in chapter 2. In order to calculate the thermal binding energy of the electronic particles at the defect, it is necessary to fit the total intensity as a function of temperature to equation 2.7.8. The best fit line to equation 2.7.8 is plotted in figure 6.4.3, and the value of the dissociation energy E_i is found to be 16(±2)meV. The luminescence intensity decreases rapidly at low temperatures (a reduction by a factor of ~5 is seen in going from 10→5.5K) and the fit to equation 2.7.8 indicates that the intensity vanishes as T→0K, corresponding to a large value for the branching ratio r (4.87×10^4). Although behaviour of this nature is unusual it is not unique and similar behaviour as a function of temperature is seen for the 767meV "P" line (Davies 1989).

To complete the description of the temperature dependence of the PL spectrum, we note that at temperatures above ~30K, a weak anti-Stokes sideband becomes

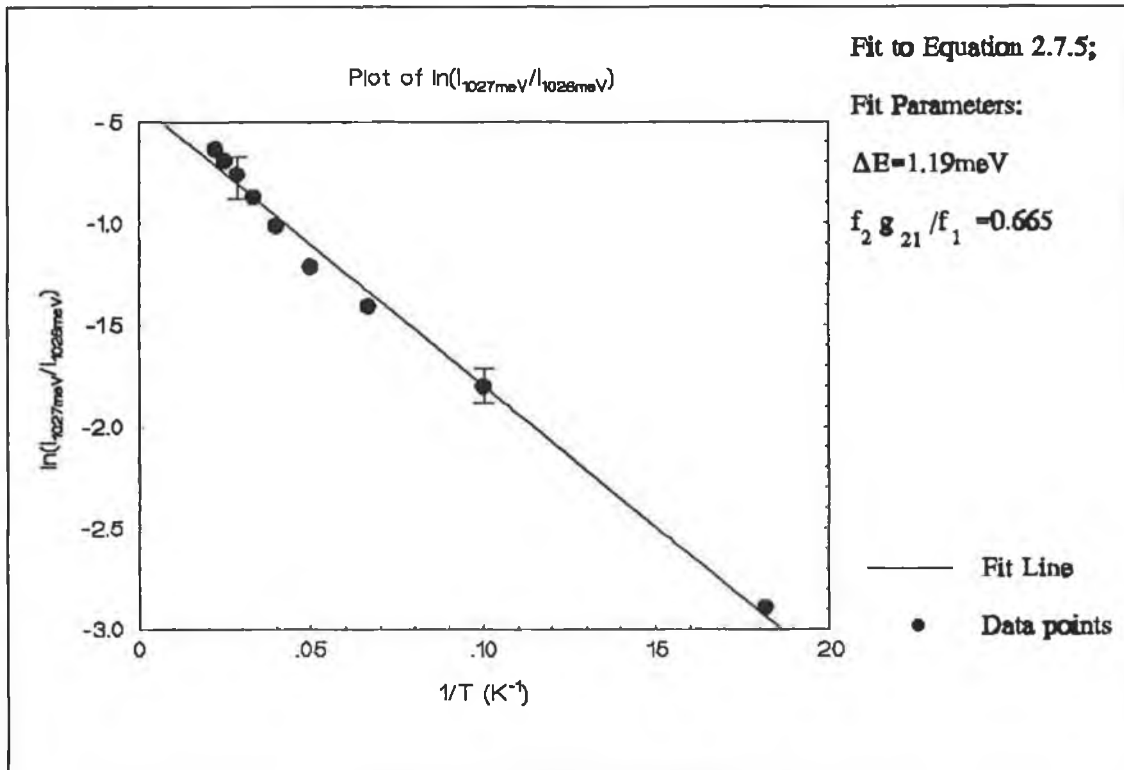

Figure 6.4.2: Plot of $\ln(I_{1027meV}/I_{1026meV})$ vs. 1/T, with indicative error bars shown

visible at ~1030.8meV. The anti-Stokes phonon is considerably lower in energy than the Stokes phonon (anti-Stokes ~ 4.7meV, Stokes ~ 6meV). At even higher temperatures (> 40K) a broad luminescence band which survives to higher temperatures becomes prominent in the spectrum.

The behaviour of the 1026meV line at high temperatures is quite similar to that of the Cd_A line discussed in chapter 4. The thermal binding energies of the defects are similar within the variance of the fitting procedure (Cd_A ~13(±2) meV : 1026meV ~16(±2) meV). References to other pseudo-donor type complexes in silicon can be found in chapter 4.

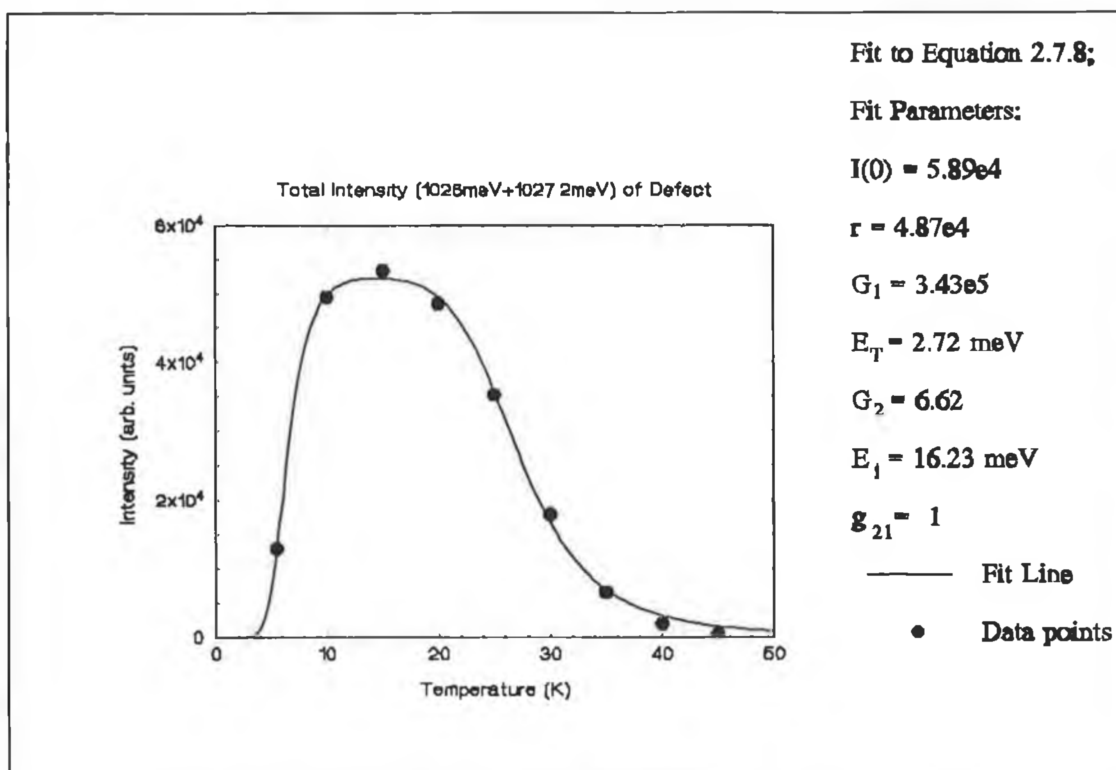

Figure 6.4.3: Plot of Total Intensity vs. Temperature for 1026meV system

6.5: Uniaxial Stress and Zeeman Spectroscopy of the 1026meV System

(i) Uniaxial Stress

Oriented CZ silicon samples were prepared by Cd implantation and annealing as described in section 6.2. The sample axis orientation, experimental procedures and equipment have been described previously in chapters 3 and 4. As was the case for the Cd_A defect, no significant polarisation information was obtained. All measurements were performed at least twice to ensure good quality, reproducible results.

Uniaxial stress and Zeeman data have to date only been obtained for the transition at 1026.1meV. No reliable data have yet been obtained for the 1027.2meV line. This is because the uniaxial stress measurements were taken at low (5→10K) temperatures for which the 1027.2meV line intensity is weak. This allowed us to follow the movements of the 1026.1meV line components without the problem of

confusion with the higher energy line. Even with this precaution, the <110> stress data for some components tended to overlap the weak 1027.2meV line components, and hence data could only be taken up to ~48 MPa for the highest energy <110> component. Experiments at higher temperatures to measure the behaviour of the 1027.2meV line will be necessary in the future (see chapter 8).

Stress parallel to the <001> crystal direction causes the 1026.1meV line to split into two components. The fan diagram and representative spectra are shown in figure 6.5.1 (a) and (b). The shift rates of the stress split components are non-linear, indicative of an interaction between states. Stress parallel to the <111> crystal direction caused the line to split into two components and the fan diagram and representative spectra are shown in figure 6.5.2 (a) and (b). The shift rates in this direction are linear, indicating the absence of any coupling potential between the states in this direction. Stress parallel to the <110> crystal direction caused the line to split into three components. The fan diagram and representative spectra are shown in figure 6.5.3 (a) and (b). The viewing direction for the data presented was along the <100> axis. The shift rates of the lines are non-linear, indicating a coupling between interacting states in this direction.

The stress data presented above show clear evidence of interaction effects, consistent with the temperature dependence data, which revealed the existence of a low lying excited state.

In order to narrow down the possible symmetry types consistent with the observed data, it is necessary to examine the possibilities outlined by Mohammed *et al.* (1982) and Kaplyanskii (1964). Because of the presence of interacting states, the predicted shift rates of the lines are not described by simple linear equations. A number of possibilities had to be considered. The distinctive phonon sideband structure of the 1026meV system is similar to that of both the 1014meV Cu-related defect (Nazare *et al.* 1992) and the 735meV Fe-related defect (do Carmo *et al.* 1988) and both these defects have trigonal symmetry (with one of the parameters set to zero to give two lines under <111> stress). We attempted to fit the 1026meV data to a trigonal model (setting certain of the parameters to zero to give two straight lines under <111> stress) with first A state interaction terms and then E state interaction terms. It was found that the trigonal model could not fit the experimental data

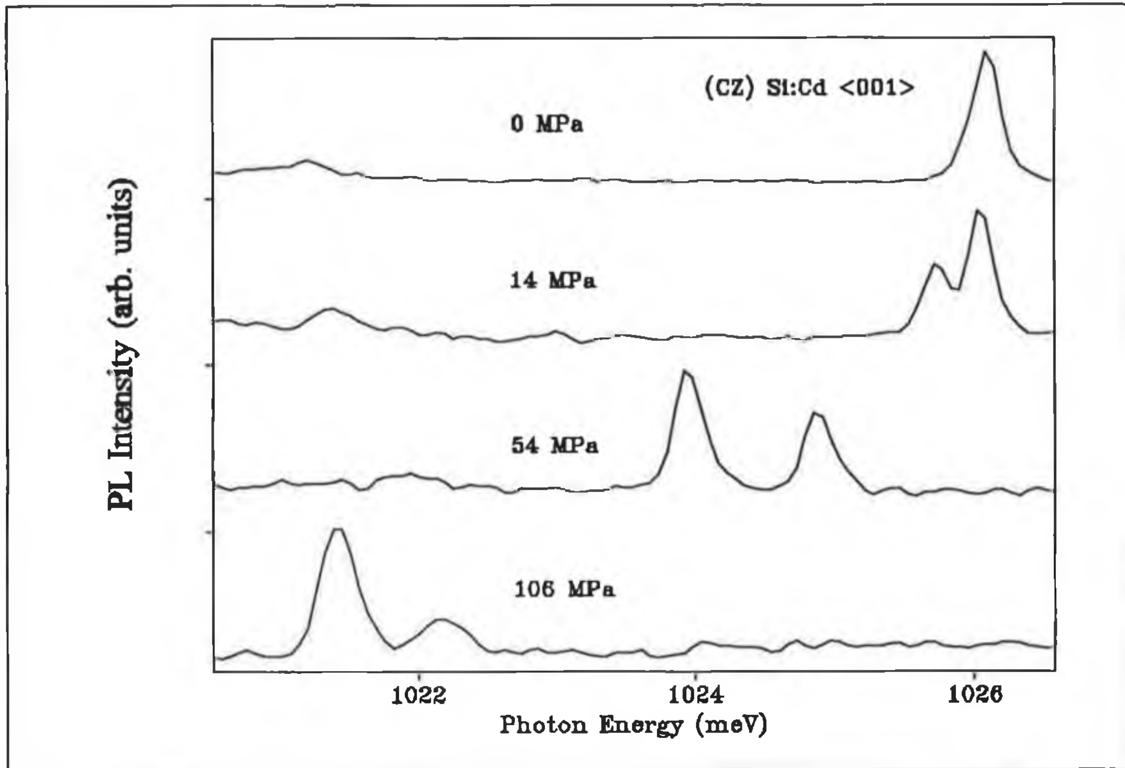

Figure 6.5.1 (a): Representative Spectra for <001> Stress

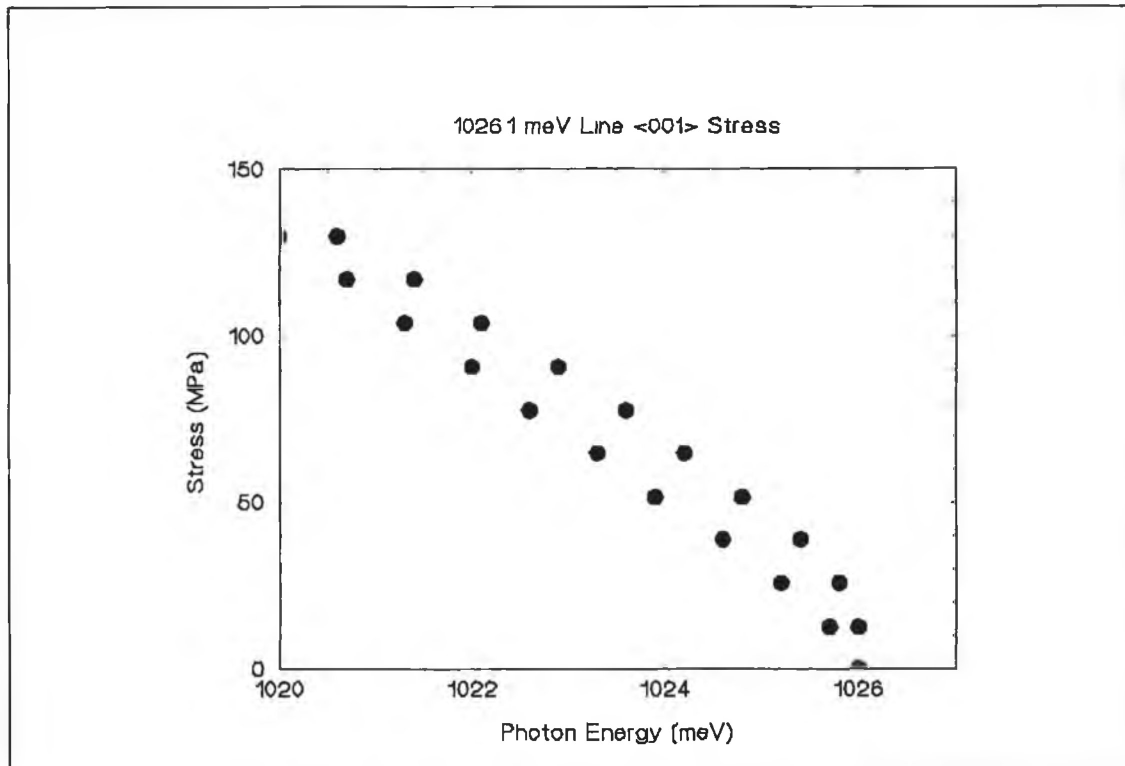

Figure 6.5.1 (b): Fan Diagram for <001> Stress

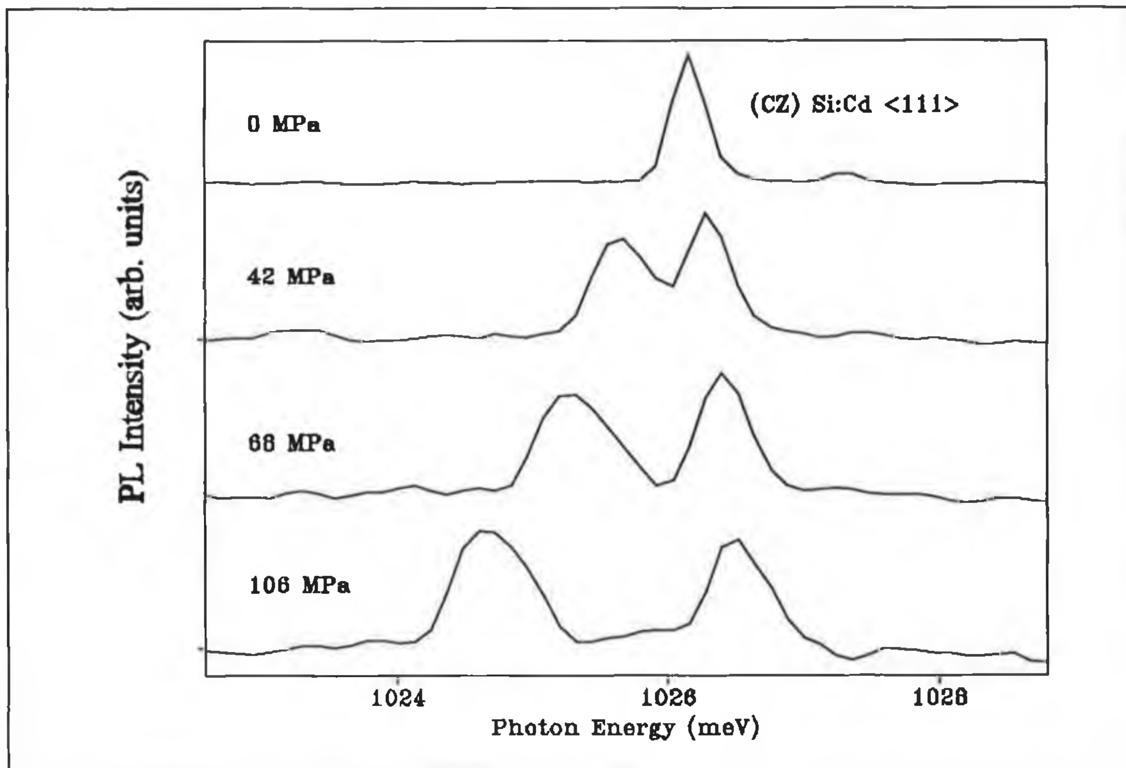

Figure 6.5.2 (a): Representative Spectra for <111> Stress

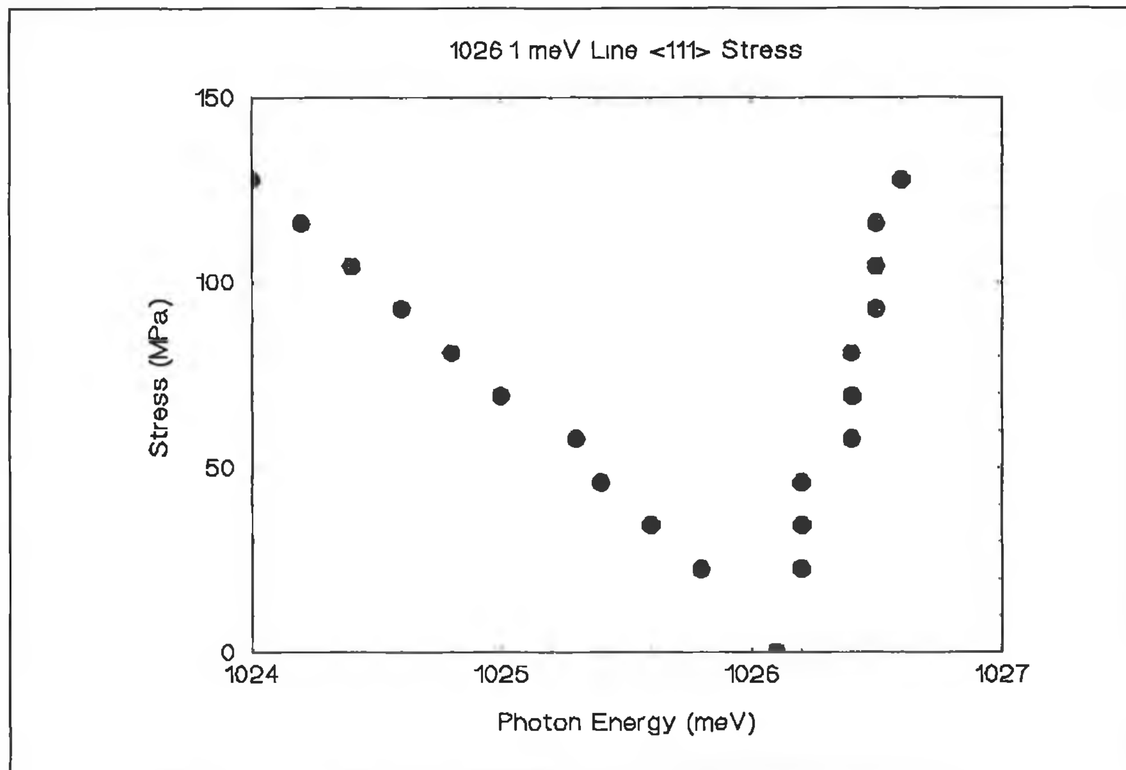

Figure 6.5.2 (b): Fan Diagram for <111> Stress

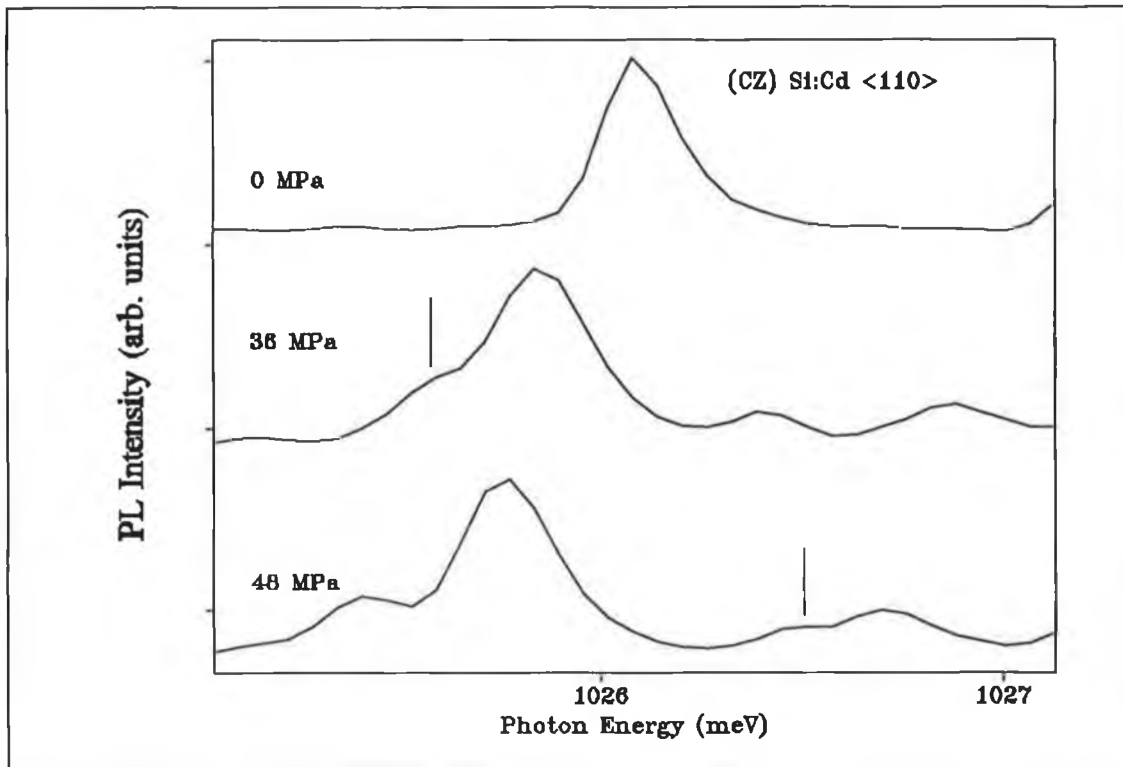

Figure 6.5.3 (a): Representative Spectra for <110> Stress

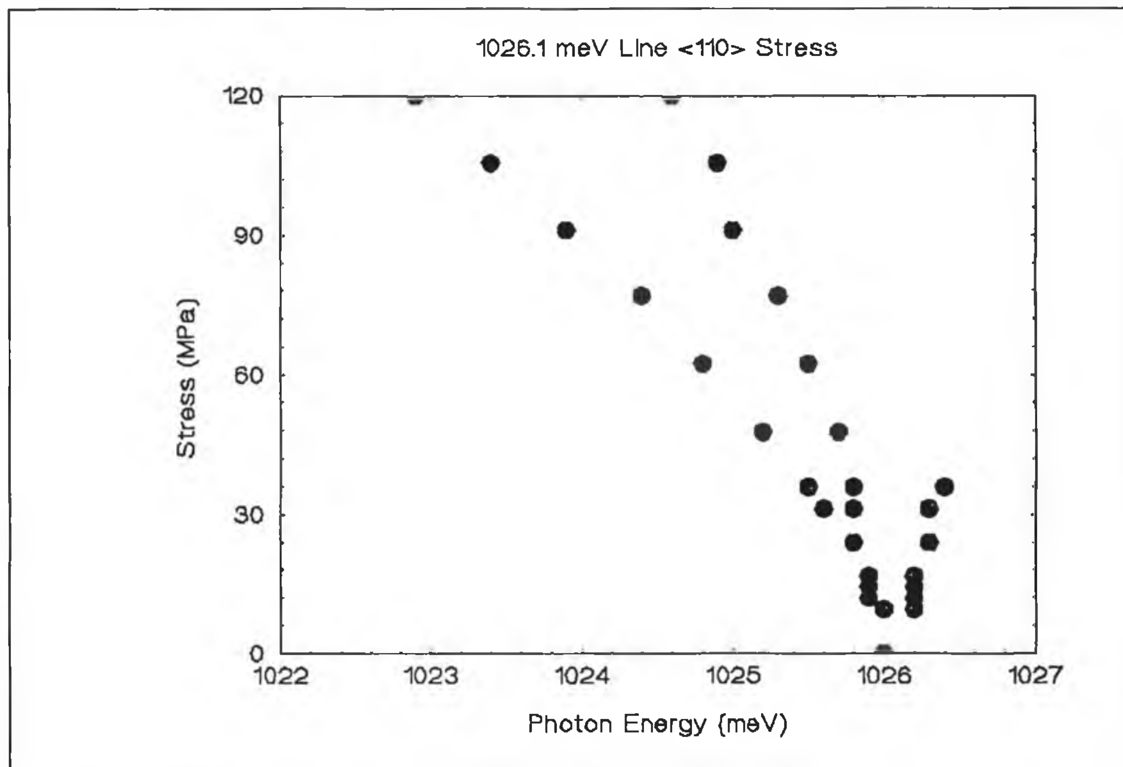

Figure 6.5.3 (b): Fan Diagram for <110> Stress

satisfactorily, and in addition the predicted intensities ratios did not match the low stress experimental values.

We then attempted to fit the data with a rhombic I model, containing interactions with an excited state. Following the approach outlined in chapter 2 to take account of interacting states, matrices of dimension > 1 such as equation 6.5.1 must be diagonalised,

$$\begin{bmatrix} \phi_{e1}|V_{stress}|\phi_{e1} & \phi_{e1}|V_{stress}|\phi_{e2} \\ \phi_{e2}|V_{stress}|\phi_{e1} & \phi_{e2}|V_{stress}|\phi_{e2} \end{bmatrix} \qquad (6.5.1)$$

where $\phi_{e1,2}$ represent the two interacting levels, and V_{stress} represents the stress induced electronic potential. The diagonal matrix elements can be written;

$$\langle\phi_{e1}|V_{stress}|\phi_{e1}\rangle = a_1 s_{XX} + a_2 s_{YY} + a_3 s_{ZZ} \qquad (6.5.2)$$

$$\langle\phi_{e2}|V_{stress}|\phi_{e2}\rangle = b_1 s_{XX} + b_2 s_{YY} + b_3 s_{ZZ} + \Delta E \qquad (6.5.3)$$

where ϕ_{e1} is assumed to be lower in energy and ΔE is the energy separation between the states. The form of the off-diagonal terms is determined by which irreducible representations $\phi_{e1,2}$ belong to. The different possibilities are listed in table 2.8.6, and it can be seen that there are 4 distinct possibilities;

$\langle\phi_{e1}|V_{stress}|\phi_{e2}\rangle = c_1 s_{XX} + c_2 s_{YY} + c_3 s_{ZZ}$

$\langle\phi_{e1}|V_{stress}|\phi_{e2}\rangle = c s_{XY}$

$\langle\phi_{e1}|V_{stress}|\phi_{e2}\rangle = c s_{XZ}$

$\langle\phi_{e1}|V_{stress}|\phi_{e2}\rangle = c s_{YZ}$

In order to narrow down which option to choose, it is necessary to examine the shift rates of the lines. As was mentioned earlier, the shift rates under <111> stress are highly linear, indicating that the matrix element coupling the states vanishes for this stress direction (for all defect orientations). By tabulating the values of the different possibilities it ought to be possible to find which matrix elements vanish for <111> stresses. Table 2.8.3 gives values for s_{XX}, s_{YY} and s_{ZZ}, none of which are zero under

<111> stress for all defect orientations. Therefore it can be concluded that the off-diagonal matrix elements are not of the form $c_1s_{XX}+c_2s_{YY}+c_3s_{ZZ}$. Table 5.5.1 shows the values of s_{XY}, s_{XZ} and s_{YZ} for all defect orientations under <111> stress.

Table 5.5.1

Centre	X	Y	Z	Stress ∥ <111>		
				s_{XY}	s_{XZ}	s_{YZ}
1	110	$\bar{1}10$	001	0	$\sqrt{2/3}$	0
2	$\bar{1}10$	110	$00\bar{1}$	0	0	$-\sqrt{2/3}$
3	011	$0\bar{1}1$	100	0	$\sqrt{2/3}$	0
4	$01\bar{1}$	$0\bar{1}\bar{1}$	$\bar{1}00$	0	0	$\sqrt{2/3}$
5	101	$10\bar{1}$	010	0	$\sqrt{2/3}$	0
6	$\bar{1}01$	$\bar{1}0\bar{1}$	$0\bar{1}0$	0	0	$\sqrt{2/3}$

It can be seen from this table that the only element s_{ij} which is zero for all defect orientations under <111> stress is s_{XY}. This information allows us to write the off-diagonal matrix elements as cs_{XY}. Using table 2.8.6, it can be seen that $\phi_{e1,2}$ transform as either $A_{1,2}$ or $B_{1,2}$.

The complete matrix is then;

$$\begin{bmatrix} a_1 s_{XX}+a_2 s_{YY}+a_3 s_{ZZ} & cs_{XY} \\ cs_{XY} & b_1 s_{XX}+b_2 s_{YY}+b_3 s_{ZZ}+\Delta E \end{bmatrix} \qquad (6.5.4)$$

The parameter ΔE can be obtained from the experimentally determined value 1.1meV. We are then left with 7 adjustable parameters, $a_{1,2,3}$, $b_{1,2,3}$ and c. By diagonalising the matrix as a function of stress, and allowing these parameters to vary, a best fit to the data can be found. This procedure was carried out using a purpose-written P.C. package TRANID (McCarren 1994).

The best fit lines are shown in figure 6.5.4 superimposed on the data. The quality of the fit is reasonably good in all directions, although the fit in the <110> stress direction is poorer than in <001> and <111>. The fit parameters include

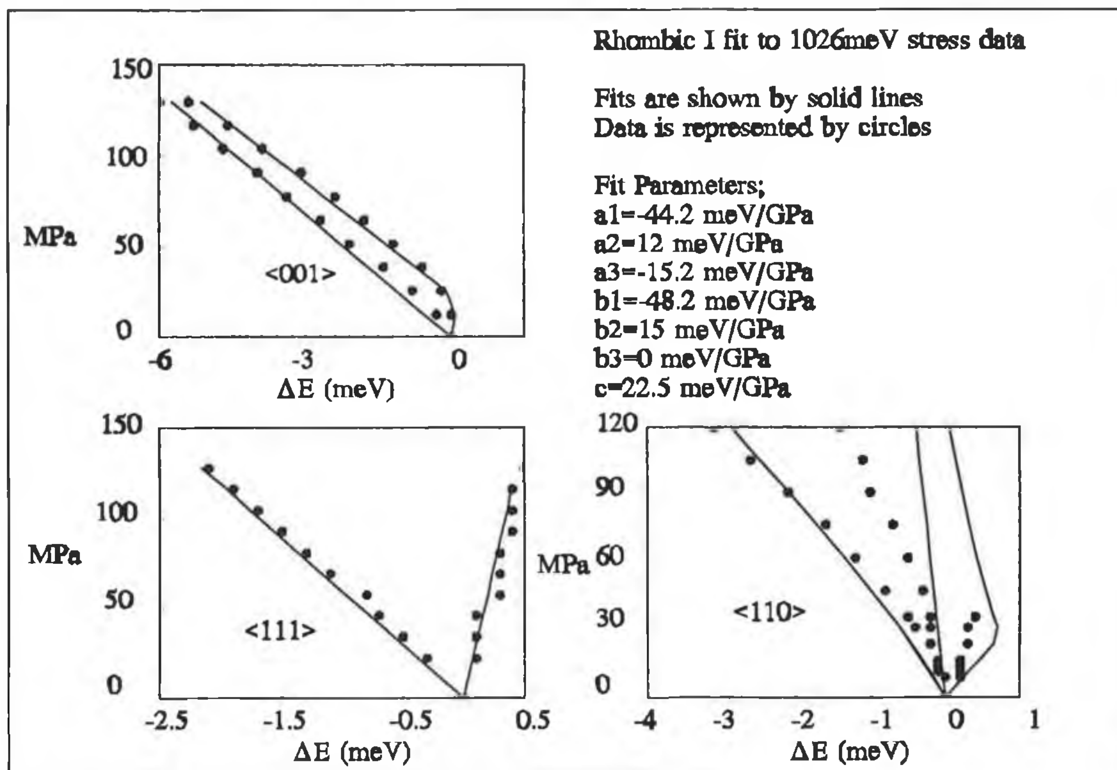

Figure 6.5.4: Rhombic I fit to Experimental Data Set

predicted values for the stress parameters of the 1027.2meV line. Future experiments are needed to compare the observed and predicted behaviour of this line under stress. Only when we have a clear picture of the behaviour of this excited state as a function of stress can we identify the symmetry of the defect unambiguously. PLE experiments on the defect excited states as a function of stress would also help in identifying the symmetry of the defect.

The parameters for the fit are;

a_1 = -44.2meV/GPa

a_2 = 12meV/GPa

a_3 = -15.2meV/GPa

b_1 = -48.2meV/GPa

b_2 = 15meV/GPa

b_3 = 0

c = 22.5meV/GPa

In order to determine the transition type (A-B or B-B, A-A) it is necessary to examine the intensity ratios of the stress-split components. Two different effects will in general cause the intensity ratios of the components to change as a function of stress. The first effect is due to mixing of states by the interaction. In diagonalising the matrix (equation 6.5.4), the correct zero-order eigenfunctions become linear combinations (whose coefficients change as a function of stress) of the unperturbed eigenfunctions. The second effect is due to thermalisation between the states (which will be a small effect at temperatures ~ 5K; kT ~ 0.4meV $<$ line separation of 1.1meV). By measuring the intensity ratios at low stresses where the level mixing and thermalisation effects will be relatively small it is possible to identify the transition type. It can be seen from the data below that the line ratios at low stress are in reasonably good agreement with the predicted values for an A-B transition at a rhombic I centre (Mohammed *et al.* 1982).

<100>

	ratio	predicted ratio
15 MPa	~1 : 2	1 : 3
54 MPa	~3 : 2	1 : 3
80 MPa	~3 : 1	1 : 3

<111>

	ratio	predicted ratio
42 MPa	~0.9 : 1	0.6 : 1
68 MPa	~0.8 : 1	0.6 : 1
106 MPa	~1 : 1	0.6 : 1

<110>

	ratio	predicted ratio
36 MPa	1.6 : 4 : 1	1 : 4 : 1
47 MPa	1.2 : 4 : 0.6	1 : 4 : 1

In spite of the absence of polarisation data, it is possible to assign this transition as a rhombic I with reasonable confidence based on the quality of the theoretical fits to the data. Using the relative intensities at low stress as a guide, the transition type can be identified as A to B. There is clear experimental evidence of the excited state of the defect interacting with another higher-lying state, and based on an analysis of the shift rates in various directions it can be concluded that the two interacting states are either A_1 and A_2 or B_1 and B_2. If the ground state of the transition is assumed to be of A_1 symmetry, then the two interacting excited states will transform as B_1 or B_2.

(ii) Zeeman Spectroscopy

Among the defects discussed in this thesis, the 1026meV defect is the only one with two adjacent excited states. The possibility that these excited states constitute a singlet-triplet pair must be considered. However the transition probabilities of the two lines are quite similar (ratio ~0.66, see section 6.4), whereas the ratio for singlet-triplet centres in silicon is found to be at most 0.2 (Davies 1984) and generally considerably less than this value. In addition our Zeeman measurements on the 1026meV line show neither a line shift nor splitting for magnetic fields of up to 5T along the <001> direction. Accordingly, we interpret the 1026meV line as a transition between spin 1/2 electron and hole states. The Zeeman data, combined with the uniaxial stress data and temperature dependence data point strongly towards the "pseudo-donor" model (discussed in detail in chapter 2) for the 1026meV centre. No Zeeman experiments have yet been performed on the 1027.2meV excited state transition.

6.6: Chemical Identity of 1026meV System

Having examined the behaviour of the 1026meV system using temperature dependence, uniaxial stress and Zeeman techniques in order to obtain information on the electronic structure and site symmetry of the defect, in this section we examine the chemical constituents of the defect.

We have already discussed (at the beginning of section 4.6) the various possible processes at work in ion-implanted material and the difficulty in identifying the chemical constituents of luminescence centres. Various isotope substitution experiments were performed on Cd-implanted CZ silicon samples which showed 1026meV luminescence. In order to determine the chemical identity of the defect, a number of possible constituents had to be considered. The experiments performed on the 1026meV system are identical to those performed on the Cd_A system and similar results are observed for both defect types, indicating that the chemical constituents of both defects are the same. We now give a brief summary of these experiments.

Cadmium: Cd was considered the most likely constituent of the defect. A great deal of circumstantial evidence pointed towards this conclusion. The defect production was not affected by changes in the ion-implantation energy, from 80keV to 200keV. Secondly, the defect was not formed in CZ silicon implanted with indium ions with almost identical mass ($mass_{In}$=115 amu, $mass_{Cd}$=116 amu). Finally, the defect luminescence was found to originate from the surface implanted layer (as discussed later in the chapter). The arguments outlined above are identical to those put forward in section 4.6 for the Cd_A defect.

Samples were implanted with ^{106}Cd (1e13cm^{-2}), ^{116}Cd (1e13cm^{-2}) and a dual implanted sample. The ZPL spectra of these samples are shown below in figure 6.6.1. The 1026.1meV line experiences a positive isotope shift of 0.1meV, and the excited state 1027.2meV line also experiences a positive isotope shift of 0.1meV when the isotopic mass is varied from 106 amu to 116 amu. Just as for the Cd_A defect, it was not possible to resolve the two lines in the dual-implant sample, but a significant line broadening was observed and a good fit to the line shape was found by adding the ^{106}Cd line to the ^{116}Cd line in the ratio 1 : 0.6, which is in good agreement with the value obtained for the Cd_A defect. A noticeable splitting was seen in the phonon sideband of the ZPL (discussed in section 6.7) which allowed an accurate measurement of the ratios of the 106 line to the 116 line. The suspected reasons for this uneven isotope distribution are discussed in section 4.6. Based on the evidence of this isotope experiment it is possible to confirm that only one Cd atom is involved in the defect.

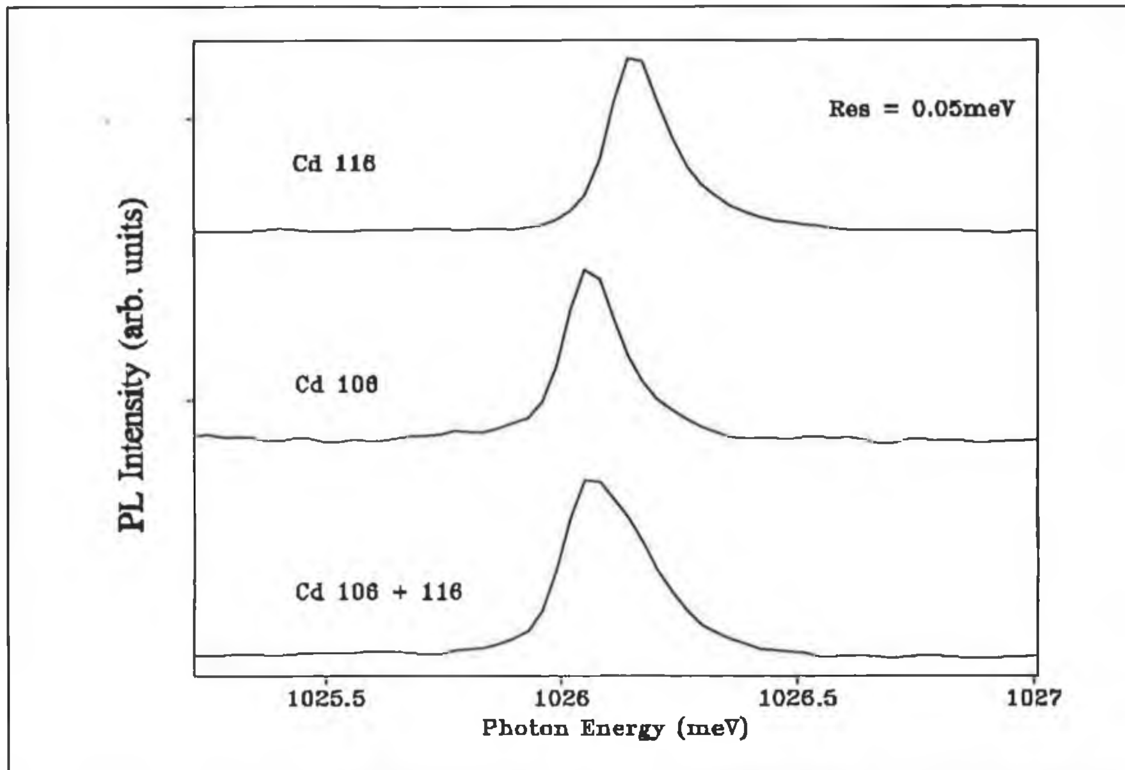

Figure 6.6.1: ZPL Spectra of 1026.1meV Line for Different Cadmium Isotopes

Oxygen: There is considerable circumstantial evidence that O is involved in this defect centre. The defect was seen only in CZ material which has a high O content (~ 10^{18} atoms/cm^3). Figure 6.6.2 shows comparative spectra of Cd-implanted CZ and FZ material subjected to the same heat treatment. A number of weak broad features of unknown origin are observed in the spectrum of the FZ material, but no evidence is seen of the 1026meV ZPL or sideband structure. Attempts at O isotope implantation have proved unsuccessful (as discussed in section 4.6) and currently O isotope diffused samples are being prepared in an attempt to unambiguously identify O as a constituent of this defect.

Damage Products: Because of the nature of the implantation process and the damage it introduces into the crystal, it is necessary to consider the involvement of damage products in the defect centre. The defect formation appears insensitive to the implantation energy as was mentioned previously, and as yet there is very little other

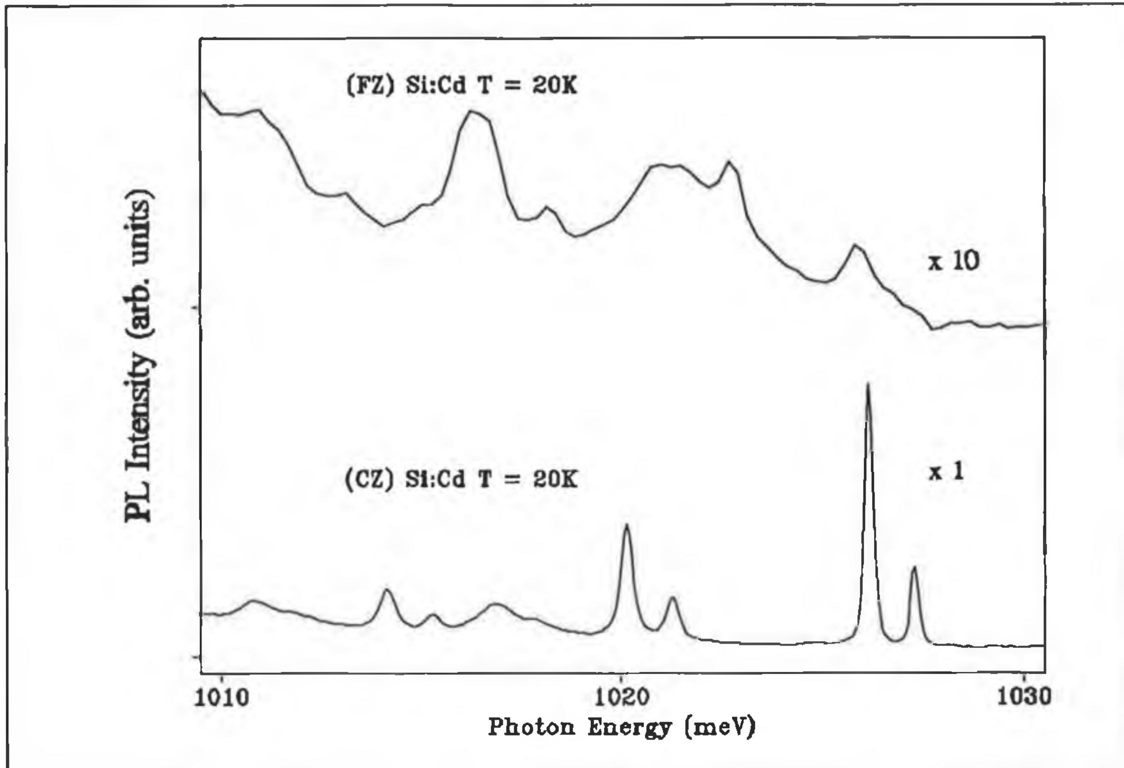

Figure 6.6.2: Comparative Spectra of FZ and CZ Cadmium-Implanted Silicon

evidence either for or against the presence of damage products in this defect complex. Comparative spectra of samples produced by Cd implantation at 200keV and 80keV are shown in figure 6.6.3. The spectrum of the sample implanted at 200keV was recorded at higher resolution ($1cm^{-1}$ 200keV:$2cm^{-1}$ 80keV) and the SNR is poorer.

Because of the low diffusion coefficient of Cd at the anneal temperatures ($D=10^{-24}cm^2/s$, Arifov *et al.* 1984) the implanted Cd moves very little from the damage region during the anneal. Computer simulation of the implantation process (described in section 4.6) reveals that Cd implantation at 200keV into silicon produces an implanted layer ~0.09μm from the surface with a width of ~0.002μm. Etching away the damaged layer therefore simultaneously etched away the implanted layer. Figure 6.6.4 shows the effect of different etch depths on the 1026meV system. The luminescence is seen to be almost gone after an etch depth of ~1μm, in good agreement with the results expected from the computer simulation of the implantation process. This experiment does not provide any definite evidence for or against the

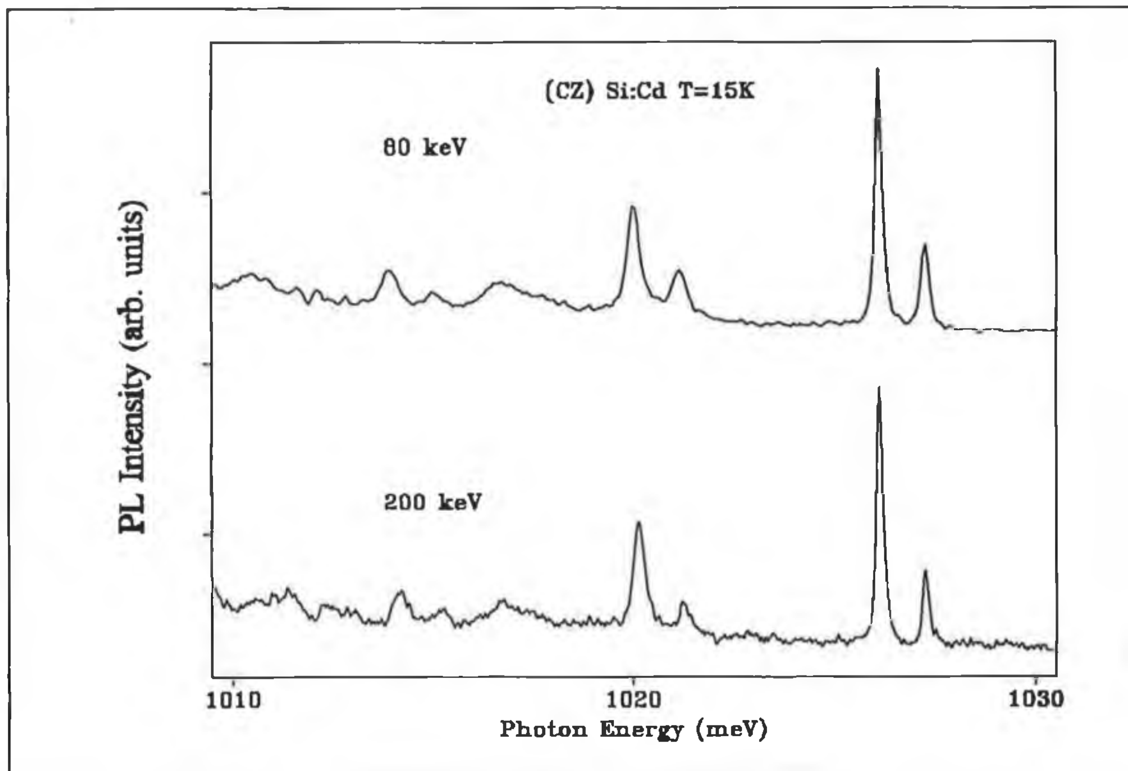

Figure 6.6.3: Comparative Spectra of CZ Silicon Implanted with Cadmium at 80keV and 200keV

involvement of damage products in the defect complex.

Hydrogen: Recent experiments have revealed the presence of H in a number of defects in silicon (Lightowlers *et al.* 1994, Safanov *et al.* 1994), and it appears that H is easily introduced into silicon both intentionally and unintentionally. Cd-H complexes have previously been observed in silicon using the method of PAC (Gebhard *et al.* 1991, Wichert *et al.* 1987). In order to examine the influence of H on the 1026meV system, deuterium was introduced into Cd-implanted samples using the method described in section 4.6. No increase in signal level or line splitting was observed for the 1026meV line or sidebands. Although this negative isotope experiment does not preclude the involvement of H in the defect, it is considered a less likely candidate than O.

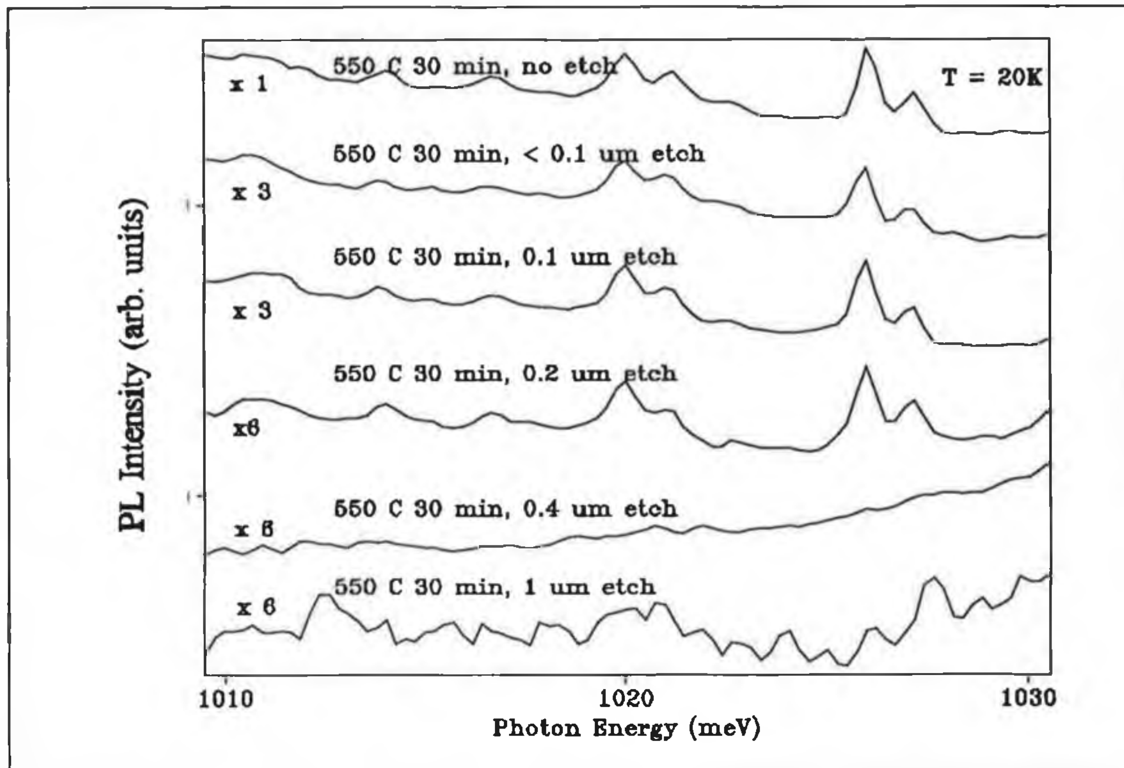

Figure 6.6.4: Effect of Etching on 1026meV Luminescence

Carbon: C is the second most common contaminant in CZ silicon. C interstitials (which are products of radiation damage) are known to be highly mobile at 550°C (Davies *et al.* 1987). For this reason it was decided to examine the behaviour of the 1026meV centre in C-rich and C-lean material. In addition, samples of CZ silicon diffused with C^{12}/C^{13} isotopes were implanted with Cd. The defect formation appears insensitive to the presence or absence of C in the sample, and no line broadening or splitting was observed in the sample diffused with C^{12}/C^{13} isotopes in either the ZPL or phonon sidebands. For this reason, C is considered an unlikely constituent of the defect.

Donor/Acceptor: The role of the residual impurities (such as boron in p-type and phosphorous in n-type) in silicon in the formation of the defect must be considered. In order to examine the effect of different dopants on the 1026meV centre, Cd was implanted into both p-type and n-type material and comparative spectra are shown in figure 6.6.5. The spectrum of the p-type material was recorded at higher resolution

($1cm^{-1}$ p-type:$2cm^{-1}$ n-type). The 1026meV system is produced in both n-type and p-type material, with roughly the same ratio to the Cd_A line in both cases. It is concluded that the dopant in the starting material is an unlikely constituent in the formation of the 1026meV defect centre.

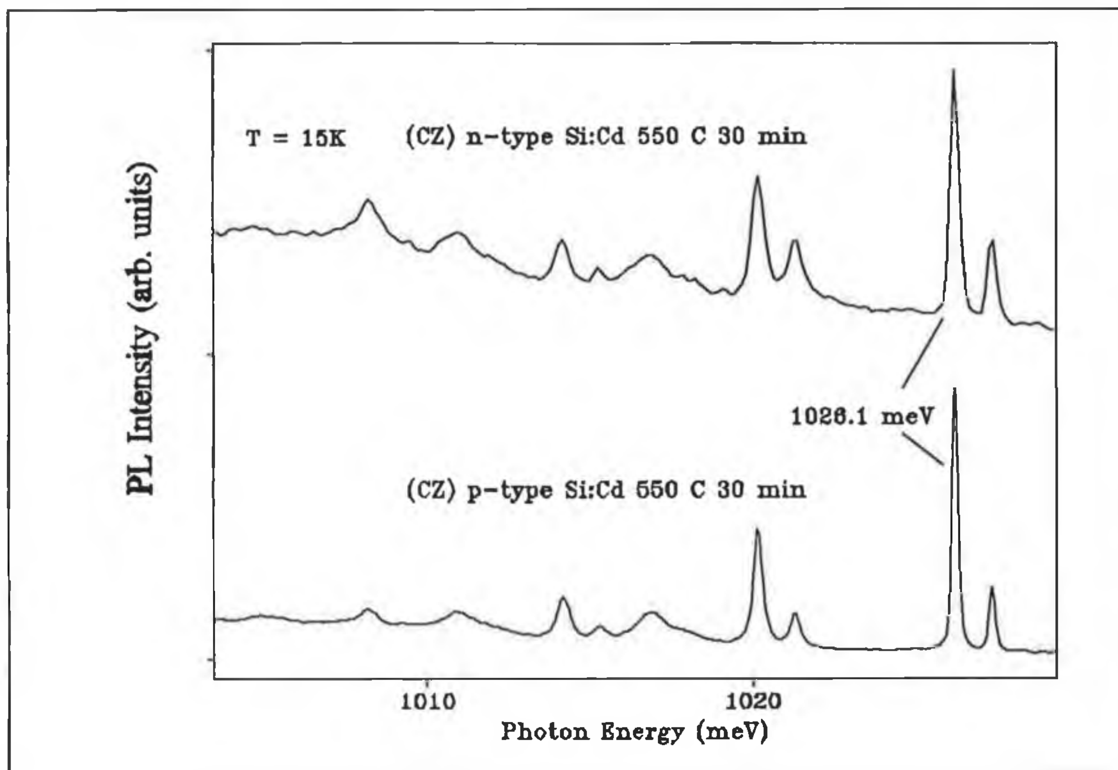

Figure 6.6.5: Comparative Spectra of 1026meV System in n-type & p-type Si:Cd

The evidence presented above indicates that the 1026meV luminescence is due to exciton recombination at a defect site with one Cd and one (or more) O atoms. The evidence from isotope substitution experiments indicates that the chemical constituents of the 1026meV defect and the Cd_A defect are very similar. In order to eliminate the role of damage products in this defect or in its production it will be necessary to introduce Cd into silicon by diffusion. Although the role of other elements cannot be ruled out, the identification of this defect as a Cd-O complex appears to be the most probable explanation.

6.7: Vibrational Sideband Structure

As we have seen in section 6.3, the 1026.1meV and 1027.2meV lines are accompanied by a phonon sideband which shows two characteristic local mode phonons of energies ~6meV and ~9.2meV. There is a considerable amount of detail in the multi-phonon sideband. Referring to figure 6.3.1, the feature labelled 1 is associated with a local mode of energy ~6meV, and the feature labelled 2 is associated with a local mode of energy ~9.2meV. The local mode energies are quite small as would be expected for the vibrations of a heavy atom like Cd. Examining the spectrum at higher temperatures, anti-Stokes phonon modes can be observed at energies higher than the ZPL. The anti-Stokes phonon energies for the 1026.1meV and 1027.2meV transitions are respectively ~4.7meV and 4.8meV. This result indicates that the vibrational potential energy curves of the excited states (although similar to each other) are quite different to the vibrational energy curve of the ground state (in contrast to the simplifying assumptions made in section 2.6 chapter 2). If the defect were to be examined in absorption, a marked asymmetry ought to be observed between the absorption and emission sideband spectra (discussed in Henderson and Imbusch 1989). The local modes 1 and 2 were investigated using ^{106}Cd and ^{116}Cd. Table 6.7.1 shows the local mode energies for isotope masses 106 and 116.

Table 6.7.1

Mode	^{106}Cd Energy (meV)	^{116}Cd Energy (meV)	Ratio
1	6.29	5.98	0.95
2	9.56	9.28	0.97

The ratios in table 6.7.1 are in good agreement with the expected factor of 0.956, indicating that the local modes are based predominantly on the vibrations of a Cd atom with respect to an otherwise static lattice. Figure 6.7.1 shows the 6meV and 9meV local modes for Cd masses of 106 amu and 116 amu. The peak labelling corresponds to that used in figure 6.3.1.

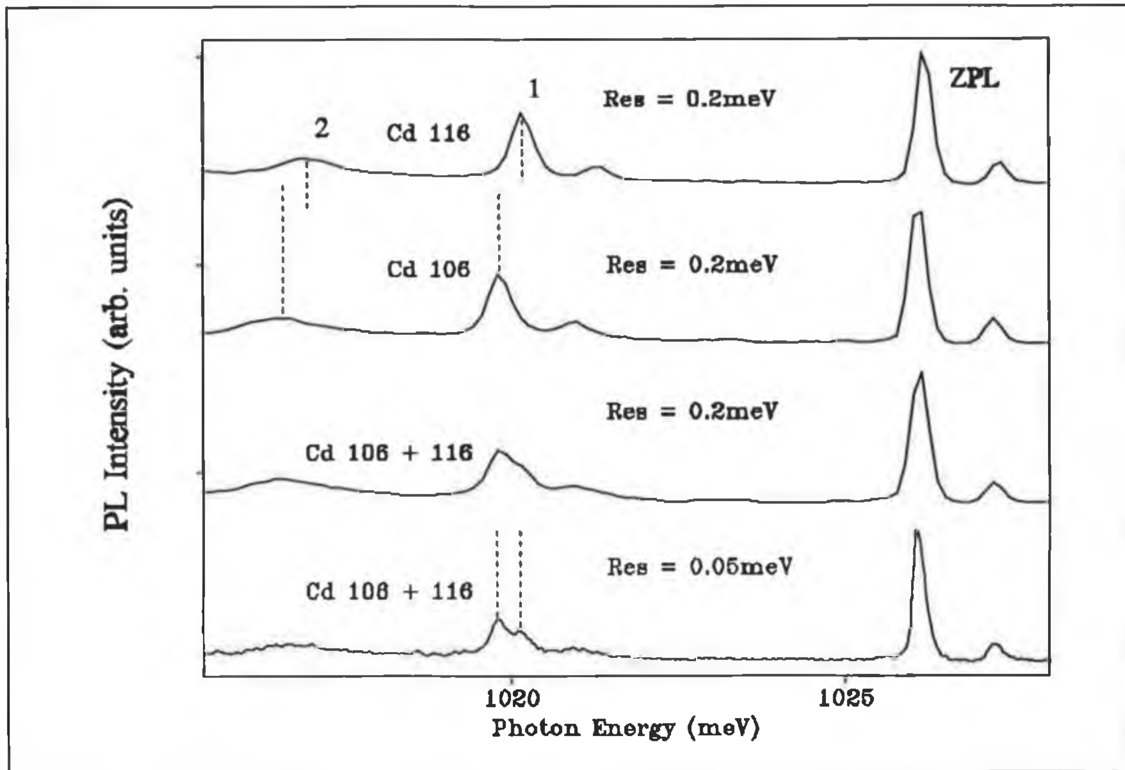

Figure 6.7.1: Local Mode Positions for Different Isotope Masses

The Huang-Rhys factor for the defect can be calculated using equations 2.6.7 and 2.6.9. Ratioing the intensity of line 1 to the ZPL (equation 2.6.7) gives S_1 (Huang-Rhys factor for mode 1, 6meV) as 0.63. The Huang-Rhys factor for mode 2 (9meV mode) is given by the ratio of line 2 to the ZPL, 0.42.

These values which are accurate to ~10%, can be checked using equation 2.6.9, which relates the total intensity to the ZPL intensity. The values for S_1 and S_2 using equation 2.6.9 are 0.7 and 0.45 respectively in agreement with those calculated by equation 2.6.7 to within a factor of ~10%.

We now use the procedure outlined in chapter 2 to reconstruct the 1st and 2nd phonon sidebands. The results of this reconstruction are shown in figure 6.7.2, along with the experimentally observed values. The theoretically predicted values compare well with the experimental values for the 1st and 2nd sidebands.

Calculating a value for the total Huang-Rhys factor S_T using equation 2.6.9 (with the total sideband integrated intensity) yields a value of 1.05, in agreement with

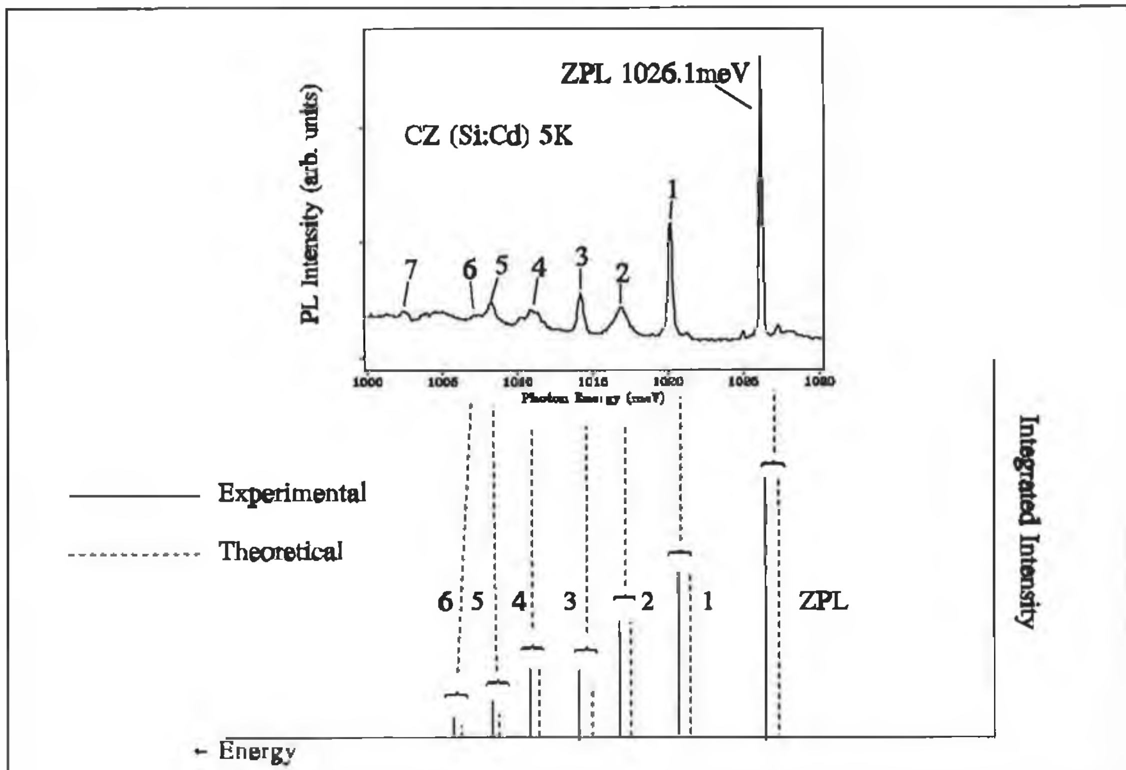

Figure 6.7.2: Comparison of Theoretical and Experimental Phonon Sideband Intensities

the expected value (S_1+S_2) of 1.05. Using equation 4.7.2 (with S=1.05 and an average phonon energy of 7.2meV) to calculate the expected shift in equilibrium position of the defect after recombination (Davies 1989) gives Q_0~0.01nm, approximately 4% of the bond length in silicon.

A similar procedure applied to the excited state transition at 1027.2meV yields values of S_1=0.61 and S_2=0.59, close to those found for the 1026meV line and indicating that the electron-lattice coupling for both excited states is very similar.

As mentioned above, we have measured the energy of the anti-Stokes phonon for the 1026.1meV transition at ~4.7meV, and have commented on the difference between this value and that of the Stokes phonons. Using the theory of section 2.10 with suitable approximations, we can relate this difference to the observed isotope shift in the ZPL (section 6.6). In order to calculate the change in ZPL for the case of a defect coupled to more than one vibrational mode, it is necessary to use equation 2.10.6, summing over all defect modes, knowing the Stokes and anti-Stokes phonon

energies for each mode. We can only observe a single anti-Stokes phonon, and because of the similarity in spectral width between this feature and the 6meV Stokes phonon we associate these two features with one other. The difference in energy between the two phonons is 1.3meV and we assume the same fractional energy difference between the 9.2meV Stokes phonon and its (unseen) anti-Stokes counterpart (2meV). Using these values for the phonon energies in equation 2.10.6, with m=106 amu and $m+\Delta m=116$ amu and summing over the two observed modes in the sideband, the expected shift in the ZPL is calculated to be ~0.073meV, in reasonably good agreement with the observed shift of 0.1meV. The situation for the 1027.2meV transition is very similar to that for the 1026.1meV transition, with an anti-Stokes phonon of energy 4.8meV. Thus the expected ZPL isotope shifts for the two lines are virtually identical, in agreement with the experimentally observed result.

Attempts to relate the uniaxial stress parameters to the Huang-Rhys factor as done in chapter 4 have given unreasonable results and we feel that because of this some questions still remain regarding the quality of the stress fit. For this reason also data on the 1027.2meV line will be extremely useful in interpreting the overall picture.

6.8: Conclusions

In this chapter comprehensive results have been presented on a minor Cd-related defect observed in CZ silicon annealed at 550°C for 30 minutes. The defect shows two ZPL at 1026.1 (±0.05)meV and 1027.2 (±0.05)meV. Analysis of the phonon sideband reveals that the defect couples strongly to two local mode vibrations of energies ~6meV and 9meV, with Huang-Rhys factors of ~0.6 and 0.4 respectively for the 1026.1meV line. Similar coupling is observed for the 1027.2meV line.

Temperature dependence measurements have revealed that the 1026.1meV line and 1027.2meV line are transitions from a pair of thermalising excited states to a common ground state. These measurements also show that the defect consists of one loosely bound particle (with a binding energy of ~16meV) and one tightly bound particle. Uniaxial stress measurements indicate that the 1026.1meV transition is an A-B transition at a rhombic I defect. Zeeman measurements show no shift or splitting

References

A. A. Arifov and D. Rakhimbaev (1984). Sov. Phys. J., **27** no. 11, 967.

G. Davies (1989). Physics Reports, **176** nos. 3 & 4, 85.

G. Davies, E. C. Lightowlers, R. C. Newman and A. S. Oates (1987). Semicond. Sci. and Technol. **2**, 524.

G. Davies (1984). J. Phys. C: Solid State Phys. **17**, 6331.

M. Gebhard, B. Vogt and W. Witthuhn (1991). Phys. Rev. Lett., **67** no. **7**, 847.

M. A. Gulamova, I. Z. Karimova and P. I. Knigin (1971). Sov. Phys. Semiconductors, **5**, 687.

B. Henderson and G. F. Imbusch (1989). "Optical Spectroscopy of Inorganic Solids", Clarendon Press, Oxford.

A. A. Kaplyanskii (1964). Opt. Spectroscopy, **16**, 329.

E. C. Lightowlers, R. C. Newman and J. H. Tucker (1994). Semicond. Sci. Technol., **9**, 1370.

A. L. McCarren, H. J. Ruskin, K. G. McGuigan and M. O. Henry (1994). IEE Proc. Sci. Meas. Technol., **141**, 185.

K. Mohammed, G. Davies and A. T. Collins (1982). J. Phys. C: Solid State Physics **15**, 2779.

A. N. Safanov and E. C. Lightowlers (1994). Mat. Sci. Forum., **143-147**, 903.

S. P. Watkins, U. O. Ziemelis, M. L. W. Thewalt and R. R. Parsons (1982). Solid State Commun. 43, 687.

Th. Wichert, H. Skudlik, M. Deicher, G. Grubel, R. Keller, E. Recknagel and L. Song (1987). Phys. Rev. Lett., 59 no. 18, 2087.

Chapter 7: 922meV Aluminium-Related Line

7.1: Introduction

In this chapter, a description and analysis is given of an Al-related defect, found in Al-doped, C-rich CZ silicon reported by Drakeford *et al.* (1988) with a ZPL at 922.29meV, referred to in the text as the 922meV defect. Preliminary data on this line have been published by Drakeford *et al.* (1988), including the form of the phonon sideband, and the defect production conditions. No data were published on the behaviour of the defect as a function of temperature, stress and magnetic fields and it is with these aspects that we are concerned here. Measurements as a function of temperature reveal that the thermal binding energy is ~15meV, and no evidence of excited states is seen. Uniaxial stress and Zeeman measurements point towards a pseudo-donor model for the defect. In the model of the 922meV line proposed by Drakeford *et al.* (1988), the 922meV line is associated with a transition at an Al-C centre. Attempts at Al diffusion and C isotope implantation performed by the same authors have yielded negative results, but nevertheless they assigned the defect to an Al-C complex on the basis of the high levels of Al and C in the starting material. These negative results were attributed to the fact that the conditions necessary to form the defect are not present close to the surface. Although we have not investigated the chemical nature of the defect, we show that strong similarities exist between this and another Al-related defect (ZPL at 886meV, Irion *et al.* 1988) under uniaxial stress.

7.2: Sample Preparation and Defect Production

The production mechanism for the 922meV Al-related defect is described in detail by Drakeford *et al.* (1988). The defect can be produced by annealing Al-doped CZ C-rich silicon for long periods (~400 hrs) at 450°C, or alternatively by annealing at 550°C for ~20 hrs, in an atmosphere of flowing argon gas and allowing the sample to cool slowly. The benefit of annealing for longer times at lower temperatures is that

the 922meV luminescence becomes dominant in the spectrum over other features such as the Al bound exciton luminescence. However, from the point of view of convenience, the use of shorter anneals at higher temperatures was found to be preferable for preliminary survey work. Samples used for temperature dependence, uniaxial stress and Zeeman measurements were annealed at 450°C for 400 hrs in order to improve the signal from the 922meV line.

7.3: Spectral Features

A low temperature PL spectrum of Al-doped C-rich CZ silicon is shown in figure 7.3.1.

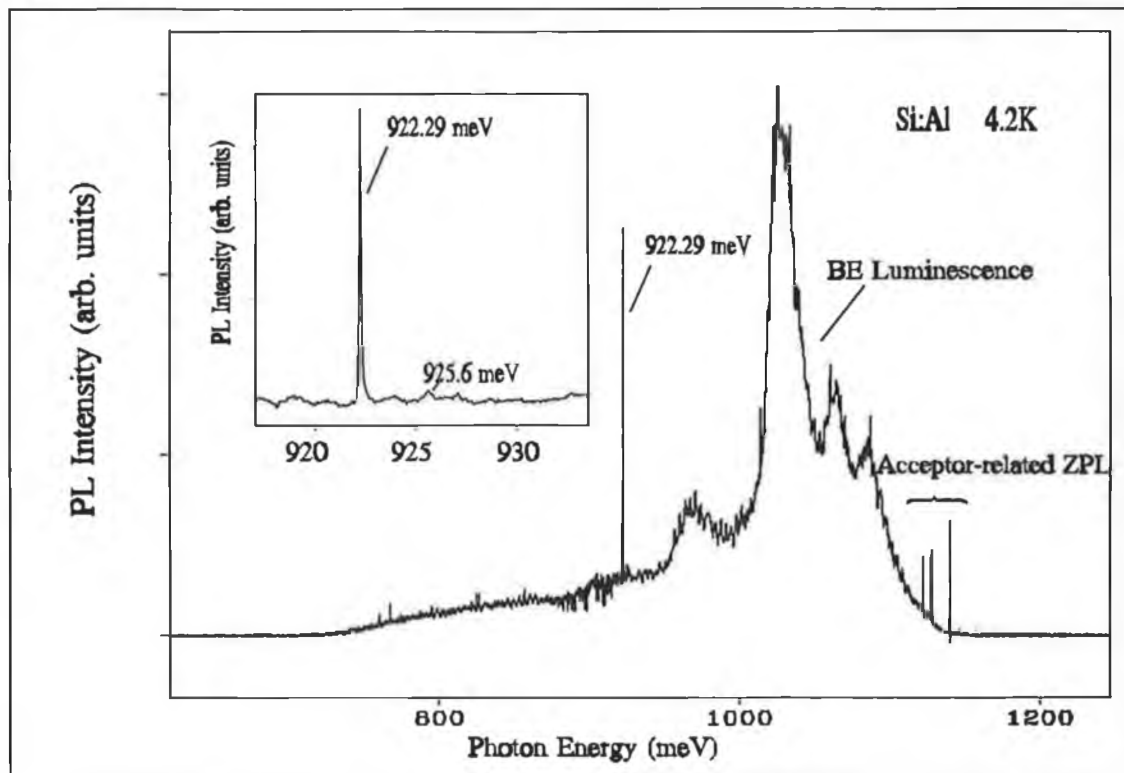

Figure 7.3.1: Low Temperature Spectrum of 922meV Al-Related Luminescence

The ZPL is located at 922.29 (±0.05) meV. This is very close to the water vapour absorption band at ~919meV and thus the phonon sideband of the defect overlaps the

water vapour band, and our studies concentrated on the behaviour of the ZPL as a function of temperature, stress and magnetic field. A spectrum of the phonon sideband can be found in the paper by Drakeford *et al.* (1988). The feature labelled 925.6meV is discussed in section 7.4. The authors attribute the broad features at higher energies to BE luminescence broadened by intercentre interactions. A number of lines in the region 1100meV-1150meV are attributed to luminescence from acceptor-related defects.

7.4: Temperature Dependence of 922meV System

Figure 7.4.1 shows the region of the 922meV ZPL for temperatures in the range 5K to 50K.

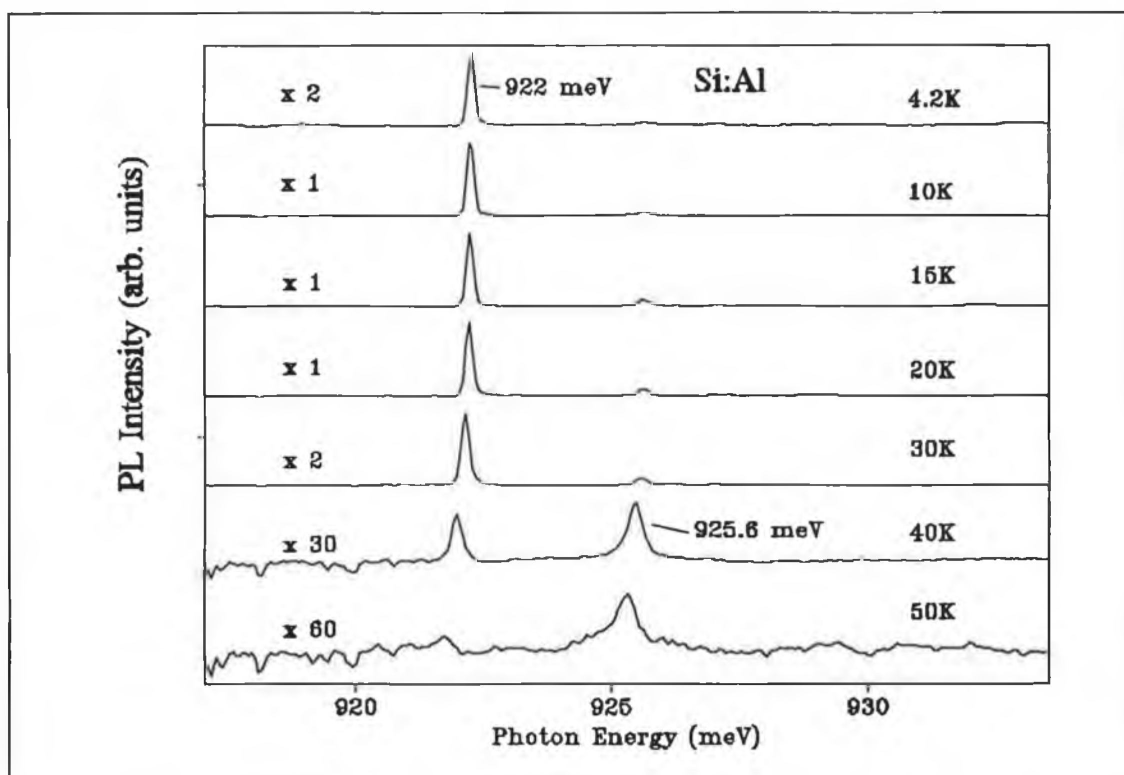

Figure 7.4.1: Temperature Dependence of 922meV Al-Related Luminescence

The intensity of the ZPL first increases, reaching a maximum at ~15K and

subsequently decreases until it is completely gone at temperatures > 50K. In order to find the thermal binding energy of the defect complex the experimental data are fitted to equation 2.7.8 and plotted in figure 7.4.2 along with the best fit line from this equation. The calculated value of the thermal binding energy is 15.8(±2)meV.

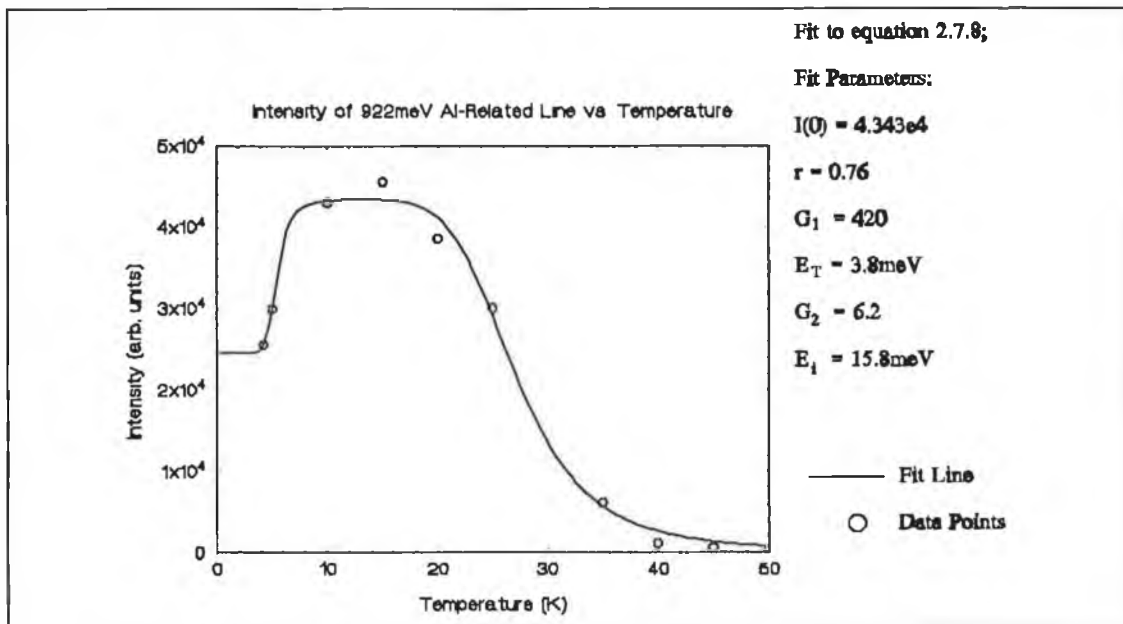

Figure 7.4.2: Plot of Intensity vs. Temperature for 922meV Line

Another interesting feature of the spectrum is the growth of a line at ~925.6meV. The temperature dependence of this line is plotted in figure 7.4.3, along with the 922meV line intensity. The insert in figure 7.4.3 shows an Arrhenius plot of the log ratio of the two lines. No thermalisation behaviour is observed, leading us to believe that the two lines arise from different centres. This is corroborated by the absence of any interaction effects in the uniaxial stress data. A C-related defect with ZPL at 925.5meV has been observed in C-rich CZ silicon annealed at 450°C (Davies *et al.* 1984 b, Magnea *et al.* 1984), and we believe that this is the line we observe at 925.6meV.

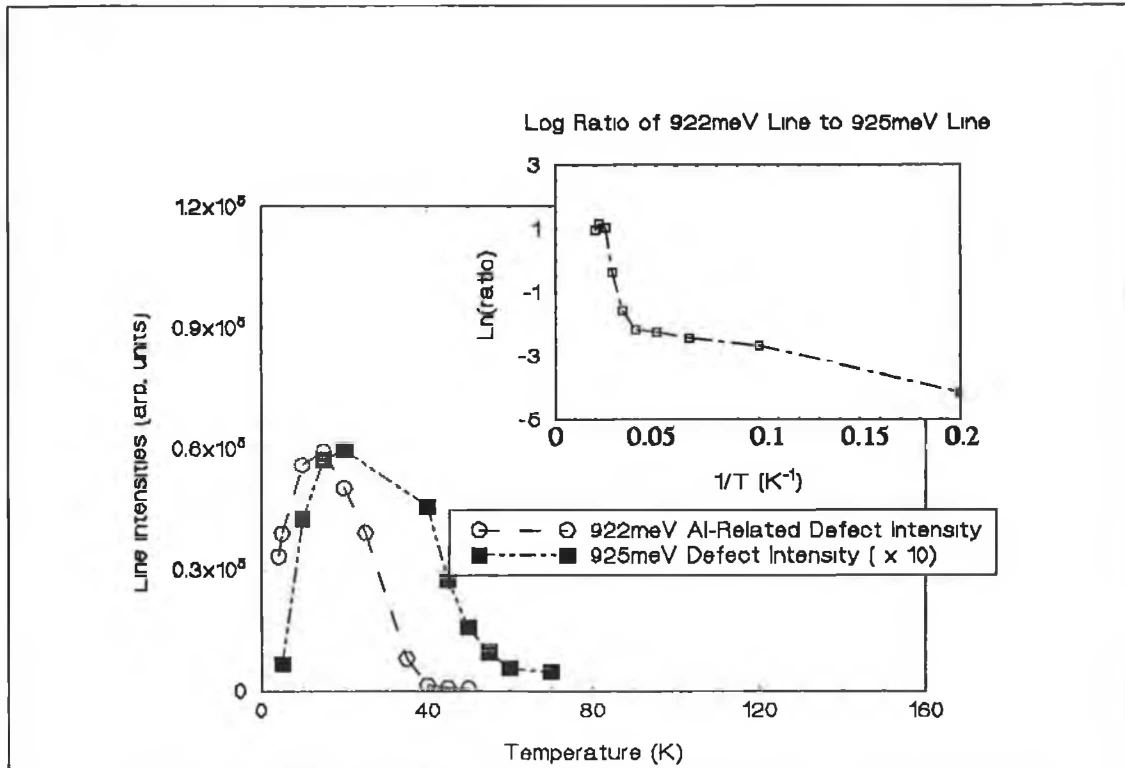

Figure 7.4.3: Comparison of 922meV Al-Related Line and 925meV Line as a Function of Temperature

7.5: Uniaxial Stress and Zeeman Spectroscopy of 922meV Line

<u>7.5.1 Uniaxial Stress Spectroscopy of 922meV Line:</u> Oriented Al-doped C-rich CZ silicon samples were prepared by annealing as described in section 7.2 above. The samples were oriented along the <001>, <111> and <110> directions. All the data shown were taken using an FT spectrometer and stress rig as described in chapter 3. No significant information was obtained from our attempts at measuring the polarisation of the stress-split components.

Stress parallel to the <001>, <111> and <110> crystal direction causes the ZPL to split into two, three and three components respectively. The fan diagrams and representative spectra are shown in figures 7.5.1 to 7.5.3. The ratios of line intensities will be discussed later in this section.

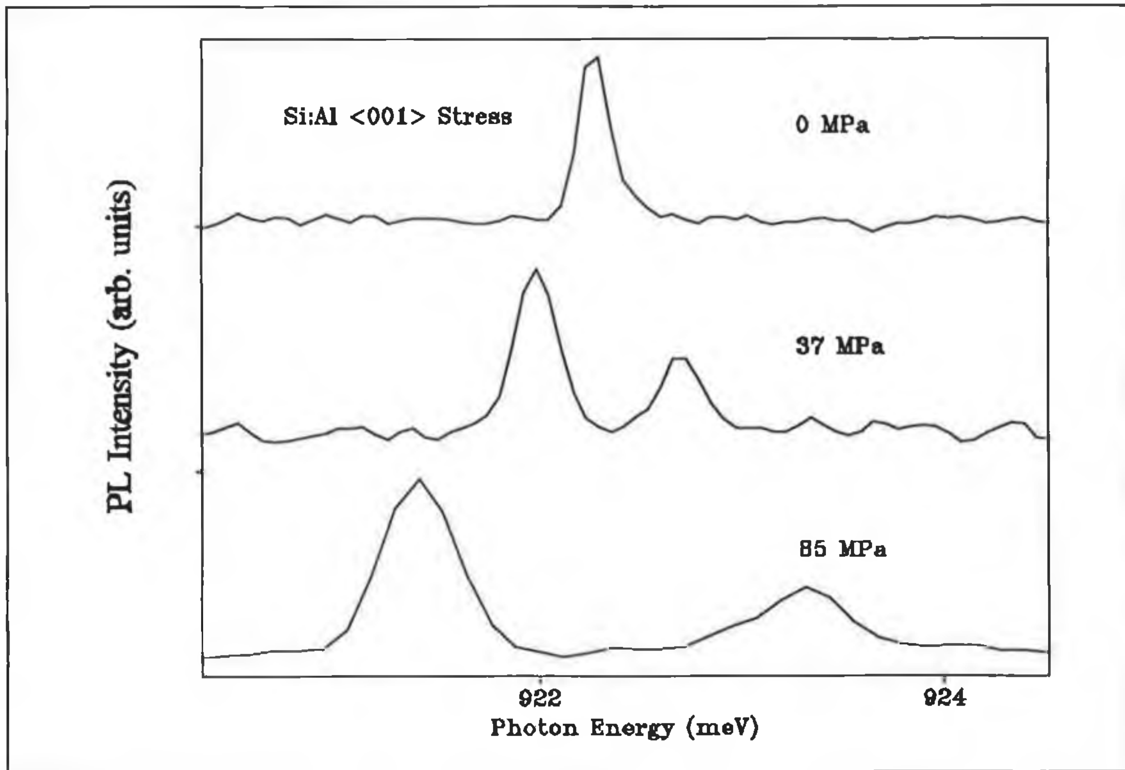

Figure 7.5.1 (a): Representative Spectra for <001> Stress

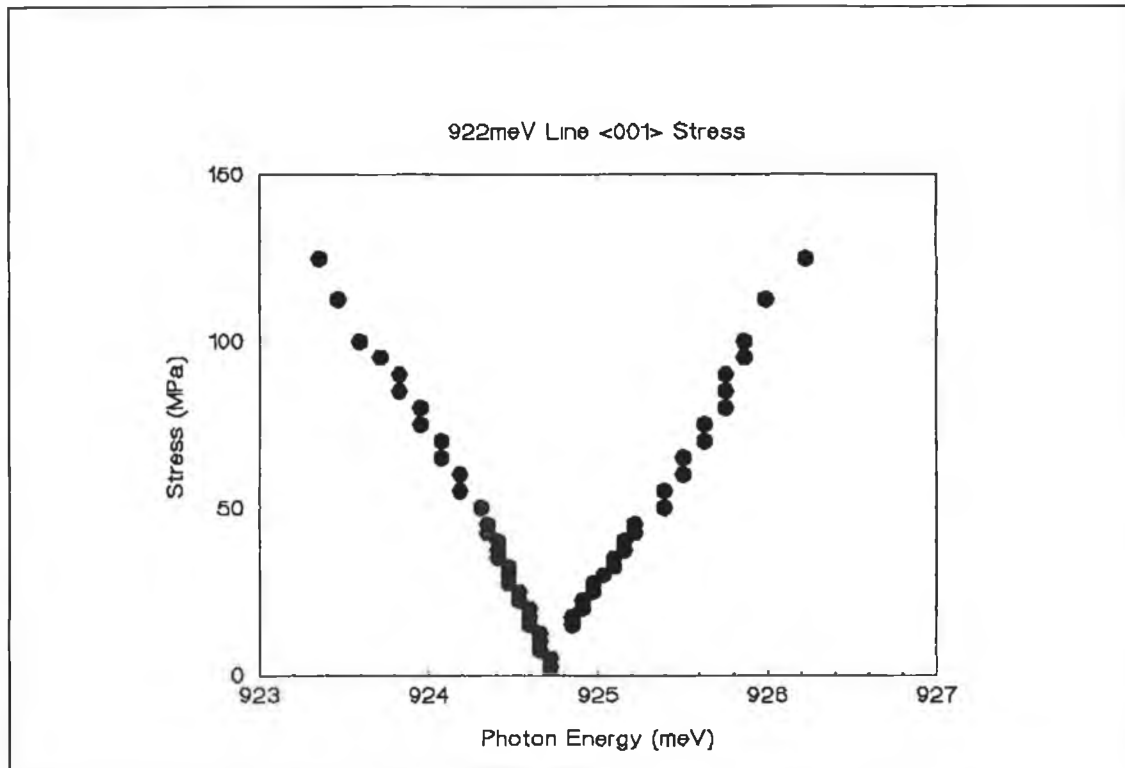

Figure 7.5.1 (b): Fan Diagram for <001> Stress

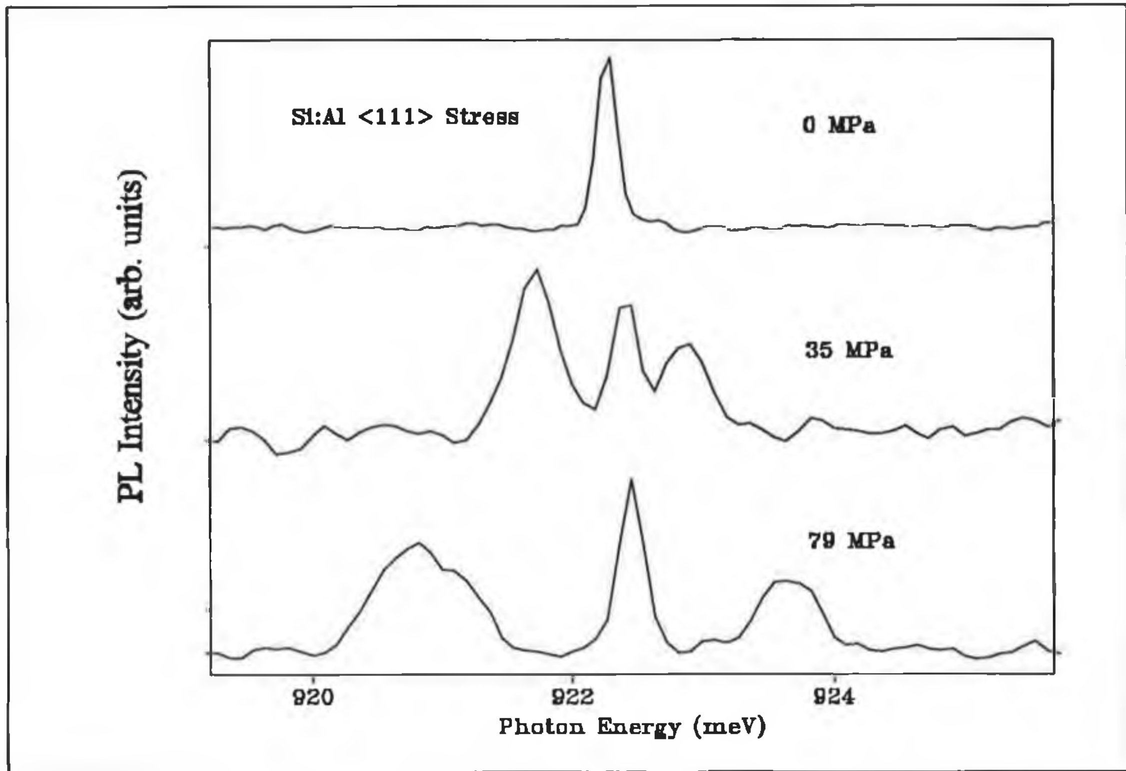

Figure 7.5.2 (a): Representative Spectra for <111> Stress

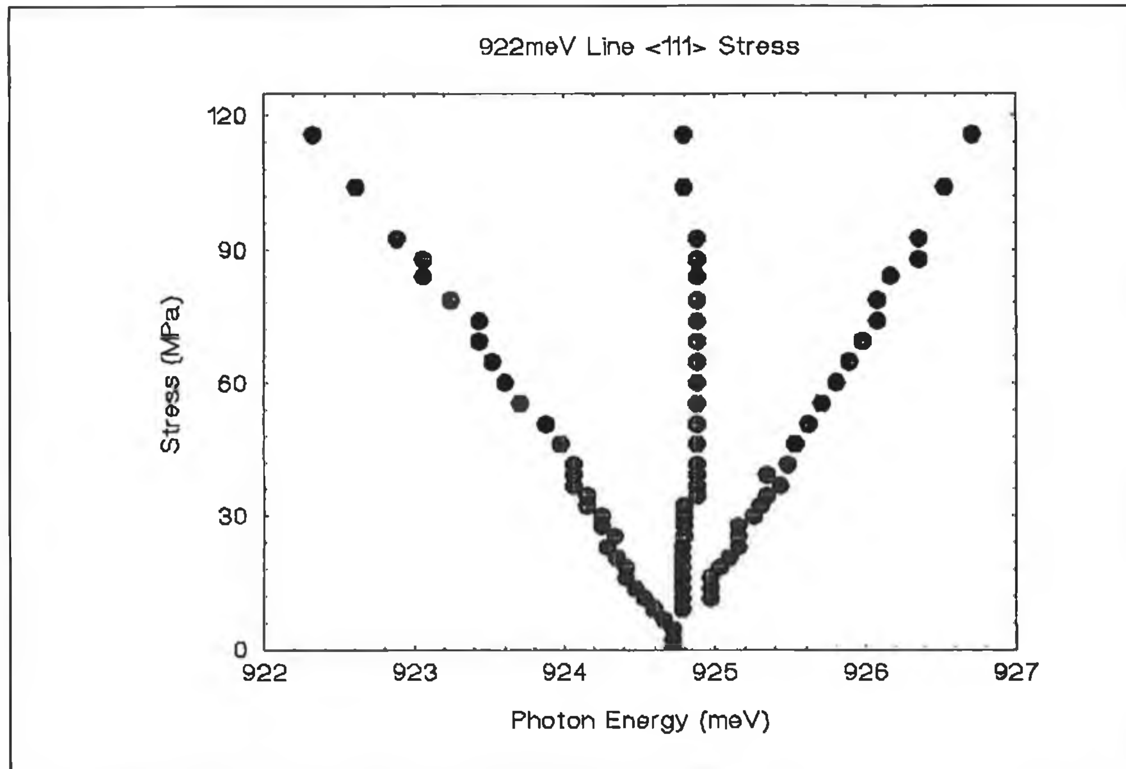

Figure 7.5.2 (b): Fan Diagram for <111> Stress

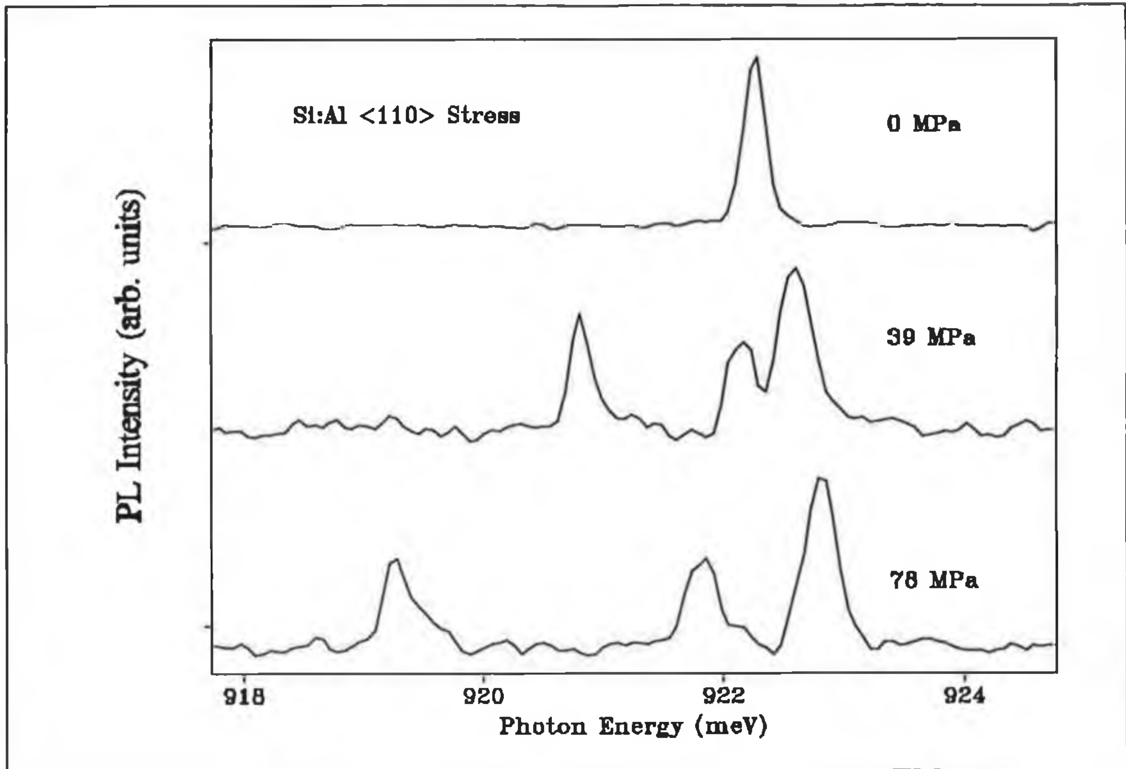

Figure 7.5.3 (a): Representative Spectra for <110> Stress

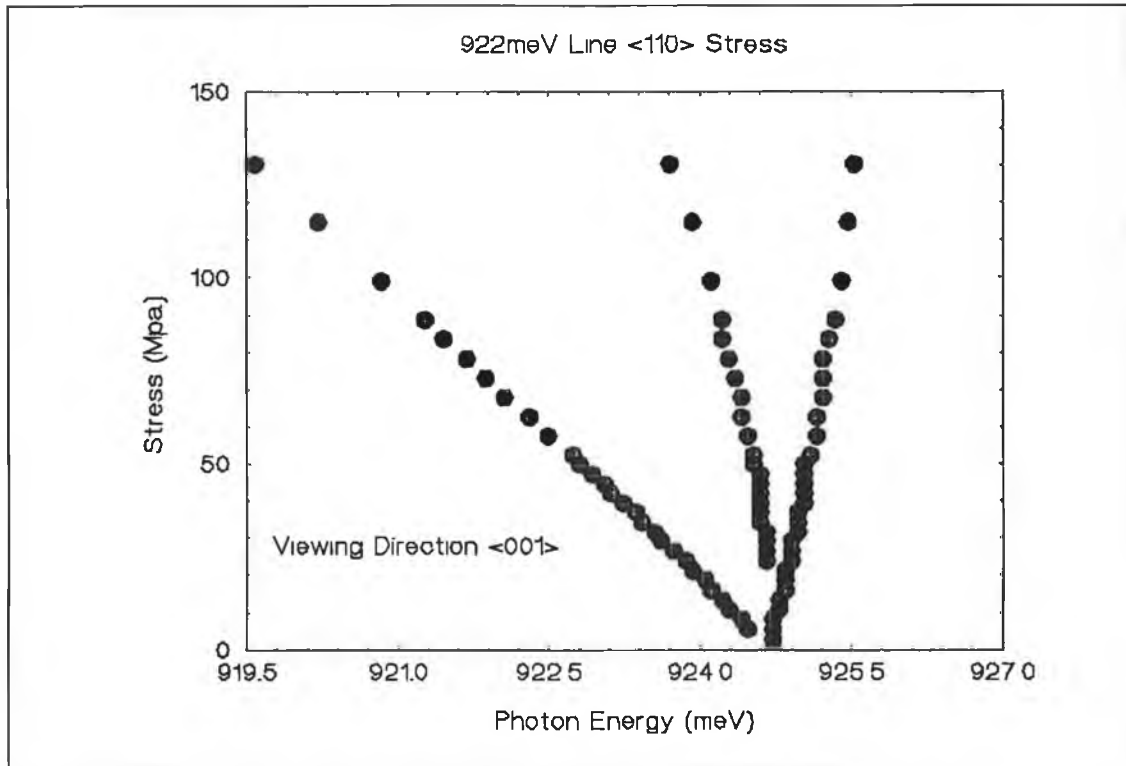

Figure 7.5.3 (b): Fan Diagram for <110> Stress

There is no evidence of interaction effects between excited states of the defect for the <001> and <111> directions in the stress range examined here. A small interaction effect is seen for one of the components under <110> stress, but is very small and will be neglected in our fitting procedure. The first step in the identification of the defect symmetry and transition type involves an inspection of the number of stress-split components in each direction. Comparing the data with the possibilities detailed by Kaplyanskii (1964), it is seen that no symmetry type produces a splitting of 2 in <100>, 3 in <111> and 3 in <110>. However, monoclinic I and trigonal A-E type transitions produce a splitting pattern of 2 in <100>, 3 in <111> and 4 in <110>. Best fits to the data using the equations for monoclinic I symmetry and trigonal A-E transitions (Mohammed *et al.* 1982) were attempted. Only the monoclinic I equations were found to produce a good fit to the data, as shown in figure 7.5.4.

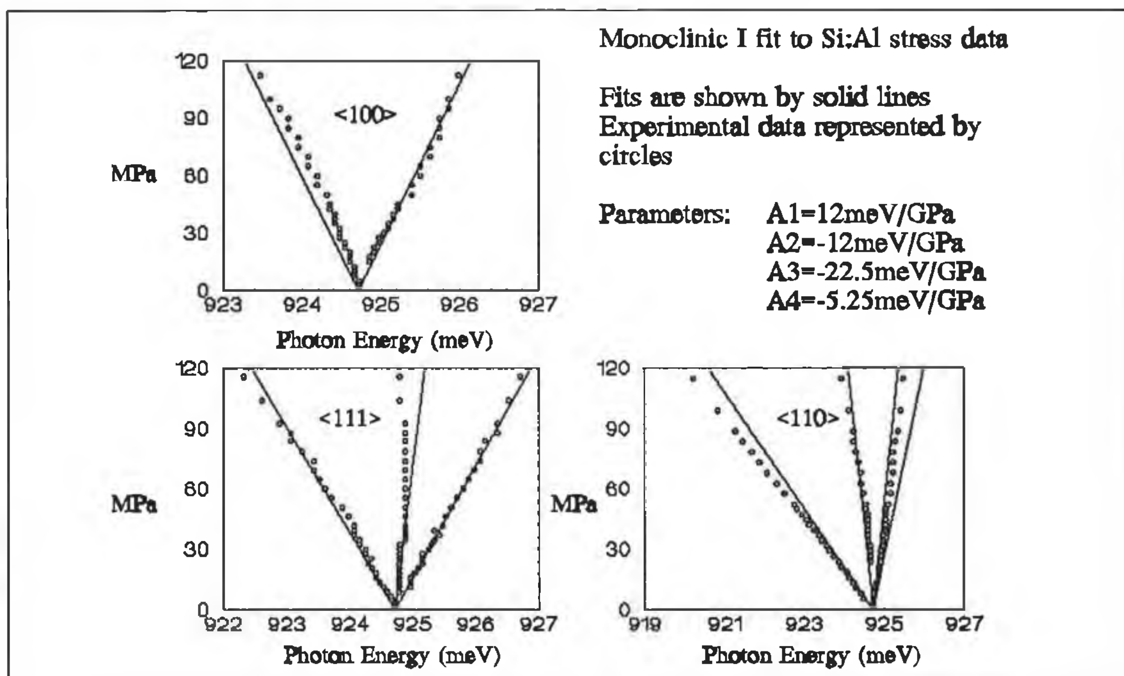

Figure 7.5.4: Monoclinic I Fit to Experimental Data Set

A good fit to the data is found for all stress directions. The stress parameters for the fit are;

A_1 = 12meV/GPa

A_2 = -12meV/GPa

A_3 = -22.5meV/GPa

A_4 = -5.25meV/GPa

Table 7.5.1 lists the experimental and theoretical shift rates for all the components of the 922meV centre using a monoclinic I fit.

In the <110> directions, the two highest energy components in the theoretical fit are quite close together (a line separation of 0.381meV compared with a line width of 0.385meV at 78MPa), consistent with the observation of only three lines under <110> stress. In addition, Zeeman measurements reveal that the transition is between purely spin-1/2 states, thus indicating non-degenerate states with quenched angular momentum. Defects with monoclinic I symmetry (C_{1h} type point group) can have only non-degenerate states (in the absence of accidental degeneracy).

Table 7.5.1

Monoclinic I fit to 922meV centre	Experimental Shift Rate (meV/GPa)	Theoretical Shift Rate (meV/GPa)
<100>	12.6	12
	-11.1	-12
<111>	17.5	18
	0.779	4
	-19.1	-19
<110>	6.66	10.5
		5.25
	-3.47	-5.25
	-39.4	-34.5

All these facts indicate that the defect has monoclinic I symmetry. By examining the defect intensities, it ought to be possible to confirm this identification

and also to establish the transition type. The intensity ratios of the stress split components in different directions are listed below in table 7.5.2, along with the expected values for an A-A type transition (dipole direction ‖ <$\bar{1}$10>, Mohammed *et al.* 1982, Jeyanathan 1994) and an A-B transition at a monoclinic I site.

Table 7.5.2

Stress Direction	Experimental (Stress < 20 MPa)	Theoretical Monoclinic A-A	Theoretical Monoclinic A-B
<100>	2.6 : 1	3 : 1	3 : 1
<111>	6 : 4.8 : 3.2	6: 5: 5	10 : 3 : 3
<110>	2 : 1.8 : (4)	2 : 4 : (4 + 2)	2 : 4 : (4+2)

The numbers in brackets in the <110> direction indicate the sum of intensity values of the two closely spaced lines. Although the experimental evidence is not entirely conclusive, it appears that the most likely candidate is an A-A transition type. In this case polarisation information would be very helpful in unravelling the origin of the different components. Further experiments are needed to obtain high quality polarisation information on the 922meV line.

We now describe data reported for Al-related defect at ~886meV seen in FZ silicon (annealed at 300°C) with very similar stress splittings (Irion *et al.*, 1988). The fan diagram from their paper is reproduced in figure 7.5.5 below. Interaction effects are seen at higher stresses, but the shift rates below 120MPa are linear. We have examined this fan diagram for low stresses (below 120 MPa), and the shift rates are reproduced in table 7.5.3 below together with the shift rates of the 922meV defect. It can be seen that the two sets of data are very similar, both in terms of numbers of components and shift rates. The fit to a monoclinic I centre by Irion *et al.*, shown in figure 7.5.5, is considerably poorer than the fit we obtain for the 922meV centre. The reason lies in the constraint imposed on their fit to ensure only three components in

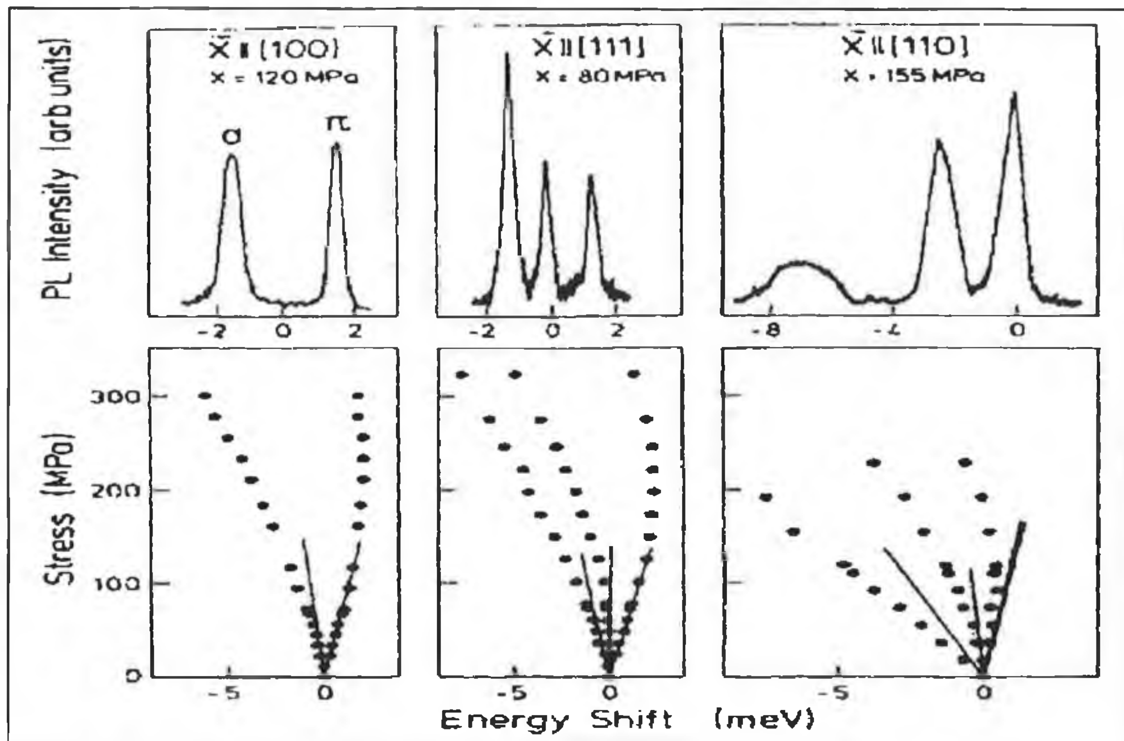

Figure 7.5.5: Fan Diagram of 886meV Defect (Irion *et al.* 1988)

the <110> data, whereas in our fit all four parameters were allowed to vary freely.

Table 7.5.3

Stress Direction	922meV Centre Shift Rate (meV/GPa)	886meV Centre Shift Rate (meV/GPa)
<001>	12.6	11.9
	-11.1	-13
<111>	17.5	16
	0.779	0
	-19.1	-16
<110>	6.66	7.9
	-3.47	-10
	-39.4	-40

The published values of the parameters for the 886meV line are;

A_1=13.5meV/GPa ; A_2=-8meV/GPa ; A_3=-16.5meV/GPa ; A_4=6.5meV/GPa which are quite similar to those for the 922meV line, the differences being due to the constraints placed on the <110> fit.

The 886meV line is associated with an A-A transition at an Al-related centre of monoclinic I symmetry. The chemical identity of the centre is tentatively proposed as an Al_i-Al_s (interstitial-substitutional) complex. The similarity of the stress behaviour suggests a link between the two centres, because the electronic perturbation operators are very similar for both defects. The model for the 922meV defect proposed by Drakeford *et al.* (1988) of an Al-C complex is a plausible candidate.

Further investigations of the link between the 886meV and 922meV defect are required in order to understand the mutual relationship between the two defects. One area in which detailed experiments are planned is Zeeman spectroscopy of the 922meV defect, and preliminary Zeeman results are presented in section 7.5.2.

7.5.2 Zeeman Spectroscopy of the 922meV Line: Zeeman measurements on the 922meV line with magnetic fields of up to 5T in the <001> direction have shown neither a line shift nor splitting. These experiments were performed on a grating spectrometer at the University of Aveiro, and the resolution of the instrument was ~0.5meV. This indicates that the 922meV transition is from a spin 1/2 electron state to a spin 1/2 hole state. A very similar conclusion is drawn for the 886meV defect (Irion *et al.* 1988) electronic structure. However, Irion *et al.* worked with much higher resolution and were able to resolve very weak sidelobes beside the ZPL corresponding to (ideally forbidden) transitions from m_s=+1/2 to m_s=-1/2 states. The splitting pattern and energy level structure are shown in figure 7.5.6. The presence of these additional features indicates that orbital angular momentum has been weakly mixed back into the states, relaxing the spin selection rule. They were also able to resolve fine structure in the ZPL which was attributed to the anisotropic g-factor of the hole. Because the side lobe splittings are so small (~0.5meV at 5T) and their intensities are so weak (~1/20th of the ZPL) in the 886meV line, similar effects would have been undetectable in our experiments on the 922meV line. Further experiments at higher magnetic fields (up to 9T) using an FT spectrometer are planned (see chapter 8) in

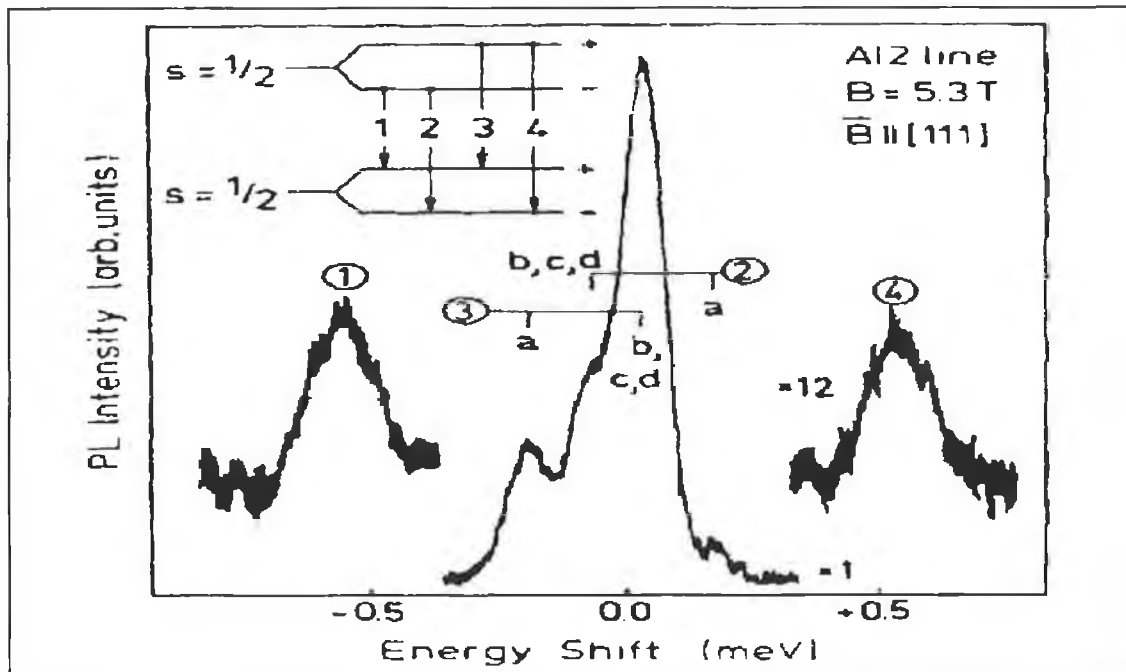

Figure 7.5.6: Zeeman Splitting of 886meV Line with Level Identification (Irion *et al.* 1988)

order to examine the fine structure of the 922meV line under magnetic fields in more detail. Irion *et al.* (1988) have attributed the 886meV defect to a monoclinic I centre reorienting around a trigonal (<111>) axis on the basis of their stress and Zeeman measurements, and a comparison of the behaviour of the 922meV defect with this should prove helpful in determining the relationship between the two defects.

7.6: Conclusion

In this chapter, results on an Al-related defect observed in C-rich CZ silicon have been described. The defect is produced by anneals in the temperature range 450°C-550°C.

Temperature dependence studies have shown that the thermal binding energy of the defect is low (~15meV), but no thermalising excited states of the defect have been observed. Uniaxial stress measurements reveal that the defect occupies a site of

monoclinic I symmetry, and indicate that the transition type is most probably A-A. Further work on the identification of the transition type (including polarisation effects) is required. Similarities between the stress splitting pattern of the 922meV line and another Al-related line at 886meV have been presented, which are suggestive of a possible link between the centres (discussed later in this section). Magnetic field studies indicate that the 922meV line is due to a transition from a spin-like excited state to a spin-like ground state. Similar experiments on the 886meV line result in the same conclusion, but because of the higher resolution used in measuring the data for the 886meV data, greater information on the fine structure of the line is found. High resolution magnetic field experiments on the 922meV defect are planned in order to further examine the similarities between the two centres.

Although the form of the phonon sideband has been published by Drakeford *et al.* (1988), we have not been able to examine the vibronic properties of the defect because of water vapour absorption effects.

At present the evidence for the involvement of Al and C in the 922meV centre is circumstantial. Experiments such as C and Al isotope substitution (initially performed with negative results by Drakeford *et al.* 1988) need to be repeated. Other methods of monitoring the C content (both interstitial and substitutional), such as IR absorption, are needed to understand the behaviour of C in Al-rich material.

C-modified complexes have been reported for both Li_4 (Lightowlers *et al.* 1984) and Be_2 (Labrie *et al.* 1987) centres in silicon. Strong similarities between the Li_4-C complex and the Li_4 complex (Davies *et al.* 1984 a) and the Be_2-C and Be_2 complexes (Labrie *et al.* 1984) have been reported. These results are interpreted as being due to a perturbation of the Li_4, Be_2 complex by replacement of a neighbouring Si atom with a C atom and a systematic shift in the ZPL position of the defect complexes with and without C is observed for Li_4 and Be_2. If the 922meV defect is assumed to be an Al-C complex obtained by replacing a neighbouring Si atom at the 886meV complex with a C atom, this trend in ZPL energy is continued, as shown in table 7.6.1.

From the data presented above it appears that the model of the 922meV centre as an Al-C centre similar to the 886meV Al-related centre is a plausible one. Further experiments are needed to examine the validity of this interpretation.

Table 7.6.1

Atomic Species	Complex without C ZPL (meV)	C modified complex ZPL (meV)	Fractional ZPL Change
Be	1076	1117	3.8%
Li	1044	1082	3.6%
Al	886	922	4%

References

G. Davies, L. Canham and E. C. Lightowlers (1984 a). J. Phys. C **17**, L173.

G. Davies, E. C. Lightowlers, R. A. Woolley, R. C. Newman and A. S. Oates (1984 b). J. Phys. C **17**, L499.

A. C. T. Drakeford and E. C. Lightowlers (1988). Defects in Electronic Materials Symp., Boston MA. USA. Mater. Res. Soc., 209.

E. Irion, N. Burger, K. Thonke and R. Sauer (1988). Phys. Rev. B **38**, 13079.

L. Jeyanathan (1994). Ph.D. Thesis, University of London.

A. Kaplyanskii (1964). Opt. Spectroscopy **16**, 329.

D. Labrie, T. Timusk and M. L. W. Thewalt (1984). Phys. Rev. Lett. **52**, 81.

D. Labrie, I. J. Booth, S. P. Watkins and M. L. W. Thewalt (1987). Solid State Commun. **63**, 115.

E. C. Lightowlers, L. T. Canham, G. Davies, M. L. W. Thewalt and S. P. Watkins (1984). Phys. Rev. B **29**, 4517.

N. Magnea, A. Lazrak and J. L. Pautrat (1984). Appl. Phys. Lett. **45**, 60.

K. Mohammed, G. Davies and A. T. Collins (1982). J. Phys. C: Solid State Physics **15**, 2779.

Chapter 8: Conclusions and Suggestions for Further Work

8.1: Conclusions

The main purpose of the research described in this thesis has been to examine defects in silicon involving principally the group II impurity Cd and one additional Al-related defect.

Cadmium-Related Defects: The main focus of the research centred on the complexing of the group II element Cd with O in silicon. Three previously unreported PL systems with ZPL at 1026meV, 983meV (Cd_A) and 935meV (Cd_B) in Cd-implanted CZ silicon annealed at 550°C were described. Measurements as a function of temperature reveal that the behaviour of each defect is consistent with a model where one particle is tightly bound with the other particle bound in the primary particle's Coulombic potential. The thermal binding energy is the same (within experimental error) for all the defects (~15meV) and corresponds roughly to the free exciton binding energy (~14meV, as discussed in chapter 2). Only the 1026meV system is found to possess more than one excited state, at ~1.1meV above the 1026meV line. Uniaxial stress measurements on the 1026meV and 983meV systems reveal low symmetry rhombic I defect sites. Preliminary uniaxial stress measurements on the 935meV system point towards a monoclinic I symmetry site for that defect. None of the defect systems show any shift or splitting in magnetic fields up to 5T. All the defects appear to conform to a pseudodonor model, with a tightly bound hole and a loosely bound electron.

Examination of the phonon sidebands for the 1026meV and 983meV defects reveals a radically different behaviour between the two defects. The 983meV system couples weakly to lattice modes and to a single low energy local mode (~9.5meV) with Huang-Rhys factor ~0.01. The 1026meV system couples strongly to two low energy (6meV and 9meV) local modes (and coupling to lattice modes appears negligible) with Huang-Rhys factors of ~0.6 and 0.4 respectively. This indicates that the microscopic environments of the two defects are very dissimilar, despite the fact that they both have rhombic I symmetry. Examination of the anti-Stokes sideband of

the 1026meV system reveals a large reduction in the local mode frequency of the excited state.

Isotope substitution experiments reveal that a single Cd atom is present in all the defects. A positive cadmium isotope shift of ~0.1meV (^{106}Cd-^{116}Cd) is seen for the ZPL of all the defects. Comparison of this isotope shift with the theoretically predicted value (based on the values of the phonon quanta in the excited and ground states) for the 1026meV system gives excellent agreement. All three defects are seen exclusively in CZ silicon, and therefore are assumed to be O-related. Based on our investigations no evidence is found for the involvement of the common impurities C and H in any of the defects. The defect production also appears unaffected by the conductivity type of the starting material. All three defects are therefore assigned to Cd-O complexes.

In order to take a more global view of the behaviour of Cd in silicon, we must compare our results with those obtained for the other group II elements Zn and Be and also to previous results reported for Cd-doped silicon. Pseudo-donor complexes at sites of rhombic I symmetry have been reported previously in both Be and Zn-doped silicon (Daly 1994, Henry *et al.* 1994), and in all these cases the thermal binding energy of the defects is small. A comparison of the Cd_A centre with the previously reported Zn_A centre (Henry *et al.* 1994) is particularly interesting. The defects show very similar behaviour under uniaxial stress, both in terms of the values of the stress parameters which are equal (within $\pm$ 5%) and also in terms of the relative intensities of the stress-split components. In both cases the ZPL are unaffected by magnetic fields up to 5T. A positive isotope shift of the ZPL is observed for both defects, and the behaviour of the local mode phonon of both systems is particularly striking. If the Cd atomic mass is replaced by the Zn atomic mass in equation 4.7.1, the Zn_A local mode phonon energy is reproduced exactly. This indicates a very similar atomic environment for the group II element in both cases. The Cd_A and Zn_A defects are seen only in CZ silicon, and both are assigned to O complexes with the group II element. The only notable difference between the two luminescence systems is that the Zn_A system has a thermalising excited state, whereas no evidence is seen of such a state for the Cd_A system. The above evidence leads us to conclude that the Cd_A defect system is the Cd-related analog of the Zn_A system. The Cd_B defect has not been studied in detail as yet, but preliminary investigations lead us to believe that it might show similarities to the

Zn_B system (Henry *et al.* 1994). The 1026meV defect, with its distinctive phonon sideband, does not appear to have any clear analog with any of the defects studied as yet in Zn-implanted or Be-implanted CZ silicon.

Previous measurements on the energy levels on Cd-doped silicon have been summarised in chapter 1. The measurements of Lang *et al.* (1991) on Cd-doped CZ silicon are of particular interest. Apart from the acceptor-related levels at E_v+485meV and E_v+450, these authors found evidence for two other unidentified Cd-related levels at E_v+200meV and E_v+205meV. In the case of all the Cd-related defects studied in this thesis, the hole is found to be the tightly bound particle, with a binding energy of ~173meV for Cd_A, 217meV for Cd_B and 127meV for the 1026meV centre. The values of the primary particle binding energy for Cd_A and Cd_B are both quite close to the energy levels measured by Lang *et al.*, the difference being ~30meV for Cd_A which is of the same order of magnitude as the relaxation energy for the defect (35meV). In addition the samples used by Lang *et al.* were subject to heat treatments similar to those used for the Cd_A and Cd_B defects. These facts lead us to suspect that the levels observed by Lang *et al.* are connected with the Cd_A and Cd_B defects, and a fresh examination of these defects using DLTS should prove helpful in examining the connection.

Aluminium-Related Defect: The study of the Al-related defect (with ZPL at ~922meV) has centred on the behaviour of the defect as a function of temperature, uniaxial stress and magnetic fields. The 922meV defect has a low thermal binding energy of ~15meV and this indicates that the defect consists of one tightly bound and one loosely bound particle. Uniaxial stress results indicate that the defect occupies a site of monoclinic I symmetry. No shift or splitting of the ZPL is seen in magnetic field up to 5T. All these results point towards a pseudodonor model for the defect. The stress splitting pattern for the 922meV system is surprisingly similar to a previously-reported Al-related centre (Irion *et al.* 1988), although the intensities of the stress split components are different in the two cases. No investigation of the relationship (if any) between the two centres has yet been made.

Previous studies of this defect by Drakeford *et al.* (1988) have indicated that this defect consists of an Al-C complex. Attempts at C isotope substitution and Al

diffusion have failed to produce this defect and thus no definitive evidence of the chemical identity of the defect has been established Drakeford *et al.* (1988). No attempt has yet been made in the course of our research to investigate the chemical identity of the 922meV system or its formation kinetics.

8.2: Suggestions for Further Work

Although the Zeeman analysis carried out on the defects in chapters 4, 5, 6 and 7 reveals no splitting under a magnetic field in the <100> direction, the behaviour in other crystal directions has not yet been analysed. As was explained in chapter 4, the majority of evidence indicates that the lines will not split in the <111> and <110> directions either. Persistent difficulties with the high-field (9T) superconducting magnet at D.C.U. have limited our experiments to low resolution scans on the <001> direction. Experiments carried out at the University of Aveiro have been performed on a grating spectrometer on the Cd_A line only in the <001> direction. A high-resolution FT spectrometer is the ideal instrument for these experiments and combined with the high-field magnet should allow a detailed investigation of the spectral lines, similar to that carried out by Irion *et al.* (1988) for the 886meV Al-related defect. High resolution Zeeman studies of this nature can give details on the nature of the bound particles, and can be used to investigate the models presented in chapter 2, and the deviation of the systems under examination from these models, in terms of orbital admixtures into the wavefunctions etc..

Completion of the uniaxial stress experiments on the excited state in the 1026meV system (at higher temperatures) and the Cd_B line are also required for a more complete understanding of the nature of these defects. Good polarisation data are required for all the defects to allow an unambiguous identification of the transition type.

O isotope samples are at present under preparation to investigate the O content of the three Cd-related defects. In addition it will be necessary to attempt to create the Cd-related defect systems by Cd diffusion into CZ silicon, rather than by implantation, in order to rule out the possibility of heavy-ion damage in the defect formation.

Furthermore, the formation conditions for the 935meV system must be firmly established. Experiments are also necessary to unambiguously establish the chemical identity of the 922meV centre in Si:Al, as discussed in chapter 7.

At present the construction of a dry N_2 chamber to house the cryostat is being planned to eliminate the water vapour absorption features seen on the spectra at ~919meV. This would allow us to examine the full phonon sidebands of the Cd_A, Cd_B and 922meV Al-related defect systems.

PLE measurements are required to study the excited state structure of the defect systems, and these measurements would also ideally be carried out in conjunction with uniaxial stress and Zeeman spectroscopy to provide a wider view of the defect behaviour.

One of the most important areas which requires study is the relationship between the Cd_A, Cd_B and Zn_A, Zn_B (Henry *et al.* 1994) defect systems. Strong evidence has been presented in chapter 4 for the theory that the Cd_A defect is a Cd-related analog of the Zn_A defect. In addition to examining the link between the Cd_A and Cd_B defects, which has been outlined in chapter 4, the relationship between the Cd_B and Zn_B defects must be studied to ascertain whether the Cd_B defect is a Cd-related analog of the Zn_B defect as suspected.

The complexing of O with impurities in silicon is an important issue in silicon science. The use of CZ wafers for VLSI chip technology and the increasing demands for even larger scale integration requires a detailed understanding of the processes by which O complexes with trace impurities in silicon. Firstly, these O-related complexes have potential applications in controlling the harmful effects of O on device manufacture (as described in chapter 1) and secondly, the behaviour of O and its complexing with impurities could also shed light on the origin of the various thermal donor species. It is hoped that the work presented here will contribute in some small way to the broader picture regarding the behaviour of O in silicon.

References

S. E. Daly (1994). Ph.D. Thesis, Dublin City University.

A. C. T. Drakeford and E. C. Lightowlers (1988). Defects in Electronic Materials Symp., Boston MA. USA. Mater. Res. Soc., 209.

M. O. Henry, J. D. Campion, K. G. McGuigan, E. C. Lightowlers, M. C. doCarmo and M. H. Nazare (1994). Semicond. Sci. and Technol. **9**, 1375.

E. Irion, N. Burger, K. Thonke and R. Sauer (1988). Phys. Rev. B **38**, 13079.

M. Lang, G. Pensl, M. Gebhard, N. Achtziger and M. Uhrmacher (1991). Appl. Phys. A **53**, 95.

Appendix A: Sample Preparation, Cleaning and Annealing

This appendix contains information on the preparation, cleaning and annealing procedures used throughout the course of the thesis.

Sample Cleaning: The samples were cleaned using the chemical cleaning procedure outlined below (known as an RCA clean);

1. Boil in methanol
2. Rinse in cold methanol
3. Boil in trichloroethylene
4. Rinse in cold methanol
5. Rinse in de-ionised (DI) water
6. Boil in NH_4OH : H_2O_2 : H_2O :: 5 : 1 : 1
7. Rinse in DI water
8. Boil in HCl : H_2O_2 : H_2O :: 5 : 1 : 1
9. Rinse in DI water x 3
10. Blow dry

Sample Etching: Samples were etched (if necessary for non-wafer samples prior to implantation etc.) using the following procedure;

1. Clean the sample using the RCA procedure described above
2. Place the sample in a 10 : 1 solution of HNO_3 : HF at room temperature, which is being constantly agitated (with a PTFE magnetic stirrer). A rule of thumb for etch depths is ~2μm is removed in 30s.
3. Rinse well in DI water
4. Blow dry

Sample Annealing: Samples were annealed using the equipment and procedures described below;

After cleaning and etching as described above the samples were placed in a 8mm inner diameter quartz tube (Heraeus semiconductor grade quartz tube was used), and this tube was connected to an argon gas line to provide a flowing argon atmosphere. This tube was then placed inside a 17mm inner diameter quartz liner tube (to prevent contamination from impurities in the furnace reaching the sample. The tube was then placed in a Carbolite/Eurotherm furnace (with temperature control accurate to ±5°C) for the appropriate length of time (usually a half-hour). Upon completion of the anneal the quartz tube was carefully withdrawn from the furnace and the samples allowed to cool slowly. If a higher cooling rate was desired the samples could be immediately dropped into an isopropanol/water solution. A schematic diagram of the apparatus is shown in figure A.1.

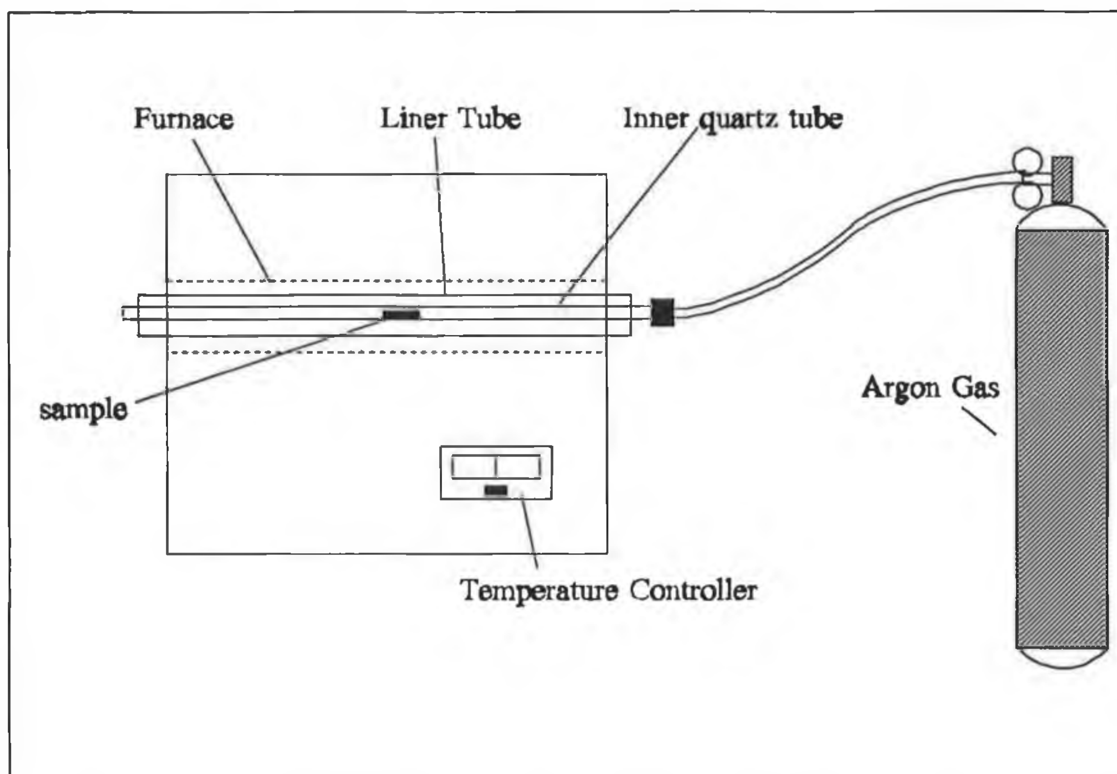

Figure A.1: Schematic Diagram of Equipment used in Annealing Procedures